Hahn-Meitner-Institut Berlin
in der Helmholtz-Gemeinschaft

Annual Report 2003
Selected Results

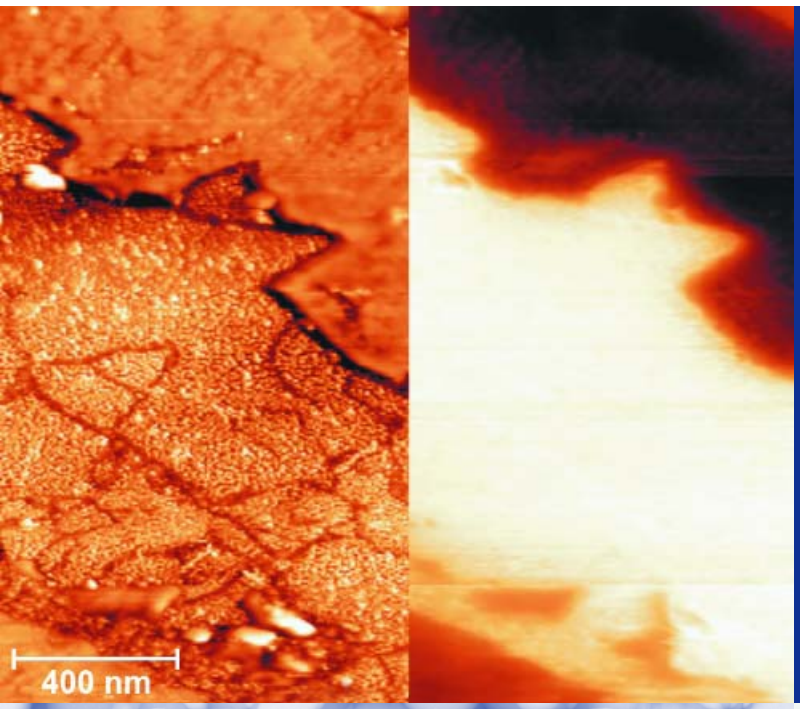

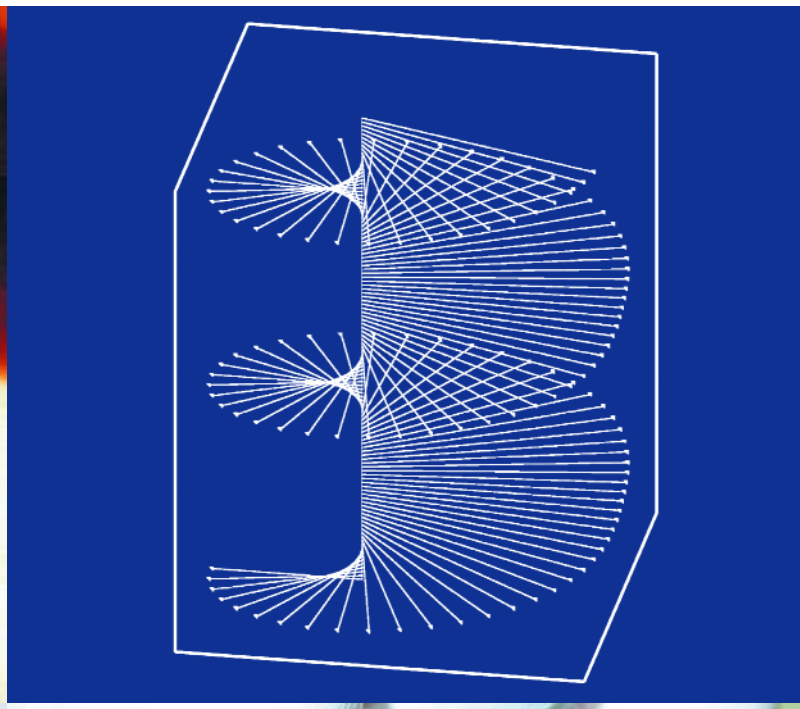

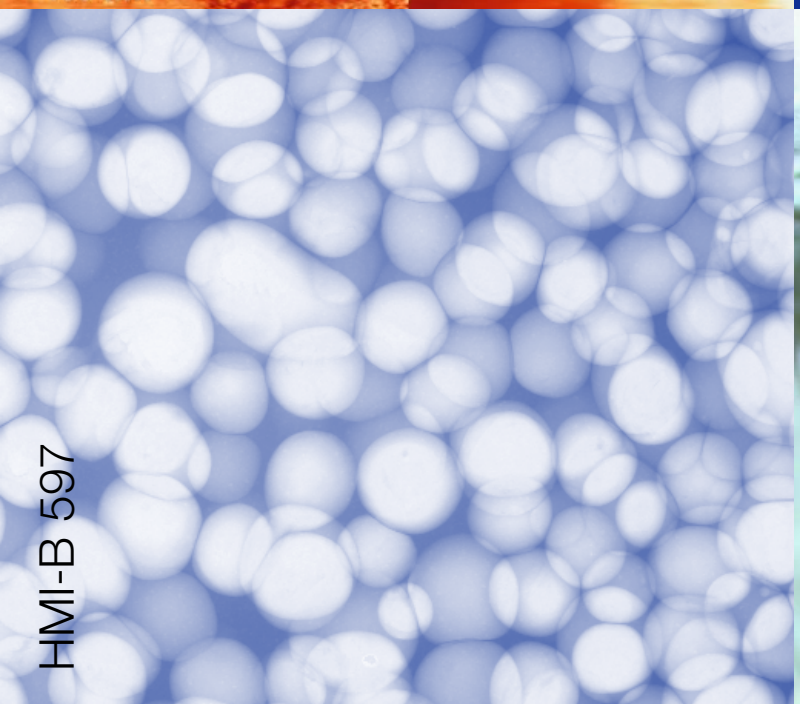

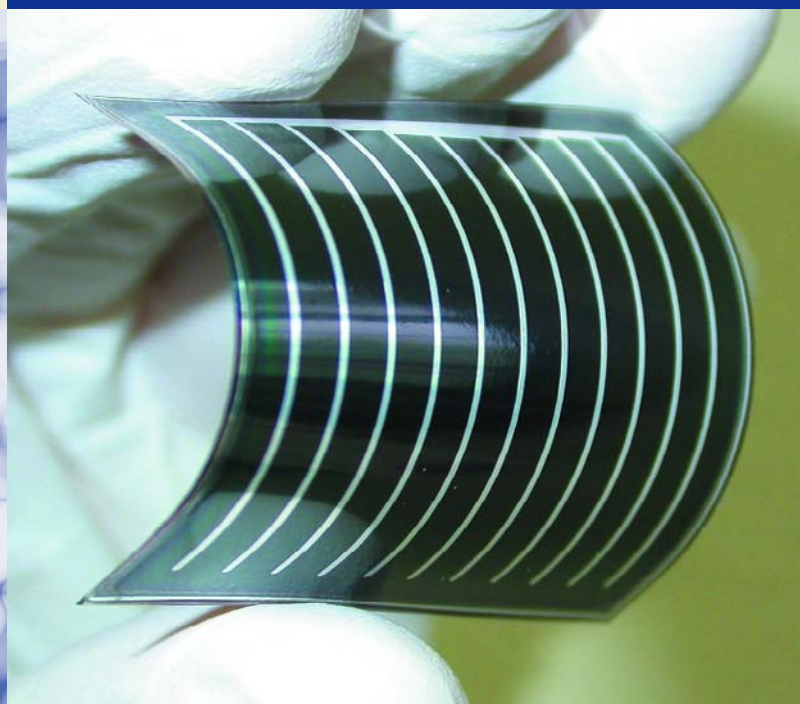

HMI-B 597

Legend to Cover Figures:

top left: Image of a $CuGaSe_2$ solar cell cross section ($1000 \times 2000\ nm^2$): topography (left); workfunction (right).
top right: Magnetic spiral in $CsCuCl_3$ at $7\ T$.
bottom left: An x-ray radiograph of a $10\ mm$ slice of aluminium foam.
bottom right: Flexible solar cell based on $Cu(In,Ga)Se_2$ (area $16\ cm^2$) on titanium foil.

Annual Report 2003
Selected Results

Hahn-Meitner-Institut
Berlin, 2004

Table of contents

HMI in brief

The **Hahn-Meitner Institute** (HMI) in Berlin is one of Germany's leading centres for research on solar-energy conversion, condensed matter and materials science. It has approximately 750 employees, including almost 400 scientists – most of them physicists and chemists. Most of the institute's annual budget of roughly 70 Million € is provided by the German Federal Government and the City of Berlin in a ratio of 9 to 1. HMI is member of the Helmholtz Association of National Research Centres, an organization comprising fifteen of Germany's largest scientific institutions.

Scientific work at HMI is organized in two divisions reflecting the two main fields of scientific activity: Solar-Energy Research and Structural Research.

Solar-energy research at the HMI is the largest effort in the field of sustainable energy within the Helmholtz Association and comprises approximately 25 % of HMI's research and development efforts. As an interdisciplinary activity between solid state physics, materials science, optics and interfacial chemistry, it aims at creating scientific and technological preconditions for significantly increasing the contribution of sustainable energy to our energy supply over the next decades. This activity is taking advantage of an already well balanced research infrastructure and the unique measurement opportunities provided by the large-scale facilities operated at HMI.

At the centre of the solar-energy research at HMI are materials and concepts for thin-film solar cells – activities covering the entire spectrum from basic research to the design of actual devices. The focus is on the currently most promising new technologies, namely thin-film polycrystalline silicon and compound semiconductors of the I-III-VI_2 and III-V type. Research projects aim at the development of efficient photovoltaic solar cells allowing for substantial cost reductions of solar power generation. The strategy is to develop existing thin-film technologies to a state of maturity and, in parallel, to explore new materials and concepts for solar cells of the future e. g. nano-composite crystalline materials.

Structural Research at HMI groups around three large scale facilities providing three complementary probes to investigate structures and materials – neutrons, fast ions and synchrotron radiation. The three facilities are the 10 MW research reactor BER II with the Berlin Neutron Scattering Center BENSC, the accelerator complex of the Ion Beam Laboratory ISL and the 3rd generation electron synchrotron BESSY. BER II and ISL are run by HMI on the institute's grounds in Berlin Wannsee. At BESSY, an independent research institution in Berlin Adlershof, HMI operates several experimental stations designed for the particular requirements of structural research.

All facilities are in the first place operated for a national and international user community. About 70 % of the beam time at the instruments is provided to scientists from other research institutes, universities and industry from Germany and from abroad. It is the HMI policy to provide these users, if necessary, with full scale technical and scientific support, this way enabling them to make best possible use of the facilities.

Fields in the focus of Structural Research at HMI are magnetic phenomena, properties and design of engineering components and materials, soft matter and biological systems. Roughly a quarter of the beam time at ISL is used for the therapy of tumours in the eye using 70 MeV protons.

A particular highlight among the HMI activities are neutron scattering studies of samples in extremely high magnetic fields and/or very low temperatures made possible by the institute's unique expertise on sample environment equipment.

Foreword

We are proud to present to you the Annual Report 2003 of the Hahn-Meitner Institute in its new format: we have selected highlights out of a large number of results in order to show the breadth and high quality of the Institute's research. This report presents results achieved by both the scientists employed at HMI and the users of our facilities. It is this combination of in-house and collaborative research, which is the backbone of the top-science produced in the Hahn-Meitner Institute.

For HMI, 2003 marked a further step on the road towards the new – *programme-oriented* – funding system of the Helmholtz Association. For our activities in the research field *Health*, it was the first year under the new funding. The Solar-Energy Division very successfully passed the evaluation of its proposed programmatic strategy for the coming five-year period. The Structural Research Division around our large-scale facilities had to prepare for its evaluation scheduled for April 2004.

We do sincerely hope that after the evaluation of the Structural Research years without evaluations of this kind will follow. It is essential that in the coming years doing science will again become the top priority of our work.

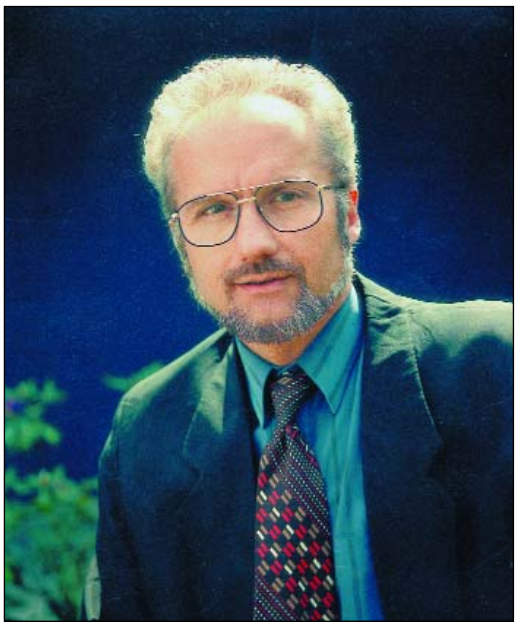

Thanks to the very high motivation of all the staff at HMI and the guests and collaborators from outside 2003 was a very successful year, despite all the additional work load caused by the evaluations. This motivation is most gratefully appreciated.

2003 has seen the beginning of activities, which will secure the top position of HMI's research and the research opportunities for guests: reappointments have been prepared in the Solar-Energy Division – they should bear fruit in 2004; in the Structural-Research Division, the foundation was laid for the construction of a second neutron-guide hall – the prerequisite for the installation of two new neutron-scattering instruments, which will further strengthen the profile of our BENSC operation.

We are sure that the scientific results of 2003 and the strategic planning prepared for the evaluation constitute an excellent basis for further strengthening HMI's scientific programme and its standing in the community.

Thanks are not only due to the HMI staff for their excellent work, but also to the funding authorities, the Federal Government, in particular the Federal Ministry of Education and Research (BMBF), the Senate of Berlin and all the third party funding agencies for their continuing support.

Michael Steiner
Scientific Director

Main entrance of the lecture-room of the Hahn-Meitner Institute

News and Events 2003

■ HMI-theorist Martin Falcke receives the 2003 Erwin Schrödinger Prize

Calcium waves participate in almost all processes in living organisms: from fertilization through muscle contraction and secretion to cell death. These waves – areas of increased concentration of calcium ions – travel across any biological cell relaying information that arrives from outside the cell to organelles inside. During their journey across the cell, the waves behave in very characteristic ways: they form typical spiral patterns and avoid certain frequency ranges, i.e., any wave attempting to travel at one of those frequencies is damped immediately.

After the ceremony: The Schrödinger laureates with representatives of the prize awarding institutions. From left to right: Prof. Dr. Walter Kröll – President of the Helmholtz Association, Dr. Arend Oetker – President of the Stifterverband, the laurates Prof. Patricia Camacho, Prof. James D. Lechleiter – University of Texas, San Antonio, Dr. Martin Falcke – HMI, Prof. Dr. Karin Mölling – Chairwoman of the Schrödinger-Prize Jury

The surprising properties of calcium communication in living cells is the central topic of the scientific collaboration of the theoretical physicist Martin Falcke (HMI, SF5 – Theoretical Physics) with the experimental biologists Patricia Camacho and James D. Lechleiter (both from the University of Texas in San Antonio). In a common effort, they succeeded in explaining the origin of the calcium waves' behaviour. In particular, Falcke developed a mathematical model showing how the different patterns emerge from the interplay of different organelles releasing and absorbing the calcium in the cell. A brief review of the scientific results behind the prize is given below.
For their groundbreaking results the three scientists received the 2003 Erwin Schrödinger Prize. The prize is awarded annually by the Stifterverband für die deutsche Wissenschaft (Donors' association for the promotion of the sciences and humanities in Germany) and the Helmholtz Association to researchers working at the interface between different fields of science. The interdisciplinary work of this year's laureates fits particularly well into the tradition of Erwin Schrödinger, the theoretical physicist who applied his theoretical approach to the understanding of the genetic code. With his book *What is Life?*, Schrödinger inspired many physicists to look into the fundamental principles of life.

The prize was presented to the laureates on Oct 16 2003 in a ceremony during the annual conference of the Helmholtz Association, which took place in the Hamburg city hall.

Understanding the patterns of life – Research at the interface of physics and biology

Every living organism consists of countless individual cells; every cell consists of many organelles and countless molecules. Only by communicating with each other, the organelles and molecules become a living cell and the cells become a living organism. Within the cells, information is transmitted in form of calcium waves – singular or periodic changes in the calcium concentration. These waves can expand or form characteristic stripes travelling through the cell forming typical patterns. As an example, consider the fertilization of an egg-cell. Here, it is crucially important that only one sperm enters the egg. Therefore, fertilization of the egg-cell must be immediately communicated to its whole surface. This information is transmitted by a calcium wave. Besides fertilization, there are countless further examples of the transmission of information with calcium as a messenger.

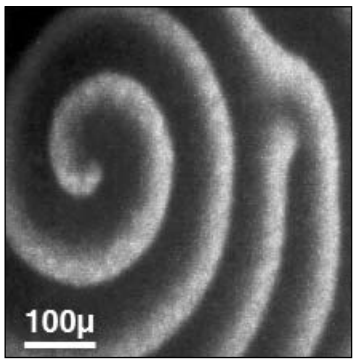

A spiral-shaped calcium wave. Calcium waves transmit information between the various organelles in the living cell. The cooperation of the laureates led to a fundamental understanding of calcium communication in cells.

The biologists P. Camacho and J.D. Lechleiter and the physicist M. Falcke had the idea of approaching unsolved problems in cell physiology by studying the behaviour of calcium waves. By thoroughly analyzing the periods, velocities and amplitudes of the waves, they expected to gain insight into the functioning of the different cell components participating in calcium dynamics.
Two kinds of cell organelles – the mitochondria and the endoplasmic reticulum – participate in calcium communication. Both act as reservoirs of calcium ions and are equipped with the ability to both release calcium into the cytosol and to absorb it from there. The amounts of calcium ions absorbed and released depend in a complicated manner on the concentration of calcium ions already present in the cytosol. For example, channels releasing calcium from the endoplasmic reticulum become increasingly permeable when the concentration in the cytosol

slightly increases but close completely as soon as the concentration becomes very high. Thus, the properties of different waves are determined by the interplay between concentration in the cytosol and permeability of the different channels.
Calcium waves form dynamical patterns such as rotating spirals. From their experiments, biologists had already known of the correlation between structure and properties of patterns formed by calcium waves. But an in-depth analysis of this correlation became possible only with the availability of a mathematical description, which combines the numerous factors and identifies the interactions within the system.
Experiments had shown that the spiral patterns disappear as soon as the mitochondria become more active than usual. It became clear that one might obtain important information from understanding the vanishing of the patterns. Calculations made it possible to demonstrate the correlation between the waves' properties – length, period and amplitude – and the calcium exchange. It turned out that calcium uptake and calcium release by the mitochondria prevent particular periods of spiral waves. Thus, mitochondria act as frequency filters. Since the information transmitted by the calcium signal is coded in the frequency, the mitochondria play a crucial role in the calcium communication.
The existence of "forbidden" frequencies had not been known before in the theory of pattern forming systems – the theory, Falcke applied in his work on calcium communication. This shows that both sides profit from the cooperation: on the one hand, the theoretician helped understand the results of biological experiments; the biologists, on the other hand, gave a stimulus for physical research that led to novel results.
Subjects of a further study were the pumps transporting calcium ions back into the endoplasmic reticulum. Surprisingly, an increase in the number of pumps led to an increase in the concentration amplitudes in the cytosol. Calculations suggested that the increase in pump performance together with the calcium transport out of the cell's neighbourhood lead to an increase in the calcium level in the storage. When the channels open, more calcium is released. Measurements confirm these predictions.

■ New Neutron-Guide Hall at HMI

December 9, 2003 marked the starting point of a new era for the Berlin Neutron Scattering Center (BENSC) at the Hahn-Meitner Institute: Representatives from the German Federal Ministry of Education and Research (BMBF) and the local government participated in the ground-breaking ceremony for a second neutron guide hall.
This hall will be erected adjacent to the existing guide hall. It will cover an area of about 1000 square meters and reach a height of 14 meters. An innovative neutron guide system using advanced supermirror optics will deliver a total of two times more neutrons to the instruments in the new hall than are delivered by the three remaining guides in the old hall. Its heart will be a 75 m long ballistic guide with a multispectral beam-extraction device. Thanks to a front end facing simultaneously the thermal source (reactor core) and the cold source, this ballistic guide will deliver both thermal and cold neutrons under good intensity conditions over an exceptionally broad wavelength range between 0.7 and 20 Å.
This broad wavelength range will be used by a novel time-of-flight diffractometer, the Extreme Sample Environment

Laying of the foundation stone for HMI's new neutron guide hall Prof Michael Steiner, scientific director of the Hahn-Meitner Institute, and the architect Bernd Tibes fill a metal box to be immured in the hall's foundations with artefacts typical for the time of the building's erection.

Diffractometer (EXED), installed at the back end of the ballistic guide. It is the time-of-flight approach in combination with the multi-spectral beam that makes EXED an ideal instrument for neutron scattering experiments at highest magnetic fields. Specifically for use at EXED, HMI, in cooperation with the Forschungszentrum Karlsruhe (FZK), strives to realize a 25 T superconducting tapered solenoid magnet. This is a further step towards HMI's ultimate goal of reaching 40 T. (For a more extended description of EXED see Highlight report on page 46.)

The blue-gray guide hall II will be attached to the existing guide hall I. The increased height of the building will allow for handling extreme environment facilities in the hall as well as for hosting laboratory and instrument control containers on three levels.

The second new instrument in the new guide hall will be a Very Small Angle Neutron Scattering (VSANS) machine. It is due to the response from an increasing demand from the life sciences user community. Compared to the traditional SANS technique, VSANS will extend the accessible momentum range by an order of magnitude towards smaller values.

The construction of guide hall II is progressing rapidly. Within six months the basement and the large media tunnel for the EXED instrument were completed.

Finally, the existing wide-angle spin-echo spectrometer SPAN will be moved to the new hall. There it will profit from the considerably higher flux provided by the new neutron guides.
As to the planned schedule, the hall itself is expected to be finished by fall 2004. The extraction assemblies for the new guide system will be built into the reactor core during a reactor shut-down from September to December 2004. Both new instruments will become operative by end of 2006 and, finally, the superconducting solenoid magnet allowing for neutron scattering experiments at fields of up to 25 T will become available in 2008.

■ HMI start-up: Sulfurcell wants to manufacture large area solar modules

The HMI start-up Sulfurcell planned to manufacture large area CIS solar modules applying a process developed at the HMI. The first goal of the enterprise is it to transfer the technology which was developed for small modules to the marketable module format 1.2×0.6 m² and to adapt it to the manufacture conditions of an industrial production. This project is designated as up-scaling and Sulfurcell can fall back to established mechanical engineering, whereas the large are processes and individual components of the equipment must be developed by the company itself. The second substantial task consists of guaranteeing the durability of a solar module. The today's manufacturers offer warranties of up to thirty years on the power output of their products. Solar modules must withstand changing and extreme climatic conditions during this period. The layer system of a CIS module reacts with sensitive power losses to dampness influence and therefore it must be encapsulated. The HMI has begun to work on encapsulation techniques and good progress could be obtained. The tasks are still not completely solved, and Sulfurcell reck-on time-intensive series of tests, in order to be able to ensure the stability requirements.
Sulfurcell counts for the development work on the competencies and motivation of the own team and on the experiences of its partners. A network branched out far connects the enterprise with research institutions and industrial enterprises. A license and a co-operation contract was concluded with the HMI. The Institute will continue to carry out research on this type of solar cells and the close co-operation will be maintained.
The manufacturing plant of Sulfurcell is located in the new quarter for science and economics, in Berlin Adlershof. In a 1,200 m² large production hall the first machines started there at the end of the year 2003. Up to twenty employees will work on the development of the production process. By the year 2006 Sulfurcell wants to place CIS modules on the market and expand the production capacities.

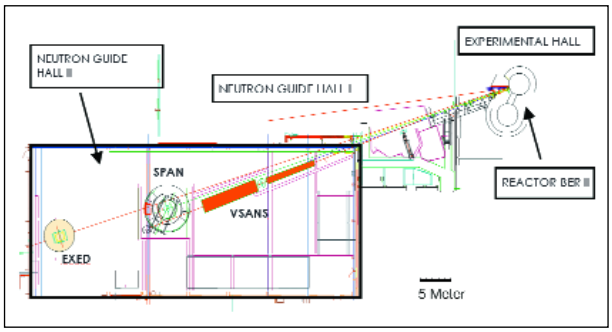

Layout of Neutron Guide Hall II

The HMI holds the top position in the international research on Copper Indium Sulfide (CIS): The material for photovoltaic is for more than ten years under research. Already seven years ago the transition took place to industrial typical coating techniques, in order to ensure the applicability of the results. By the continuous research work it was succeeded to establish a standard technique, which supplies regularly solar cells with a mean efficiency of 11 %. In the meantime the HMI holds the world record for the best CIS solar cell (0.5 cm², efficiency 12.7 %) and the best small module (5 × 5 cm², efficiency 9.7 %). Research successes of the HMI suggest further progress for the coming years with the increase of the efficiency. The innovation potential of the technology is today already so interesting that the recently founded enterprise Sulfurcell concluded a license agreement with the HMI in order to use the technology in an industrial pilot production. The reasons are first of all the cost reduction potential of the technology, secondly the high energy yield of the CIS modules and thirdly their favorable environmental balance:

1. The cost analysis for a potential production showed that CIS modules can be manufactured at least 50 % more cost effective than the solar modules from crystalline sili-

The manufacturing plant of Sulfurcell in Berlin Adlershof

con dominating the market today. The utilisation of small amounts of semiconductor material as well as the favorable manufacturing methods contributes to the cost reduction. The employment of a thin film system in place of a crystal wafer from electronic-grade silicon reduces materials requirements to a hundredth and makes it possible to use simple glass as substrate for the photovoltaic active layers. The thin films of a CIS module can be manufactured using the large area coating methods of the glass industry and do not require the batch processing of small wafers, which is necessary with crystalline silicon modules.
2. CIS modules are placed with almost 10 %-efficiency in the mid range, concerning the energy yield per efficiency per cent they are at a top position. The energy yield of a solar module is determined only insufficiently by the frequently discussed efficiency. The (standard) efficiency is the relationship of the produced electricity to the irradiated light energy measured in the laboratory (noontime sun exposure, 25°C module temperature). Under real environmental condition solar plants work frequently at higher temperatures and under smaller incident light radiation than under laboratory conditions. Under these conditions CIS modules supply a substantially higher energy yield than silicon or CISe modules. Thus Fraunhofer Institute for Solar Energy Systems computed for the location Florida that a CIS solar cell achieves with 10,4 %-efficiency the same energy yield as a CISe solar cell with 12,8 %. Besides, the energy yield of a CIS module is little affected if parts of the module are shaded. Hard shadows of masts, trees or house walls impair their efficiency substantially less, than it is to be observed with silicon modules.
3. The CIS technology is frequently referred to as “CIS of the 2. Generation” and it can count on very good market chances. A substantial reason is the outstanding environmental balance of the CIS technology. The Technical University of Berlin evaluated the environment-friendliness of a potential CIS production and provided an environmental balance. CIS modules need only one year in order to return the energy needed for their production. Causes are the absence of high temperature steps and the use of the highly reactive sulphur. In addition, due to the avoidance of selenium and the small heavy metal content in the CIS modules, their toxicity is on the low level of crystalline silicon modules.
The success of Sulfurcell is now to be measured at the results of the development and success at the market. The crucial steps of the transfer of technology are still in store for the enterprise: Up-scaling of the technology and set up of a stable production and product development. We dependent on partnerships – Hahn-Meitner Institute is the most important and will be in the future, on its research work and support we build. For all aids and fellow combatants applies our cordial thanks.

Nikolaus Meyer, Sulfurcell

■ 5 Years of Experience in Proton Therapy for Ocular Tumours in Germany

In June 1998 proton beam therapy of ocular tumours was introduced at the Hahn-Meitner Institute. Thus, this very efficient method of treating cancer of the eye became available in Germany for the first time. Since then, more than 400 patients have been treated successfully. From its beginning, the treatment was conducted in cooperation with the University Hospital Benjamin Franklin (now Charité – Campus Benjamin Franklin). In late 2002 the University Hospital Essen became the second cooperating hospital.

Background

Most patients treated for eye cancer at HMI suffer from a choroidal melanoma – a malignant tumour of the choroid (the middle layer of the eye-ball composed of layers of blood vessels that nourish the back of the eye. The choroid, along with the iris and ciliary body, are also referred to as the uvea.). Between 500 and 600 new cases are notified in Germany each year. The tumour does not only endanger the eye’s vision, but can be lethal due to the risk of

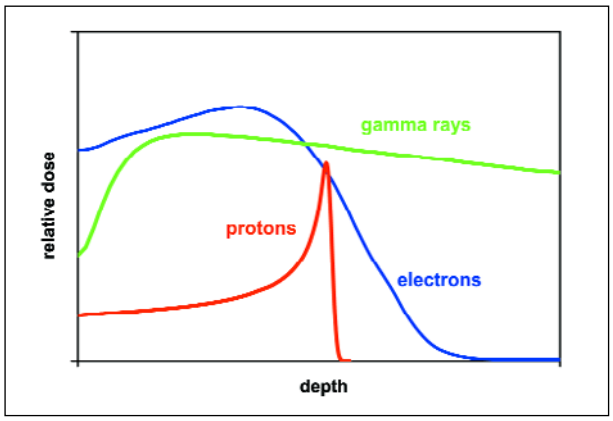

Dose distribution versus depth for different types of radiation. In contrast to electrons and gamma-radiation, protons deposit their energy in a very narrow area – the so-called Bragg peak. This property makes proton beams particularly suited for the treatment of eye-tumours: they destroy the tumour leaving surrounding healthy tissue virtually unharmed.

metastasis. Therefore, the removal or destruction of the tumour is of essential importance for the patient's survival. But, in addition to local tumour control as a primary goal, the objective of a curative therapy is the retention of the patient's vision.
Therefore, enucleation – the complete removal of the eyeball – is increasingly replaced by a variety of surgical, laser or radiation therapies.

Proton therapy

At HMI ocular tumours are treated with high-energy protons (68 MeV) provided by the accelerators of the Ion-Beam Lab ISL. In contrast to other kinds of radiation applied in tumour therapy, high energy protons deposit almost the whole dose in a rather small well-defined region – a fact reflected in the Bragg peak in the dose distribution (Fig. 1). This makes proton therapy particularly suitable for those cases where the tumour is located in the vicinity of critical structures like the optical nerve, the optic disc or the macula that would be damaged in other forms of radiotherapy. By exactly forming the proton beam's cross section and adjusting its energy, it often becomes possible to avoid these critical structures during the irradiation.

Study shows high quality of treatment at HMI

In a recent study, the treatment outcome for patients with uveal melanomas has been evaluated.

Material and Methods

245 consecutive patients with primary mela-noma of the uvea have been treated from June 1998 to April 2003 at HMI. In 96.2 % of all patients a uniform fractionation scheme was applied. It consisted of single doses of 15 CGE (Cobalt Gray Equivalent), and a total dose of 60 CGE applied on 4 consecutive days. Follow-up is available for 229 patients. Since May 2000, 45 of the patients with large tumours of at least 5 mm prominence have been treated with an endoresection – the surgical removal of the irradiated tumour – following proton beam treatment.

Results

The study population in general and the subset of those treated with an endoresection were comparable in terms of age (median 60.9 years vs. 58.7 years) and visual decimal acuity (0.5 vs. 0.5). As expected, tumours treated by additional endoresection were larger (median prominence 8.8 mm vs. 3.5 mm, median base of the tumour 15.4 vs. 10.3 mm) and were not in direct proximity to critical structures as optic disc (median 2.3 mm vs. 1.5 mm) and fovea centralis (median 3.4 mm vs. 0.6 mm). At the time of median follow up (18.4 months) local control is 96.4 % and 95.5 % at 3 years. Eye retention rate is 92.6 % at 20 months (median follow-up) and 87.5 % at 3 years. The subset of patients treated with an endoresection did fairly well: Although those tumours were larger in volume, their outcome does compare favourably with the others. Local control is 98 % at 18 months (the time of median follow-up for this parameter is 18.1 months) and eye-retention rate is 88.6 % after 2 years.

Positioning of the patient during eye-tumour therapy
The patient's head is immobilized by means of a mask and a bite block, both custom made.

Conclusions

Proton beam irradiation of uveal melanomas at the Hahn-Meitner Institute after the first 5 years of its initiation reveals local tumour control- and eye-retention rates in the range of other centres with larger experience. Delivering high treatment quality in hadron therapy from the beginning has been achieved. As there will be a learning curve as documented in other centres, there is hope for a further rise in results with increasing experience and a longer follow-up period. The concept of endoresection after proton beam irradiation seems promising but will need further evaluation with more patients and a longer follow-up period.

Outlook

The promising results achieved in the treatment of ocular tumours and the growing knowledge gathered over the years would seem a reasonable basis for a large scale proton therapy centre jointly run by HMI and Charité medical school.

Authors of the study:
S. Höcht[1], W. Hinkelbein[1], N.E. Bechrakis[2], M.H. Foerster[2], P. Martus[3], D. Cordini[4], H. Fuchs[4], J. Heufelder[4], H. Homeyer[4], H. Kluge[4]

1 Klinik für Radioonkologie und Strahlentherapie, Charité Universitätsmedizin Berlin Campus Benjamin Franklin (CCBF), 2 Augenklinik – CCBF, Institut für Medizinische Informatik, 3 Biometrie und Epidemiologie – CCBF, 4 HMI, SF4 – Eye-Tumour Therapy Team

■ Trace element research: Towards New Frontiers and Good-bye to an Old Campaigner

(Workshop on *Metalloproteins and Metalloidproteins* and colloquium in honour of Prof. Dietrich Behne on his retirement from the HMI)

It is a well-known fact that several elements, although they are present in the organism at only very low concentrations, are none-the-less indispensable for maintaining human and animal health. Recent research has indicated that most of these essential trace elements are bound to

proteins and that their biological effects are thus due to the functions of a multitude of specific trace element-protein-complexes. With the recent advances in biochemical and molecular biological methods and in the physical and chemical analytical techniques, we now have the tools to study these compounds, especially with regard to their biological roles and to their applicability in the diagnosis and therapy of diseases. At our department Molecular Trace Element Research in the Life Sciences we are mainly concerned with the identification and investigation of novel metallo- and metalloidproteins and, with the multidisciplinary know-how available in our group and the possibility of combining modern methods from both the life sciences and trace element analysis, are at the cutting edge in this field.
Our involvement in this area triggered the idea to initiate a workshop series on Metalloproteins and Metalloid-proteins and in this way to bring together the German research groups from the different scientific disciplines which are concerned with metalloprotein research, establish contacts between these groups and encourage or intensify interdisciplinary collaboration.

Prof. Dietrich Behne welcoming the participants of the Workshop on *Metalloproteins and Metalloidproteins*

The second annual meeting of this series, organized together with the Gesellschaft für Mineralstoffe und Spurenelemente (GMS) was held at the HMI from Nov. 6–8, 2003, Its multidisciplinary character was underlined by the fact that amongst the 150 participants there were physicists, crystallographers, mathematicians, chemists, biochemists, molecular biologists, pharmacologists, nutritional scientists, dieticians, and physicians. 34 lectures and 18 poster presentations dealt with analytical aspects, redox processes, antioxidative systems, interactions between metals and proteins, and pathobiochemistry. The studies showed that with the advances in the development of specific chemical, physical, analytical, crystallographic, mathematical, biochemical and molecular biological methods and their appropriate combination, trace element research is being pushed towards new frontiers. The contributions from out department included a plenary lecture, two lectures and 9 poster presentations. One of them by K. Bukalis et al. on trace-element containing proteins in the lungs received the first prize of the poster awards, and the Heinz-Zumkley Prize, donated by the GMS, was awarded to Dr. Andrea-Nicole Richarz from our department for her PhD thesis on the analysis of metal-containing proteins.

Colloquium in honour of Prof. Dietrich Behne

A colloquium in honour of Prof. Dietrich Behne, the head of our department and an old campaigner in this field of research, on his retirement from the HMI was incorporated into the conference. Prof. Behne has had a long-standing relationship with the HMI, having started here as a chemistry student in autumn 1962 with his diploma thesis, followed by his dissertation, both with Prof. Zimen in nuclear chemistry on the separation of isotopes. After his PhD he moved to analytical chemistry and radiochemistry and began studies on the determination of trace elements by means of neutron activation analysis and radiochemical methods. From 1968 to 1970 he worked in England at Reading University and at the nuclear centres in Harwell and Aldermaston to deepen his knowledge of neutron activation analysis of biological materials. After his return to Berlin he introduced these methods and their application in the life sciences as a novel area of research at the new nuclear reactor BER II and also taught analytical chemistry and radio-chemistry at the Freie Universität Berlin. He did not content himself, however, with purely analytical tasks, but extended his studies in trace element research more and more into the biochemical and medical fields. Over the years this resulted in the development of a unique multidisciplinary research group in which, in addition to neutron activation analysis, synchrotron radiation X-ray fluorescence and other analytical methods, radiotracer techniques, nutritional studies on laboratory animals, cell culture experiments and various biochemical and molecular biological procedures are being combined in order to investigate the biological functions of the trace elements and their role in health and disease. In his laudatio, Prof. Köhrle from the Institute of Experimental Endocrinology at the Charité emphasized Prof. Behne's scientific versatility and his expertise in several different disciplines as one of the outstanding characteristics of his scientific career and the-basis for his achievements and success. Accordingly his publications cover a wide range of themes including methodological studies on the development and use of element analytical methods and radiotracer techniques in the life sciences, the combination of these procedures with biochemical and molecular biological methods, studies on trace element biochemistry and trace element metabolism, medical studies on the role of trace elements in health and disease and metalloprotein research. The most important contributions have, however, been his studies in selenium research where he detected that this trace element is present in the body in the form of numerous selenoproteins with key functions in the mammalian organism and that an insufficient selenium supply may lead to serious diseases. His discovery that a selenoenzyme is responsible for the production of the thyroid hormone T3 and that thus not only iodine but also selenium is needed for a normal thyroid hormone metabolism, has

had a great impact in thyroid endocrinology, and due to this finding the selenium status of patients is now taken into consideration in hospitals in the diagnosis and treatment of thyroid hormone-related diseases. In recognition of this work Prof. Behne was awarded the Klaus-Schwarz Commemorative Medal in 1991 for the identification of the type I deiodinase as a selenoenzyme and the elucidation of the role of selenium in thyroid hormone metabolism. His recent finding that another selenoenzyme is necessary for the normal development of the sperm and thus for male fertility may gain similar importance in the diagnosis and treatment of human male infertility.
Although considerable progress has been made in research on trace elements and trace element containing proteins since Prof. Behne first began his studies, many questions still remain to be answered and, with the research project Selenoproteins and Metalloproteins as part of the programme Environmental Health within the Helmholtz Association, the department will continue this work.

Antonios Kyriakopoulos, SF6

■ Outstanding, rapidly done with open mind

Adlershof thesis award for physicist of the Hahn-Meitner Institute
The city for science, economics and media assigned for the second time the Adlershof thesis award for outstanding work of its scientific new generation. The 32 years old physicist Dr. Christoph Böhme received the award endowed with 3.000 Euro in the context of the Adlershofer Campus week on December, 3rd, 2003. Founders of the award are in equal parts the Joint Initiative of Non-University Research Institutions in Adlershof (IGAFA), the Humboldt University Berlin (HU) and the WISTA MANAGEMENT Ltd.
The awarded thesis of Christoph Böhme “Dynamics of charge carrier recombination” was prepared under the supervision of Prof. Dr. Walther Fuhs at the Silicon Photovoltaic Department of the Hahn-Meitner-Institute located in Adlershof in only 27 months and was accepted in January 2003 at the Physics Faculty of the University of Marburg with “summa cum laude”.
Christoph Böhme developed in his work the theoretical and the experimental basis for a new measuring method (pulsed electrical detected magnetic resonance, pEDMR) for the analysis of defects in semiconductor layers and devices. The analysis of defects is a pre-condition for the increase of the capability of semiconductor components, particularly regarding their miniaturization. With his measuring method the laureate enters not only new ground in the material sciences, but gives also a substantial new stimulus for the spin-based quantum computing. Böhme’s work was already published in twelve renowned technical periodicals, presented at international conferences; a patent request for the measuring method is posed. The laureate studied in Heidelberg and at the North Carolina State University (the USA) and acquired in parallel the German Diploma in Physics and the Master of Science.
Since 2002 he works as a scientist at the Hahn-Meitner-Institut in Adlershof.
The Adlershof thesis price is to document the quality of the research and the co-operation of science and economics in the biggest German science and technology park. Decisive for the award is scientific excellence (mark, number of the publications and patents, appraisals) and graduation duration.

Source: IGAFA, science office

■ First light from the 7-Tesla Wiggler

Almost as an early Christmas gift to themselves, on December 11 2003 HMI scientists working at the Berlin electron storage ring BESSY in Berlin-Adlershof for the first time opened the beam shutters to allow x-rays produced by the 7-Tesla wiggler to enter their beamlines. On a fluorescence screen, this radiation was registered as “first light” (see picture). The wiggler belongs to the class of insertion devices – special magnetic structures built to create extremely intense x-rays. No other insertion device world-wide has as many poles with such a high magnetic field in a comparatively small space. Thus, it is the strongest source of hard, penetrating x-rays at BESSY. In the five years preceding the first light, this unique device was planned and developed in close collaboration between HMI and BESSY and, finally, built by the Budker Institute in Novosibirsk (Russian Federation). As the machine reaches the frontiers of what is feasible today in this field, a number of technical problems had to be overcome before the first successful tests. Now the radiation from the wiggler is available to supply the beamlines and experimental stations built up by HMI’s scientists.

HMI’s 7-Tesla wiggler at BESSY

The radiation produced by the wiggler will be used in materials research, magnetism and other fields of structural research. As part of the BENSC user-service, the experimental facilities at the wiggler beamlines will be available to external researchers from universities and other scientific institutes. The new facilities complete the suite of experimental opportunities available at BESSY. Several of the more than 40 experimental stations operated at BESSY

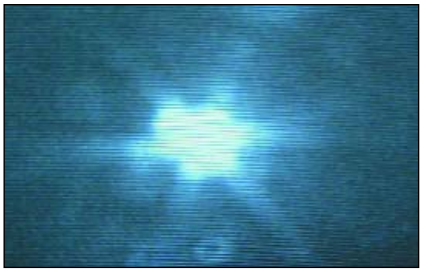

First light from HMI's 7-Tesla wiggler visible on a fluorescence screen. December 11 2003, 12:00 Noon

are run or used by HMI. Among these is an experimental station for the investigation of magnetic nanostructures and thin magnetic films (cf. Highlight Report page 32) installed at an undulator – another insertion device built in close HMI-BESSY collaboration. With the inauguration of the wiggler, synchrotron radiation becomes – in addition to neutrons and fast ions available in Berlin-Wannsee – the third main pillar of structural research at HMI.

Ralf Feyerherm, SF2

■ Materials department inaugurates new metal foam lab at TU-Berlin

Aqueous solutions, polymers and glass can be foamed. For a long time scientists have had the ambition to foam metals in order to create novel materials combining the advantages of the unique foam morphology with the known properties of metals. In the past 10 years, many new processes for making metal foams – mostly from aluminium or aluminium alloys – have been developed to such a level of sophistication that more and more industrial applications are emerging. There are two main ways of producing metal foams: the powder metallurgical foam production route and the gas injection route. In the former case, metal powder is mixed with a powdered blowing agent and subsequently condensed. When heated, the metal melts and the blowing agent produces a gas that creates the bubbles in the foam. In the latter case, a gas is injected into the molten metal creating the foam structure. Although metal foaming technology is quite advanced now, the properties of metal foams and the physics of metal foam generation and evolution are only starting to be explored.
The metal-foam group formed around Prof. John Banhart (HMI, SF3 – Materials) is working on the characterisation of the foaming process of metals and metal alloys. The group is looking for ways to improve current manufacturing processes and to develop new ones. Since late 2003, this work has been done at the Technische Universität Berlin, in cooperation with the Hahn-Meitner Institute. Two main labs are available: the x-ray-lab, where both foaming methods are investigated, and the main lab dedicated to research on the powder metallurgical route. Here, powder mixing and milling machines, metallic sieves, a 100 tons hot press and several foaming furnaces are available. With this equipment, the whole process from the precursor material production to the foaming itself can be performed and all production parameters can be adjusted for the investigation.
For the real time in situ analysis of the foaming process, a microfocus x-ray measurement place was designed and built. X-ray radioscopy is used to resolve the internal pore structure during foaming and observe the foaming dynamic. The measurement place is supported by a picture-analysis software that allows calculating the foam expansion, find the critical cell-wall thickness and measure coalescence rates.
In the near future, the acquisition of a specially designed dilatometer is planed. This facility will allow analysing the formation and decay of metal foams in a form applying various in-situ-foaming techniques. This way, time-dependent volume expansion can be easily monitored.

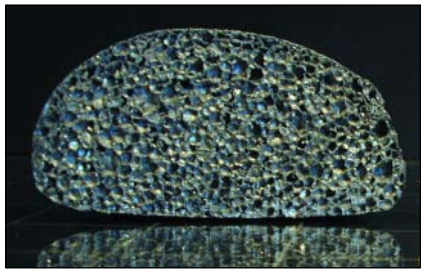

A zinc foam

The scientists of the metal-foam group are interested in the phenomena and mechanisms responsible for the formation and stabilization of pores in the metal foaming process. If one wants to study the very early stages of foaming, i.e., stages in which the pores are just being formed, one has to apply methods that act on the appropriate length scales which range from some tens of nanometres to several micrometers. Optical or electron microscopy is suitable for investigations whenever two-dimensional information is sufficient. High-resolution x-ray tomography allows for a precise determination of three-dimensional features. Often, however, one is less interested in mapping individual pores, but wants to obtain a three-dimensional average of a pore size distribution. Such distributions can

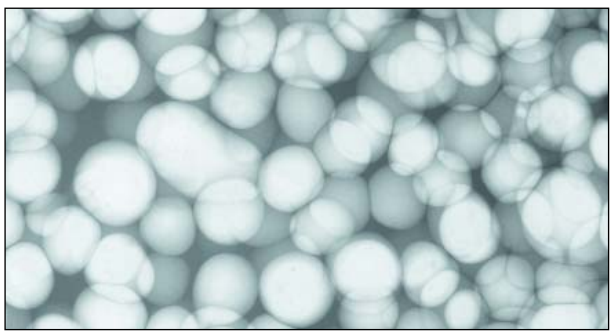

An x-ray radiograph of a 10 mm slice of aluminium foam

be useful, for example, as input data for model calculations of the foam generation process. Ultra small-angle neutron scattering (USANS) is a promising method for obtaining this information because scattering of cold neutrons at very small wave vectors provides data in exactly the size range required.

Francisco Garcia-Moreno, SF3

■ HMI hosts Workshop on Orbital Physics and Novel Phenomena in Transition Metal Oxides.

The physical properties of complex transition metal oxides (TMO) are driven by a rich interplay between charge, spin, and lattice interactions. Nature has already shown how powerful this interplay is in these materials: superconductivity with the highest critical temperatures, ferroelectricity with exceptional dielectric response, colossal magnetoresistance, and negative thermal expansion from 2 to 1400 K. TMOs are an exceptional laboratory for studying a variety of interactions on the nanoscale lengths where they compete.

Participants of the HMI Workshop on Orbital Physics and Novel Phenomena in Transition Metal Oxides

An example of the competition between charge, lattice and spin degrees of freedom is in the doped manganites perovskites. Here a magnetic interaction propagated by a hopping charge (double-exchange) competes with an enhanced electron-phonon coupling via the Jahn-Teller active Mn^{3+} ion. At the right electronic doping this competition produces a transition from the ferromagnetic-metallic ground state to an insulating state at elevated temperatures, with a change of resistivity of several orders of magnitude. The orbital configuration of the Mn^{3+} is important in these materials as the sign of the exchange (antiferromagnetic or ferromagnetic) is controlled by the polarization of the e_g orbitals (see figure).
A workshop on Orbital Physics and Novel Phenomena in Transition Metal Oxides was hosted at the Hahn-Meitner Institute on the 24th and 25th of September 2003 to discuss the latest developments in this exciting area of research. The meeting was attended by about 50 participants from Germany and greater Europe, twice as many as last year's workshop. Talks focused on both recent experiments and new developments in theory. For example Orbital Ordering and the role of orbitons in $LaMnO_3$ was discussed by Rilana Krüger (University of Hamburg) while Sylvie Hébert (CRISMAT, Caen) presented recent developments in the field of cobalt oxide thermoelectric materials. Theoretical work on charge ordering in manganites was presented by Daniel Komskii (University of Cologne) with significant contributions from Peter Horsch and Giniyat Khaliullin (Max Planck Institute for Solid State Research, Stuttgart) on frustration and orbital ordering in manganites and titanates.
Participants from the Hahn-Meitner-Institut presented work on the lattice dynamics (Heloisa N. Bordallo, HMI, SF1 – Methods and Instruments), and magnetic short range ordering in CMR manganites (Jens-Uwe Hoffman, HMI, SF2 – Magnetism), while Christopher J. Milne (HMI, SF2) presented recent work on the synthesis and structure of a newly discovered novel superconductor $Na_xCoO_2 \cdot yH_2O$. The synthesis of nano-clusters of transition metal oxides was discussed by Abdelkrim Chemseddine (HMI, SE4 – Dynamics of Interfacial Reactions). This workshop so far has stimulated significant interest in transition metal oxides both within HMI and in the wider community. Currently partly due to this workshop efforts are underway to seek funding from the German Research Foundation (DFG) for such work under a Priority Programme (Schwerpunktprogramm). In addition collaborations between HMI and other groups are beginning. Currently there is a samples synthesis effort in the department SF2 for the fabrication of powder and single crystals samples of various interesting TMOs such as manganites and superconducting $Na_xCoO_2 \cdot yH_2O$, while the BENSC

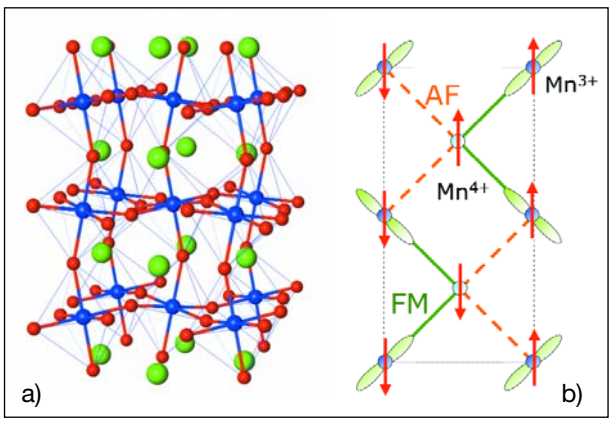

a) Crystal structure of a typical manganite perovskite. Mn atoms bond to O-atoms (red) to form MnO_6 octahedra (shown in transparent blue). The darker blue spheres are typically trivalent or divalent rare earths. A mixture of 3+ and 2+ rare earth elements is used to electronically dope these materials.
b) Focusing only on the electronic configuration of the Mn atom we illustrate the importance of orbital degrees of freedom for an ordered arrangement of Mn^{3+} and Mn^{4+} ions in a perovskite. The interaction shown as a solid line is ferromagnetic (parallel spins) as a filled Mn^{3+} e_g orbital points towards a Mn^{4+} ion (which has a vacant e_g orbitals). Interactions between vacant e_g orbitals lead to antiferromagnetic superexchange (dashed line).

user program routinely provides beam time to investigate these materials from groups throughout Germany and Europe.
This meeting was sponsored by both the HMI and the University of Hamburg (Michael Rübhausen). The organizers are grateful for the participation of Marie Haltod.

Dimitri N. Argyriou, SF2

■ Development of a new Kelvin-Electronic for Omicron GmbH

For the measurement of the absolute work function on nanometer scale and meV sensitivity with Kelvin probe force microscopy (KPFM) a second feedback circuit in standard non-contact atomic force microscopy (NC-AFM) is needed. To separate the information of the tip-sample interaction induced by the Van der Waals forces (used for the topography measurement) and the electrostatic forces, which is induced by the contact potential (CP) between tip and sample, an additional ac-voltage is applied between tip and sample. With lock-in technique the oscillation amplitude of the electrostatic force induced by the ac-voltage can be determined and minimized by a compensating dc-voltage which is applied to the sample. This compensation voltage corresponds to the CP and can be used to calculate the work function of the sample when knowing the work function of the tip. For NC-AFM in ultrahigh vacuum (UHV) the first resonance frequency of the cantilever (~70 kHz) is used for the detection of the topography. A resonant and therefore very sensitive way of detecting the electrostatic force separately but simultaneously to the topography is the use of the second resonance frequency of the cantilever (~420 kHz) for the ac-voltage. In this setup ac-amplitudes as small as 100 mVpp can be used, which is especially important for measurements on semiconducting samples to avoid a tip induced surface band bending.
Omicron nanotechnology is one of the world's leading supplier of solutions for analytic requirements under UHV-conditions in the fields of surface science and nanotechnology especially regarding scanning probe microscopy. Ch. Sommerhalter started in 1998 at the HMI to implement the Kelvin-mode for measuring the work function simultaneously to the topography in a UHV-AFM manufactured by Omicron. After 4 years development and successful utilization of this novel technique in the scanning probe group of SE2 we started a cooperation with Omicron to develop a complete electronic setup for commercialisation. This setup consists of specially designed high and low pass filters to separate the signals of the first and second resonance frequency of the cantilever, a PI-controller to minimize the lock-in signal by applying an adequate compensation voltage and an adder to combine the ac- and dc-signal which are applied to the sample. Very high requirements are imposed on all parts regarding the frequency and phase stability, exact determination of the time constant and proportional gain and the noise level which is the lower mV range. The HMI department of electronic development (DH), especially B. Namaschk, was deeply involved in the fast and successful realization of this project. Omicron successfully launched the Kelvin-electronics as a product in the fall 2003.

Thilo Glatzel, SE2

■ Quantum Well structures measured by UHV-Kelvin Probe Force Microscopy in cooperation with KTH – Stockholm

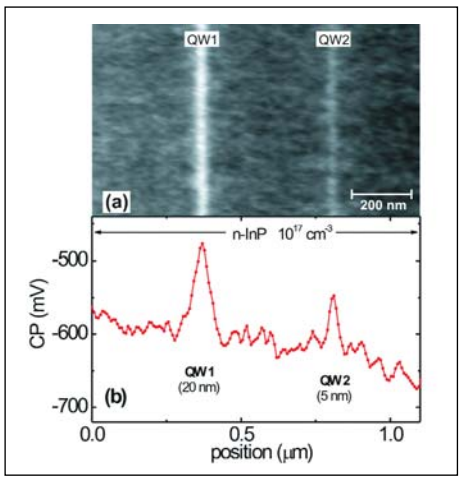

KPFM measurement on the InGaAs/InP quantum well structure showing two quantum wells. a) Contact potential (CP) image (contrast ΔCP = 230 mV). b) Typical single line scan showing the quantum wells.

Within the HERCULAS project a student (Olivier Douheret) from the Royal Institute of Technology (KTH) in Stockholm joined the KPFM group of SE2 in the summer 2003. The EU-project is focused on the qualitative and quantitative determination of the doping concentration with scanning probe techniques, e.g. SSRM, SCM and KPFM. Within this cooperation we succeeded to characterize the electronic structure of InGaAs/InP quantum well by cross-sectional Kelvin Probe Force Microscopy (KPFM) measurements in ultrahigh vacuum. The KPFM signal, as presented in the figure, have clear peaks at the position of the quantum wells, showing a systematic trend for different wells. It was demonstrated for the first time that UHV-KPFM is capable of detecting quantum wells as narrow as 5 nm. The results lead to a clear evidence for charge carrier accumulation in the quantum wells. Complete quantitative analysis of quantum well properties is impeded by a tip averaging effect and due to surface and oxide interface states. In the future complete 3D-Poisson/Schrödinger simulation including these effects will be used to extract the charge carrier concentration accumulated in the quantum wells.

Thilo Glatzel, SE2

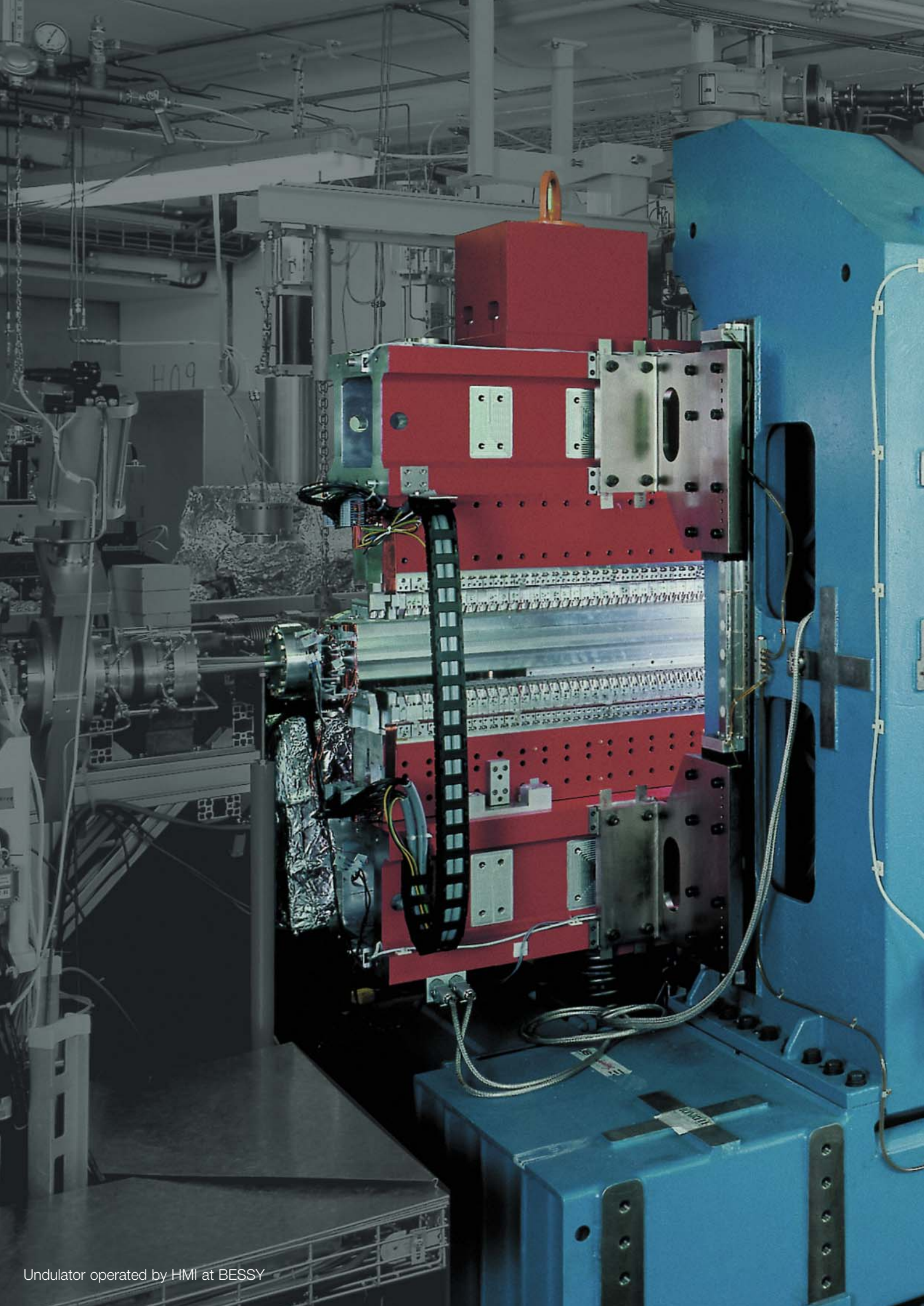

Undulator operated by HMI at BESSY

User Service

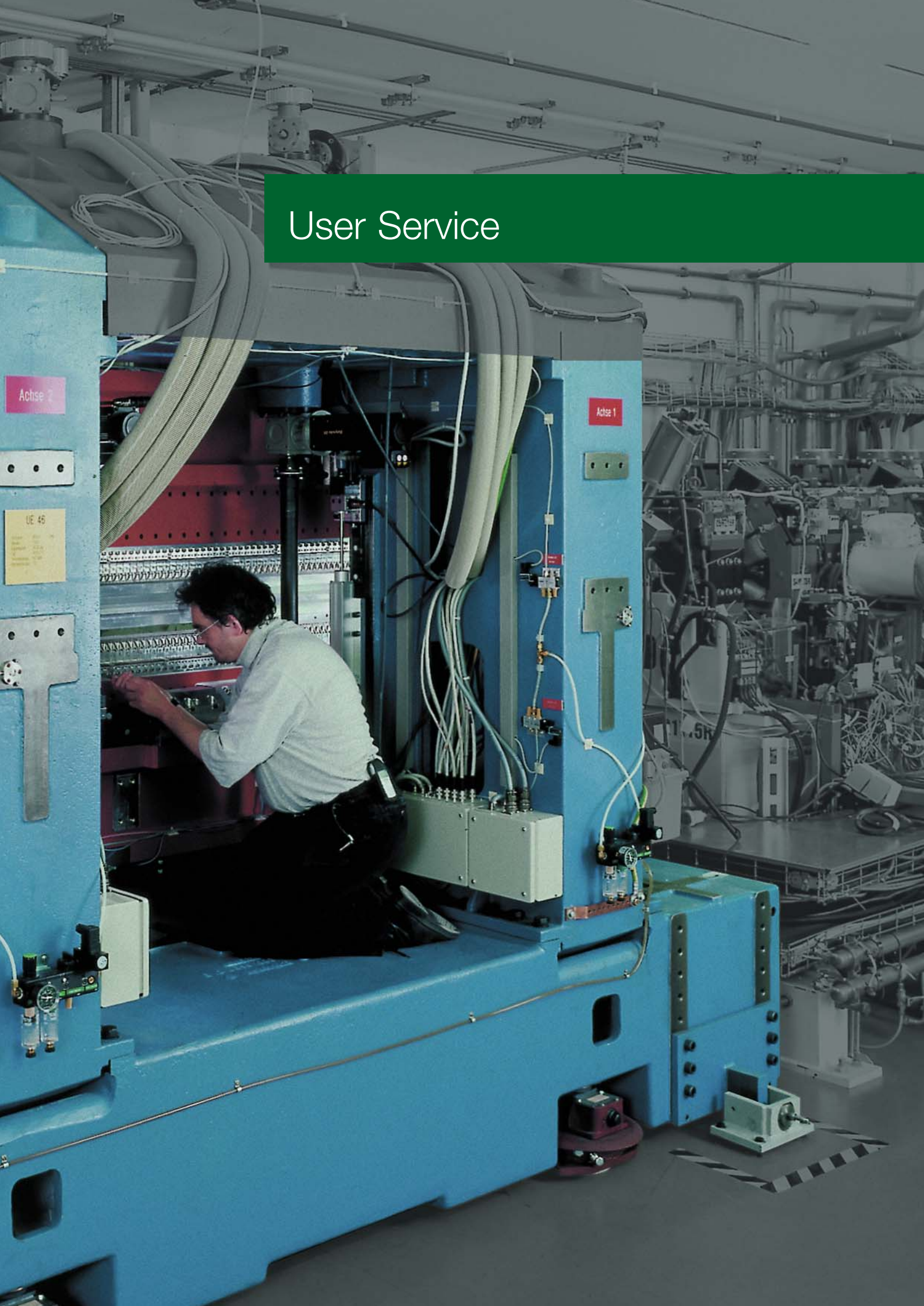

BENSC Operation

Director: Prof. Ferenc Mezei

It is the mission of the Berlin Neutron Scattering Center (BENSC) to develop and operate the scientific instruments at the Berlin research reactor BER II. About 70 % of the beam time at the most important instruments is made available to external scientific user groups from all over the world.

On a **regional and national scale** BENSC performs a principal task of the Hahn-Meitner Institute:
Service for research groups from
- German Universities
- other public funded research institutions.

The relevant duties assigned to BENSC cover a broad range from contributions to scientific education up to performance of high ranking scientific research. An aim of increasing importance is
- scientific and technical support for industrial applications

On the **international scale** BENSC plays an important role in the round of European research centres. The growing international importance of BENSC is underlined by the fact that the number of short-term guest scientists from abroad exceeds the number of German visitors (see table 1). The European use of BENSC is stimulated by substantial support from the European Commission.

Profile of BENSC

The profile of BENSC is characterized by the exceptionally wide range of the **instrumentation**, which allows experiments to be performed in many areas ranging from basic to applied research. Several advanced BENSC instruments provide neutron intensities and resolutions competitiv with the best available worldwide, including those operating at high flux reactors. Most of the instruments have the option of using polarized neutrons.

Allocations 2003 for short-term projects	accepted projects	allocated days
D - Univ.	34	252
D - other	30	222
EU + Assoc + CH	76	526
RU + UA	14	93
USA, CAN, AU, JP	10	199
	164	1292

Table 1: Allocations of BENSC beam time for short term projects

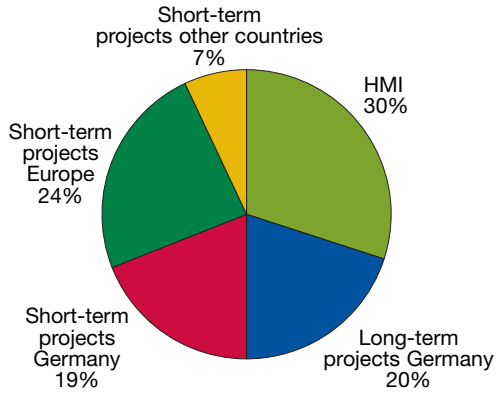

Fig. 1: Distribution of the BENSC instrument-time

Examples for unique advanced instrument options are, e.g.,
- the polarized neutron option SANSPOL
- the multidetector option the time-of-flight spectrometer NEAT
- the spin-echo instrument (SPAN) with the wide-angle NSE option
- the flat-cone diffractometer
- and especially the sample environment.

The leading role of BENSC for **sample environment at extreme conditions** is accepted worldwide: Experiments can be performed over a very large range of temperatures and/or magnetic fields. The temperature range for routine use is 15 mK to beyond 1200 K; and magnetic fields up to 17 Tesla have been made available to routine user operation. The unique Cryostat ($1.5\ \mathrm{K} < T < 300\ \mathrm{K}$) with a split pair superconducting magnet and a vertical field up to 17 Tesla is the world's leading magnet system in a neutron scattering facility and up-to-now available only at BENSC.

The advanced instrumentation and the unique sample environment capabilities attract renowned research groups Europe- and world-wide, and even from other powerful neutron sources. Four examples of highlight results from external user groups are included in the Scientific-Highlights Section of this Report.

BENSC User Service

The BENSC user services provided for scientists of German universities and other national and international research institutions include

- Allocation of beam time to individual (short term) projects of external groups on the basis of peer reviewing by an international user committee and extensive scientific and technical support for the preparation, the experiments and the data evaluation. Logistic support and travel support for young researchers is provided.
- Long-term scientific and technical projects on the basis of co-operation agreements.

An amount of at least 50 % of the beam time of the 14 most important instruments operated by BENSC is reserved for individual scientific projects; up to 20 % of the beam time would be made available for long-term co-operation projects.

Long-term co-operations

Long-term co-operation projects are primarily in the interest of the respective co-operations partners; but they also increase the manpower at BENSC and broaden the capacities for scientific support to the external users. In the path breaking field of soft matter research for instance, which formerly was not a core field of HMI's own scientific program, BENSC has established close collaborative links with the Institute of Biochemistry, TU Darmstadt; Institut für Physikalische Biologie, Univ. Düsseldorf; Iwan-N.-Stranski Institute of the TU Berlin; Max-Planck Institute of Colloids and Interfaces in Golm/Potsdam.

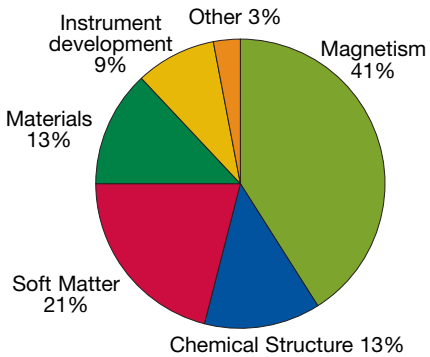

Fig. 2: Fractions of Experimental Reports in HMI-B595 listed by field of science

The most important long-term co-operation partners from the region of Berlin-Brandenburg are:

- Stranski-Laboratorium der Technischen Universität Berlin (Prof. G.H. Findenegg)
- Max-Planck-Institut für Kolloid und Grenzflächenforschung, Golm/Potsdam, (Prof Dr. H. Möhwald)
- Technische Universität Berlin, Institut für Werkzeugwissenschaften und -technologie, Metallphysik, (Prof. W. Reimers)
- Technische Fachhochschule Berlin, (Prof. W. Treimer)

Other national long-term co-operation partners in 2003 are

- Institut für Kristallographie, Universität Tübingen (Prof. J. Ihringer)
- Max-Planck-Institut Festkörperforschung, Stuttgart (Prof. B. Keimer)
- Institut für Biochemie, Technische Universität Darmstadt, (Prof. N. Dencher)
- Institut für Physikalische Biologie, Universität Düsseldorf, (Prof. G. Büldt)
- Institut für Festkörperphysik, Technische Universität Dresden (Prof. M. Loewenhaupt)
- FB Materialwissenschaften, Technische Universität Darmstadt, (Prof. H. Hahn)
- Institut für Festkörperphysik, Technische Universität Darmstadt, (Prof. H. Wipf)

Individual short-term research proposals of external users

It is the key issue of the BENSC user service to provide external groups with beam time and intensive scientific support for individual scientific experiments. This service is meant for both German groups and the international scientific community. The inclusion of new applications for beam time is decided by an internationally composed Scientific Selection Panel. For 2003, more than 165 short-term projects of external users have been accepted by the panel (see table 1).

Co-operation with Industry

The support for industry is mainly based on co-operation agreements, where the partners provide the samples and in return profit from the highly specialized know-how of the BENSC staff and from the advanced analytical methods available at BENSC, with use of neutrons and with complementary use of X-ray or synchrotron radiation. Major co-operation partners in 2003 have been

- MTU Aero Engines GmbH, München
- MTU Friedichshafen GmbH
- Ford Forschungszentrum Aachen GmbH
- Walter AG, Tübingen
- DaimlerChrysler AG, Stuttgart/TUM-Tech GmbH München

Extension of BENSC User Service to HMI instruments at BESSY

To promote complementary use of neutrons and synchrotron radiation, especially in materials science, HMI had initiated an EFRE-supported refurbishment project for the synchrotron source BESSY, including the development and installation of two new insertion devices for the BESSY ring. One of the insertion devices, the Undulator UE46, is operational already since 2002; with full user service at the (PGM-) beam line for magnetic nanostructures and magnetic films in 2003. The use of this beam line is detailed in table 2.

	weeks	
HMI in-house research	11	30 %
External Users under BENSC	4	11 %
External Users under BESSY	7	19 %
BESSY in-house research	15	40 %

Table 2: Distributuion of 2003 experiment time for the UE46-PGM beam line at BESSY

The second insertion device, a 7T Wiggler, has been installed in 2003 (see News-Report on page 110) and will serve two beam lines:

a. white beam for the Materials Science Diffractometer (Residual Stress and Texture Analysis)
b. monochromatic beam for Resonant Magnetic Scattering and High-resolution Diffraction.

The commissioning phase for these two beam lines will start in summer 2004.

BENSC – A European neutron facility, Support from the European Commission for Access to BENSC

The remarkably high number of guest scientists from member countries of the European Community have been stimulated by successfully applying for funds from the programs of the European Commission to support the transnational access to large scale research infrastructures. The EU funding for BENSC and users of BENSC under the Access action of the 5th Framework Programme (FP5) of the EU added up to 2,1 Mio €.

Some relevant numbers for FP5 support are:

4 years (2/2000–12/2003),
330 projects,
700 visits of European users,
2213 neutron instrument days delivered.

The EU-support will be continued under forthcoming FP6: For the 4 years period 2004–2007 BENSC will receive more than 2,3 Mio € for European access and for joint instrument development actions.

An analysis of the distribution of the beam time allocation for EU users demonstrates that a high number of users does not only come from countries which do not have a national research neutron facility, such as Italy, Spain or Greece. Strong user contingents also come from the UK and France to take advantage of options which are not available at their national neutron facilities or at the leading European reactor neutron source, the ILL in Grenoble.

Scientific results of the external users at BENSC

The scientific interim reports on most recent experimental results provide rapid dissemination of the BENSC users' results. The reports are published annually under the label of *BENSC EXPERIMENTAL REPORTS*, and the year 2003 Volume, HMI-B 595 (ISSN 0936-0891), is distributed to all users of BENSC in May 2004 as CD ROM and/or in printed form. The reports for 2000 through 2004 are also available on the BENSC internet pages.
(http://www.hmi.de/bensc/report2003/start_en.htm)

This rapid distribution of results is complemented by oral and poster contributions to national and international conferences. Publication in internationally renowned peer reviewed journals normally follows the experiments with a delay of 1 to 2 years. Since as a rule at least one collaborating BENSC scientist is among the authors the year 2002 publications of external users are included in the publication lists of the departments SF1, SF2 or SF3. A complete compilation of the year 2003 publication lists for all BENSC users and BENSC staff members is included in the a.m. volume *BENSC EXPERIMENTAL REPORTS 2003*, HMI-B595, May 2004. The majority of the BENSC publications has an external user as principal author, and a remarkably high fraction is published in high ranking journals (see table 3).

Journal **Impact Factor** (2002)	**Journal**	**Number** of BENSC publications 2003 with external user as principal author
30,40	**Nature**	3
7,232	**Phys. Rev. Letters**	2
6,201	**J. Am. Chem Soc**	1
4,207	Appl.Phys. Lett.	1
4,064	Biochemistry	1
3,912	FEBS Lett.	1
3,751	Macromolecules	1
3,327	**Phys. Review B**	8
3,248	Langmuir	5
3,048	Carbon	1
2,986	Phys. Review A	1
2,683	J. Mat Chem	1
2,4 - 1,4	Phys. Review E, J. Appl. Phys., Faraday Disc., Chem Phys., J. Appl. Cryst., Polymer, Macromol. Biosci., J. Phys.: Cond. Mat., Eur. Phys. J. B, etc.	30

Table 3: Number of external BENSC users' 2003 printed publications in high ranking journals, based on results of experiments under BENSC User Service

NAA-Laboratory and Irradiation Service at BER II

D. Alber, G. Bukalis, B. Stanik, A. Zimmer
HMI, SF6

The laboratory for neutron activation analysis (NAAL) at the reactor BER II provides radiation services for universities, scientific institutions and industry. Typical fields of applications are:

- Trace elements analysis with neutron activation analysis (NAA) for example in biology, medicine, geology and archeology. Certification of reference materials.
- Irradiation experiments, such as isotope production for medical applications, sources for Mößbauer spectroscopy and production of tracers for industrial applications.

The operation and further development of the irradiation devices at BER II and of the NAA measuring systems are a central task of the department SF6.

Irradiation devices

Four irradiation devices are available for different applications.

DBVK: rotatable irradiation device in the reactor core
DBVR: rotatable irradiation device in the Be-reflector of the reactor core
TBR: dry irradiation device outside the Be-reflector
SRT: fast rabbit system

DBVK and DBVR are used for long term irradiation experiments. Up to nine aluminum containers can be irradiated simultaneously.
Short time irradiation experiments are carried out by means of TBR and SRT.

Status 2003

- The fast rabbit system SRT was not in use in 2003, due to man-power problems. The control system as well as the acquisition system has to be renewed.
- The work for upgrading the in-core position DBVK is still in progress.
- Planning of the renewal of the control units of DBVK and DBVR.

Device	$\Phi_{thermal}$ [1/cm²s]	Φ_{fast} [1/cm²s]	Containers
DBVK	1,5E+14	4,3E+13	9*
DBVR	7,5E+12	1,9E+10	9
TBR	3,4E+12	2,2E+10	1
SRT	4,4E+11	3,9E+10	1

*Temporarily restricted to 4

Irradiation experiments 2003

A total of 1969 samples were irradiated in 2003. 71 % of the 185 irradiation experiments, were performed with the DBVK or DBVR. With these devices it is possible to irradiate up to 24 samples simultaneously in one aluminum container. About 60 % of the irradiation experiments and the analysis of samples was done for external users.

Internal users

Most of the internal users are from the Dept. SF6, but irradiation and analyses were also performed for users from depts. SF1, SF2, SF3, and SE5.

External users

Universities:
FU Berlin
HU Berlin
University Dresden
University Hamburg
University Karlsruhe
University Leipzig
TU München
University München
University Mainz
University Zürich
University Modena
University Lausanne

Research Institutes:
BAM, Berlin
GSF, Neuherberg
IIF, Leipzig
DGKC, Bonn
IZW Institute of Zoo Biology and Wildlife Research, Potsdam

Industry:
TruTec Process Diagnostics
Pilkington Deutschland AG

Utilisation of the Irradiation Devices

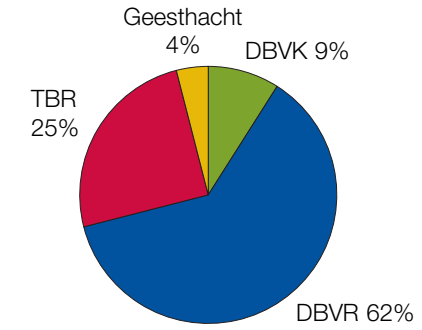

2003 Irradiated Samples

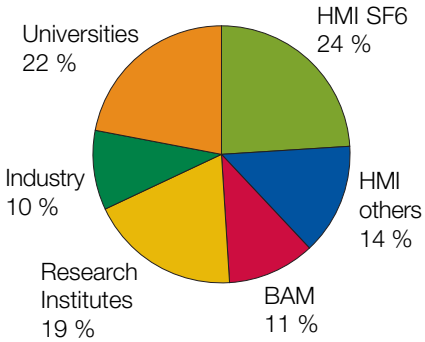

ISL Operations and Developments

Scientists: H. Homeyer, P. Arndt, W. Busse, A. Denker, W. Pelzer, C. Rethfeldt, J. Röhrich
Operators: J. Bundesmann, R. Grünke, G. Heidenreich, H. Lucht, E. Seidel, H. Stapel

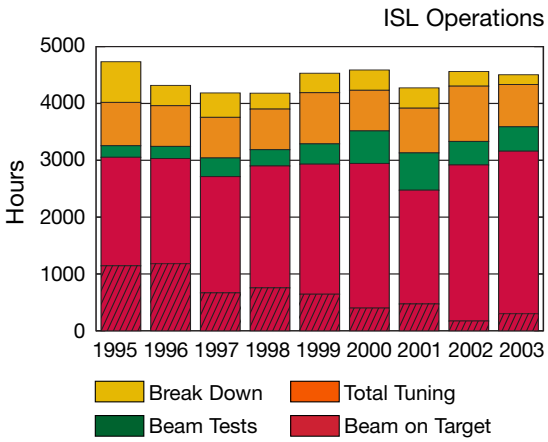

Fig. 1: ISL Operations since 1995: ISL has managed to operate the facility with an average of 3000 hours of beam-time on target. The hatched parts are low energy (Van-de-Graaff) beams. It can be observed that the demand for high energy beams and the reliability (less breakdowns) increased and the total tuning time stays relatively constant, which is due to the fact that the number of users with different beam settings increased. In addition, high levels of beam quality were asked for by many users.

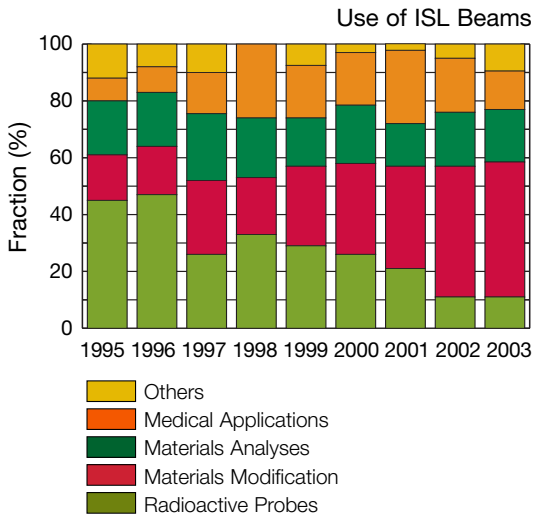

Fig. 2: Use of ISL ion beams. Materials modifications have become the largest part of research and development at ISL.

The ion-beam laboratory ISL offers ion-beams from various accelerators and accelerator combinations with energies ranging from some tens of eV to several hundred MeV dedicated to the application of ion-beam techniques. Internal and outside users study the basics of the interaction of ions with solids. They modify and analyse materials with ion beams and they perform radiotherapy of eye tumours with fast protons in a joint venture with university clinics. Users have at their disposal 15 different irradiation areas equipped with specific instrumentation.

ISL operations went rather smoothly in 2003. As seen in Fig. 1 the time for unscheduled downtimes reached a new all-time low. Simultaneously the production of high energy beams within the scheduled operation time of 4300 hours climbed to a new all-time high of nearly 3000 hours. Several reasons contributed to this excellent outcome:
I) improved operations of the ion source for Au ion beams which have become the most attractive beam used in 2003,
II) better reproducibility for the phase matching between the RFQ and the cyclotron, resulting in shorter tuning times,
III) training of the operators and
IV) a larger demand for high energy proton beams, providing an effective use of the time between therapy sessions either for high-energy PIXE or radiation hardness testing.

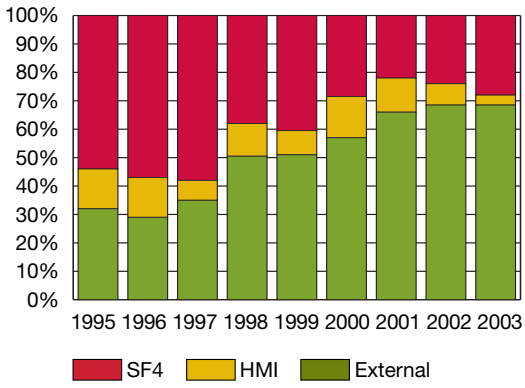

Fig. 3: ISL's development into a user facility. External users including proton therapy use more than 2/3 of the beam-time.

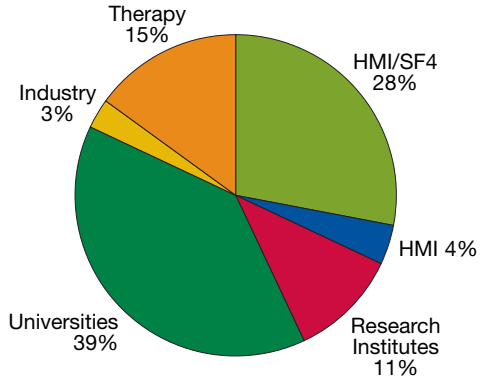

Fig. 4: Origin of ISL Users: The university share has again increased. This is due to their active involvement in the materials modification programme.

Any user has access to the ISL via a programme advisory committee, which meets annually, and decides on the applications for beam time solely on the basis of the proposals' scientific merit. 41 different projects (27 in 2002) involving more than 100 (70 in 2002) scientists received beam time in 2003. In total, more than 80 projects are active at ISL. At its annual meeting, the programme advisory committee accepted 41 proposals, 24 new ones and 17 addenda to running experiments.

Materials analysis in 2003 used exclusively fast ions, either heavy ions for ERDA or protons for high-energy PIXE. They used an almost constant share of beam time (see Fig. 2). Eye tumour therapy was performed at 9 therapy blocks, however, the medical applications used less beam time than 2002 for research work, reflecting changes in personnel. The most active field, concerning new proposals as well as amount of beam time is materials modification and ion-solid interaction.

The amount of beam time used by external users was again more than 2/3 of the overall time (see Fig. 3). Looking at the origin of the users, the universities increased once more their share, due to the on-going trend in the scientific programme towards ion-beam modification of materials.

The set-up of new target stations was pursued, and three of them went into operation in 2003: two of them are dedicated to interaction of ions with solids and one is to recoil implantation.

The tendency of using lightest and heaviest ions available consisted. The most requested beam was gold, now used for nearly one third of the overall beam time. In addition, so-called cocktail beams, ions with the same charge/mass ratio and the same velocity, have been produced: 2 MeV/u Ne/Ar and 3.5 MeV/u Kr/Xe. We assume an increasing demand for these cocktail beams, as they will allow rapid changes of the ion species and therefore the energy deposition.

Besides the installation of new target stations, most of the development was to increase the reliability of the facility in general. The quadrupole power supplies in the extraction beam line have been exchanged. The set-up of the new platform for the injection into the RFQ continued. When this platform is in operation, we expect a reduction of tuning times, as the ECR-source can be prepared parallel to a running experiment.

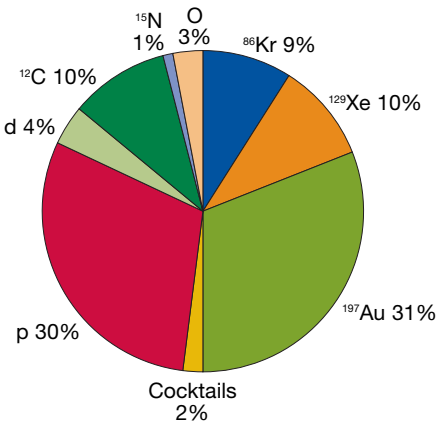

Fig. 5: Fast ion beams used at ISL: in 2003, most of the beam time used either the lightest or the heaviest ions available. In addition, so-called cocktail beams have been produced.

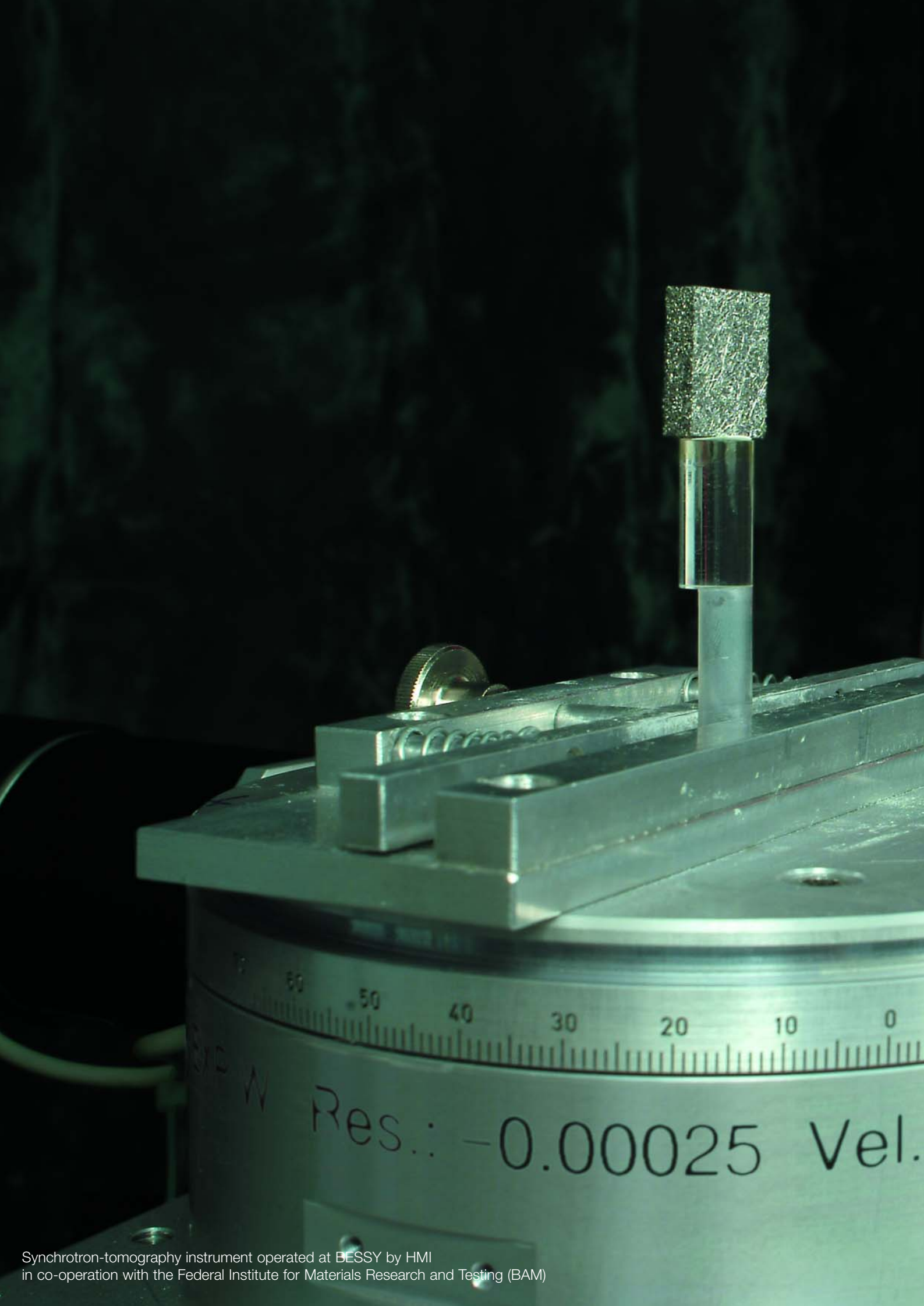

Synchrotron-tomography instrument operated at BESSY by HMI
in co-operation with the Federal Institute for Materials Research and Testing (BAM)

Scientific highlights Structural Research 2003

Antiferromagnetic order as a competing ground state for electron-doped high-transition temperature superconductors

H. J. Kang[1], M. Matsuura[2], Pengcheng Dai[1,2], J. R. Thompson[1,2], J. W. Lynn[3], Shou-Cheng Zhang[4], D. N. Argyriou[5], K. Prokeš[5], Y. Onose[6], Y. Tokura[7,8], Y. Kurita[9], Seiki Komiya[9], Yoichi Ando[9]

■ 1 Department of Physics and Astronomy, The University of Tennessee, Knoxville, Tennessee, USA ■ 2 Condensed Matter Sciences Division, Oak Ridge National Laboratory, Oak Ridge, Tennessee, USA ■ 3 NIST, Center for Neutron Research, National Institute of Standards and Technology, Gaithersburg, Maryland, USA ■ 4 Department of Physics, Stanford University, Stanford, California, USA ■ 5 HMI, SF2 ■ 6 Spin Superstructure Project, ERATO, Japan Science and Technology, Tsukuba, Japan ■ 7 Correlated Electron Research Center, Tsukuba, Japan ■ 8 Department of Applied Physics, University of Tokyo, Tokyo, Japan ■ 9 Central Research Institute of Electric Power Industry, Komae, Tokyo, Japan

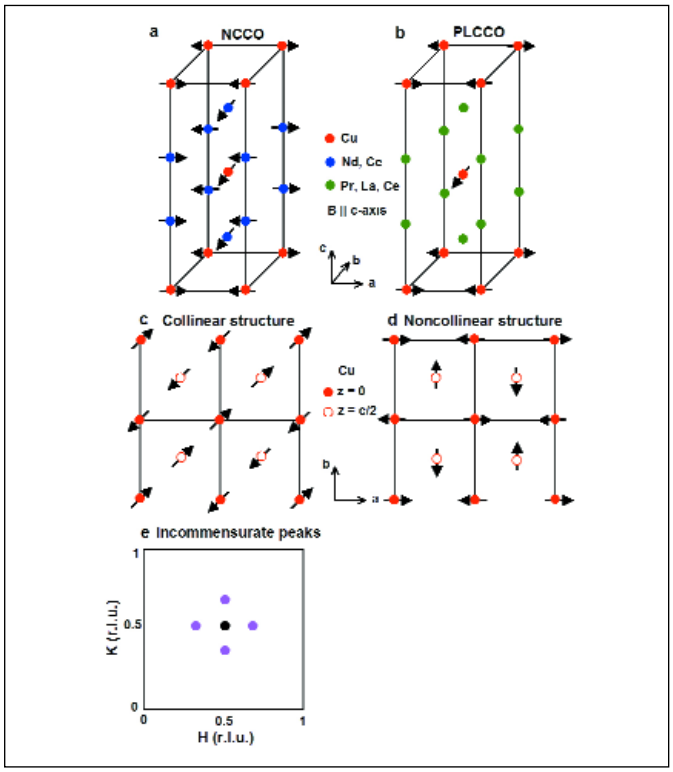

Fig. 1: Noncollinear spin structure of a) phase I/III in NCCO b) in PLCCO. The oxygen atoms are not shown for clarity. c) Collinear spin structure has the spins in adjacent layers parallel or antiparallel. d) The spins in adjacent layers are orthogonal in noncollinear structure. e) Data from neutron scattering on a copper oxide (sketch). The black circle is the Bragg peak coming from antiferromagnetism of the undoped parent compound. The pink circles are incommensurate peaks, which are shifted away from AF Bragg peaks. The incommensurate peaks reflect a periodic structure with a period slightly differing from the period of the crystal. Here, these peaks are associated with the separation of holes, when holes are doped.

The discovery of high-transition temperature (high-T_c) superconductivity in copper oxides (cuprates) in 1986 created unprecedented research activities in studying these materials. The parent compounds of the high-T_c cuprates are antiferromagnetic Mott insulators [1]. The crystal structure of these materials is distinguished by typical CuO_2 planes. Each Cu^{2+} in such a plane has one unpaired electron and the spins of these electrons form an antiferromagnetic long-range order. When holes or electrons are doped into these planes, the long-range antiferromagnetic ordered phase is destroyed and the copper oxide materials become metallic and superconducting with persistent short-range antiferromagnetic spin correlations. Much work has focused on understanding the interplay between magnetism and superconductivity [1], because spin fluctuations may mediate electron pairing for superconductivity. Soon after the discovery of hole-doped superconductors, Tokura and his coworkers found the electron-doped superconductor $Nd_{2-x}Ce_xCuO_4$ (NCCO) [2]. Although both hole-doped $La_{2-x}Sr_xCuO_4$ (LSCO) and electron-doped NCCO have two-dimensional CuO_2 planes, their phase diagrams versus doping concentrations are asymmetric. For hole-doped LSCO materials, antiferromagnetism rapidly weakens with increasing doping x and is replaced by superconductivity over a wide range of x with a maximum T_c at $x = 0.15$. For electron-doped materials, as-grown materials are nonsuperconducting antiferromagnetic insulators and superconductivity can only be induced after annealing the $x > 0.11$ samples in a narrow x range. Therefore, finding the similarities and differences of the n-type and p-type cuprates would be very important in understanding the mechanism of high-T_c superconductivity.

Since high-T_c cuprates are layered materials, superconductivity is highly anisotropic and the application of a magnetic field along the direction perpendicular to the CuO_2 planes can suppress superconductivity much easier than the same field applied parallel to the CuO_2 planes. For LSCO, superconductivity coexists with incommensurate (Fig. 1e) quasi two-dimensional spin-density wave modulations in the underdoped regime, where the superconducting transition temperature T_c is below the highest value [3]. Application of a magnetic field along the c-axis enhances the static incommensurate spin-density wave order [4, 5]. Since a similar field applied in the CuO_2 plane has little effect on superconductivity and spin-density wave order [6], these results suggest that the incommensurate spin-density wave order competes with superconductivity.

For electron-doped materials, our ultimate goal is to determine if similar spin-density wave exists and, if so, to measure their magnetic field-induced effect. The Cu^{2+} spins have a simple antiferromagnetic (AF) collinear structure (Fig. 1c) in the parent compounds of hole-doped materials such as La_2CuO_4 and $YBa_2Cu_3O_6$. Below 30 K, the Cu^{2+} spins in the parent compound of electron-doped Nd_2CuO_4 and Pr_2CuO_4 form the noncollinear antiferromagnetic structure of Fig. 1a and b, due to the exchange coupling between Cu^{2+} and rare-earth ions. We use neutron scattering to investigate the magnetic field effect in electron-doped high-T_c superconductor $Nd_{1.85}Ce_{0.15}CuO_4$ [7]. However, the annealing process necessary to make superconductivity in this material also induces a cubic $(Nd,Ce)_2O_3$ as an impurity phase [8]. Because Nd in $(Nd,Ce)_2O_3$ has a magnetic ground state and is lattice matched with $Nd_{1.85}Ce_{0.15}CuO_4$ in the CuO_2 plane, application of a c-axis aligned magnetic field on $Nd_{1.85}Ce_{0.15}CuO_4$ will also induce paramagnetic scattering from $(Nd,Ce)_2O_3$. For zero momentum transfer along the c-axis, the lattice from NCCO and $(Nd,Ce)_2O_3$ are lattice matched. As a consequence, the results obtained in [7] may be ambiguous [8] and are subject to debate [9].

There are two ways to resolve this impurity problem and determine the intrinsic properties of electron-doped materials. First, even though the lattice parameters of the cubic impurity $(Nd,Ce)_2O_3$ are lattice matched with NCCO in the ab-plane, its c-axis lattice constant is about 10 % smaller than that of NCCO. This lattice constant mismatch gives incommensurate scattering in NCCO at positions such as (0.5, 0.5, L) L=2.2, 4.4, and so on. Therefore, one can separate the impurity scattering by simply performing a c-axis aligned magnetic field experiment at non-zero integer L positions, such as L = 1, 2, and 3 as such scattering can only arise from NCCO. To do this, we performed an experiment at HMI using the HM-2 horizontal field magnet to probe the AF order at (0.5, 0.5, 3) position. The antiferromagnetic reflection (0.5, 0.5, 3) of NCCO shows clearly the field-induced effect (Fig. 2a), while the impurity reflection (2, 0, 4) shows no observable field-induced effect at NCCO position (0.5, 0.5, 4.4) (Fig. 2b). These results unambiguously demonstrate that application of a c-axis aligned magnetic field enhances the residual antiferromagnetic order [10].

The second method to resolve this impurity issue is simply to perform field-induced experiments on samples where the impurity phase has a nonmagnetic ground state. For this purpose, we grew single crystals of $Pr_{0.88}LaCe_{0.12}CuO_4$ (PLCCO), where Pr^{3+} has a nonmagnetic singlet ground state and the impurity phase $(Pr,La,Ce)_2O_3$ has no observable field-induced effect up to 12 T (see Fig. 3 b) [11]. The as-grown PLCCO has the same noncollinear Cu spin structure as phase I/III of NCCO, except a small induced Pr moment is antiparallel to the Cu moment direction. Since the rare earth Pr^{3+} moment contribution is negligible in PLCCO and the impurity phase $(Pr,La,Ce)_2O_3$ does not show any field effect, PLCCO is an ideal material for investigating the phase transition from the superconducting state to the AF ordered state.

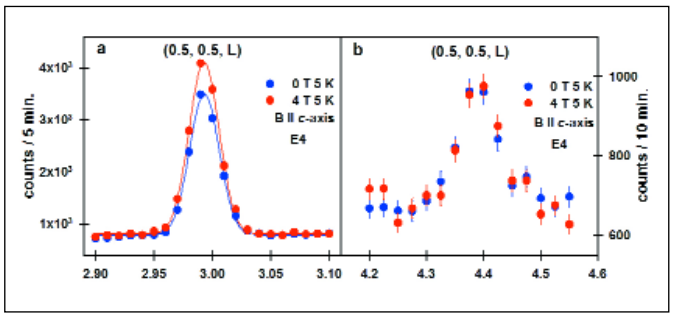

Fig. 2: The field effect on $Nd_{1.85}Ce_{0.15}CuO_4$
a) The L scan at AF position (0.5, 0.5, 3) of NCCO shows that a c-axis aligned field enhances the AF order.
b) The impurity reflection (2, 0, 4), which is at (0.5, 0.5, 4.4) in NCCO shows no field effect.

We first investigate at zero-field how as-grown AF ordered insulator is transformed into a superconductor. We find that the existence of commensurate spin-density wave modulations in underdoped PLCCO is similar to that in LSCO [12]. We then study the effect of an applied magnetic field on spin-density wave modulations at HMI. The c-axis aligned magnetic field on $Pr_{0.88}LaCe_{0.12}CuO_4$ induces the AF order at (0.5, 0.5, 0) position (Fig. 3 a), whereas no field-induced effect is observed at (0, 0, 2.2) from impurity phase (Fig. 3 b) [11]. Therefore, it is clear that the observed field effect at (0.5, 0.5, 0) cannot arise from the impurity phase and a c-axis aligned field also affects the spin-density wave modulation in electron-doped materials.

In summary, our experiments performed using high-magnetic fields at HMI show that the spin-density wave order can be enhanced by an applied field irrespective of electron and hole doping. These results can provide quantitative constraints on theoretical understanding of the interplay between magnetism and superconductivity in high-T_c copper oxides.

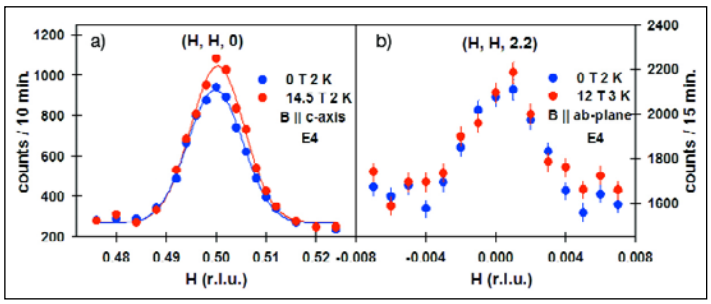

Fig. 3: The field effect on $Pr_{0.88}LaCe_{0.12}CuO_4$ a) The AF order is induced at (0.5, 0.5, 0), when superconductivity is suppressed by a field along the c-axis. b) The impurity position (0, 0, 2.2) has no field effect.

[1] M. A. Kastner, R. J. Birgeneau, G. Shirane, and Y. Endoh, Rev. Mod. Phys. **70**, 897 (1998).

[2] Y. Tokura, H. Takagi, and S. Uchida, Nature **337**, 345 (1989).

[3] H. Kimura, K. Hirota, H. Matsushita, K.Yamada, Y. Endoh, S-H Lee, C. F. Majkrzak, R. Erwin, M. Greven, Y. S. Lee, M. A. Kastner, and R. J. Birgeneau, Phys. Rev. B **59**, 6517 (1999).

[4] S. Katano, M. Sato, K. Yamada, T. Suzuki, and T. Fukase, Phys. Rev. B **62**, R14677 (2000).

[5] B. Lake, H. M. Rønnow, N. B. Christensen, G. Aeppli, K. Lefmann, D. F. McMorrow, P. Vorderwisch, P. Smeibidl, N. Mangkorntong, T. Sasagawa, M. Nohara, H. Takagi, and T. E. Mason, Nature **415**, 299 (2002).

[6] B. Lake, K. Lefmann, N. B. Christensen, G. Aeppli, D. F. McMorrow, P. Vorderwisch, P. Smeibidl, N. Mangkorntong, T. Sasagawa, M. Nohara, H. Takagi (unpublished).

[7] H. J. Kang, Pengcheng Dai, J. W. Lynn, M. Matsuura, J. R. Thompson, Shou-Cheng Zhang, D. N. Argyriou, Y. Onose, Y. Tokura, Nature **423**, 522 (2003).

[8] P. K. Mang, S. Larochelle, M. Greven, Nature **426**, 139 (2003).

[9] H. J. Kang, Pengcheng Dai, J. W. Lynn, M. Matsuura, J. R. Thompson, Shou-Cheng Zhang, D. N. Argyriou, Y. Onose, Y. Tokura, Nature **426**, 140 (2003).

[10] M. Matsuura, Pengcheng Dai, H. J. Kang, J. W. Lynn, D. N. Argyriou, K. Prokes, Y. Onose, Y. Tokura , Phys. Rev. B **68**, 144503 (2003).

[11] H. J. Kang, Pengcheng Dai, H. A. Mook, M. Matsuura, J. W. Lynn, Y. Kurita, Seiki Komiya, Yoichi Ando, (unpublished).

[12] H. J. Kang, Pengcheng Dai, H. A. Mook, M. Matsuura, J. W. Lynn, Y. Kurita, Seiki Komiya, Yoichi Ando, (unpublished).

[13] The NCCO and PLCCO samples are provided by Y. Tokura's group at The University of Tokyo and Y. Ando's group at Centeral Research Institute of Electric Power Industry, Komae, Tokyo 201-8511, Japan, respectively.

Neutron diffraction and theoretical model studies of the field induced magnetic phases of the $ErNi_2B_2C$ superconductor

A. Jensen[1,2], K. Nørgaard Toft[1], A.B. Abrahamsen[1], N.H. Andersen[1], J. Jensen[2], P. Hedegård[2], J. Klenke[3], K. Prokeš[3], P. Smeibidl[3], S. Danilkin[3] and V. Sikolenko[3]

■ 1 Materials Research Department, Risø National Laboratory, Roskilde, Denmark ■ 2 Ørsted Laboratory, Niels Bohr Institute fAPG, Copenhagen, Denmark ■ 3 HMI, SF 2

Introduction

Magnetism and superconductivity are two basic properties of materials that have been studied intensively for many years. While a solid understanding of magnetism has been developed during the last fifty years, there are significant basic properties that remain to be explained in superconductivity, as exemplified by the mechanism underlying high-temperature superconductivity. Superconductivity and static magnetic order are generally considered as competing phases. Back in the fifties and sixties, it was observed that superconductivity was strongly suppressed or extinguished by substitution of magnetic impurities at a 1% level [1, 2]. However, in the seventies it was revealed that true long-range magnetic order co-existed in Chevrel phase superconductors like RMo_6S_8 and the related RRh_4B_4 (R = rare earth) [3]. Here it is argued that the detrimental effect of the rare earth ions is avoided, because they form a fully ordered sublattice that is isolated from the conduction electrons. Furthermore, the ordering sets in at rather low temperature (approximately 1 K) and has a modulated structure that averages out on a length scale of the superconducting order parameter. In the late eighties all attention was given to the high-temperature superconductors where highly interesting, but so far unraveled, interactions exist between the magnetic and the superconducting electrons or holes within the same copper-oxide planes.

The rare-earth nickel boron-carbides RNi_2B_2C have attracted much attention after their discovery in 1994 [4, 5], because superconductivity and antiferromagnetism co-exist for R = Dy, Ho, Er and Tm at comparable temperatures $6\ K \leq T_c \leq 11\ K$ and $1.7\ K \leq T_N \leq 11\ K$ [6]. Here, T_N is the Néel temperature. Above this temperature, the antiferromagnetic order in a crystal is lost, similarly to the superconducting properties that are lost above the critical temperature T_c. $ErNi_2B_2C$, in particular, is interesting because magnetization studies have indicated weak ferromagnetism below $T_c = 2.3$ K in zero-field and because several magnetic phases develop in an applied magnetic field [7]. Single-crystal neutron-diffraction studies in zero field [8] have corroborated these results and confirmed the earlier neutron powder-diffraction findings [6] that the magnetic phases are characterized by a transversely polarized spin-density wave with an ordering vector (wave vector) $Q \approx 0.55\ a^*$ (or b^*, where a^* and b^* are reciprocal lattice vectors) and with the spins lying in the basal plane of the tetragonal crystal structure (see Fig. 1). If $Q = 0.5\ a^*$ was a stable configu-

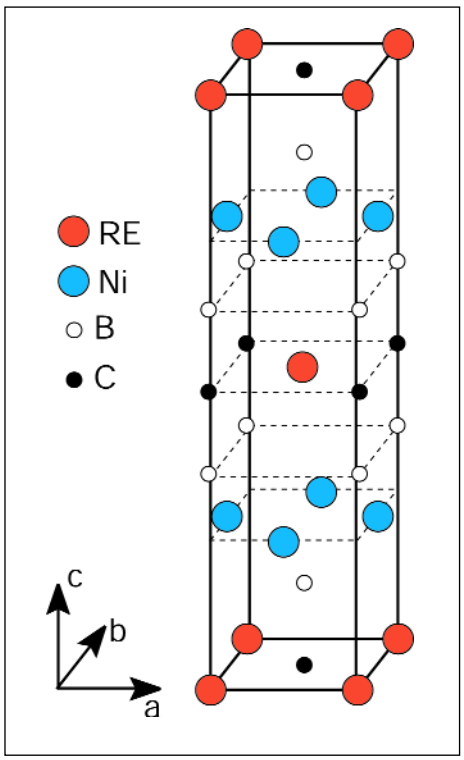

Fig. 1: Crystal structure of the rare-earth borocarbides

ration, the magnetic structure would consist of ferromagnetic sheets, and since the unit cell contains two Er-ions, the stacking sequence would be double layers: up-up-down-down etc. However, nesting at the Fermi surface results in phases with $Q \geq 0.55\ a^*$ and introduces phase slips in the stacking of the commensurate sequences.

Recently, a mean-field model has been established and shown to account for most of the observed experimental data, including the transition from weak ferromagnetism to antiferromagnetism at 2.3 K shown in Fig. 2 [9]. The model suggests that the magnetic transitions result from a series of structures with ordering vectors $Q = n/m\ a^*$ (or b^*) with $0.55 \leq n/m \leq 0.60$. The present neutron-diffraction study aims to establish the modulation vectors of the stable magnetic phases and to compare the results with the predictions of the mean-field model. A detailed account of the model is published in ref. 9, and the experimental results and model analyses are presented in ref. 10.

Results and discussion

Two stable structures have been identified with ordering vector $Q = 11/20\ a^*$ (or b^*) in zero field [9]. Above $T_c = 2.3$ K there is an equal number of up and down spins, but below T_c one of the spin directions becomes more populated, leading to weak ferromagnetism as visualized in Fig. 2. At low temperatures the structures are squared-up and not sinusoidal as they are close to T_N.

A field applied along [0 1 0] results in the formation of two different domains. Since the spins are Ising like, the most favorable domain has $Q = n/m\ a^*$. When increasing the field H more up-spins are formed and phase transitions between structures with different commensurate modulation vectors result, as shown in Fig. 3a. The transverse domain stays at $Q \approx 16/29\ b^* \approx 0.55\ b^*$ and decreases gradually in intensity as the field is increased. The H-T-phase diagram in Fig. 3a agrees well with data derived from bulk measurements [7, 11].

When applied along [0 0 1] the critical field for the antiferromagnetic phase is as high as ~ 17 T at 1.8 K. The phase diagram, studied in fields up to 12 T (the magnetic torque detached the crystal at higher fields), is shown in Fig. 3c. A gradual change of Q from $\approx 11/20$ to $\approx 5/9\ a^*$ (or b^*) results when the field and/or the temperature is increased.

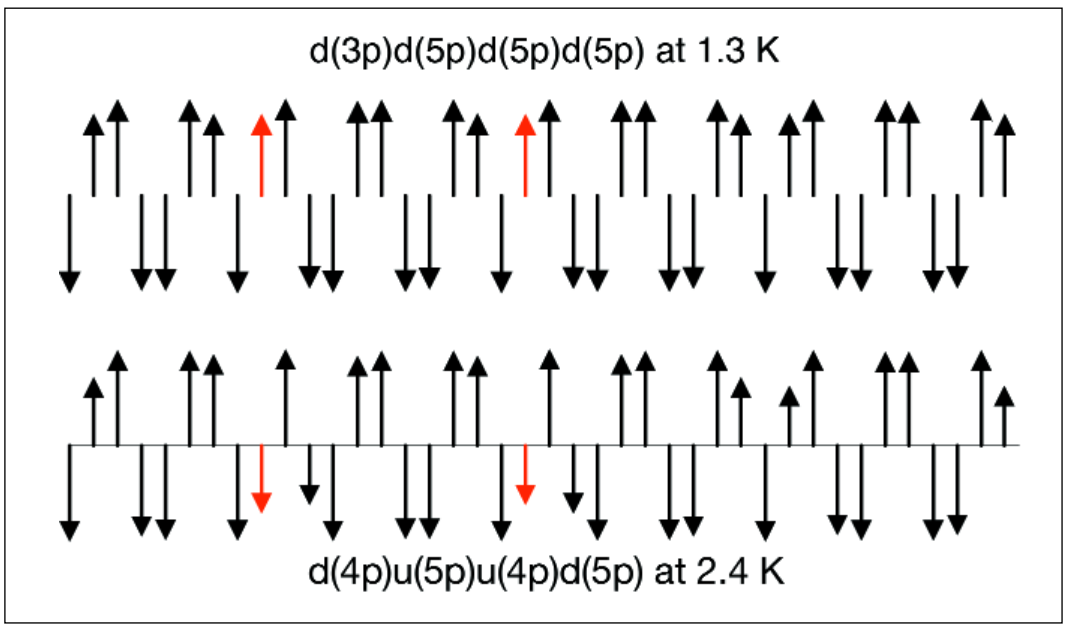

Fig. 2: One period of 40 layers of the $Q = 11/20$ zero-field structures calculated below the Curie temperature at 1.3 K, and in the antiferromagnetic phase at 2.4 K (the red arrows indicate those layers in which the moments are reversed at the transition).

Studies performed with the field along the [1 1 0] direction reveal a series of ordering vectors $Q = Q_p + Q_\delta$ as a function of field and temperature. The principal ordering vector Q_p along a^* or b^* ranges from $Q_p \approx 11/20$ to $\approx 18/31$ reciprocal lattice units rlu, as shown in Fig. 3b. A peculiarity is a small, but clearly observable, rotation of the principal ordering vector Q_p by an orthogonal component $Q_\delta \approx -0.005\ b^*$, which occurs close to and above the superconducting critical field, H_{c2}.

The mean-field model has been a valuable tool in the interpretation of the neutron diffraction and the bulk magnetization data. It accounts for the stability of many of the observed phases, but not for the small finite Q_δ. This small rotation shows that the exchange interaction has anisotropic components.

Acknowledgements
This work is supported by the EU Commission under contract HPRI-CT-2001-00138 on neutron-diffraction experiments at BENSC, the Danish Technical Research Council via the Framework Program on Superconductivity, and the Danish Natural Science Research Program via DANSCATT.

[1] M.B. Maple, Applied Physics **9**, 173 (1976)
[2] A.A. Abrikosov and L.P. Gorkov, Sov. Phys. JETP **12**, 1243 (1961).
[3] M.B. Maple and O. Fischer (edt.): *Superconductivity in Ternary Compounds, Topics in Current Physics*, Vols. I and II, (Springer, Berlin, 1982).
[4] R. Nagarajan et al. Phys. Rev. Lett. **72**, 274 (1994).
[5] R.J. Cava et al. Nature **367**, 254 (1994).
[6] J.W. Lynn et al. Phys. Rev. B **55**, 6584 (1997).
[7] P.C. Canfield et al., Physica C **262B**, 249 (1996).
[8] S.-M. Choi et al., Phys. Rev. Lett. **87**, 107001 (2001).
[9] J. Jensen, Phys. Rev. B **65**, 140514 (2002).
[10] A. Jensen et al., Phys. Rev. B **69**, 104527 (2004).
[11] S.L. Budko and P.C. Canfield, Phys. Rev. B **61**, R14932 (2000).

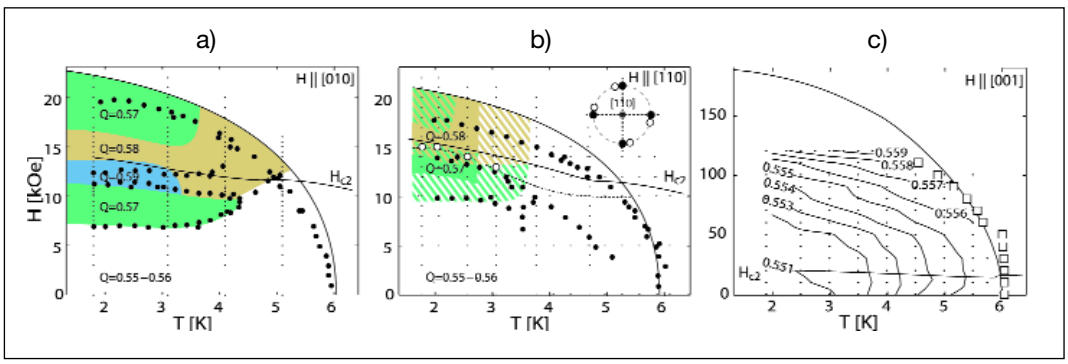

Fig. 3: Magnetic phase diagrams of $ErNi_2B_2C$ for the magnetic field applied along **a)** [0 1 0] , **b)** [1 1 0] and **c)** [0 0 1]. Small black dots mark the (T, H) points where the measurements were made. The outermost boundary lines in **a)** and **b)** interpolate points where the magnetic intensity disappears. In **c)** the boundary line is the Néel temperature determined by the mean-field model. A fine solid line marks the superconducting critical field H_{c2}, and the solid circles indicate the magnetic phase lines derived from magnetization measurements [11]. Four commensurate phases are presented in the phase diagram **a)** with H || [0 1 0]. In **b)**, H || [1 1 0], coloured areas indicate the existence of one of the three phases, and the striped areas represent coexistence of two phases. The modulation vector has a finite transverse component above the dashed line, and the open circles indicate that the orthogonal component is zero at lower field. The insert shows schematically how the magnetic reflections are rotated in reciprocal space. In **c)**, with H || [0 0 1], the contours indicate that Q increases continuously as function of H and T; the open squares represent the Néel temperature derived from the data.

Boundary Layers of Water at Polymer-Liquid Interfaces

R. Steitz, S. Schemmel, G.H. Findenegg
■ Technische Universität Berlin

Interfaces of hydrophobic substrates against aqueous media are of broad interest in view of their ubiquitous presence in biological and other types of colloidal systems. It is generally believed that the adsorption of apolar molecules from aqueous solutions onto a hydrophobic surface, like their aggregation in water, is caused by hydrophobic interactions [1]. Recent theoretical studies [2] have indicated, however, that the nature of the solvation of small and large apolar species in water is quite different: Hydrogen bonding of water persists around small molecules but is depleted near large species, leading to a drying phenomenon, i.e. a drastic reduction of the local density of water near the surface of large species, which is absent for species of radius less than ca. 1 nm. Modern techniques like X-ray and neutron reflectometry are ideally suited to experimentally cross check above predictions on extended systems. The fraction of reflected X-rays or neutrons is a direct measure of the density profile across the interface on the molecular scale. Neutron reflectometry (NR) is particularly useful as it offers the possibility to enhance the sensitivity by changing the scattering contrast, mostly by replacing weak scattering protons (^{1}H) by strong scattering deuterons (^{2}H = D) without distorting the chemical nature of the system under investigation.

Neutron reflectivity experiments on the interface of deuterated polystyrene films (d-PS) and heavy water (D_2O) revealed that water is depleted (to ca. 90 % bulk water density) in a ca. 3 nm thick boundary layer of the liquid phase against the hydrophobic substrate [3]. This finding coincides with reports on two similar systems [4, 5] where water depletion layers were also observed. All findings can be explained in the general context of wetting (or non-wetting) and in particular in the context of above mentioned theory of a drying transition [2] where the depletion of water is seen as a (weak) dewetting of the hydrophobic walls (d-PS coating, alkane monolayer) in contact with the bulk aqueous phase [6].

On a macroscopic scale, the wetting behaviour is characterized by the contact angle of the liquid at the surface of the substrate. Commonly, the advancing contact angle of macroscopic droplets of water, ϑ, is taken as a measure of the hydrophobicity (and wettability) of surfaces (see Fig. 1):

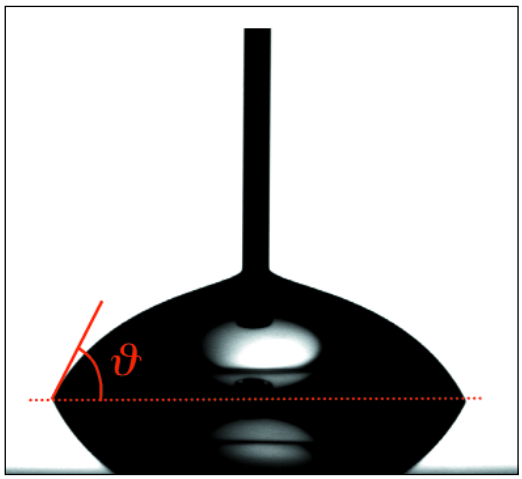

Fig. 1: Image of a water droplet (diameter ca. 3 mm) on a polymer substrate at which the contact angle ϑ at the three-phase contact line (substrate/ liquid/ vapor) is less than 90°. This is a signature of a weakly hydrophobic or hydrophilic substrate.

Contact angles $\vartheta > 90°$ indicate hydrophobic surfaces, while $\vartheta < 90°$ indicate weakly hydrophobic or hydrophilic surfaces.

For water on d-PS coatings, $\vartheta = 90°$, and thus it is not unexpected to find that water is depleted in the boundary layer against d-PS surfaces. It is more of a surprise that water is also depleted near ethyleneoxide-terminated self-assembled monolayers (EG3-OMe SAMs), for which the water contact angle is only 63° [5]. Furthermore, measurements of force as a function of distance between two organic surfaces immersed in aqueous solutions, performed by Ishida et al. [7], indicated the onset of hydrophobic interactions at even lower water contact angles ($\vartheta \approx 40°$). This observation is remarkable as the onset of hydrophobic interactions is an indicator for incipient drying of the surfaces.

Contact angles in the range of 30–70° are also typical for water or aqueous solutions at polyelectrolyte coatings. In the present work we prepared multilayer films, Si/PEI/(d-PSS/PAH)$_6$ (ϑ = 63°) and Si/PEI/(d-PSS/PAH)$_6$/d-PSS (ϑ = 37°), from the respective polyelectrolytes PEI (polyethylene-imine), d-PSS (deuterated polystyrene sulfonate) and PAH (poly-allyl-hydrochloride), by "layer-by-layer" deposition [8] on top of silicon single crystals. The polyelectrolyte-coated silicon single crystals served as the top of a flow cell made up by a Teflon trough (see Fig. 2).

Polyelectrolyte multilayers absorb substantial amounts of water [9]. The scattering length density, Nb, of the films and of the water phase can be matched by using appropriate mixtures of D_2O and H_2O, and in this way the film/water interface should become invisible to the impinging neutrons in the absence of a depletion layer. Thus, polyelectrolyte coatings are ideal model systems to check the relation between water contact angle and the appearance of water depletion by neutron reflectometry.

Fig. 2 shows reflectivity curves for a given polyelectrolyte coating (ca. 30 nm thickness) against pure D_2O, pure H_2O and a contrast-matching D_2O/H_2O mixture. From these and further results for a series of different D_2O/H_2O mixtures the scattering length density (sld) of the polyelectrolyte film at given D_2O/H_2O compositions of the water phase was extracted from fits to the spectra (solid lines in Fig. 2, bottom) and plotted versus the scattering length density of the water phase. By this procedure the matchpoint of polyelectrolyte film and bulk water phase was found to be $5.03 \cdot 10^{-6}$ Å^{-2}. For this condition the Kiessig fringes stemming from the interference of neutrons that are reflected at the silicon/film and at the film/water interface, respectively, are completely suppressed (Fig. 2 bottom left, middle curve). This finding proves that the polyelectrolyte coatings are indeed contrast matched, but it also indicates that there is no significant depletion of water at the hydrophilic polyelectrolyte/water interface. At least it is safe to say that water depletion is much less pronounced than observed at the hydrophobic d-PS/water interface. The same conclusion also holds for the d-PSS terminated films.

Interestingly, the contact angle of water on the PAH-terminated polyelectrolyte multilayers is almost the same as on the EG3-OMe terminated SAMs of reference [5]. Nevertheless, the wetting behavior of these two surfaces appears to be quite different. While the water-sorbing polyelectrolyte coatings do not induce a depletion layer of water, pronounced depletion of water is found at the non-swelling SAMs. This demonstrates that the water contact angle cannot be taken as an unambiguous indicator of the onset of the drying transition of water at hydrophobic surfaces. Apparently our knowledge about interfaces that are generally considered "simple" is far from complete.

[1] Israelachvili, J., *Intermolecular and Surface Forces*, 2nd Ed., Academic Press: London, UK, 1992, p. 128 ff.
[2] Lum et al., J. Phys .Chem. B, **103**, 4570 (1999).
[3] Steitz et al., Langmuir, **19**, 2409 (2003)
[4] Torben et al., Phys. Rev. Lett. **90**, 086101 (2003).
[5] Schwendel et al., Langmuir, **19**, 2284 (2003).
[6] Ball, Nature, **423**, 25 (2003).
[7] Ishida et al., J.Coll Interface Sci, **216**, 387 (1999).
[8] G. Decher, Science **277**, 1232 (1997).
[9] Steitz et al., Colloid Surfaces A, **163**, 63 (2000).

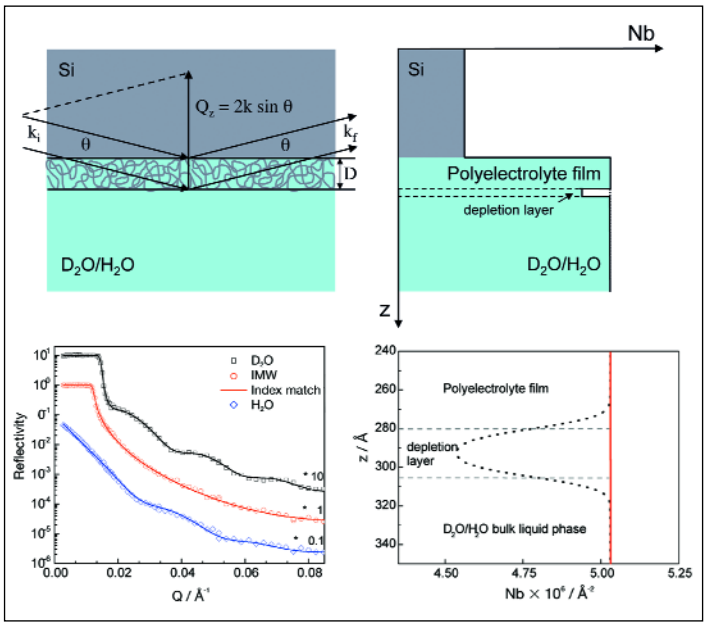

Fig. 2: Scattering geometry (**top left**), schematic scattering length density profiles (**top right**), reflectivity curves (**bottom left**) and zoom-in on the scattering length density profile at the polymer/water interface (**bottom right**). Note that the polymer film sandwiched between the silicon backing and the water fronting is invisible to the incident neutron beam upon appropriate index-matching of the liquid phase (red solid lines, bottom left and right). In this case the neutrons are reflected from the silicon/polymer interface only and thus the characteristic oscillations of the reflectivity curve are lost. The black dotted line shows the profile of the scattering length density across the polymer/liquid interface. For details see text.

Neutron Autoradiography of the painting *Armida abducts the sleeping Rinaldo* (~1637) by Nicolas Poussin

C. Laurenze-Landsberg[1], C. Schmidt[1], L.A. Mertens[2], B. Schröder-Smeibidl[2]
■ 1 Berlin Picture Gallery (Gemäldegalerie Berlin) ■ 2 HMI

Fig. 1: Nicolas Poussin, Replica, *Armida abducts the sleeping Rinaldo*, (c. 1637), Berlin Picture Gallery, 120 × 150 cm², Cat No. 486

In close collaboration, the Berlin Picture Gallery (Gemäldegalerie Berlin, Stiftung Preußischer Kulturbesitz) and the Hahn-Meitner Institute investigate old masters paintings by means of neutron autoradiography. Neutron autoradiography is a very effective, non-destructive, but rather exceptional method applied in the examination and analysis of materials and techniques used in painting. It allows the visualization of structures and layers under the visible surface and, in addition, enables one to identify in detail the elements contained in the pigments. The instrument B8 at the Berlin Neutron Scattering Center BENSC is dedicated to these investigations.

Isotope	Half life	Pigment
^{56}Mn	2.6 h	Brown colours, Umber, Ocre
^{64}Cu	13 h	Azurite, Malachite
^{76}As	1.1 d	Smalt, Realgar, Auripigmente
^{122}Sb ^{124}Sb	2.7 d 60 d	Naples-Yellow
^{32}P	14 d	Bone-black
^{203}Hg	47 d	Vermillion
^{60}Co	5.3 a	Smalt

Table 1: Main isotopes and pigments used in neutron autoradiography and their half-lives

Neutron autoradiography – the method and the instrument

Usually, when examining paintings, museums apply methods based upon the use of photon radiation. However, the information provided by these methods is limited. Infrared reflectography reveals black carbon-based media, whilst X-ray transmission-records only indicate the distribution of heavy elements like iron or lead, e.g. in the pigment lead-white. As a complementary method, neutron autoradiography is capable of revealing different paint layers piled-up during the creation of the painting. In many cases, the individual brushstroke applied by the artist is made visible as well as changes and corrections introduced during the painting process. By using paintings that have been reliably authenticated, one can identify the unique style or "hand" of a particular artist.

The experimental principle

The experimental principle is simple: In the first step, the painting is irradiated at the instrument B8 by neutrons from the research reactor BER II. Some of the atomic nuclei within the painting capture one of the neutrons thus becoming radioactive. The probability of capture depends on the activation cross-section specific for every isotope. During the irradiation, the painting is fixed on a support in front of the neutron guide end (open area: 3.5 × 12.5 cm²). The surface of the painting is adjusted under a small angle (< 5°) with respect to the axis of the guide. This way, the main free path of the neutrons within the paint layer becomes much longer than in the case of perpendicular transmission. The support is then moved up and down with a velocity of a few cm/s allowing for a uniform activation of the total area of the panel. Due to the short irradiation time, only 4 of 10^{12} atoms became radioactive on average, insofar the method is considered as a non-destructive investigation. After irradiation, the neutron-induced radioactivity decays with time. Around a dozen of different light and heavy isotopes – emitting β- (electrons) and γ-radiation – are created. The most important isotopes, their half-lives and the corresponding pigments are presented in Table 1. The induced β-decay blackens highly sensitive films or imaging plates thus unveiling the spatial distribution of the pigments. The big advantage of neutrons lies in the fact that different pigments can be represented on separate films. This is due to a con-

trast variation created by the differences in the half-lives of the isotopes. The γ-spectroscopy provides information about the element composition in the pigments. The image plate technique allows for direct digital analysis and processing.

The investigation of the painting *Armida abducts the sleeping Rinaldo* (c. ~1637) by Nicolas Poussin

Nicolas Poussin (1594–1665), one of the main representatives of pictorial classicism in the Baroque period, was French, but spent his entire career in Rome with the exception of two years as court painter to Louis XIII. The illustrations in his paintings address scenes from the Bible and from classical antiquity. Already in 1625, the legend of the sorceress Armida and the crusader Rinaldo had inspired Poussin to a painting named *Armida and Rinaldo*, now owned by the Dulwich Picture Gallery in London, that is accepted as being an original. In contrast, the painting at the Berlin Picture Gallery *Armida abducts the sleeping Rinaldo* (Fig. 1) showing a different but similar scene, is up to now listed in the Berlin Gallery's catalogue as a copy.

To clarify the open question of the ascription, an investigation by means of neutron radiography was carried out at the Hahn-Meitner Institute. The record of an X-ray radiography (Fig. 2) applied as a complementary method did not contribute to the solution of the problem revealing primarily the image of the wooden frame. Because of the size of the painting, the neutron radiography had to be carried out in two separated irradiations. In Fig. 3, one of the autoradiographs is depicted. The different sets of image plates were processed digitally and assembled afterwards. Already this first record, showing the distribution of the short-lived isotope ^{56}Mn contained in the brown pigment umber, reveals surprising conceptual changes – so called *pentimenti*: additional trees (highlighted in Fig. 3) not present in the final painting. Obviously, these *pentimenti* are corrections made by the master himself. A copyist would not have been aware of these changes. Therefore, these *pentimenti* are strong and important hints that this painting can possibly be ascribed to Nicolas Poussin himself.

Summary
With neutron autoradiography painting techniques or conceptual changes and corrections of a painting become visible. The art historian or the restorer obtains valuable information about the artist's brushstroke and the actual condition of the painting. In some cases, decisions about the authenticity can be made. In addition, this method is used more and more as an instrument supporting the restoration of paintings. The example presented above impressively demonstrates the efficiency of neutron autoradiography as a method for the examination of paintings.

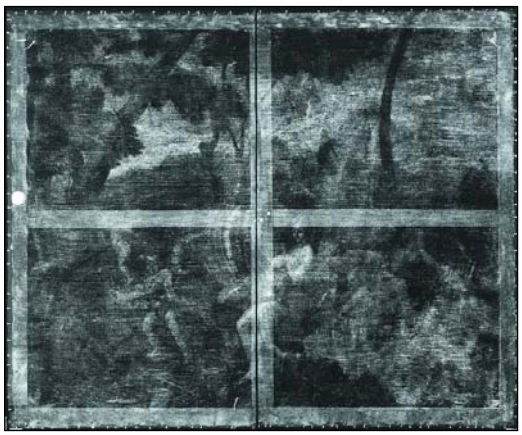

Fig. 2: Nicolas Poussin, Replica, *Armida abducts the sleeping Rinaldo*, X-Ray transmission record, Picture Gallery Berlin

Fig. 3: Nicolas Poussin, Replica, *Armida abducts the sleeping Rinaldo*, 1st neutron autoradiography assembled from 12 image plate records: In order to investigate the whole picture, two separated irradiations were carried out and finally recomposed.

Plastic deformation of amorphous silicon under swift heavy ion irradiation

A. Hedler[1], W. Wesch[1]; S. Klaumünzer[2]
■ 1 Friedrich-Schiller University, Jena ■ 2 HMI, SF4

All investigated amorphous materials show anisotropic plastic deformation under swift heavy ion irradiation (SHI) as a consequence of multiple anisotropic high electronic energy deposition referred to as ion hammering [1–3]. In the past years this effect has been discussed controversially [4–7]. The viscoelastic thermal spike theory by Trinkaus et al. [4, 5] represents a good description for glasses which show a continuous transition to the liquid state. However, a verification of the model for amorphous semiconductors, which show a phase transition of first order, has not been undertaken. With its well-known physical properties amorphous Si (a-Si) seems to be a suitable candidate to be investigated first.

Single-crystalline, 370 µm thick, one-side polished Si wafers were amorphized by means of multiple Si implantation at 77 K with energies of 0.25–9.5 MeV and ion fluences of $3–7 \cdot 10^{15}$ cm^{-2} at the Tandetron accelerator of FSU Jena. Rutherford-backscattering spectrometry, infrared-reflection spectrometry and cross-sectional transmission electron microscopy imaging revealed a homogenous amorphous surface layer with a thickness of $d = 5.7$ µm. In order to measure surface shifts with a precision of 1 µm an Au grid layer of 40 nm thickness has been produced on the sample surface by subsequent Au evaporation through a Ni net.

Swift heavy ion irradiation of the samples was carried out at HMI with the conditions described in Table 1.

Ion/Energy	Θ	T_0[K]	S_e[keV/nm]
390 MeV Xe^{21+}	45°	77, 300	15.8 ± 0.2
350 MeV Au^{26+}	45°	77, 300	18.8 ± 1.0
600 MeV Au^{30+}	45°	77, 300	21.3 ± 0.3

Table 1: Irradiation conditions: the angle of the ion beam with respect to the surface normal Θ, the irradiation temperature T_0 and the mean value of the electronic energy deposition in the a-Si layer S_e as calculated by SRIM-2003.

By mounting the sample on a holder with a movable aperture micrographs of the transition region between irradiated and unirradiated surface parts were taken in-situ with a long-distance microscope. As an example, Fig. 1 shows a micrograph of the surface shift of a sample irradiated with electronic energy deposition $S_e = 18.8$ keV/nm at $T_0 = 77$ K indicating the occurrence of plastic flow of a-Si under SHI.

In order to quantify the plastic flow process, the dependence of the surface shift Δx on the ion fluence Φt has been measured for each SHI condition. Fig. 2 shows the results for the irradiations at $T_0 = 77$ K.

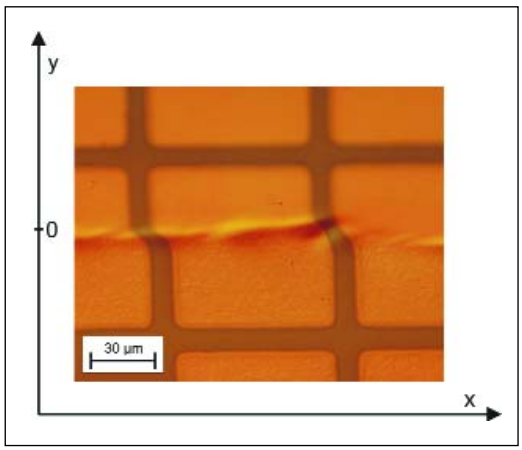

Fig. 1: Micrograph of a calibrated a-Si sample. The grid distance is 85 µm. The upper part ($y \geq 0$) has not been irradiated, the lower part ($y \leq 0$) has been irradiated at $T_0 = 77$ K with 350 MeV Au and an ion fluence of $\Phi t = 1.65 \cdot 10^{15}$ cm^{-2} under an angle of $\Theta = 45°$ from left.

A linear dependence of $\Delta x(\Phi t)$ and an intensified plastic flow with increasing S_e have been observed. For room-temperature irradiation and small fluences the data points lie slightly below those in Fig. 2. The linear increase of $\Delta x(\Phi t)$ is a well-known feature of the ion hammering

effect of embedded amorphous layers within crystalline surroundings and can be understood with the extended Maxwell model [1–3]

$$\dot{\underline{\varepsilon}} = \underline{\underline{A}} \cdot \Phi + \dot{\underline{\varepsilon}}_{elast} + \dot{\underline{\varepsilon}}_{visc} \qquad (1)$$

which describes the macroscopic deformation $\underline{\varepsilon}$ as a superposition of the ion hammering effect, characterized by the deformation yield tensor $\underline{\underline{A}}$, with the elastic and viscous properties of the layer, characterized by $\underline{\varepsilon}_{elast}$ and $\underline{\varepsilon}_{visc}$, respectively. In case of quasi-static equilibrium and stress-free surfaces this model has a solution far from the interfaces, which describes the surface shift as a function of the ion fluence

$$\Delta x = 3A_0 d \cdot \sin 2\Theta \cdot \Phi t. \qquad (2)$$

The tensor $\underline{\underline{A}}$ reduces to the scalar A_0 denoted as deformation yield per ion and determines the slope of the linear dependence $\Delta x(\Phi t)$ and thus the strength of the anisotropic growth. Trinkaus et al. assigned A_0 to the ion-solid-interaction and could derive an expression for the dependence of A_0 on both the irradiation condition (energy deposition, irradiation temperature) and the target material properties [4–5].

Being aware of the layer thickness d and the incident angle of the ions Θ the dependence of the deformation yield A_0 on the electronic energy deposition S_e can be calculated for both irradiation temperatures by using Eq. (2). The results are shown in Fig. 3. As a rough approximation a linear dependence of $A_0(S_e)$ has been observed for both irradiation temperatures. For constant energy deposition A_0 decreases with increasing T_0 due to enhanced stress relaxation in the surroundings of the ion path [4-5] resulting in a lower slope $\mathrm{d}A_0/\mathrm{d}S_e$ for the higher T_0. The energy deposition threshold of the plastic deformation can be assigned to $S_{e0} = 14.2\ \mathrm{keV/nm}$ and is independent of the irradiation temperature. The observed value of the normalized deformation yield for $T_0 = 77\ \mathrm{K}$ $\mathrm{d}A_0/\mathrm{d}S_e = 4.6 \cdot 10^{-14}\ \mathrm{m^3/J}$ is an order of magnitude lower than typical values for metallic glasses [4-5] and is obviously due to the first order phase transition occurring during the thermal spike phase in a-Si.

Further investigations should be directed to a possible explanation of the observed normalized deformation yield at the low irradiation temperature with an extended Trinkaus theory including the phase transition of first order in a-Si.

[1] S. Klaumünzer, Multisc. Phenom. in Plasticity, 441 (2000).
[2] A. Gutzmann, S. Klaumünzer, P. Meier, Phys. Rev. Lett. **74**, 2256 (1995).
[3] A. Gutzmann, S. Klaumünzer, Nucl. Instr. & Meth. B **127/128**, 12 (1997).
[4] H. Trinkaus, A.I. Ryazanov, Phys. Rev. Lett. **74**, 5072 (1995).
[5] H. Trinkaus, J. Nucl. Mater. **223**, 196 (1995).
[6] L. Cliche, S. Roorda, M. Chicoine, R.A. Masut, Phys.Rev.Lett. **75**, 2348 (1995).
[7] M. Chicoine, S. Roorda, L. Cliche, R.A. Masut, Phys. Rev. B **56**, 1551 (1997).

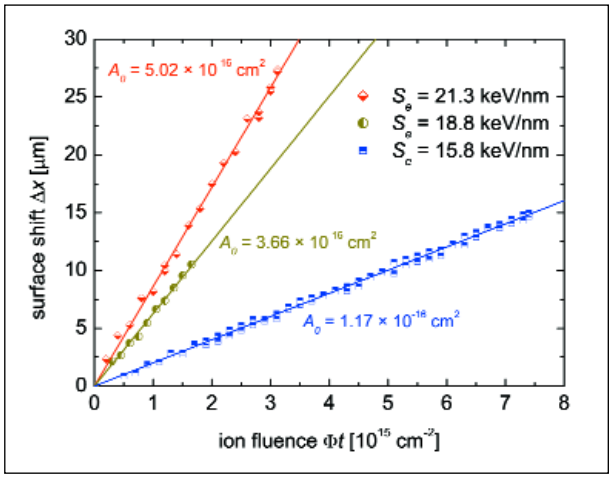

Fig 2: Dependence of the surface shift Δx on the ion fluence Φt for the irradiations at T_0 = 77 K.

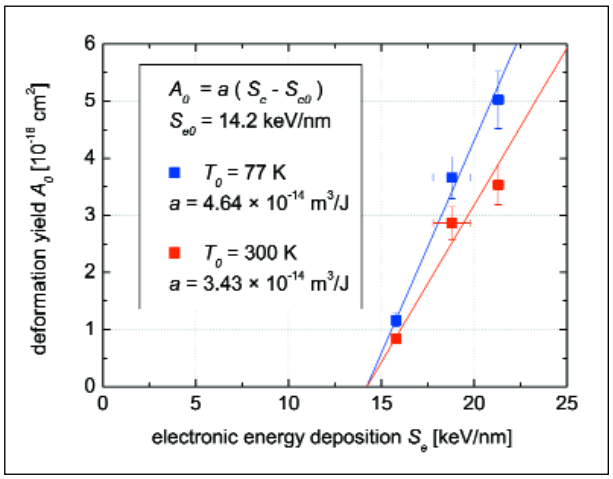

Fig. 3: Dependence of the deformation yield per ion A_0 on the electronic energy deposition S_e. The threshold value of S_e is denoted as S_{e0}.

Surface modification by irradiation with swift heavy ions

W. Bolse[1], B. Schattat[1], H. Paulus[1], I. Zizak[2], N. Darowski[2], S. Klaumünzer[2]
■ 1 Institut für Strahlenphysik, Universität Stuttgart ■ 2 HMI, SF4

Swift heavy ions at energies of the order of MeV/amu are slowed down in a solid predominantly by electronic excitation and ionization of the target atoms, while nuclear energy deposition by elastic collisions is negligible. Defect creation and amorphous track formation due to electronic energy deposition, which has been observed especially in insulators, demonstrate that part of the electronic excitation energy is transferred to the lattice. In thin film packages, swift heavy ion irradiation results in atomic mixing at the interfaces. In former experiments it was shown that interface mixing in oxide bilayers occurs as soon as a certain threshold S_{ec} is exceeded, which is given by track formation threshold of the less sensitive material of the bilayer [1, 2]. The threshold for interface mixing of NiO/SiO_2 is given by NiO, where we have investigated the track formation, too.

Samples and irradiation

NiO single crystals prepared for transmission electron microscopy (TEM), as well as NiO bulk material and the thin layer system NiO/SiO_2 have been irradiated with 90 MeV to 350 MeV Ar, Kr, Xe and Au ions at $T = 80$ K and low fluences, (~10^{10} cm^{-2}), where the single ion impacts are clearly separated from each other.

The irradiations were performed at Hahn-Meitner Institute, Berlin. No tracks were observed after irradiation with 90 MeV Ar ions, while discontinuous track fragments became visible after irradiation with 140 MeV Kr ions. This is in good agreement with the intermixing and self organization behaviour in NiO/SiO_2-bilayers, where the effects could only be observed after irradiation with ions heavier than Ar [3]. Continuous tracks, with their number density being in agreement with the ion fluence, were formed during irradiation with 230 MeV Xe and 350 MeV Au, respectively.

In Fig. 1, the top view of a NiO-sample irradiated with 350 MeV Au is shown, while in Fig. 2 the sample was tilted by 40°, displaying continuous tracks. Furthermore, spherical nanoparticles have been formed at the ends of these tracks. Fresnel contrasts, which evidence voids, were observed along the tracks and prove that the center of the tracks is empty. The void formation conforms with the nanoparticle formation at the surface. Similar nanoparticles have been observed at the top of NiO/SiO_2 due to swift heavy ion irradiation with low fluences.

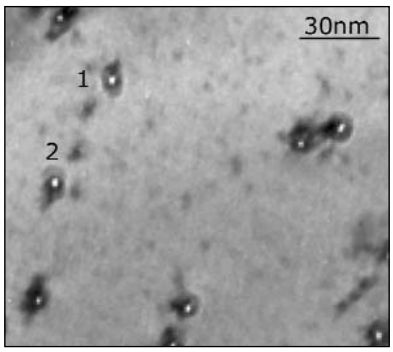

Fig. 1: TEM image of the single NiO crystall irradiated with $4 \cdot 10^{10}$ cm^{-2} 350 MeV Au. The image was taken normal to the surface.

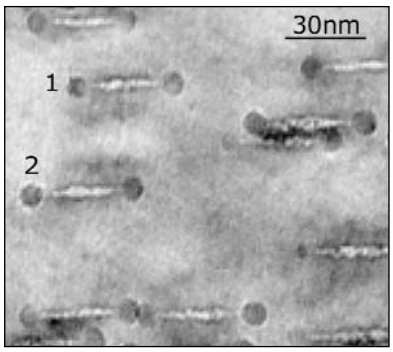

Fig. 2: Same position on the same sample as in the Fig. 1. Sample was tilted 40° for the TEM. Note the corresponding tracks marked with numbers in the figures 1 and 2. The irradiation led to the creation of hollow tracks with small spheres at the ends.

Experiment

X-ray scattering methods have been proven to be a powerful tool for non-destructive analysis of the shape, size distribution and density fluctuations of solid state matter. Using the 6-circle goniometer at the KMC2 beamline at BESSY and the available area sensitive detector, it was possible to study the diffuse small angle scattering (SAXS), recording the beam reflected from the sample surface (GISAXS). This geometry allows one to gain information about structures at the surface with a size of a few nanometers, and is therefore well-suited for the investigation of the pellets on the irradiated NiO-samples. The shape of the pellets, their size distribution and parts of the ion track near the surface can be studied and characterized.

The goniometer at the KMC2 beamline is optimized for surface investigations using the grazing incidence angle geometries, and, in combination with the well collimated beam and the area sensitive detector, it is suitable for GISAXS measurements.

After the sample surface was aligned with the incident beam, fast qualitative reflectometry measurements were performed to estimate the angle of total reflection for the specific sample. Changing the incident angle in the GISAXS experiment allows the study of different depths under the surface. If the GISAXS measurement is performed with incident angle smaller than the total reflection angle, only objects which are above the surface are detected. If the incident angle is larger, part of the photons is penetrating the surface and being scattered on the objects below the surface. This way, the scattering of the pellets and the hollow tracks can be measured separately.

Results and Discussion

Since only one half of each sample was irradiated, we were able to measure the scattering from the unirradiated part, and use these measurements for the background correction.

Fig. 3 shows the detected scattered intensity from the thin NiO/SiO_2 irradiated with $5 \cdot 10^{10}$ 350 MeV Au ions/cm^2. The resolution and the signal to noise ratio were not very satisfactory, so only a part of the planned evaluation was performed. The scattering pattern measured on the unirradiated part of the sample was subtracted from the pattern measured on the irradiated part. The resulting scattering pattern was fitted with the model function of monodisperse spheres laying on the sample surface to obtain the radius of the pellets. The resulting radius of the pellets was 6.2 nm. Thick NiO single crystals showed no difference in scattering function between the irradiated and the unirradiated part.

Although GISAXS offers more information on the surface objects, it was not possible to evaluate the measured data with the expected success. Low intensity of the primary beam and large noise made the detection of the hollow tracks impossible. However, we were able to detect and estimate the size of the spheres on the surface of some irradiated samples. This experiment showed that GISAXS provides information on irradiated samples which are very hard to measure with other methods.

In 2005, a new SAXS experimental station is going to become operational at the 7 T wiggler at BESSY. The new station is optimized for the surface scattering, and we plan to continue this experiment at the new device. We hope to be able to measure not only the radius of the spheres, but also the radius and the dimensions of the hollow track.

[1] W. Bolse, B. Schattat, Nucl. Instr. Meth. B **190**, 173 (2002).
[2] B. Schattat, W. Bolse, S. Klaumünzer, F. Habsmeier, A. Jasenek, Appl. Phys. A **76**, 165 (2002).
[3] W. Bolse, B. Schattat, A. Feyh, Appl. Phys. A **77**, 11 (2003).

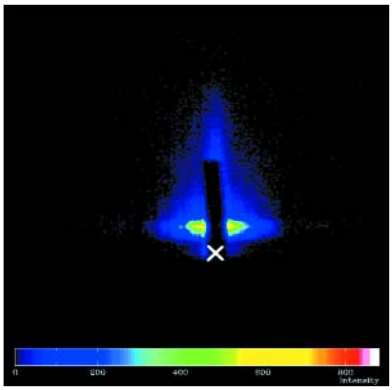

Fig. 3: Enlarged image from 2d area detector. The white cross marks the position of the primary X-ray beam. The sample surface is parallel to the *x*-axis of the detector, and the photons are reflected upwards. The dark box in the middle is the shadow of the beam stopper, which protects the detector from the directly reflected beam. The scattering in the surface direction can be seen left and right from the reflected beam.

Tendaguru Sauropod Dinosaurs – Characterization of Diagenetic Alterations in Fossil Bone

M. Stempniewicz, A. Pyzalla
■ Institut für Werkstoffkunde und Materialprüfung, Technische Universität Wien, Austria

Sauropod dinosaurs, and more specifically Barosaurus africanus and Brachiosaurus brancai, were animals of tremendous size. The physiological and biochemical consequences of this size and the resulting weight estimated to reach up to 100 t [1] makes these dinosaurs subject of our interest. In the project presented here we investigate the structure of the animals' fossilized bones – a study exclusively based on the fossil record, i.e. the excavated skeletons.

In fossilized sauropod bone significant structural changes may have occurred due to the interdiffusion between the bone and the environment it was buried in for about 150 million years. In order to assess these diagenetic changes (alterations to a material's original mineralogy and texture due to geological processes), the chemical composition of several fossilized bones from the Tendaguru dinosaur bed (Tanzania, East Africa) is studied. These bones were excavated during the Tendaguru Expedition run by Janensch in the years 1909–1913 [2] and have been stored at the Museum of Natural History of the Humboldt-University in Berlin (NHUB). Cores were taken from the middle shafts of femora and humeri of the sauropod skeletons by PD Dr. M. Sander, University of Bonn. We investigated the cores, i.e. cross-sections through the middle shafts, in order to determine their structure on different hierarchical levels as well as their texture (orientation distribution of the crystallites). Since material from individuals belonging to the same species, yet buried in different stages of ontogenetical development, is available, we expect that the growth process of the sauropods can be studied.

For the assessment of diagenentic changes in the sample material quantitative analyses of their elemental composition were necessary. The measurements were performed at the ISL-cyclotron by means of the PIXE method (Proton Induced X-Ray Emission). All experiments were carried out in air with a 68 MeV proton beam with an area of (2 × 2) mm^2. The cross sections obtained from the cores were scanned radially from the priosteal surface (outer surface of the bone) to the border of the trabecular ("spongy") bone at the endosteal surface (inside surface of bones that borders the bone marrow cavity). The characteristic X-rays emitted from the targets were collected by an HPGe-detector. From the obtained spectra quantitative analyses were performed.

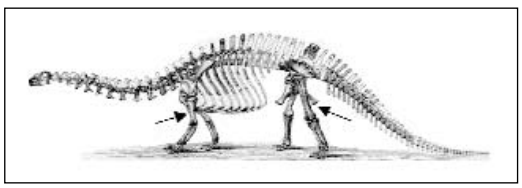

Fig. 1: General built of a sauropod dinosaur with indicated humerus and femur bones (arrows).

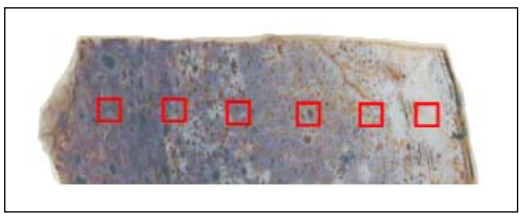

Fig. 2: Radial cut of a cross section of a femoral shaft of the Barosaurus africanus individual with indicated measurement points. Spot size: 2 × 2 mm^2.

Fig. 2 shows a typical radial cut of a cross section with measurement points located on it. Concentration profiles from all samples are similar (Fig. 4). Among the observed element distributions those of manganese, strontium and uranium are the most interesting. Though the bones remained buried for 150 million years, the elements are still not evenly distributed. Uranium and strontium concentrations differ in absolute concentrations, but they seem to follow the same pattern. Strontium, that exchanges calcium in the apatite structure, shows relatively higher concentrations toward the outer surface. Manganese, in turn, is present only inside the bone (in the pores), its concentration increases toward the inner part of the bone. The absence of manganese in the cortex indicates that only minor diagenetic alterations of the bone occurred, since this element was not incorporated in the biological processes during the lifetime of the sauropods. Iron is enriched in certain areas and causes the typical brownish tint. There are several biological and geochemical processes that might explain these observations.

In our previous studies of the Tendaguru skeletons, we determined the crystallographic structure of the bone mineral, its habit and density [3]. In addition, the application of PIXE yielded concentrations of various elements and their distribution over the sample. From the results we conclude that some chemical alterations occurred (strontium incorporation into bone mineral) but they were not very significant since manganese is only present in the pores and does not infiltrate the bone cortex. Therefore, the bone mineral particles are not fully recrystallized and further analyses of the crystallites can be interpreted in contexts of an individual's life history. More details may be found in [4].

The authors gratefully acknowledge Dr. Andrea Denker from ISL for her invaluable help during and after experiments.

[1] J. Peczkis, *Implications of body mass estimates for dinosaurs*; Journal of Vertebrate Paleontology **14**, 520–533 (1994).
[2] W-D. Heinrich, *The Taphonomy of Dinosaurs from the Upper Jurrasic of Tendaguru (Tanzania) Based on Field Sketches of the German Tendaguru Expedition (1909–1913)*, Mitt. Mus. Nat. kd. Berl., Geowiss. **2**, 25–61 (1999).
[3] M. Stempniewicz, B. Camin, A. Pyzalla, *Preliminary Investigation of Fossil Bone: XRD and XPS study*, Proceedings of the 13th Conference of European Society of Biomechanics, Acta of Bioengineering and Biomechanics, 4 (2002) Suppl.1.
[4] M. Stempniewicz, A. Pyzalla, M. Sander, P. Hinkel, S. Weiss, A. Denker: *Microscopical and PIXE Studies of Giant Sauropod Bones*, in preparation.

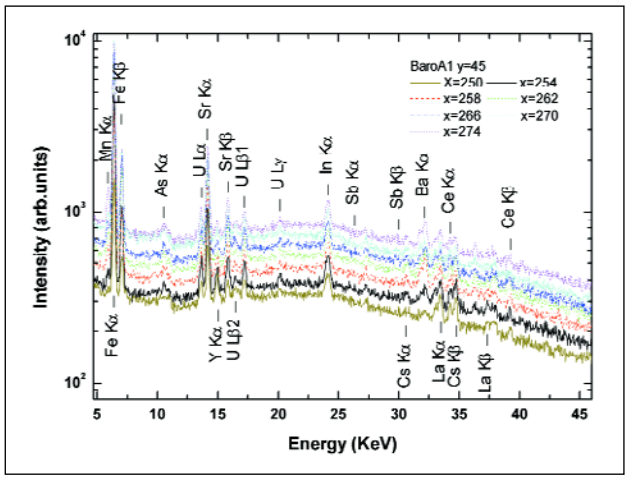

Fig. 3: PIXE spectrum recorded on different points of one section (Barosaurus africanus femur).

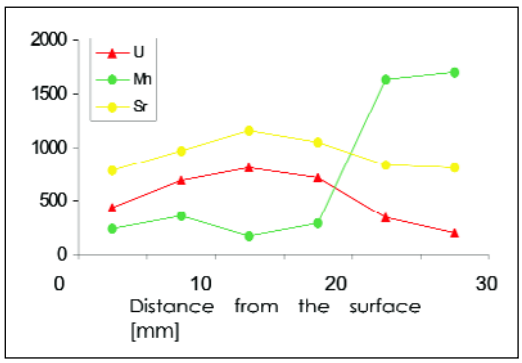

Fig. 4: Representative elemental distributions obtained by scanning a radial cut of a cross section (Barosaurus africanus femur).

Fluid and particle retention in the hippos Kathi and Josef of the Berlin Zoo investigated by Neutron Activation Analysis

A. Schwarm[2], S. Ortmann[2], M. Clauss[3], D. Alber[1], D. Behne[1]
■ 1 HMI, SF6 ■ 2 Institute of Zoo and Wildlife Research (IZW), Berlin ■ 3 Institute of Animal Physiology and Animal Nutrition, Oberschleissheim, Germany

There are two basic forms of digestive systems among herbivorous mammals: In foregut fermenters such as ruminants (i.e. cow, sheep, goat) and other non-ruminating mammals with forestomachs (i.e. hippo, kangaroo) the fermentation of the food by microorganisms proceeds the enzymatic digestion while in hindgut fermenters (i.e. horse, rhino, rabbit) it is the other way round. In most hindgut-fermenting mammals, larger particles are preferentially excreted as they are more difficult to digest and their retention would limit further food intake. In ruminants which submit retained larger particles to repeated chewing, has selective large particle retention been considered to be advantageous. It has been assumed that other mammalian herbivores with forestomachs have a particle retention mechanism similar to that of ruminants, but this has not yet been investigated.

Fig. 1: The hippopotamus Kathi

In order to obtain first information on this matter, the particle retention was investigated in one animal each of two non-ruminant mammalian foregut fermenters, the Common hippopotamus (Hippopotamus amphibious, Kathi) and the Pygmy hippopotamus (Hexaprotodon liberiensis, Josef) kept at the Berlin Zoo. The study was carried out by means of an elemental tracer technique. Hay particles with a length between 1 and 2 mm were labelled with chromium, larger particles with a length between 1 and 10 mm with cerium. Cobalt-EDTA was used as a fluid marker. The animals were given the mixed labelled hay particles and labelled water as a single dose. Before and for five days after the administration, the faeces of the animals were collected as often as possible.

The concentrations of chromium, cerium and cobalt in the faeces samples were determined by instrumental neutron activation analysis. After the samples had been dried and homogenized, 20–25 mg aliquots were sealed in ampoules made of highly pure silica, and, together with standard samples, were irradiated with thermal neutrons at the Berlin reactor BER II (neutron flux density $6 \cdot 10^{12}$ cm^{-2} s^{-1}, irradiation period 2 d, decay period 3 d). Of the radionuclides thus produced, the gamma rays of ^{51}Cr, ^{141}Ce and ^{60}Co were used for the quantitative analysis.

Figs. 2 and 3 show the concentrations of the three elements in the faeces collected at different periods of time after administration of the labelled dose. From these values the mean retention time was calculated. For Kathi the mean retention time was 77.4 h for the Cr-labelled 1–10 mm long hay particles and 73.4 h for the Ce-labelled 1–2 mm long particles and for Josef 62.7 h and 60.8 h, respectively. As was to be expected, the mean fluid retention time determined by means of the Co analysis was much shorter (35 h for Kathi and 27 h for Josef).

These results are a first indication that the forestomach physiology of the hippos differs from that of ruminants, insofar as the former have a faster excretion of the larger particles. In this respect, hippos might be representative for other non-ruminant foregut fermenters.

The study also showed that instrumental neutron activation analysis which allows the simultaneous determination of several elements in dried biological materials without any further sample preparation, is very well suited to be applied in tracer studies using multi-elemental labelling techniques.

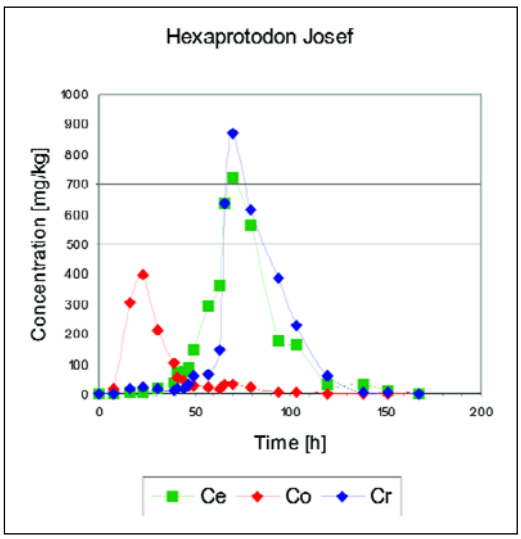

Fig. 2: Concentrations of Ce, Co and Cr in the faeces samples of Josef at different periods of time after administration of the labelled dose

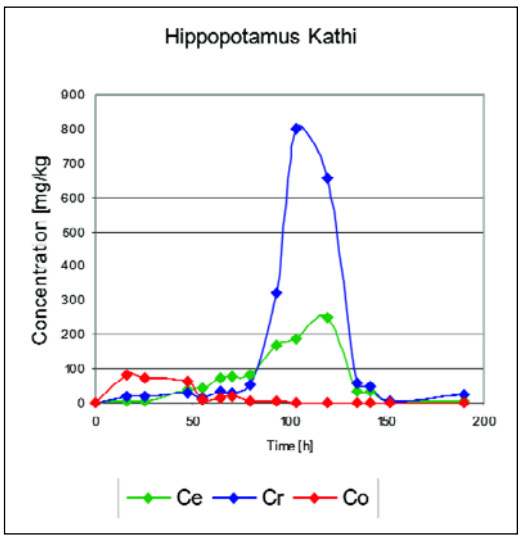

Fig. 3: Concentrations of Ce, Co and Cr in the faeces samples of Kathi at different periods of time after administration of the labelled dose

EXED – an instrument in progress

J. Peters, K. Lieutenant, D. Clemens, F. Mezei
■ HMI, SF1

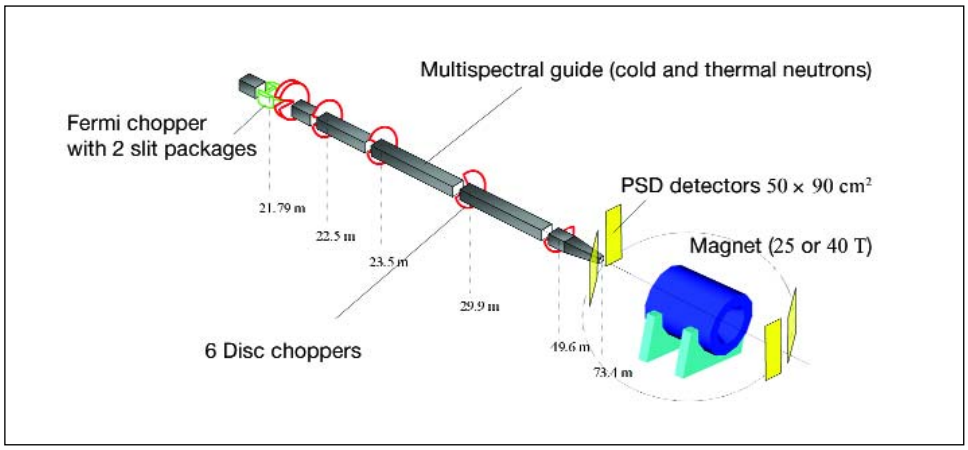

Fig. 1: Schematic view of the EXED instrument. The grey tubes correspond to a ballistic neutron guide (straight guide and the compressor). The neutron pulses are produced alternatively by a Fermi chopper (in green) or by a counter rotating double disk chopper (in red), which are exchangeable. The other disk choppers (in red) are frame overlap and a wavelength band chopper. The position sensitive gas detectors are presented in yellow and can be moved around the sample and the magnet. The blue structure is a magnet that might be used with the instruments. The sample is placed at its centre; the scattered neutrons leave in both forward and backward directions through the conical openings at the magnet's ends. The opening angles of the cones confine the range of accessible scattering angles.

The Extreme Environment Diffractometer EXED will be a central element of the instrumentation in HMI's new neutron guide hall, which is currently under construction (cf. News article on page 9). As a powder diffractometer, EXED will be mainly used for investigations of crystal and magnetic structures, in particular in substances available in form crystal powder only. In the development of this instrument several novel technologies will be applied, some of them developed at HMI. The instrument will be prepared for use with the planned 25-Tesla and 40-Tesla magnets thus contributing to HMI's position as a leading centre for the application of extreme sample environments with neutron scattering. Currently, the design of the instrument is in progress. EXED is expected to become operational by the end of 2006 and then serve as a user instrument at BENSC.

When monochromator crystals are employed in powder diffractometers, they select from the stream of neutrons incoming from the source those with a particular wavelength. The neutrons are then scattered in the sample and from the change in the direction of their motion one can deduce the momentum transmitted during the scattering process and finally the crystal's structure. Instead of being equipped with a monochromator, EXED is based on the time-of-flight (TOF) principle. In this case, a system of choppers – rotating slotted disks – selects packages of neutrons with wavelengths in a predefined range. These neutrons are then scattered on the sample and recorded by a detector. Since the wavelength of the neutrons is correlated with their velocity and their energy does not change during the scattering process, from the time of a neutron's arrival at the detector the particle's wavelength can be inferred. From the wavelength and the scattering angle one can calculate the momentum transfer – the scattering vector Q.

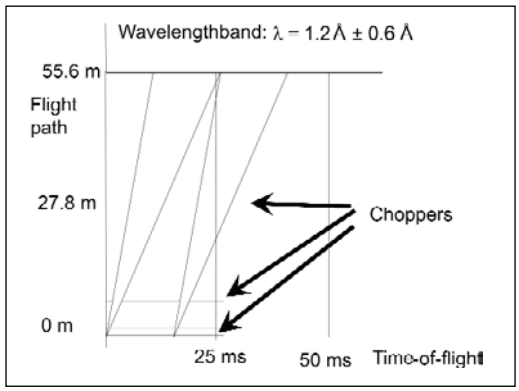

Fig. 2: Time-of-flight diagram for the chopper diffractometer. The diagonal lines correspond to neutrons with the extreme values within the chosen wavelength band of $\lambda = 1.2$ Å $\pm$ 0.6 Å cut by the chopper system out of the neutron stream. In this example, a wavelength band of $\Delta\lambda = 1.2$ Å can be obtained, as for a larger band subsequent neutron packages would overlap.

For pulsed neutron sources the time-of-flight technique is inherent. However, compared to a common crystal monochromator instrument, it offers a number of advantages on a continuous neutron source, too:

- higher resolutions, comparable to those now achieved at synchrotron radiation sources;
- efficient measurements for crystals with small distances between the crystal planes (d-spacing);
- more efficient in terms of neutron intensity for conventionally high resolution neutron diffraction work;
- full coverage of the relevant domain of scattering vectors Q at very limited angular access in scattering angles. Thanks to the variety of wavelengths in the incoming neutron package, the whole range of relevant values of momentum transfer during the scattering process can be observed within a small range of scattering angles. This property is important as the geometry of the new magnets for extreme sample environments will strongly confine the observable range of scattering angles (see Fig. 1).

EXED will be installed on an innovative multispectral neutron guide – a neutron guide delivering both the thermal and the cold neutron spectrum to the sample at about $80\ \mathrm{m}$ from the neutron source. Computer simulations using the Monte Carlo method [1] give an estimate of the maximum flux at the sample of $3 \cdot 10^6\ \mathrm{n/(cm^2/s)}$, which is comparable to the flux achieved by the General Materials Diffractometer GEM at the ISIS laboratory in England. The multispectral guide allows for an incoming wavelength range of 0.7 to 20 Å, i.e. a d-spacing ranging from $0.35 - 10$ Å, i.e. a momentum transfer Q domain of $0.63 - 17.9\ \mathrm{Å^{-1}}$ can be studied in the high resolution backscattering configuration at scattering angles ranging from $155 - 178°$. The symmetric forward scattering range of $2 - 25°$ will make Q values of $0.01 - 3.9\ \mathrm{Å^{-1}}$ accessible.

With a flight-path of $54\ \mathrm{m}$ between the chopper and the sample, the highest resolution will be achieved using a $36000\ \mathrm{RPM}$ curved Fermi chopper for a pulse length of $6\ \mu\mathrm{s}$ full-width half-maximum (FWHM). The resolution will be adjustable to the needs of the experiment by extending the pulse length to up to $4000\ \mu\mathrm{s}$ with the help of alternate choppers (lower resolution straight Fermi chopper and a disc chopper pair with variable slit width). The highest resolution in backscattering geometry will achieve $\delta d \sim 3.5 \cdot 10^{-4}$ Å, i.e. $\delta d/d \sim 2 \cdot 10^{-4}$ for common d-spacing in the 2 Å range. The wavelength range to be explored will be defined by the phases and angular velocities of the choppers and can be scanned continuously (for example, see Fig. 2).

The instrument has completely been simulated with the Monte Carlo software package VITESS, developed at HMI for the simulation of neutron scattering experiments [1]. First results show a good agreement with tabulated experimental data for an Al powder sample (see Fig. 3) and confirm the theoretically calculated best total resolution achievable at this instrument in backscattering direction.

[1] VITESS website:
http://www.hmi.de/projects/ess/vitess/

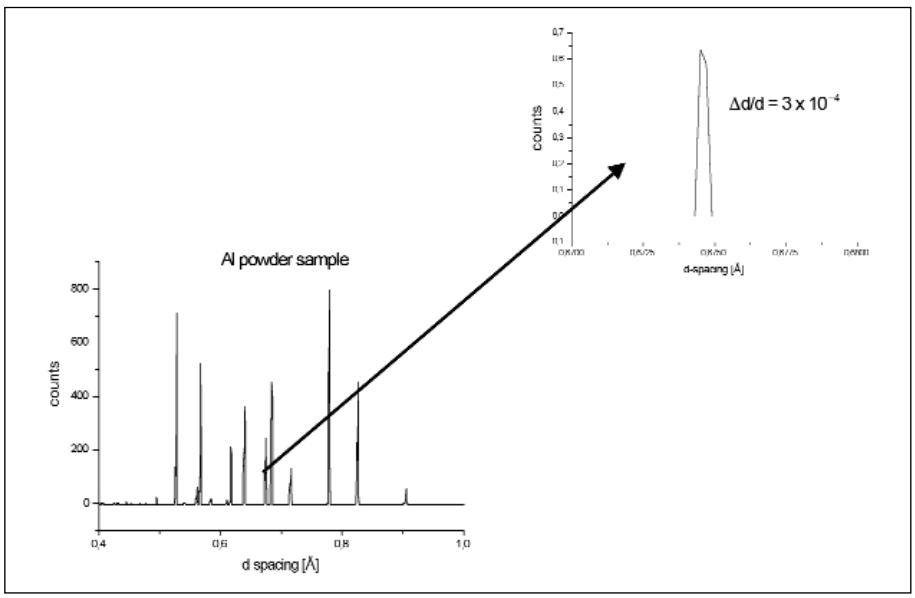

Fig. 3: Powder pattern MC simulation results (VITESS – at the lhs) for $0.7\ \text{Å} < \lambda < 1.8\ \text{Å}$ and $156\ ° < 2\theta < 179\ °$ as a function of the d-spacing (the distance between parallel planes in the crystal structure). At $2\theta \approx 176\ °$ and $\lambda = 1.34$ Å (rhs), nearly the highest total resolution of $\delta d/d \sim 3 \cdot 10^{-4}$ is obtained.

Relaxation in a glassy magnet

C. Pappas[1], F. Mezei[1], G. Ehlers[2], P. Manuel[3], A. Hillier[3], R. Cywinski[4] and I.A. Campbell[5]
■ 1 HMI, SF1 ■ 2 ILL, Grenoble, France and SNS, Oak Ridge, Tennessee, USA ■ 3 ISIS, Rutherford Appleton Laboratory, Chilton, Didcot, UK ■ 4 Physics & Astronomy Department, University of Leeds, Leeds, UK
■ 5 Laboratoire des Verres, University Montpellier II, Montpellier, France

The glass transition, characterised by a dramatic slowing down of the dynamics without any noticeable change in the spatial order, is a generic phenomenon, seen in systems as different as disordered magnets, polymers and biological substances. In spite of its universality, it is still controversial whether this is a real phase or a gradual freezing. The difficulty is due to the absence of an observable static order parameter in the low temperature phase. In fact the "snapshot" structure factor $S(Q) = S(Q, t=0)$, which reflects the short and medium range static correlations, shows no essential change when passing from the high temperature liquid or paramagnetic to the low temperature frozen glassy phase. In this situation the observation of dynamic scaling relations, which are the direct consequence of the homogeneity hypothesis in the vicinity of a critical instability can reveal the crucial signature of a true phase transition.

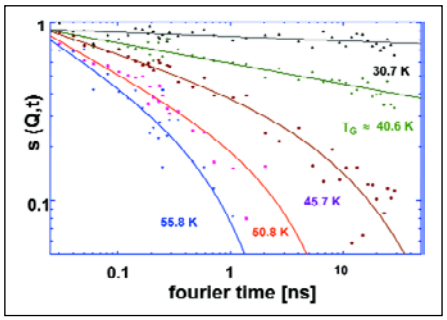

Fig. 1: Temperature dependence of the normalised intermediate scattering function $s(Q,t)$ of $Au_{0.86}Fe_{0.14}$. at $Q = 0.4$ nm^{-1} with the Neutron Spin Echo spectrometer IN15 (ILL) for $T = 30.7$ K (black), 40.6 K (~T_G, green), 45.7 K (brown), 50.8 K (red) and 55.8 K (blue) respectively. The continuous lines are the best fits to the data of a simple power law decay below T_G and of the Ogielski function $t^{-x}\exp(-(t/\tau(T))^{\beta})$ above T_G.

Spin glasses are the simplest realisation of glassy systems from the experimental as well as from the theoretical point of view and show the characteristic non-exponential relaxation from well above the freezing temperature T_G down to the low temperature phase, where the relaxation stretches from the typical microscopic times, some 10^{-13} s, to the age of the universe. Neutron Spin Echo (NSE) spectroscopy covers times ranging from 10^{-12} to some 10^{-8} s, i.e. from characteristic microscopic times up to times, which already belong to the "long" time relaxation domain and for this reason it is the method of choice for styding glassy dynamics. NSE measures the intermediate scattering function $s(Q,t) = S(Q,t)/S(Q,t=0)$, which in spin glasses is Q-independent and delivers a direct determination of the spin autocorrelation function $q(t)$.

Figure 1 shows in a log-log scale the NSE spectra of the classical metallic Heisenberg spin glass $Au_{0.86}Fe_{0.14}$ at $Q = 0.4$ nm^{-1} as measured at the IN15 spectrometer of the ILL with a wavelength of 0.8 nm. The spectra extend over a dynamic range of three orders of magnitude and by combining these data with spectra obtained at a wavelength of 0.45 nm at the BENSC spectrometer SPAN the time domain of the observation is extended up to almost 4 decades (Fig.2). $s(Q,t)$ is strongly non-exponential and the large dynamic range allows one for the first time to distinguish between the different forms, which have been suggested to describe the relaxation [1].

From quite general scaling arguments relaxation above a continuous phase transition must be of the form $t^{-x}\, f(t/\tau(T))$, where $\tau(T)$ diverges as $(T-T_G)^{-z}$, so that at the transition it reduces to a simple power law with an exponent x related to the standard critical exponents through $x=(d-2+\eta)/2z$, with η the Fisher exponent, d the space dimensionality and z the dynamical exponent. As seen in Figs. 1 and 2, $s(Q,t)$ follows a simple power law decay at T_G (~40.6), $s(Q,t) \propto t^{-x}$, with $x = 0.116\pm0.007$, which is in excellent agreement with $x = 0.116\pm0.026$ the value calculated from the well established exponents of Heisenberg spin glasses, known from macroscopic susceptibility measurements [2]. This is the first time that it was possible to verify critical scaling in a glassy system by relating quantities of very different nature and measured by different methods on very different time scales, namely the microscopic time dependence of the autocorrelation function at times between the microscopic time and 10^{-7} s on the one side and the macroscopic a.c. susceptibility at time scales greater than 10^{-3} s together with the static non-linear susceptibility on the other.

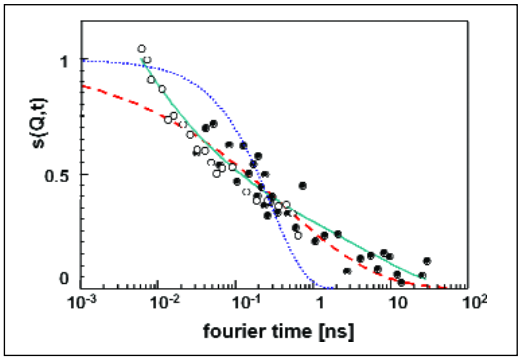

Fig. 2: NSE spectra of $Au_{0.86}Fe_{0.14}$ collected at the ILL spectrometer IN15 (full symbols) and at the BENSC spectrometer SPAN (open symbols) at 45.6 K. The continuous green line represents the fit of an Ogielski function $t^{-x}\exp(-(t/\tau(T))^{\beta})$. The red dashed and blue dotted curves correspond to a stretched exponential and a simple exponential decay respectively.

Above T_G neither a pure exponential nor a stretched exponential decay describe the relaxation. In fact, the spectra are impressively similar to the $q(t)$ found in large scale Ising spin glass simulations by A. Ogielski [3], which revealed the existence of a phase transition in three-dimensional Ising spin glasses. There is a clear power law decay at short times with a cut-off at longer times, which is not exponential. Ogielski chose to represent $f(y)$ by the stretched exponential or KWW function, familiar in fragile glass dynamics, and obtained excellent fits with $q(t)\propto t^{-x}\exp(-(t/\tau(T))^{\beta})$ and β tending to 1/3 at T_G, as expected from general arguments in glassy systems [4]. The power law part of this so-called Ogielski function describes the main part of the relaxation above T_G and the NSE spectra lead to an accurate determination of the exponent x. On the other hand, the stretched exponential only describes the tail of the relaxation and the parameters $\tau(T)$ and b are obtained to low accuracy.

A full description of the relaxation was made possible by complementing the NSE results with zero field Muon Spin Relaxation (μSR) measurements done on the very same sample. All μSR spectra strongly deviated from a simple exponential form and the non-exponential relaxation stretches over an unusually broad temperature domain up to almost room temperature, i.e. ~ 6 T_G. The fit to the stretched exponential form leads to the temperature dependence of the exponent β, seen in Fig. 3. Close to T_G β tends to 1/3 but becomes even smaller than 1/3 in the very vicinity of T_G, which clearly indicates the more complex relaxation than a simple stretched exponential form found with NSE.

The μSR spectra inform on the long time tail of the Ogielski function, which describes the spin autocorrelation function above T_G. When fitting the "log time" part of the NSE spectra to a simple stretched exponential the values of β are in excellent agreement with those found by μSR (Fig. 3). Muon depolarisation is due to the interaction with the Fe local magnetic moments. NSE on the other side measures the spin autocorrelation function and the collective dynamics of Fe spins. The agreement between μSR and NSE shown in Fig. 3 should therefore not be taken for granted. It is the direct consequence and at the same time an additional proof of the intrinsically homogenous nature of the non-exponential relaxation in spin glasses.

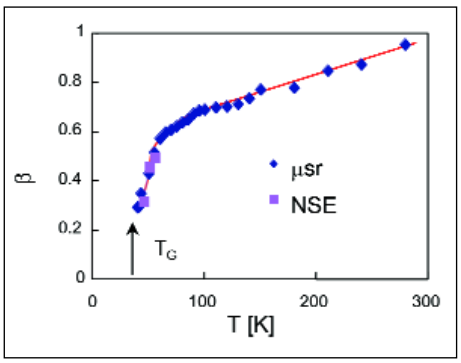

Fig. 3: Temperature dependence of the exponent β deduced by fitting the stretched exponential function $\exp(-(t/\tau(T))^{\beta})$ to the muon depolarisation spectra. The squares were obtained by fitting the tails of the Neutron Spin Echo spectra to the stretched exponential function.

For intensity reasons, NSE measurements were only possible close to T_G and below. The μSr spectra on the other side were recorded up to room temperature. They reveal the existence of two distinct regimes with a clear crossover around 60 K, which can be seen as the crossover between the low temperature critical spin glass relaxation and the high temperature Arrhenius-like relaxation. β increases very slowly above ~60 K and only around room temperature the relaxation becomes exponential with β~1. This anomalous paramagnetic relaxation can arguably be identified with the Griffiths phase, which should extend up to the Curie temperature of the non-diluted reference ferromagnetic phase. The very high Curie temperature of pure Fe, 1140 K, would therefore explain the extremely large temperature domain of non-exponential relaxation in this disordered system.

[1] C. Pappas, F. Mezei, G. Ehlers, P. Manuel, I.A. Campbell, Phys. Rev. B **8**, 054431 (2003)
[2] L. P. Lévy, Phys. Rev. B **38** (1988) 4963
[3] A.T. Ogielski, Phys. Rev. B **32** (1985) 7384
[4] L.W. Bernardi, S. Prakash and I.A. Campbell, Phys. Rev. Lett. **77** (1996) 2798

Pre-equilibrium emission in 1.2 GeV proton-induced spallation reactions

C.-M. Herbach, D. Hilscher, U. Jahnke
■ (HMI, SF1) for the NESSI-collaboration: HMI, FZJ, GANIL, Univ. of Warsaw, Univ. of Rochester

Spallation reactions[1] induced by medium-energy proton beams have a wide field of interest in science as well as in practical application: in cosmology and astrophysics, cosmic ray physics, planetary and geochemical science, and – last but not least – in nuclear physics on the one hand, and for generation of neutrons in spallation neutron sources on the other hand. Spallation neutron sources, such as the future European Spallation Source ESS, in turn, are needed as a favorable alternative to conventional nuclear reactors in basic research, for the transmutation of nuclear waste or possibly to replace conventional nuclear power stations by accelerator-driven hybrid systems.

Fig. 1: The NESSI detector at the COSY accelerator.

During recent years the NESSI collaboration (HMI, FZJ, GANIL, Univ. Warsaw and Univ. Rochester) investigated systematically GeV-proton induced spallation reactions [1–7]. The motivation for this program is twofold. First, the above mentioned applications call for an experimental validation of the underlying basic spallation reaction models in order to ensure that the present models and codes have reached an adequate precision which would allow one to perform reliable simulation calculations. For instance, structural materials of the target station of a spallation neutron source, which are exposed to GeV proton beams, must withstand the intensive generation and retention of large levels of hydrogen and helium, the amount of which has to be calculated reliably in such a complex environment. Second, the interest of nuclear physics stems from the fact that proton as well as antiproton induced reactions generate nuclei with high thermal excitation energy with a minimum of compression, deformation, and spin – quite in contrast to heavy ion induced reactions which excite the latter collective degrees of freedom rather strongly. These properties enable one to study the decay of highly and *thermally* excited nuclei, in particular fission at high excitation energies.

Spallation reactions can be considered as three-step reaction mechanisms. The first step is treated by an intra nuclear cascade (INC) [8] which excites the nucleus to high excitation energies depending on the impact parameter. During a second intermediate step, particles are emitted prior to the attainment of a statistical equilibrium and in the third step the equilibrated nucleus de-excites by light-particle evaporation. While the first and the last step are well understood and described in various models the second step, the intermediate pre-equilibrium emission of composite particles, is presently not well understood and theoretically discussed in terms of very different assumptions. Furthermore, the pre-equilibrium emission of fast composite particles in spallation reactions has so far not been studied systematically and very few experimental results are available. The neglect of this reaction phase in simulation calculations, however, turned out to be a too crude simplification. In the reaction p(2.5 GeV)+Au, for example, more than 50 % of the deuterons are emitted from pre-equilibrium [5] and the total energy carried off by fast composite particles amounts to about 95 MeV.

Here we give a brief overview about preliminary results which have recently been obtained with the NESSI detector (Fig. 1) at the COSY accelerator in FZ Jülich for the reaction of 1.2 GeV protons with target nuclei of Al, Ti, Fe, Ni, Cu, Zr, Ag, Ho, Ta, W, Au, Pb, and Th. The data have been measured with six triple-ΔE-E telescopes [6] consisting of three silicon detectors (25 μm, 80 μm and 1000 μm) backed by a 7 cm long CsI crystal which were positioned at angles of 30°, 75°, 105°, and 150°.

[1] In 1947 Glenn T. Seaborg coined the term spallation for reactions in which a heavy nucleus is hit by a highly energetic light projectile, e.g. a proton, which leads to the ejection of a large number of light particles (neutrons, protons, alpha particles) or heavier fragments.

Energy spectra of ^{1,2,3}H and ^{3,4}He observed in the reaction p(1.2GeV)+Zr are compared in Fig. 2 with results of simulations with the code INCL2.0 [8] for the Intra-Nuclear Cascade and the code GEMINI [9] for the subsequent statistical evaporation. The calculated yields of evaporated particles have been scaled to fit to the experimental data. They are used to separate the contributions from pre-equilibrium emission in the measured spectra and to correct the data for losses due to the lower energy detection threshold. The angular dependence of the spectra reveals that the pre-equilibrium emission occurs predominantly into the forward hemisphere while the evaporation is almost isotropic.

The experimental results for the integrated cross sections of evaporated particles are summarized in the upper panel of Fig. 3. The data are well reproduced by the predictions of the simulation calculation with INCL2.0+GEMINI.

The relative contribution of the pre-equilibrium emission σ_{pre} to the total production $\sigma_{eva}+\sigma_{pre}$ of composite particles is shown in the lower panel of Fig. 3. The data indicate that the contributions of pre-equilibrium emission are slightly enhanced for heavier targets. The smallest portion of $\sigma_{pre}/(\sigma_{eva}+\sigma_{pre})$ is found for ^{4}He with 10–15 %, while the other contributions are as high as 40–60 % for ^{2}H and ^{3}He and 25–40 % for ^{3}H. These observations together with our previous results [5] for p(2.5 GeV)+Au definitely call for a consideration of fast composite-particle emission in present reaction models. A refined evaluation of the data will be devoted to the evolution of pre-equilibrium emission with excitation energy.

[1] L. Pienkowski et al., Phys. Rev. C **56**, 1909 (1997).
[2] D. Hilscher et al., Nucl. Instr. Meth. A **414**, 100 (1998).
[3] M. Enke et al., Nucl. Phys. A **657**, 317 (1999).
[4] A. Letourneau et al., Nucl. Instr. Meth. B **170**, 299 (2000).
[5] A. Letourneau et al., Nucl. Phys. A **712**, 113 (2002).
[6] C.-M. Herbach et al., Nucl. Instr. Meth A **508**, 315 (2003).
[7] D. Hilscher et al., J. Nucl. Mater. **296**, 83 (2001).
[8] J. Cugnon et al., Nucl. Phys. A **620**, 475 (1997).
[9] R.J. Charity et al., Nucl. Phys. A **483**, 391 (1988).

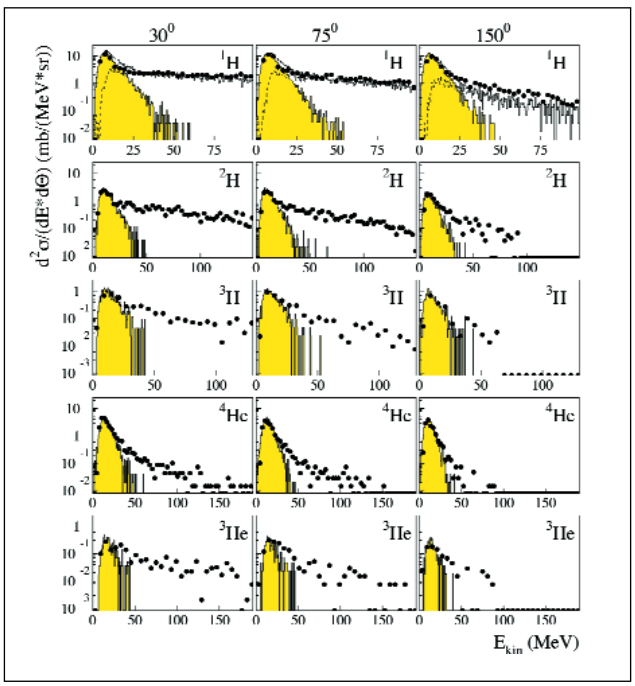

Fig. 2: Kinetic energy spectra of ^{1,2,3}H and ^{3,4}He as measured for p(1.2 GeV)+Zr at 30°, 75°, and 150° (dots). Results from simulations (INCL2.0+GEMINI) are plotted as gray area for evaporated particles and as open area (dashed line) for INC protons.

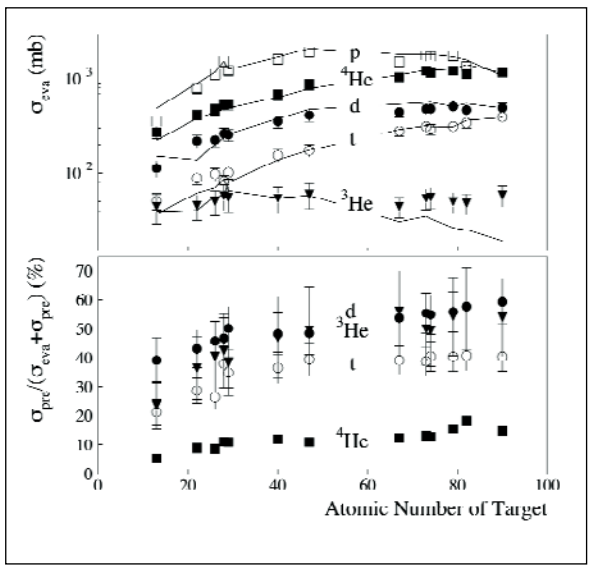

Fig. 3: Integrated production cross sections of ^{1,2,3}H and ^{3,4}He in reactions with 1.2 GeV protons, plotted as a function of the atomic number of the target nucleus. The upper panel shows the measured cross sections (symbols) for evaporated particles in comparison with results from INCL2.0+GEMINI simulations (lines); the cross sections for pre-equilibrium emission of composite particles (lower panel) are given relative to the total yield.

Surface and interface magnetization of ultrathin films

H. Maletta
■ HMI, SF2

Today's magnetic materials are not the bulk materials of old, but atomically engineered structures of nanometer dimensions with ferromagnetic, antiferromagnetic and non-magnetic components. This development is clearly fueled by the already successful applications in modern information technology and the further need for even smaller magnetic devices. At the same time, confinements on the nanoscale can give rise to new and fascinating phenomena in magnetism which are challenging to be understood from fundamental physical aspects, too. The study of such advanced materials requires new experimental techniques that are capable of probing them on the nanometer length scale. Our group at HMI has studied various properties of such materials by applying both the neutron beams at BENSC and the synchrotron x-rays at the new HMI-undulator beamline at BESSY.

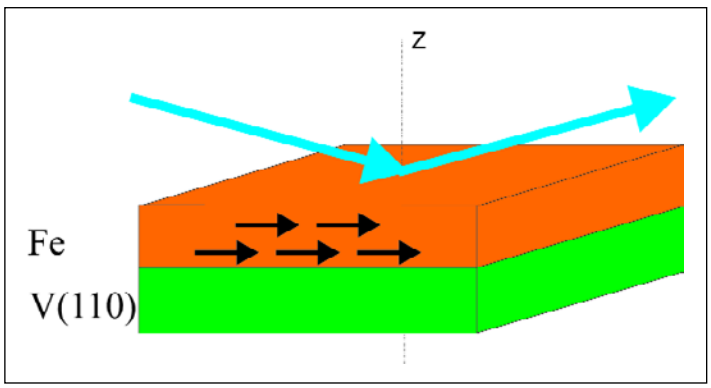

Fig. 1: Schematic view of the reflection measuring geometry with an ultrathin iron (Fe) film grown on a vanadium (V) crystal. Blue arrows: incoming and reflected beams. Black arrows: Orientation of the magnetic moments in the Fe layer.

Reflectometry with polarized neutrons

Reflectometry with polarized neutrons (PNR) is a well established technique for the study of thin film magnetism. One measures the reflectivity – the ratio of reflected neutron intensity to the total incoming intensity – as function of the incident angle at very small angles (grazing incidence). Due to the geometry (Fig. 1), one is primarily sensitive to the density or magnetization depth profile perpendicular to the film surface (in z direction). We have successfully developed a unique option [1] where one can measure the properties of even uncapped thin films by *in-situ* PNR, i.e. the preparation, structural characterization and PNR measurement are performed in the same UHV chamber. As a first example we determined the absolute value of the magnetization of thin epitaxial iron (Fe) films with a free surface grown on a vanadium V(110) single crystal as function of the thickness of Fe. In addition, we found that the magnetization is changed in value when the sample is capped with a V layer.

X-ray resonant magnetic reflectometry

In a second step, we studied the same samples with synchrotron x-rays [2] on the new HMI undulator beamline at BESSY. It provides highly intense x-rays which are variable in polarization (linear and circular) and tunable in energy from 200 eV to 1800 eV. Whereas PNR is well suited to measure the absolute value of the total magnetization, the study with polarized soft x-rays enables one to separate the element-specific components via the magnetic circular dichroism effect (XMCD). Indeed, we detected a small induced V magnetization being antiparallel to Fe. Our XMCD absorption measurements are consistent with details of the Fe magnetization indicated in Fig. 2. In order to confirm the magnetic details at the free surface and interface we are just preparing the next experiments where we will perform the X-ray resonant magnetic reflectometry (XRMR) method.

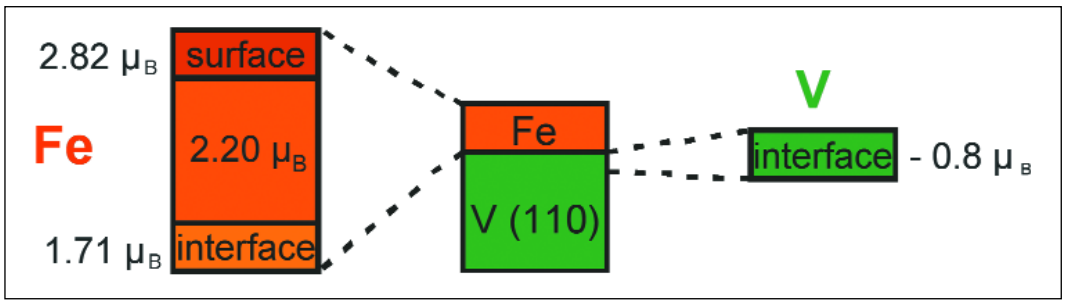

Fig. 2: Details of the magnetization of Fe/V(110) (schematic view).

The XRMR method is a new tool which has been developed by us in collaboration with the MPI Stuttgart [3] on the basis of our knowledge on PNR. It utilizes the effect that the magnetic cross section of x-rays is resonantly enhanced by orders of magnitude near an absorption edge. Recently, the first experiments were successfully performed on a sandwich sample Pt/Co/Cu, i.e. on a 2 nm thin cobalt (Co) film grown on a copper (Cu) substrate and capped with a platinum (Pt) layer. The quantitative results summarized in Fig. 3 indicate that the magnetic moment of Co is enhanced by up to 30 % near the interface to the Pt layer, but reduced by 25 % near the Cu substrate. The element specific technique enabled us also to tune the x-ray energy to the value of the Pt absorption edge revealing a small induced magnetization in the Pt cap layer which decays exponentially within a 1 nm depth. Hence, it is demonstrated that high sensitivity for small magnetic moments can be achieved by applying XRMR.

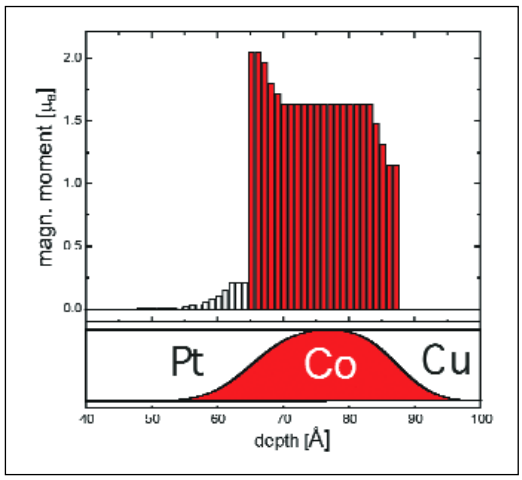

Fig. 3: Magnetization depth profile of Pt/Co/Cu (schematic view) obtained by XRMR at the Co and Pt site. The analysis includes the interface roughness as indicated below.

Outlook

These methods are considered as new tools for systematic investigations of details of magnetization properties at buried interfaces and free surfaces as a function of roughness or ligand layer composition of various magnetic layered systems. Work is underway in a collaboration in order to interpret the results quantitatively by calculations of the effects of reduced coordination numbers and hybridizations on the magnetic moment value. Nowadays, such systems work as basic components of devices in information technology for instance for magnetic sensors and magnetic random access memories (MRAMs) due to the giant magnetoresistance (GMR) effect, and may be relevant in future *spin-tronic* devices.

[1] T. Nawrath, H. Fritzsche, F. Klose, H. Maletta, Phys. Rev. B **60**, 9525 (1999).
[2] D. Schmitz, J. Hauschild, P. Imperia, Y.T. Liu, H. Maletta, J. Magn. Magn. Mater. **269**, 89 (2004); and to be published.
[3] J. Geissler, E. Goering, M. Justen, F. Weigand, G. Schütz, J. Langer, D. Schmitz, H. Maletta, Phys. Rev. B **65**, 020405 (R) (2002); and submitted for publication.

Field distorted magnetic spirals: a neutron diffraction study of the magnetism in the frustrated quantum antiferromagnet $CsCuCl_3$

N. Stüßer[1], U. Schotte[1], A. Hoser[2]
■ 1 HMI, SF2 ■ 2 Institut für Kristallographie, RWTH Aachen

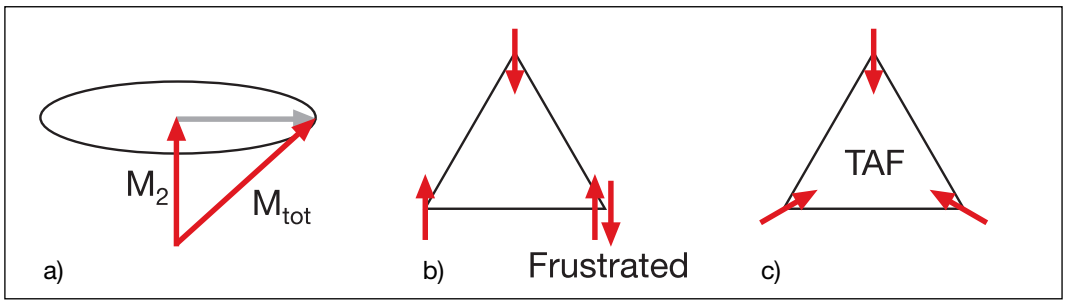

Fig. 1: a) In quantum mechanics only one component of the magnetic moment M_{tot} is defined e.g. M_z. The perpendicular components are uncertain and can be considered to fluctuate on the ellipse. These fluctuations are basically a result of Heisenberg's uncertainty relation.
b) Geometrical frustration: Three spins located at the corners of a regular triangle cannot simultaneously order antiparallel to each other.
c) If moments are free to rotate in a plane antiferromagnetic coupling between neighbours leads to the formation of a triangular antiferromagnet (TAF). All spins are inclined by 120° to their neighbours.

Since the foundation of quantum mechanics the study of quantum effects has been a subject of continuous interest in fundamental solid state physics. In particular magnetic systems have served as models to test theories in this field. For magnetic systems quantum fluctuations can play an important role in the formation of magnetic structures. Differing from the classical description, in quantum physics a magnetic moment can never be completely aligned. Only a part of the total moment can be aligned along one direction and the perpendicular components are uncertain. One can consider this situation as a moment fluctuating around some mean value determining the size of the ordered moment (Fig. 1a). Quantum theory tells us that these fluctuations are relatively enhanced for small moments which are found e.g. at Cu^{2+}-ions. Another topic of current interest is the investigation of systems with geometrical frustration [1]. In geometrically frustrated systems, two body interactions like couplings of magnetic spins can not all be realized due to some special geometry of the underlying lattice of the spins (Fig. 1b,c). This is realized in $CsCuCl_3$ which will be presented now showing our most recent results on the study of quantum effects on a system with geometrical frustration.

Since a few years, we have been investigating the magnetic structure of $CsCuCl_3$ crystals as a function of temperature and magnetic field [2]. Different magnetic phases could be identified and could be related to the influence of quantum

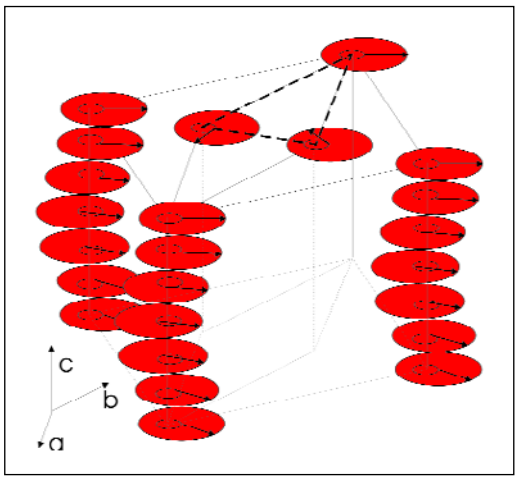

Fig. 2: Magnetic structure of $CsCuCl_3$ below 10.6 K. A long wavelength spiral is formed in c direction. A triangular 120° structure is present in the ab plane.

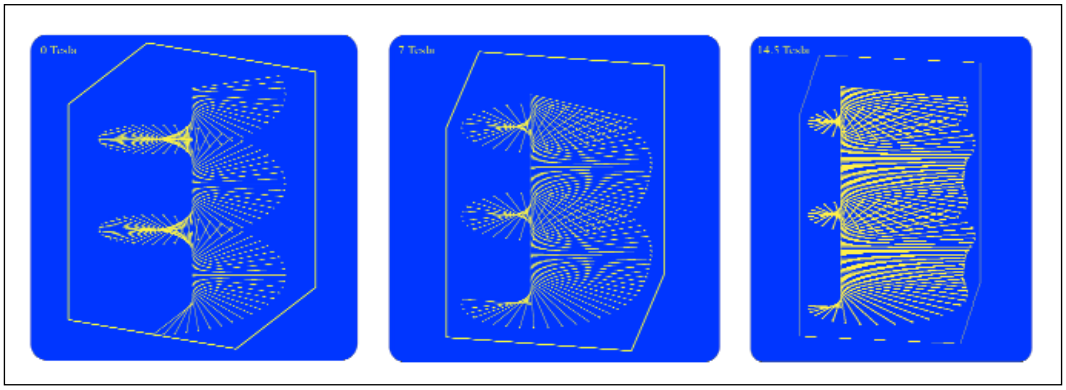

Fig. 3: Magnetic spiral of $CsCuCl_3$ at 0 T, 7 T, and 14.5 T

fluctuations. Let us first briefly introduce the magnetic structure of $CsCuCl_3$ at zero field (Fig. 2). Below 10.6 K the spins at the Cu^{2+}-ions are magnetically ordered: a triangular spin arrangement with 120°-type structure is formed in the *ab* plane and an incommensurate spiral occurs along the *c* axis with a repetition length of about 71 layers. Fig. 2 shows only a small section of the structure which should be repeated in the *ab* plane and extended along *c*. The spiral is a result of a competition between a dominating ferromagnetic coupling of adjacent spins along *c* which tries to keep spins parallel, and a so called antisymmetric coupling which tries to keep spins perpendicular. The compromise is an incommensurate winding of the spins with a pitch angle of about 5° between neighbours. The 120° structure in the *ab* plane is caused by geometrical frustration. The antiferromagnetic coupling which favours an antiparallel spin alignment of neighbours cannot be satisfied simultaneously for three spins on a triangle. This situation is called frustration. If the spins are free to rotate in the *ab* plane – as is the case for $CsCuCl_3$ – the 120° structure will correspond to the minimum in energy. It is found experimentally that the ordered spins have a reduced moment in agreement with theoretical calculations [3, 4]. The spin reduction is a direct consequence of quantum fluctuations together with the geometrical frustration. We were interested to see how the application of a magnetic field changes the magnetic structure for such a frustrated system in order to test recent theoretical predictions. Therefore, diffraction experiments were performed at a neutron spectrometer located at our BER II reactor of the Hahn-Meitner Institute. A beam of neutrons with a well defined energy was diffracted at a single crystal of $CsCuCl_3$. The crystal was mounted in one of our high field magnets which allows the application of field strengths up to 14.5 T. In order to study the quantum effects which become significant close to zero temperature, the experiments were carried out at 2 K and the diffracted neutrons were measured as a function of scattering angle. We analysed the diffraction patterns and yielded a detailed picture of the magnetic structure which cannot be obtained by any other experimental technique.

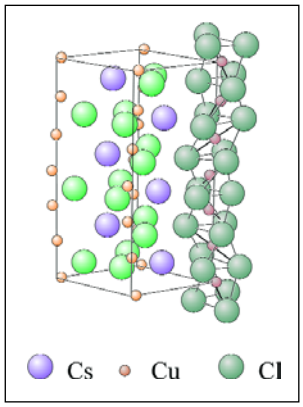

Fig. 4: $CsCuCl_3$ crystal structure

The pictures of the spirals distorted by an applied field for different field strengths are shown in Fig. 3. Our analysis clearly revealed that the field distorted-spirals can be described as a rotation of spins towards the field direction and the spin reduction is lifted for those spins pointing towards the field direction. Spins in opposite direction spread apart and the spin reduction has even increased for spins pointing opposite to the applied field. This behaviour can be found in principle in the whole phase diagram since thermal fluctuations have a similar effect as quantum fluctuations.

[1] A. P. Ramirez, *Handbook of Magnetic Materials,* 13 (2001).
[2] N. Stüßer, U. Schotte, A. Hoser, M. Meschke, M. Meißner, J. Wosnitza, J. Phys. Condensed Matter **14**, 5161 (2002) and references therein.
[3] K. Adachi, N. Achiwa, M. Mekata, J. Phys. Soc. Japan **49**, 545 (1980).
[4] N. Elstner, R. R. P. Singh, A. P. Young, Phys. Rev. Lett. **71**, 1629 (1993).

Neutron tomography at HMI

N. Kardjilov[1], A. Hilger[1], I. Manke[1], M. Strobl[2], W. Treimer[2]
■ 1 HMI, SF3 ■ 2 Technische Fachhochschule Berlin (TFH)

Introduction

Neutron tomography is a powerful non-destructive method for the investigation of a large variety of different objects. It allows one to visualize the inner volume of a sample without destroying or dismantling it. The tomography principle is based on the mathematical reconstruction of the 3-dimensional volume from 2-dimensional projections collected while the sample is rotated around a defined axis.

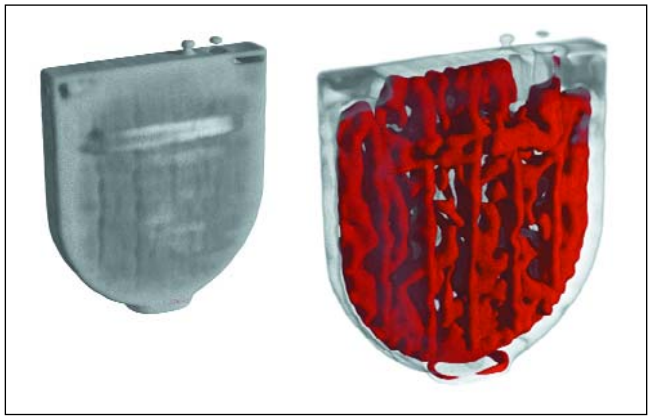

Fig. 1a: 3D-tomography image of a Lithium Iodide battery. Lithium distribution (**left**) and general view (**right**)

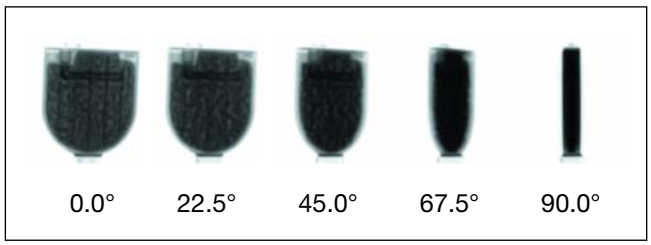

Fig. 1b: Some of the 200 single neutron-radiography projections used for the 3D-tomography reconstruction shown in Fig. 1a.

For the collection of the projection set, various kinds of transmission radiation can be used (for instance X-rays, positrons, neutrons etc). The various rays used in these experiments differ in their interaction mechanism with matter. As electrically neutral particles, neutrons interact directly with the atomic core. This is not the case for X-rays, which interact mainly with the electronic shell of the atom. The different interaction mechanisms of neutrons and X-rays with matter make neutron tomography a complementary technique to the classical X-ray tomography.

In contrast to tomography with X-rays, tomography imaging with cold neutrons is – on the one hand – highly sensitive to light elements and organic materials. On the other hand, cold neutrons pass easily through metals and other materials composed of heavy elements.

Neutron radiography setups are usually placed at multipurpose, high-flux neutron sources as nuclear research reactors or spallation sources. Therefore, the design and construction of a new neutron radiography facility is a large-scale, long-term project including the optimization of a great number of parameters concerning the beam geometry, the shielding design, the electronic control systems and many others.

A new tomography facility with cold neutrons is under construction at the reactor BER II of the Hahn-Meitner Institute, Berlin. The new beam line is placed at the end of a curved neutron guide which faces the cold neutron source of the reactor. The presence of a neutron guide helps achieve an extremely high cold neutron flux in the order of approx. 10^9 n/cm^{2}s at the sample position (30×50 cm^2) with a negligible background of gamma radiation and fast neutrons. These conditions are very suitable for investigations of strongly absorbing samples or real-time imaging of fast processes. The first test experiments at this measuring position have been already performed. Some of them are presented below.

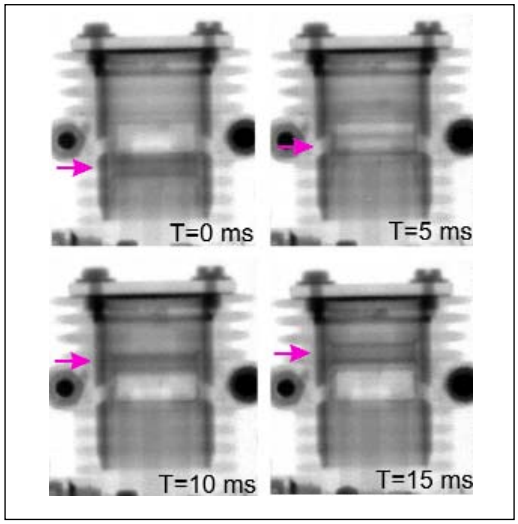

Fig. 2: Four neutron-radiography snapshots of a combustion engine at different piston positions. The arrows show the position of the piston. The experiment was performed at a rotation speed of 1110 rpm. The exposure time was 1 ms. For a defined piston position 200 images were recorded. The time delay between two piston positions was set to 1 ms.

Tomography investigation of a Lithium Iodide battery

Lithium (Li) has one of the highest attenuation coefficients for cold neutrons among the elements. So the task to investigate a Lithium Iodide (LiI) battery by means of neutron tomography was a challenge for the recently established tomography facility at HMI. Despite the difficulty that for some of the 2-dimensional projections the neutrons had to pass through almost 3 cm of LiI, it was possible to successfully reconstruct the 3-dimensional image (Fig. 1). The results of this investigation may help increase the life-time of LiI batteries used in pacemakers.

Real-time imaging

As a test sample for the real-time imaging experiment, a model aircraft combustion engine was investigated. The dimensions of the motor were ($W \times H \times T$) $70 \times 70 \times 30$ mm^3. For the first tests, the engine was driven by a coupled electromotor.

Data collection was based on the so-called stroboscopic method for investigations of repetition processes: a set of images was recorded exactly at the same position of the piston in the cylinder. After adding up all the images for the corresponding piston position, an average snap shot with better statistics was obtained. The whole combustion cycle was visualized by such “frozen” snap shots. Images at four piston positions are shown in Fig. 2. The next step in this work will be to investigate the fuel injection in a running motor driven by a combustion process.

Geological samples

In a further experiment, the density variation and the distribution of different minerals in a granite sample was investigated. This information gained helps make conclusions about the formation of granite. In this case, the presence of the mineral kaolinit (marked with orange in Fig. 3) in the sample is an evidence that the material underwent a hydrothermal alteration. This was probably due to a flow of hot water through it, which caused the transformation of the large feldspar crystals frequently presented in granite into kaolinit: $KAlSi_3O_8 + H_2O \rightarrow Al_2Si_2O_5(OH)_4$. This kind of experiments may help find a precise quantitative classification of different types of geological materials.

Future developments

In the near future a new experimental station for neutron tomography will be built at HMI. Here, a better collimation of the neutron beam will be achieved with the help of a system of apertures. In this way, the spatial resolution of the tomography experiment will be improved from the current value of 250 μm to 100 μm. Further improvements of the resolution will follow from the application of advanced neutron imaging techniques such as energy-selective and phase-contrast neutron imaging as well as imaging with polarized neutrons.

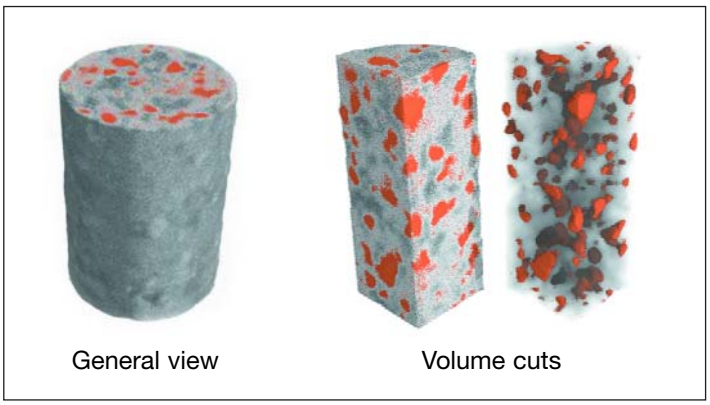

Fig. 3: The tomographic reconstruction of a granite cylinder shows the spatial distribution of the mineral kaolinit ($Al_2Si_2O_5(OH)_4$) in the sample (orange). The presence of four hydroxyl groups in the chemical composition leads to a strong contrast for Kaolinit crystals in the tomography reconstruction as neutrons are strongly scattered by hydrogen.

Characterisation of Precipitates in a Stainless Maraging Steel by Three-Dimensional Atom Probe and Transmission Electron Microscopy

N. Wanderka, S. Höring
■ HMI, SF3

The three-dimensional atom probe (3 DAP) is the best technique to investigate the early stages of precipitation with nano-sized deviations from the homogeneous composition. In the present case this technique was used for the study the influence of small differences in the composition on the precipitation behaviour of a maraging steels.

Maraging steels is the generic term used for low-carbon steels forming precipitates in the martensitic phase during tempering. The term is a combination of *martensite* and *ageing*. Owing to an excellent combination of high strength and hardness, ductility and toughness, combined with good corrosion resistance, stainless maraging steels are used in many technological sectors where weight saving is of great importance such as aerospace and automotive.

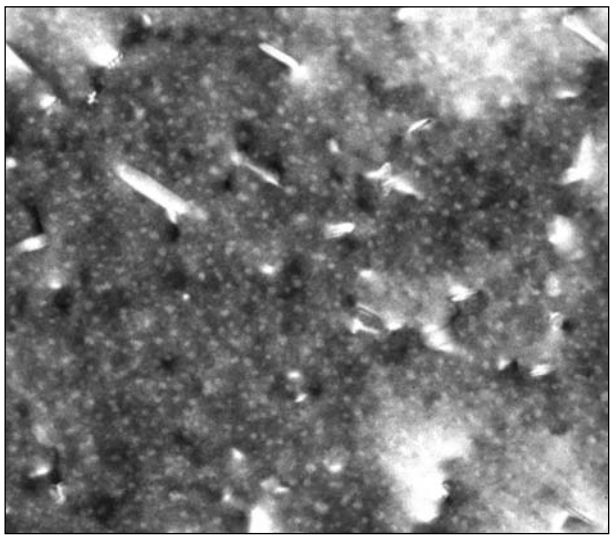

Fig. 1: TEM bright field image of the model alloy of maraging steel aged at temperature of 475°C for 100 h.

Technical steels are mixtures of very large numbers of alloying elements, some of them in very small quantities. In addition to that, maraging steels are characterized by low carbon content. Small variations in the composition of the alloying elements can change their precipitation behaviour drastically. Depending upon composition and heat treatment, a variety of different precipitates will be formed. In the present case, a model alloy for maraging steel with the composition 75.1Fe-13.1Cr-8.4Ni-1.1Si-0.96Ti-0.7Al-0.5Mo-0.1Mn-0.05C (at. %) was investigated. The 3 DAP analysis was combined with transmission electron microscopy (TEM) which is able to identify the crystallographic structure of precipitates and to give information about the number densities and volume fractions of different kinds of precipitates on a larger scale.

The investigations were concentrated on the chemical analysis of the phases after different heat treatments at 475°C. The alloy was aged at 475°C for 12 h and for 100 h. The longer time was necessary for the production of sufficiently large particles for the TEM investigations. The composition of the small precipitates (not shown here) is 44.7Fe-5.1Cr-26.1Ni-5.7Si-10.5Ti-1.7Al-0.6Mo (at. %). I.e. they are rich of Ni, Al, Ti and Si. The number density of the small precipitates is about $8.3 \cdot 10^{24}$ m^{-3} as estimated from the number within the volume analysed by 3DAP.

The typical microstructure of the alloy after 100 h aging time is shown in the TEM micrograph in Fig. 1. Besides small spherical precipitates embedded in the matrix, larger needle- or plate-like particles are visible. In Fig. 2 the three dimensional reconstruction of the positions of Ni, Al and Ti atoms is presented for the same state of the material. Several atom clusters can be identified. Some of them contain more than 20 at. % Cr. The composition of the Cr rich particles is 46,5Fe-40,9Cr-7,3Ni-0,9Si-0,8Ti-0,4Al-0,6Mo-2,6Mn-0,5C (at. %). In addition to these particles, regions enriched in Ni, Al and Ti are also visible. The composition of the small spherical Ni-rich particles is almost as in the material aged for 12 h. These particles do not grow much, i.e. from 2.5–3 nm to 4 nm during extended heat treatment (12 h to 100 h). The larger Ni rich particles (> 15 nm) in the middle and the upper left corner of the analysed volume have the composition: 23,4Fe-6,0Cr-49,3Ni-1,5Si-6,0Ti-10,6Al-2,7Mo-Mn (at.%).

In Fig. 3, the concentration depth profiles of Cr, Ni, Fe, Al and Ti in two precipitates and the matrix are presented. They were taken along the indicated small box (shown also in Fig. 2). This box was aligned approximately perpendicular to the interface between Ni- and Cr rich precipitates. The concentration values were calculated for slices 0.4 nm thick. In our case, the first formed crystalline precipitate is rich in Si, whereas in a further steel of similar composition the formation of Ni_3Ti precipitates has been found [1, 2].

The comparison of the present results with literature on the maraging steels IRK91 [3, 4] and on a steel free of Co [1, 2] shows that the precipitation behaviour of these 3 maraging steels differs significantly, though their composition shows only small variations.

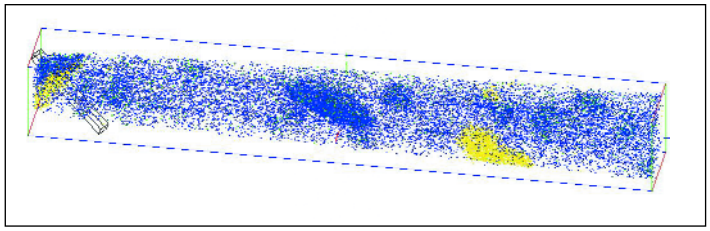

Fig. 2: Three dimensional reconstruction of Ni (blue), Ti (green), Al (dark green) atom positions in the analysed volume 11 × 11 × 92 nm³. Cr rich areas (yellow) with 20 at.% Cr concentration are displayed in the same volume.

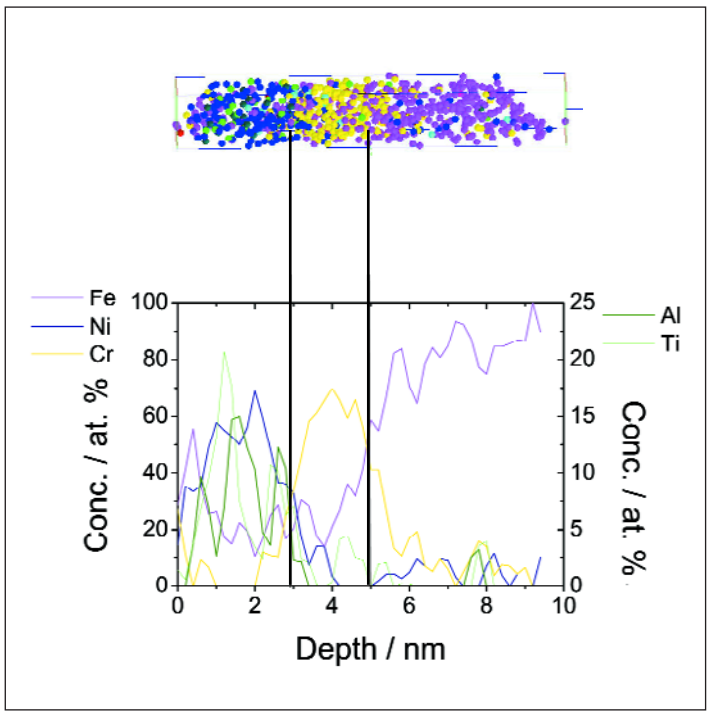

Fig. 3: Concentration depth profiles of Cr, Ni, Al, Ti and Fe through different precipitates and the matrix along the indicated small box shown in Fig. 2 (left end). This box is depicted above the diagram (colours are the same as in Fig. 2, however, Fe atoms (pink) are added).

[1] A. Gemperle, J. Gemperlova, W. Sha, and G.D.W. Smith, Mater. Sci. Techn. **8**, 546–554 (1992).
[2] W. Sha, A. Cerezo, G.D.W. Smith, Metall. Trans. A **24A**, 1241–1249 (1993).
[3] K. Stiller, M. Hättestrand, F. Danoix, Acta Mater. **46**, 6063 (1998).
[4] K. Stiller, F. Danoix, M. Hättestrand, Mater. Sci. Eng. A **250**, 22 (1998).

Pseudo-crystalline ordering of nanoparticles in ferrofluids induced by magnetic fields.

A.Wiedenmann, M. Kammel, A. Hoell
■ HMI, SF3

Ferrofluids are stable magnetic colloids in which nanometre sized magnetic particles are prevented from lumping together either by electrostatic repulsion or by coating with organic chain molecules acting as surfactants. Renewed interest in these materials is motivated by potential biomedical applications such as cancer therapy. Here small amounts of a ferrofluid are injected into the cancerous tissue. A cyclic variation of an external magnetic field then heats the fluid destroying cancer cells usually particularly sensitive to overheating.

Small angle scattering (SAS) is an analytical technique providing statistical information about structures in the nanometre range. It is therefore particularly suited for investigations of such liquids. While X-ray scattering (SAXS) probes mainly the particle core (due to its high electron density), neutron scattering (SANS) gives access to composition and density of the organic shell, the core and the magnetic particle moments. Spin-polarized neutrons (SANSPOL) provide an additional contrast for the magnetic core and allowed mesoscopic constituents of poly-disperse ferroluids to be identified quantitatively. In very diluted Co-Ferrofluids (The magnetic core consists of cobalt), we were able to evaluate precisely the average radius of the magnetic core of 3.7 nm and the composition of the shell of constant thickness 2.3 nm. Here we focus on the set-up of field induced correlations as a function of the particle concentration, the strength and the orientation of the applied magnetic field and the temperature.

In Fig. 1 the results of SANS-measurements performed on Co-Ferrofluids with non-polarised neutrons in a horizontal magnetic field of 1.1 T perpendicular to the incident beam are shown. The results are presented in the usual form of a SANS-pattern showing the intensity of the scattered beam in dependence of the scatte-

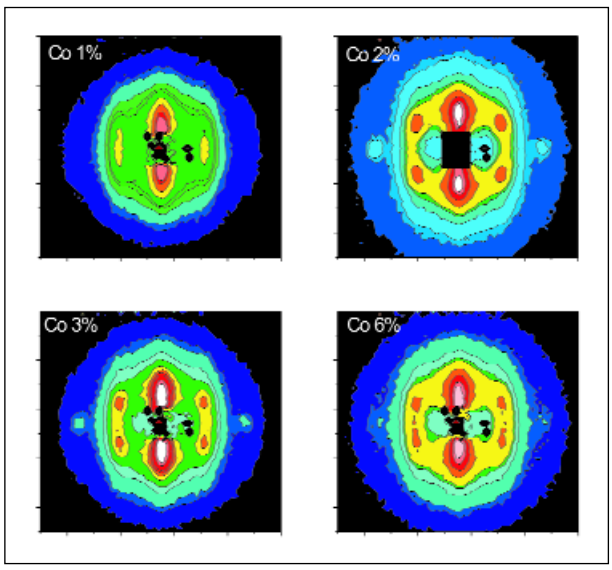

Fig. 1: 2D-SANS pattern of Co-Ferrofluids of different concentrations in a horizontal magnetic field H of 1 T applied perpendicular to incident neutrons: Above 1 vol. % Co well defined peaks (orange spots) represent the pseudo-crystalline hexagonal ordering of particles while below streaks perpendicular to H indicates chain like particle arrangements.

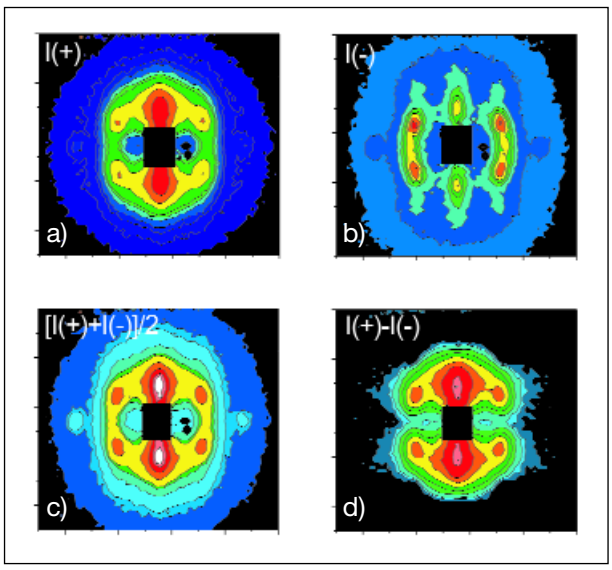

Fig. 2: 2D-SANSPOL (SANS with polarized neutrons) intensities for 2 vol % Co-Ferrofluids sample for both neutron polarization directions a), and b) the average corresponds to the pattern of non-polarized neutrons c) and the difference pattern represents the nuclear-magnetic cross-term for one and the same particle (d).

ring vector Q, i.e., essentially in dependence of the direction in which the particles are scattered. In this pattern, different intensities are represented by different colours ranging from blue for low intensities to orange and red for high intensities. In our measurement, we observed pronounced peaks (orange spots) for samples with more than 1 vol. % Co. These peaks – a sign of regular arrangement of the particles – disappeared in zero field.

In Fig. 2, SANS-intensities measured with polarized neutrons are shown. $I(-)$ and $I(+)$ are the results of experiments with the neutron spins parallel and antiparallel to the magnetic field H respectively, are shown in Fig. 2 as a typical example the for 2% Co-Ferrofluids. The average $[I(+)+I(-)]/2$ corresponds to the scattering pattern of non-polarised neutrons while the difference pattern $I(+)-I(-)$ of Fig. 2 reflects the nuclear-magnetic cross term resulting solely from one and the same particle. From Fig. 1 and Fig. 2 four peaks forming angles of ± 30° with the horizontal direction of the applied magnetic field are clearly distinguished. Two additional peaks in the horizontal direction result solely from nuclear contrast and disappear completely in the cross-term.

A SAXS study performed on the ID01 beamline at ESRF, Grenoble on the same samples in a horizontal magnetic field applied perpendicular to the incident beam fully confirmed the set-up of very narrow peaks with increasing field.

The peaks observed in the small angle scattering experiments correspond to a pseudo-crystalline ordering of the Cobalt particles in an external field. For samples above 1 vol.% Co, inter-particle interactions are induced by an applied magnetic field that gives rise to pseudo-crystalline ordering of Cobalt core-shell particles. The particles are arranged in hexagonal planes, with the magnetic moments parallel to the [110] direction. Two types of equivalent textures were found to be present simultaneously, corresponding to a stacking of the hexagonal planes in vertical (type I) or the horizontal direction (type II). The pseudo-crystalline particle arrangements are schematically shown in Fig. 3.

The in-plane nearest neighbour distance of a_{hex}=21.9 nm was found to be almost independent of concentration (and temperature) whereas the distance between neighbour planes strongly varies from sample to sample between c=70 nm and 25 nm. The ordering follows the direction of the applied field, i.e. the magnetic moments and the [110] directions are always aligned along the magnetic field. In addition, the Q^{-1} behaviour of the intensity observed at low scattering vectors in the direction perpendicular to the magnetic field indicates that some particle moments are arranged in the attractive head-to-tail conformation and aligned along the magnetic field presence of segments of uncorrelated chains.

The pseudo-crystalline lamellar hexagonal particle arrangement has never been observed experimentally before in magnetic colloids. This contradicts the theoretical predictions of de Gennes and Pincus that the competition between repulsive (hard-core) and attractive (vander-Waals) interaction with magnetic dipole-dipole interaction should give rise to a spontaneous arrangement of particles in chains or rings with magnetic moments parallel to each other. In an external magnetic field these chains are expected to be aligned along the field direction.

On the other hand, theoretical studies performed by Hess using molecular dynamics have predicted that above a critical value of the magnetic dipole moment a transition from the uniaxial to a lamellar, symmetry-breaking ordering should occur with almost close-packed in-plane structures. The results presented here confirm for the first time experimentally the transition from field induced chain-like to lamellar ordering.

The work is supported by the German Research Foundation (DFG project No WI-1151).

[1] A. Wiedenmann in Lecture Notes in Physics, ed. S. Odenbach (2002), 33-61.
[2] A. Wiedenmann, M. Kammel, A. Hoell, P. Boesecke; Phys Rev. E **68** 031203, 1–10 (2003).

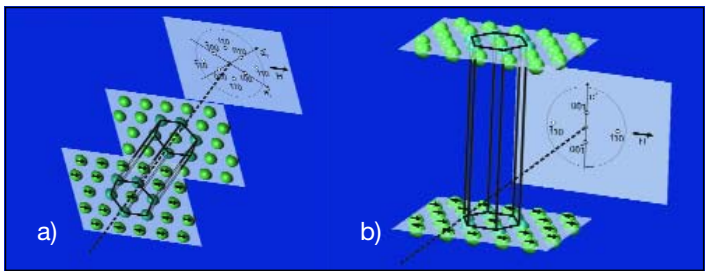

Fig. 3: Schematic representation of particle arrangements in hexagonal symmetry in textures of type I (a) and type II (b) and the corresponding reciprocal lattice points observed in the detector plane. The horizontal magnetic field is perpendicular to the incident beam.

Modification of the Ti Texture using swift heavy ions

I. Zizak[1], N. Darowski[1], G. Schumacher[1], S. Klaumünzer[1]; W. Assmann[2], J. Gerlach[3], I Großhans[4]
■ 1 HMI, SF4 ■ 2 Ludwig-Maximilian-Universität, Munich ■ 3 Leibniz Institute for Surface Modification, Leipzig ■ 4 University of Augsburg

Accelerated ions interact with solids through nuclear and electronic interaction. At very high energies, the nuclear energy loss (S_n) is much smaller than the electronic energy loss (S_e), and the interaction between the ions and the solid leads to excited electrons in the solid. A part of the electronic excitation energy is converted into atomic motion, e.g. via the electron-phonon coupling. This motion can lead to lasting changes in the structure of the irradiated solid.

Recently, a change in crystallite orientation of polycrystalline titanium (Ti) films was detected after the irradiation with 200 MeV gold (Au) ions [1]. In order to study the mechanisms of this texture modification, a new series of experiments was performed at HMI. In the present report, variations of the incoming beam's angle, the irradiation dose, and the grain size of the samples are reported.

The experiment

A bulk Ti sample with an average grain size of approximately 5 μm was compared to fine-grained Ti films deposited on the Si (001) wafer (grain size of the order of magnitude of 100 nm). The thickness of the film was 3 μm. All samples were cut into 8 × 8 mm² square pieces and uniformly irradiated at room temperature with 350 MeV Au ions up to a fluence of $5 \cdot 10^{14}$ ions/cm². Because the deposited Ti films already possessed a texture, we irradiated the thin samples under two different angles, 20° and 45°, to avoid correlation effects between the ion beam direction and the existing orientation distribution. The textures of irradiated samples were studied using the synchrotron radiation beam at the KMC2 beamline at BESSY [2]. In order to avoid absorption by the substrate, the diffraction was measured in reflection geometry. The size of the focused beam at the sample position was 200 × 200 μm².

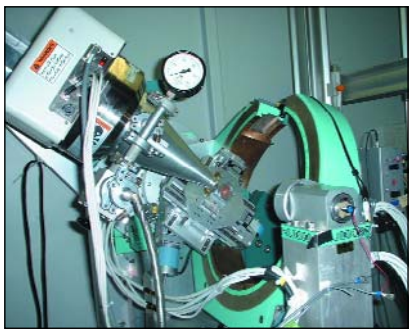

Fig. 1: Improved experimental device used in the investigation of texture changes in thin titanium films with X-rays at BESSY. The figure shows the sample mounted on the goniometer head and the area detector during the measurement. The incoming X-ray beam enters the figure from the right.

Representation of the results – the pole figure

A pole figure describes the spherical distribution of the crystal lattice planes. In a standard Bragg experiment, the intensity of the diffracted beam is proportional to the volume of the sample irradiated by X-rays, and to the fraction of the planes which are satisfying the Bragg condition, i.e., the plane normal halves the angle between the incoming and diffracted beam. When the sample is rotated in two directions and the measured intensity is mapped versus the sample orientation, the distribution function of the selected planes can be measured.

In the pole figure, the polar angle is projected onto the distance from the center and the azimuthal angle onto the angular distance from the x-axis (pointing from the center to the right). The crystallographic planes which are parallel to the surface give rise to the maximum in the middle of the figure, and the planes whose normal lies in the surface plane will have a maximum on the perimeter of the figure.

Since the unambiguous determination of the crystal orientation in three dimensions requires at least two angles, the orientation distribution function (ODF) requires even in simple cases at least two pole figures of non-parallel plane sets in crystal, so the experiment has to be repeated for another Bragg angle.

Results

In the unirradiated state, the thick sample showed a texture specific for rolled metal sheets. This texture did not change even after irradiation with $5 \cdot 10^{14}$ ions/cm². The grain size seems to have an important influence on introduced grain orientation.

Below $5 \cdot 10^{14}$ ions/cm^2, the textures of the films showed no changes. First changes became visible above this value and the resulting textures depended on the beam direction. Since already at a dose of about 10^{13} ions/cm^2 the sample is completely covered with tracks, we conclude that texture modification does not occur in single ion tracks but reorientation of the crystallites requires multiple track overlap.

The rate of texture change was similar for samples irradiated under different incident angles, both textures showed the first changes only above 10^{14} ions/cm^2. The resulting textures are different, and depend on the ion beam direction.

Fig. 2 shows three sets of pole figures, for an unirradiated thin film, and for thin films irradiated with the maximal dose, $5 \cdot 10^{14}$ ions/cm^2. There is a maximum in the middle of the (002) and (101) pole figures for all three samples. We already showed in our previous experiment [5] that the Ti layer starts to grow with the (101) plane parallel to the surface, but above a certain thickness it grows with the (002) plane parallel to the surface. We assume that the maximum in the middle (101) pole figure comes from the deeper regions of the film, which are closer to the substrate, and the (002) maximum from the grains nearer to the surface. We also see that the maximum in the middle of the (101) pole figure is not much affected by ions.

The angles 20° and 45° were chosen in such a way that one of them lies below and one above the direction of the (101) plane normal in the unirradiated sample (approximately 27° from surface). If we look at the (002) pole figures of the irradiated sample, we can see that the (002) peak in the 20° sample moves to the left, and in the 45° sample to the right. This behaviour suggests the affinity between the (101) plane normal and the direction of the ion beam. Also, as in the previous experiment [5], a break of the fibre texture into six distinct maxima was observed.

A more quantitative comparison with the previous experiment is difficult due to the different qualities of the Ti layers used in the experiments. Different growing rates and/or temperature resulted in different initial states. Furthermore, a slight difference in the ion energy may cause a variation in the dynamics of the texture alteration.

[1] H.D. Mieskes, W. Assmann, F. Grüner, H. Kucal, Z.G. Wang, and M. Toulemonde, Physical Review B **67**, 155414 (2003).
[2] A. Erko, I. Packe, C. Hellwig, M. Fieber-Erdmann, O. Pawlitzki, M. Veldkamp, W. Gudat, AIP Conf. Proc. **521**, 421 (2000).
[3] H. Dammak, A. Barbu, A. Dunlop, D. Lesueur, Phil. Mag. Lett. **67**, 253 (1993).
[4] H. Dammak, A. Barbu, A. Dunlop, D. Lesueur, Phil. Mag. A, **79**, 147 (1999).
[5] I. Zizak, N. Darowski, J. Gerlach, A. Wenzel, *ISL Annual Report 2002*, 43.

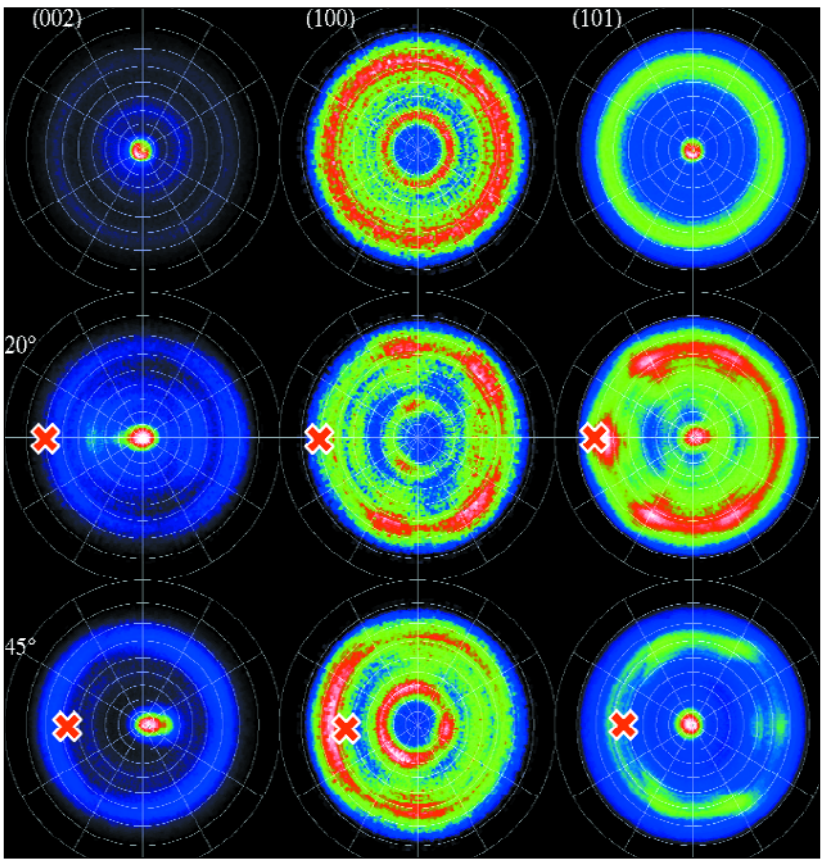

Fig. 2: Pole figures of thin titanium layers: unirradiated sample (top row), irradiated under 20° (middle row) and 45° incident angle. The pole figures show the spherical distribution of the crystal lattice planes with a particular orientation. Here the figures for the crystal planes (002), (100) and (101) are given. The red cross marks the irradiation direction. The comparison of the (101) results for the unirradiated sample and the sample after irradiation under 20° shows that the irradiation led to a recrystalization of the sample with the direction of the ion beam coinciding with the preferred orientation of the crystallites. See text for detailed discussion of the results.

Nonthermal Melting of BeO Films Induced by Swift Heavy Ions

K. Czerski[1], G. Schiwietz[1], M. Roth[1], F. Staufenbiel[1]; P.L. Grande[2]
■ 1 HMI, SF4 ■ 2 Universidade Federal do Rio Grande do Sul, Porto Alegre, Brazil

Introduction

Swift heavy ions passing through a solid lead to a lasting structural change along their paths. The process leading to the creation of these ion-tracks is a central research topic in the field of ion-solid interaction. Spontaneous lattice relaxation was originally proposed by Watson and Tombrello [1] as a possible ion-track formation-mechanism. According to this, a high electronic excitation density induced by swift heavy ions in a solid produces a large internal pressure of the electron gas leading to an expansion and destruction of the crystal lattice. Alternatively, the modification of the electron screening between target ions directly decreases the cohesion of the solid [2] and consequently causes a fast, non-thermal melting within the ion track region. Up to now, this process was observed only for a few semiconductors in pump and probe experiments with femtosecond lasers [3, 4]. The estimated melting time amounted to several hundreds of femtoseconds.

Here we present an evidence of an ultrafast band gap collapse and nonthermal melting of beryllium oxide BeO thin films induced by swift heavy ions and investigated by means of the Auger electron spectroscopy.

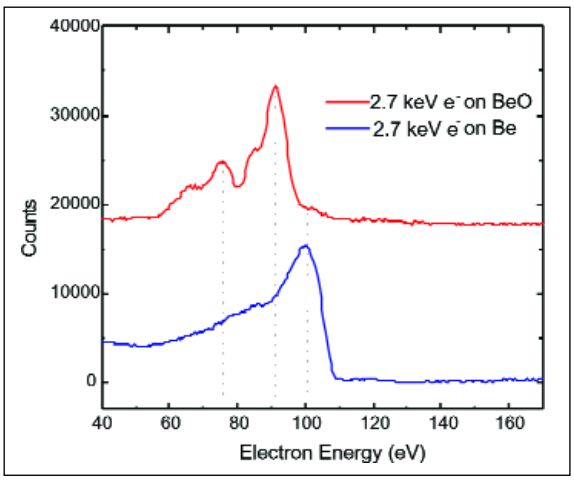

Fig. 1: Electron induced Auger spectra for metallic beryllium (blue) and beryllium oxide (BeO – red)

The Experiments

The experiments were performed using highly charged argon (Ar), xenon (Xe) and gold (Au) beams from the ISL cyclotron at energies of several MeV per nucleon. We applied a thin carbon foil placed in front of the UHV target chamber to increase the charge states of the projectiles and the energy density deposited in the target. The BeO films of about 10 nm thickness were produced by implanting 500 eV oxygen ions into an atomically clean Be target or alternatively by oxidation of Be under an oxygen atmosphere of about 10^{-7} hP. To test the targets' quality we measured the KVV (K-valence-valence) Auger electron spectra induced by 2.7 keV electrons from an electron gun mounted at the target chamber. In Fig. 1 a single line with the maximum at 100 eV originating from metallic Be and a multipeak spectrum characteristic for BeO with the main line shifted by about 10 eV towards lower electron energy are presented. The electron beam was focused to a spot size smaller than 1 mm and positioned at the target with a precision of about 0.3 mm. The electron and ion-beam induced Auger-electron spectra were measured by a 45° parallel-plate electrostatic spectrometer located at an angle of 135° with respect to the ion-beam direction.

Auger electron spectra measured during irradiation of BeO thin films by Ar^{7+}, Ar^{15+} and Xe^{31+} ions are depicted in Fig. 2. The lines at energy of about 140 eV correspond to the K^2VV Auger decay arising from double ionization of the K shell. The KVV spectra differ significantly from that obtained repeatedly for the electron incidence (Fig. 1) during the beam time. In addition to the multipeak BeO spectrum, the line characteristic for the metallic Be appears. The strength of the "metallic contribution" increases with increasing stopping power of the projectiles. It is very small for the Ar^{7+} ions whereas it dominates for the Xe^{31+} beam. The spectra obtained for the Au^{41+} incidence [5] show no BeO contribution any more. The broadening of the metallic KVV line compared to the electron induced one results from the increased temperature of the electron gas the time scale of the

Auger decay [6] amounting to about 13 fs. The line broadening coincides with that obtained for irradiation of the metallic Be target [7]. Furthermore, the line positions agree with those observed for the electron incidence. This excludes any ion track potential and thus the Coulomb explosion as the ion-track formation mechanism in BeO.

Discussion

The appearance of the metallic Be Auger line in the spectra of the BeO target is a very remarkable result. It indicates that the electron bandstructure of BeO collapses completely already before the Auger decay, i.e. faster than 13 fs. Moreover, the same Auger decay energy of 101 eV for the metallic Be and BeO targets suggests that the cohesion energy and thereby the atomic distances in both cases should be similar. On the other hand, the ionic bonds of BeO are much stronger than those characteristic for the metallic phase. Thus we can conclude that the Auger emission from BeO takes place already after a lattice relaxation to the metallic liquid phase. A simple estimation of the relaxation time based on the known difference in the cohesion energy and bond lengths leads to a value of about 5 fs [5] in agreement with the experimental results. This is about one order of magnitude faster than the similar transition to the metallic phase observed for silicon in the femtosecond-laser irradiation-experiments [4].

Another important experimental result is the observation of the energy-density variation of the insulator-metal phase transition. Similarly to the laser experiments, the phase transition can occur only at a high electronic excitation density that corresponds in ion-beam experiments to a high stopping power value. The onset of the nonthermal melting arises already for the irradiation by Ar^{7+} ions. A saturation of the effect, corresponding to the ultrafast melting the entire region of the ion track, could be reached for Xe^{31+} and Au^{41+} ions.

Outlook

BeO as a wide gap ionic crystal is predestined to study the short time instabilities of the lattice due to dense electronic excitation. However, the relation between the crystal structure and the critical density of electrons in conduction bands within the confined geometry of an ion track should be investigated in more detail. The spontaneous lattice relaxation, because of its short time scale, can be the most effective ion-track formation mechanism for insulators and semiconductors irradiated by swift heavy ions.

[1] C.C. Watson, T.A. Tombrello, Rad. Eff. **89**, 263 (1985).
[2] P. Stampfli, Nucl. Instr. Meth. B 107 (1996) 138; P. Stampfli, K.H. Bennemann, Phys. Rev B **46**, 10686 (1992).
[3] K. Sokolowski-Tinten et al., Phys. Rev. Lett. **81**, 3679 (1998); K. Sokolowski-Tinten, D. von der Linde, Phys. Rev. B **61**, 2643 (2000).
[4] S.I. Kudryashov, V.I. Emel'yanov, JETP Lett. **73**, 228 (2001).
[5] K. Czerski et al., *ISL Annual Report* 2002, p. 12.
[6] G. Schiwietz et al., Europhys. Lett. **47**, 384 (1999).
[7] F. Staufenbiel et al., *ISL Annual Report* 2002, p. 14.

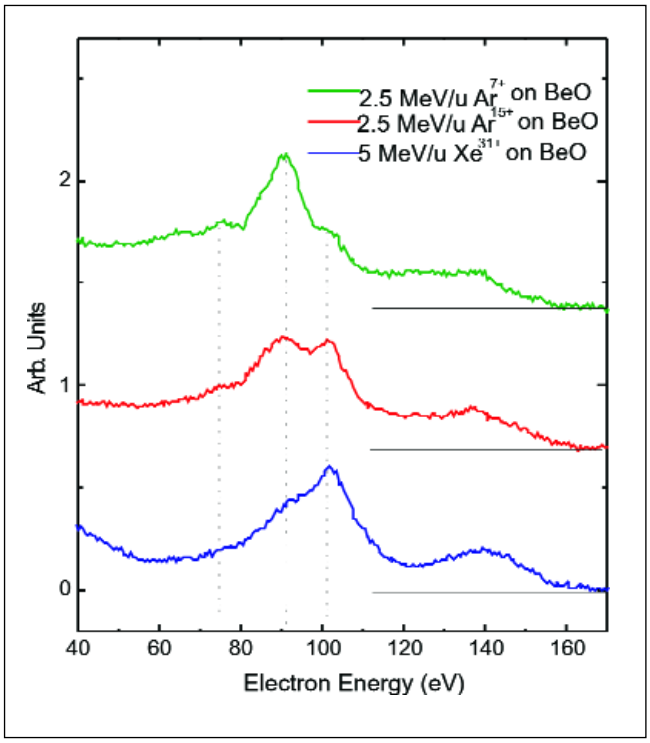

Fig. 2: Ion induced Auger spectra for BeO irradiated with swift heavy ions of different mass and charge state. With increasing mass and charge the peak corresponding to metallic beryllium becomes increasingly prominent, the BeO-peak vanishes (cf. Fig. 1).

TEMPOS – A universal ion track-based electronic building block

D. Fink[1], A. Petrov[1], W. Fahrner[2], K. Hoppe[3]
■ 1 HMI, SF4 ■ 2 FernUniversität Hagen, FB Elektrotechnik, Hagen ■ 3 Fachhochschule Südwestfalen, FB Elektrotechnik und Informationstechnik, Hagen

Contemporary electronic structures frequently consist of single crystalline silicon wafers with a dielectric layer (usually silicon oxide or oxy nitride) layer on top. Suppose that these structures are irradiated with swift heavy ions and etched, and the etched tracks there-upon filled with a material of sufficiently high resistivity, then one obtains paths for charge transport between the conducting silicon channel induced below the oxide, and the surface of that oxide layer. If additionally highly resistive material is deposited onto the oxide surface and connected by two electrodes (denoted in Fig. 2 by “o” and “w”), and simultaneously the silicon wafer backside is contacted by another electrode (“v” in Fig. 2), then one obtains a family of novel electronic elements. Due to their peculiarity to use narrow conducting pores as charge transport paths, these structures have been named TEMPOS which is the abreviation of *Tunable Electronic Material with Pores in Oxide on Silicon*.

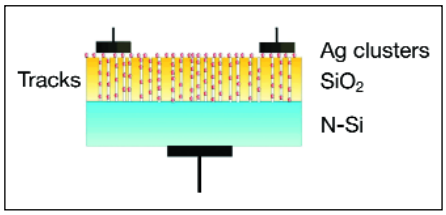

Fig. 1: Principle construction of a TEMPOS structure. In this example a highly resistive layer of dispersed Ag nanoclusters is used as filling material.

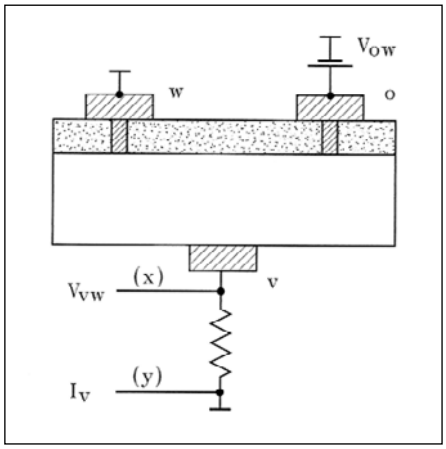

Fig. 2: The TEMPOS symbol adopted by us, and the principle setup of a basic TEMPOS circuit.

Concerning their electronic behaviour, TEMPOS (patent pending) structures lie in between tunable resistors, capacitors, diodes, transistors, photocells, batteries, and sensors, which explains their universality. Fig. 1 shows the principle construction of these structures, and Fig. 2 shows the corresponding electronic circuit.

The function of these TEMPOS structures is determined by the material and the thickness of the dielectric layer, the diameter, the length, shape and areal distribution of the etched tracks, the type and the distribution of the (semi)conducting matter deposited within these tracks and on the dielectric surface, and of course also by the type of silicon substrate. These many new parameters give rise to unpredicted posssibilities. For example, complementary npn and pnp structures can be obtained just by tailoring the track conductivity only (e.g. by different etching times but identical deposition conditions), Fig. 3. In classical silicon electronics, this is possible only by changing the substrate doping.

TEMPOS structures can be easily tailored for special tasks, by adequate choice of the material in the ion tracks and on the sample surface. For example, TEMPOS elements with dispersed silver clusters as highly resistive material can be used as base structures for low frequency noise generators, point-like light emitters, signal frequency amplifiers, low-, high-, and band passes, amplifiers, amplitude modulators, astabile multivibrators etc. Further, resistive, conductive and capacitive sensors for temperature and light, photocells, photo-transistors and optocapacitive remote controls of local oscillators have already been realized with this structure.

TEMPOS structures containing fullerite, phthalocyanine, or II/IV semiconductor nano-crystals as highly resistive material show resistive, conductive and capacitive sensoric properties for humidity and gases such as alcohol or acetone.

Circuits have been designed that transform a certain degree of humidity or a certain gas concentration towards frequency, current or voltage, and the corresponding TEMPOS elements can also be used as light, temperature, humidity or alcohol controlled voltage supplies (Fig. 4). At present we test the electronic response of TEMPOS structures upon deposition of new materials in tracks and surfaces, such as of

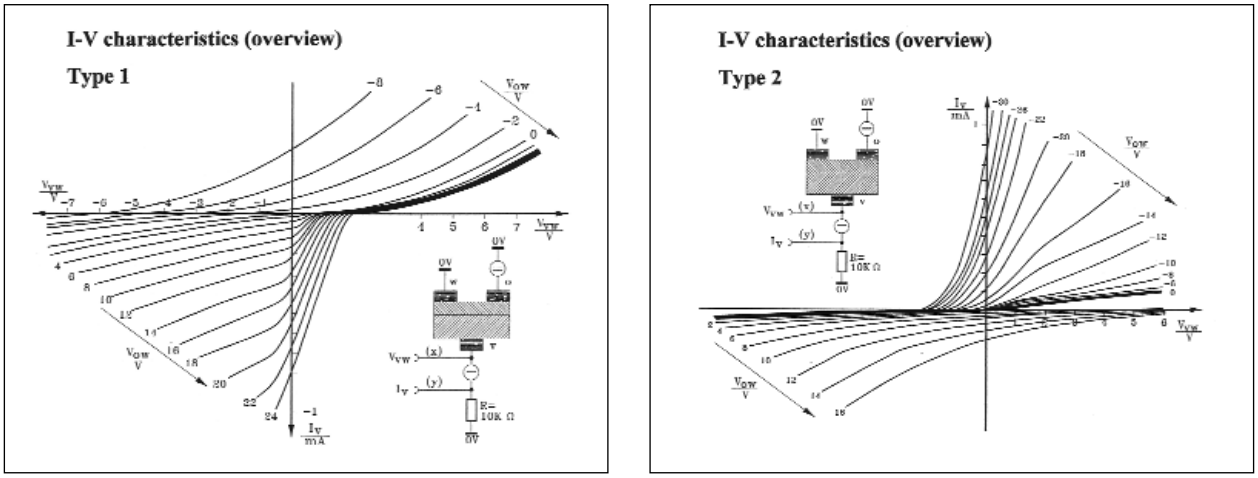

Fig. 3: The two basic types of TEMPOS characteristics, produced by track etching up to different diameters, for the same substrate doping and track filling. Left: Type 1 (npn-Type) after little track etching. Right: Type 2 (pnp-Type) after strong track etching. One can also obtain a similar characteristics when keeping the same track diameter but changing the substrate doping.

nanocrystal/polymer composites, with the nanocrystals being as well metals as II/IV compounds. Also the deposition of lithium niobate and of oxides of Zn, Ti and Sn is under examination, and hopefully deposition of buckytubes and ferrofluides in the tracks will follow. When selecting doped polysilane or diamond films as dielectric layers, intrinsically conducting latent tracks with smaller diameters emerge after the ion irradiation, thus enabling higher track densities. It is also intended to fill porous silicon films on TEMPOS structures with adequate matter. The aim of all these works is to develop various types of light emitters and photodetectors and a great variety of sensors with both resistive and capacitive response upon various gases and liquids, upon accoustic and magnetic signals, on upon accelerations and on particle irradiation.

Probably TEMPOS structures are radiation hard as the new additional track of an accidentally impinging highly energetic charged particle will not alter much the behaviour of a structure that already contains some typically 10 millions of conducting tracks/cm^2.

With ~1000 € being the typical price for one hour beamtime at a heavy ion accelerator with a flux of ~10^9 ions/*s*, one can easily estimate that the production of an individual ion track costs around $3 \cdot 10^{-10}$ €. This signifies that the cost of irradiation of a silicon wafer of 10 cm diameter – sufficient for producing at least some 1000 TEMPOS structures – will be around ~0.20 €, which is negligible as compared with other production costs. On the other hand, the cost of production of standard TEMPOS structures will be lowered as, in principle, no doping, no cleanroom, no high vacuum (apart from that in the accelerator), and no lithography is required. For the sake of easy handling in our first experiments, we made our TEMPOS prototypes as large as a few mm in size, but they can, in principle, be diminished considerably. The size of the smallest possible 3-contact-TEMPOS element is given by the distance of two ion tracks, hence is in the order of a few 100 nm to a few µm. Non-gated 2-contact-TEMPOS structures can even restrict to one track only, hence can be reduced down to the 10 nm level.

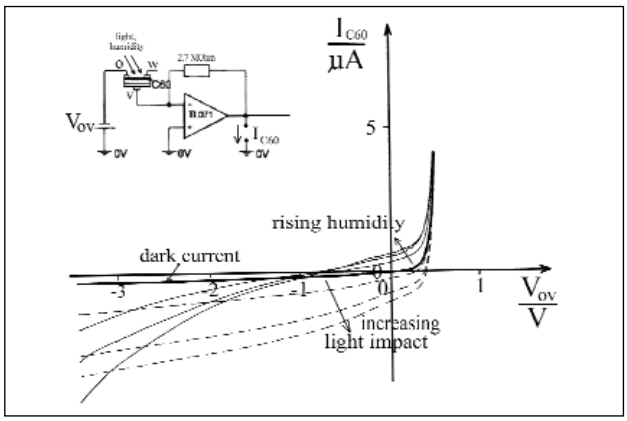

Fig. 4: The change of the DC dark current of a C_{60}-TEMPOS-structure (thick curve) upon visible light impact (day light; dashed curves) or humidity increase (solid thin curves). The presence of alcohol vapor shifts the curve in the same direction as light impact. The measurements shown are performed for zero gating voltage V_{ow}.

Decomposition behaviour of as-received and oxidized TiH_2 powder

B. Matijasevic[1], J. Banhart[1], I. Zizak[2], N. Darowski[2], G. Schumacher[2]
■ 1 Technische Universität Berlin and HMI, SF3 ■ 2 HMI, SF4

Metallic foams are excellent engineering materials offering high energy absorbing capacity, reduced thermal and electrical conductivity, as well as enhanced mechanical and acoustic damping. This material combines properties of cellular materials together with those of metals. The high stiffness-to-mass ratio leads to a variety of applications especially in automotive industry. (See also news report on page 15.)

One very promising and proved way to produce metal foams is the powder metallurgy route [1]. A precursor material tablet is produced by compacting a powder mixture including small amounts of blowing agent powder. Heating of this material causes gas release by decomposition of the embedded blowing agent and thus expansion of the material.

The overall aim is to produce a stabilized blowing agent compatible with the foaming process [2]. The alloy composition and the type of the blowing agent have to be chosen such that the blowing agent gives rise to an ideal foaming behavior with formation of a homogeneous pore size.

Up to now titanium hydride (TiH_2) turned out to be the best foaming agent to reach homogeneous pore formation and pore size distribution. As there is a mismatch between the melting point of commercial aluminum alloys and the decomposition temperature of TiH_2 (400°C), the latter should be subjected to thermal and/ or oxidizing treatments.

By this an oxide layer is formed on the surface of the titanium hydride powder particles. This layer delays gas release, from the particles, so that during heating up of the powder mixture the blowing first takes place when the melting temperature of the alloy is reached. The thickness and composition of the layer depends of the used temperature and time period of oxidation (Fig.1).

By the present investigation the influence of various pre-treatments in air on the release of hydrogen from TiH_2 is examined. For this purpose the decomposition of TiH_2 powders is examined by differential scanning calorimetry (DSC) [3], thermogravimetric analysis (TGA) [1,4,5] and mass spectrometry (MS, Fig. 2). The morphology of the powder was obtained by scanning electron microscopy (SEM).

Cold pressed TiH_2 powder pre-heated in air at 520°C for 180 minutes was studied in situ during the heating in air. Synchrotron radiation experiments were performed at the KMC2 beamline at BESSY the synchrotron radiation source in Berlin. Powder diffractometry was performed using an area sensitive detector, which allowed the acquisition of the whole range of the diffraction pattern simultaneously. The sample was mounted on in the focus of a radiation heater (Fig. 3). The temperature of the sample was controlled using two thermocouples mounted on the sample stage. In the preliminary experiment the temperature was changed from room temperature up to 700°C with the constant rate of 5 K per minute.

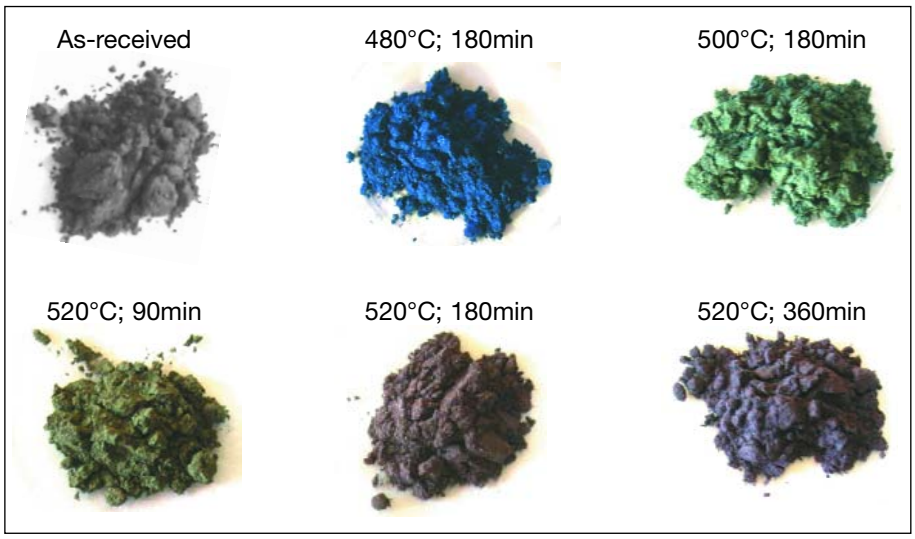

Fig. 1: TiH_2 oxidized at different conditions. The colour of the powder depends on the thickness of the oxygen layer.

The area sensitive detector was covering the angles between 34° and 45°, so it was possible to acquire the most important Bragg reflexes of the different compounds assumed in sample (Fig. 4). Data evaluation showed that we were able to determine the content of hydrogen in the sample and to follow the evolution of the Ti/H ratio using a phase diagram.

We identified the same titanium oxides, which were measured after the pre-treatment on a laboratory X-ray source (see Fig. 4). After the initial change of the TiO_2 intensity, the amount of oxides stayed constant, while the concentration of hydrogen increased considerably. The structure of titanium-hydride changed at higher temperatures to bcc β-phase because of the loss of hydrogen. After the cooling the sample consisted of a mixture of cph α-Ti and fcc δ-$TiH_{1.5}$. Advantage of the in-situ measurements is the possibility to monitor exactly the phase transition, using only one sample for the whole range of temperatures.

These preliminary in situ X-ray diffraction experiments at BESSY are combined with transmission electron microscopy (TEM) to get some additional information about the structure of the oxide layer covering the hydride particles.

In the future we plan to perform the in-situ diffraction experiment during the pre-treatment of the blowing agent at different temperatures and annealing time, as well as the decomposition of the hydride and in the inert atmosphere.

[1] Baumgärtner F, Duarte I, Banhart; J. Adv Engn Mat **2**, 168–174 (2000).
[2] Banhart J. German Patent 100 (15) 2000.
[3] Centeno-Sanchez RL, Kennedy AR, Wood JV; In: Banhart J, Ashby MF, Fleck NA, editors. *Cellular metals and metal foaming technology*, Bremen: MIT-Verlag (2001) 69–76.
[4] Gergely V, Clyne TW, In: Banhart J, Ashby MF, Fleck NA, editors. *Metal foams and porous metal structures*, Bremen: MIT-Verlag; (1999) 83–89.
[5] Kresse R. In: Banhart J, Ashby MF, Fleck NA, editors. *Metal foams and porous metal structures*, Bremen: MIT-Verlag; (1999) 109–112.
[6] Kennedy AR, Lopez VH, Mater. Sci. Eng. A **357**, 258–263 (2003).

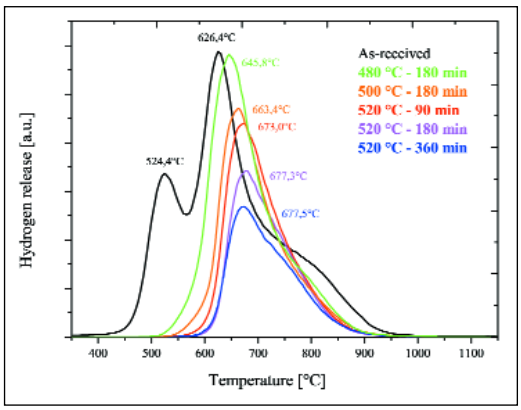

Fig. 2: Release of hydrogen as a function of heat treatment. The decomposition of the TiH_2 is impeded due to the slow diffusion of the hydrogen through the oxide layer.

Fig. 3: The sample was mounted on a ceramic holder and irradiated with a halogen lamp. The incoming X-rays entered the figure from the right-hand side. Scattered photons were reflected through the metal cone on the left side to the detector.

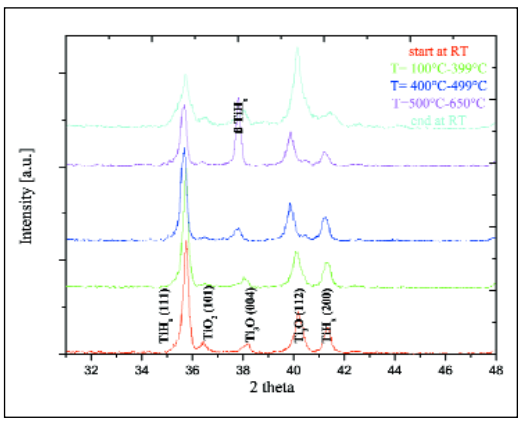

Fig. 4: Alterations of the peak intensities during heating and cooling of a pre-heated powder.

Gelation in suspensions of “sticky” particles

Klaus Kroy
■ HMI, SF5

What are gels?

Colloidal gels are (metastable) solids made from small (nm–μm sized) colloidal particles that do not seem to fit very well into the usual classification scheme of the states of matter into (crystalline) solids, liquids, gases, and plasmas. Like for a glass, a snapshot of a gel may resemble a liquid, yet its macroscopic mechanical behaviour is elastic, and therefore it qualifies as a solid. Unlike glasses, gels can moreover exhibit elastic behaviour at extremely low particle densities. These gels then have a ramified (fractal) structure. In a recent collaboration with the Soft Condensed Matter Group of the University of Edinburgh, we argue that the gel state is not so much characterized by its structural properties, but by the fact that it is the result of a kinetic arrest transition [1, 2]. In other words, a gel is not a solid because of certain obvious structural properties – as is usually argued for the common paradigm of a solid, namely a crystal – but simply because upon smoothly varying some (structural) control parameter, its dynamics suddenly became extremely slow. This is in close analogy to the glass transition, and in fact at high densities the critical behaviour at both transitions is theoretically very well described by the same mathematics, known as mode-coupling theory (MCT). For dense fluids giving rise to homogeneous gels (classified as type-I gels in the diagram) this analogy has recently been established by combined theoretical and experimental efforts reviewed in [3].

The classical paradigm revisited

In general, it is not easy to decide whether a system will be in the liquid or in the solid state by simply looking at the system parameters. One might argue that for a solid system an uninterrupted chain of bonded particles needs to percolate throughout the whole sample volume. For (infinitely) strong bonds this is indeed the answer, and the gel transition can be identified with percolation. If the bond energy is not much more than the thermal energy, the answer is less obvious, however. Even if bonds percolate, they are not permanent but only transient. This, on the other hand does not exclude elastic behaviour either. Take a slightly polydisperse glass of hard spheres, for example, without any attraction. At high enough density it undergoes a kinetic glass transition into a “jammed” solid state that obstructs the pathway to optimum packing. Hence, while transient bonds do not guarantee elasticity, elasticity can emerge even without any bonding at all. In the last example polydispersity serves to avoid crystallization, but in other cases gravity or other effects causing extreme slowing-down of crystal nucleation, can effectively lead to the same result.

Figures 1–3: Helen Sedgwick,
School of Physics, University of Edinburgh

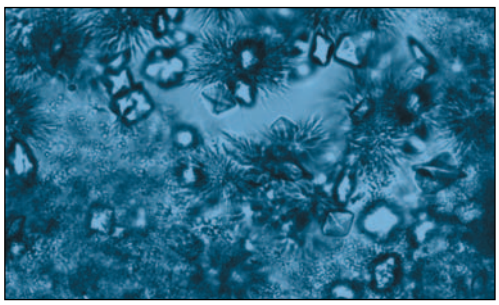

Fig. 1: Optical micrograph showing a transient gel of the globular protein lysozyme formed by the addition of NaCl. Various crystals can be observed to nucleate out of the gel as the gel collapses typically half an hour after formation. (preprint cond-matt/0309616)

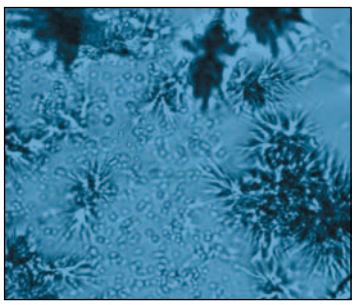

Fig. 2: Optical micrograph showing the non-ergodic homogeneous gel-beads (the small spherical objects) observed in solutions of lysozyme on the addition NaCl, and subsequent crystal nucleation (the larger structures).

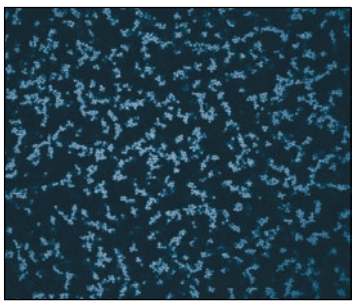

Fig. 3: Confocal micrograph showing the gelation of colloidal particles into ramified aggregates.

Interference of phase separation

Attractive interactions complicate the picture compared to the glass transition of purely hard spheres, because they can induce phase separation into effective liquid and gas phases (the whole colloidal suspenion is of course still embedded into a solvent), as familiar from the idealized van-der-Waals fluid. For a range of the attraction less than the particles' hard cores, this gas-liquid phase separation is thermodynamically metastable with respect to crystallization. However, it still dominates the phenomeology since crystal nucleation is comparably slow. It thus becomes important to understand the interaction of liquid-gas phase separation and kinetic arrest. Since both phenomena are kinetic in nature, it is not surprising that this interplay depends on the time scales imposed by external conditions.

Gel classification

Take a dilute solution of nm-sized globular proteins e.g. lysozame as an example (Figs. 1, 2). To a good approximation the protein interaction can be idealized as that of hard spheres with some short-ranged attraction. The attraction depends on the salt concentration in the solution. When the system is "qenched" into the gas-liquid coexistence region by adding salt to the solution, phase separation into protein-rich drops and an almost pure solvent background occurs. Since the proteins are so small, they diffuse very quickly, so that phase separation proceeds fast relative to the mixing process. Hence gelation in this case can be classified as arising from a "slow quench" leading to gels denoted as type II gels and to gel beads (see diagram and Fig. 2) at low protein volume fractions. Such are the gels that typically plague protein crystallographers, and a better understanding of their physical origin may hopefully guide them in devising more rational protocols. Although they may later crystallize, the crystals formed are not necessarily suitable for x-ray analysis (Fig. 2). For the comparably "large", micron sized colloids, on the other hand, phase separation kinetics may well be slow compared to the time scale for switching on the attractions. In contrast to the situation for the small proteins, in this case gelation is due to a "rapid quench" and produces type III gels and at low volume fractions (and in presence of spurious long range repulsions) fractal clusters (see diagram and Fig. 3).

Type-II gels are homogeneous on short scales but strongly heterogeneous at the mesoscale: they result when the characteristic coarsening textures produced by phase separation get "frozen in" during the coarsening process, as a result of an MCT-like arrest of the denser phase [2]. In contrast type-III gels are assemblies of long-lived nonequilibrium structures locally resembling those obtained from irreversible cluster aggregation (cf. Fig. 3) and thus heterogeneous also on short scales. To distinguish from fully irreversible aggregates, in which the bonds formed are permanent, the type III process is sometimes called "weak gelation". The underlying speculative view of gelation as a double ergodicity breaking (on the monomer scale and on the cluster scale) [1] seems indeed to be supported by recent numerical simulations [4].

[1] K. Kroy et al. *A cluster mode-coupling approach to weak gelation in attractive colloids*. Phys. Rev. Lett. (2004) (in the press).

[2] H. Sedgwick et al. *Non-equilibrium behavior of lysozyme solutions: beads, clusters and gels*. cond-mat/0309616.

[3] K. N. Pham et al. *Multiple glassy states in a simple model system*. Science **296** (2002) 104.

[4] E. Del Gado et al. *A unifying model for chemical and colloidal gels*. Europhys. Lett. **63** (2003) 1.

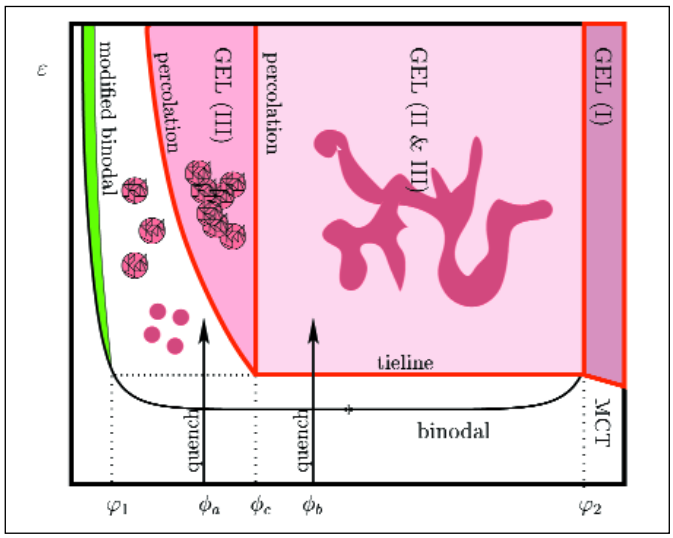

Diagram: Schematic cut through the phase diagram of adhesive hard spheres along a plane spanned by volume fraction ϕ and attractive strength ε. The interaction of gas-liquid phase separation with MCT-kinetic arrest gives rise to a variety of metastable gel phases. At high colloid volume fractions ϕ, where MCT can be applied directly, homogeneous gels form (**region I**). At lower ϕ phase separation may create macroscopically heterogeneous gels (**region II**) and homogeneous gel beads if the quench is slow (cf. Figs. 1, 2), while more tenuous gels (**regions II & III**) and ramified clusters consisting of non-equilibrium particle aggregates result from rapid quenches (cf. Fig. 3). The predicted critical behaviour at the transition is that of percolation along the vertical gel boundaries, while mode-coupling critical behaviour is expected across the tieline or MCT-line. (cond-mat/0403684)

“VV dip” in light-scattering of supercooled liquids experimentally confirmed

Thomas Franosch
HMI, SF5

Glass-forming liquids exhibit the striking property of a strong temperature dependence of transport coefficients such as viscosity. A small decrease of temperature by, say, $10\,\mathrm{K}$ can induce a factor of 10 in viscosity. The underlying dynamical process that deals with the strong steric hindrance in the molecular motion of the dense liquid is referred to as structural relaxation.

Light scattering has been the ideal tool to investigate these processes, since the dynamical window of these experiments allows one to monitor the evolution of structural relaxation in the temperature range where the liquid changes its behaviour from a viscous liquid to an elastic solid. The theory of light scattering in supercooled liquids was well worked out for liquids at high temperatures but failed to describe the transition to low-temperature amorphous solid.

Recently a collaboration of the Theoretical Physics group of the Hahn-Meitner Institute extended the description of long-wavelength dynamical processes in moderately supercooled liquids, see Ref. [1, 2]. The extension includes a generalization of the elasto-optical Pockel’s coupling used in the theory of elasto-dynamics to highly viscous fluids exhibiting a slow structural relaxation in the frequency window of light-scattering. Elasto-optical coupling implies that a molecular liquid is found to respond to shear flow by partial alignment of the molecular axis giving rise to the phenomenon of flow birefringence. A theoretical consideration based Onsager's reciprocity theorem reveals that this effect has an inverse effect, viz. a steady change of the molecular orientation causes a mechanical shear stress in the liquid. Both effects are consistently described by the same mechanism via the translation-rotation coupling.

For light-scattering experiments the time-dependent thermal fluctuations of the dielectric tensor are the cause of the frequency shift of the scattered beam with respect to the incident one. Since the dielectric properties change upon a local expansion or compression of the liquid as well as upon aligning the axis of a fraction of the molecules, a strong coupling to the hydrodynamic modes is expected. The new aspect of our recent work has been to include the translation-rotation coupling in the description of the light-scattering spectra. The expected spectrum within this approach differs in important respects from the commonly used model. The new feature is an effective frequency-dependent optical coupling mediated by the appearance of the translation-rotation coupling that connects density fluctuations, i.e. phonons propagating through the liquid, to dielectric fluctuations.

As a result of the extension of the theory by translation-rotation coupling, the Brillouin resonance corresponding to the acoustic-like excitation is decorated with an effective frequency-dependent light-matter coupling, thereby slightly modifying the spectral shape of the resonance seen by polarized light scattering with respect to methods sensitive to density fluctuations only.

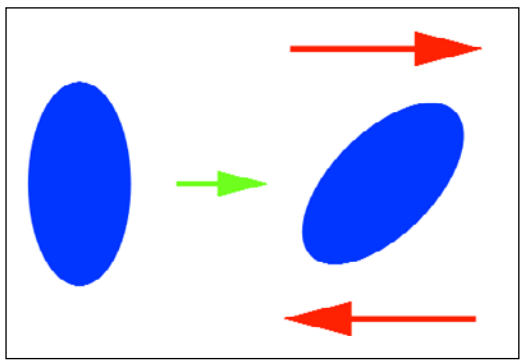

Fig. 1: Molecular alignment by shear flow

The prediction we have made for a weighted difference spectrum of polarized and backscattering depolarized spectra was a small but measurable negative contribution for a certain range of temperatures.

This feature cannot be explained within the conventional approach since it entirely relies on the translation-rotation mechanism. We have therefore proposed to use a simple test to quantify the importance of translation-rotation coupling by searching for the possibility of a negative region of the mentioned difference spectrum.

Recently the experimental group H.Z. Cummins in New York started to remeasure light-scattering of Salol [3, 4], one of the most prominent glass-forming liquids used in the field. The new experiment was necessary to achieve high-precision data in order to perform the difference spectra proposed above. The data for 90 degrees polarized scattering are shown in Fig. 1 and exhibit the thermal evolution of the Brillouin resonance upon incremental supercooling. The difference with respect to the reference depolarized backscattering data is plotted in Fig. 2. The negative contribution (called VV dip by the authors) for a range of temperatures at the low-frequency tail of the resonance is clearly observable and nicely demonstrates the implications of translation-rotation coupling at least for this particular liquid. The experiment constitutes a milestone since it gives evidence that the approaches commonly used have to be reconsidered.

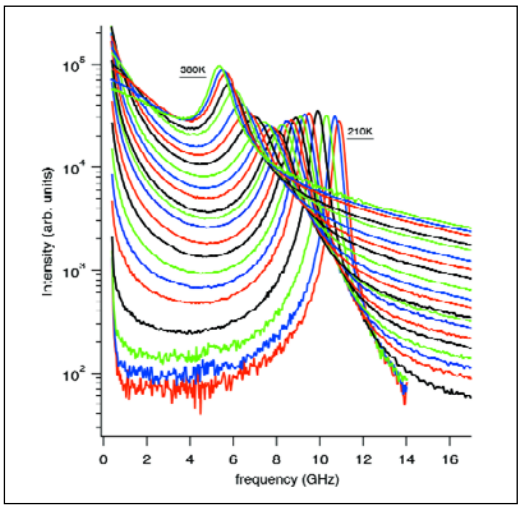

Fig. 2: Polarized Brillouin scattering data at 90 degrees scattering angle of Salol for different temperatures.

The authors of Ref. [3, 4] also carefully analyzed their data within our recently developed theory and found full compatibility with our results. The theoretical considerations thus provided a qualitative and quantitative description of Salol where earlier approaches fail in both respects.

[1] *Light scattering by longitudinal acoustic modes in molecular supercooled liquids I: phenomenological approach*, R.M. Pick, T. Franosch, A. Latz, and C. Dreyfus, Eur. Phys. J. B **31**, 217 (2003).
[2] *Light scattering by longitudinal acoustic modes in molecular supercooled liquids II: Microscopic Derivation of the Phenomenological Equations*,T. Franosch, A. Latz, and R.M. Pick, Eur. Phys. J. B **31**, 229 (2003).
[3] *Brillouin Scattering Study of Salol: Exploring the Effects of Rotation-Translation Coupling*, H, Zhang, A. Brodin, H.C. Barshilia, G.Q. Shen, H.Z. Cummins, R.M. Pick, submitted to Phys. Rev. Lett. (2004).
[4] *Brillouin Scattering Study of Salol: Exploring the Effects of Rotation-Translation Coupling*, H, Zhang, A. Brodin, H.C. Barshilia, G.Q. Shen, H.Z. Cummins, R.M. Pick, Phys. Rev. E (2004) in press.

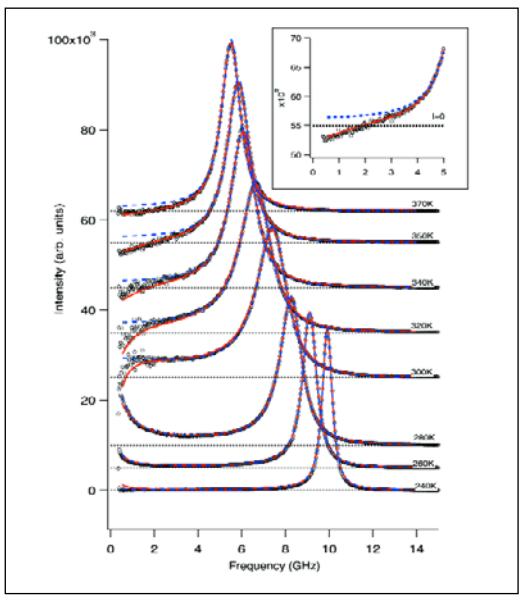

Fig. 3: Difference spectra of Salol for different temperatures. Solid lines are fits to the theory of [1, 2]. Broken lines are fits to a density-fluctuation only model.

Trace elements in the protection of the respiratory tract

K. Bukalis, A. Kyriakopoulos, D. Behne
■ HMI, SF6

The surface of the organs of the respiratory tract, trachea and lungs, is continuously exposed to gases and particular matter present in the atmosphere. As many of these pollutants are powerful oxidants, these tissues need specific protection against oxidative processes. Several enzymes with key roles in the antioxidative defense system are known to contain metals and metalloids such as copper, iron, manganese, selenium and zinc as essential constituents of their active centers. In addition, there may be further protective trace-element containing proteins not yet known. It is therefore of great interest to identify these compounds and to find out about their biological functions.

A first series of experiments has been carried out on the lung of the rat to analyze the trace elements present and to obtain information on their chemical forms and on their possible sites of action within the different cell compartments.

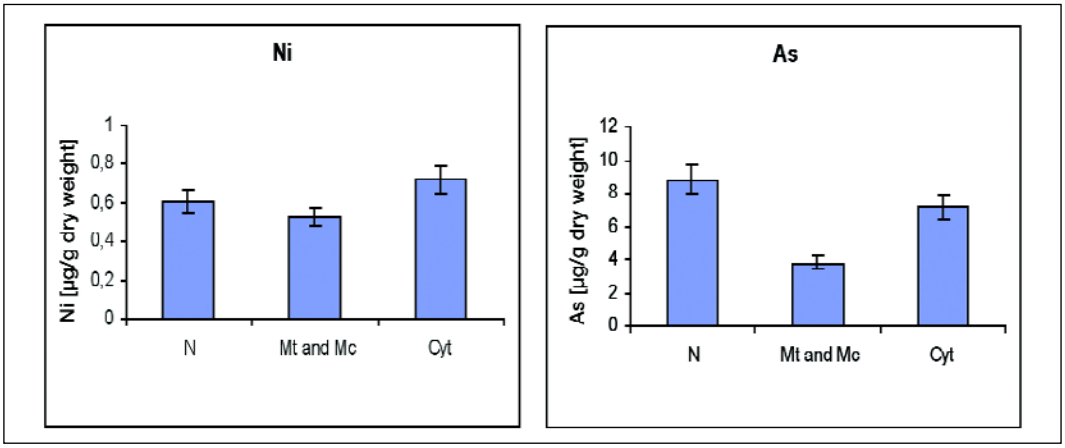

Fig. 1: Concentration of nickel and arsenic in the cytosolic (Cyt), mitochondrial and microsomal (Mt and Mc) and nuclear (N) fractions in the lung of rats.

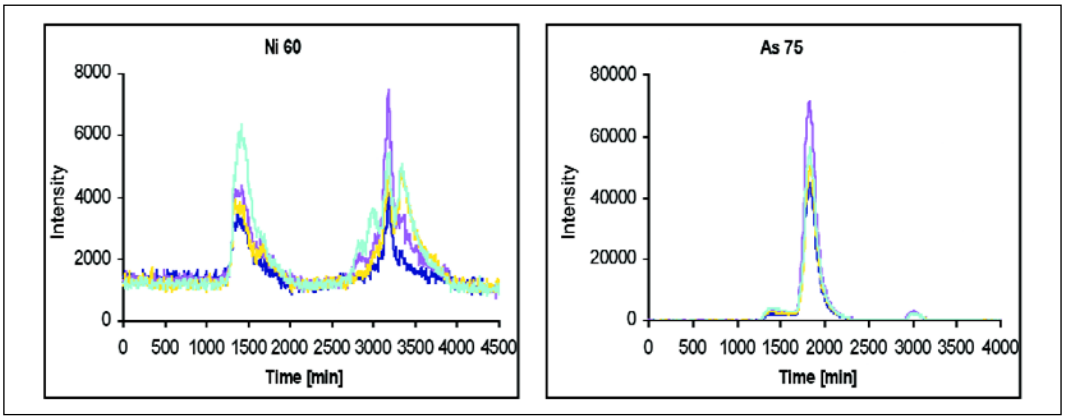

Fig. 2: Distribution profiles of nickel and arsenic after chromatographic separation of lung cytosol.

In these studies element analytical methods and radiotracer techniques have been combined with biochemical separation procedures. Subcellular separation of the tissues into the nuclear, cytosolic, mitochondrial and microsomal fractions has been achieved by differential ultracentrifugation. Instrumental neutron activation analysis (INAA) and graphite furnace atomic absorption spectrometry (GFAAS) have been used to determine the concentrations of several trace elements in the lung and in the subcellular fractions. After separation of the cytosolic proteins by size exclusion chromatography (SEC), mass spectrometry using an inductively coupled plasma (ICP-MS) has been employed to obtain first information on the trace element-containing proteins present in this compartment. The selenium-containing proteins in the whole organ and in the subcellular fractions have been investigated by labeling of rats in vivo with ^{75}Se, gel electrophoretic separation of the proteins and autoradiographic detection of the tracer.

The use of the different microtechniques of element analysis allowed the quantitative determination of several trace elements such as arsenic, cobalt, copper, iron, manganese, nickel, selenium and zinc. Of special interest was the high concentration of arsenic which in the lung exceeded those in the liver by a factor of 4 and the fact detected here for the first time that both arsenic and nickel were present in relatively high amounts in the lung cell nuclei (Fig. 1).

The chromatographic fractionation of the proteins present in the liquid cytosolic phase of the lung cells and determination of the element distribution in the separated protein fractions by means of ICP-MS indicated that all the elements investigated were bound to proteins. Copper, iron, manganese, selenium and zinc are known to be essential constituents of redox-active enzymes, but there is the possibility that in the lung these elements may also be contained in further proteins not yet identified. As shown in Fig. 2, arsenic and nickel were likewise found to be protein-bound. So far nothing is known about interactions between these elements and lung proteins. However, the fact that both elements are enriched in this organ and are found in distinct proteins fractions suggests the existence of specific arsenic- and nickel-containing proteins rather than an accidental non-specific uptake. Further studies are therefore needed to investigate more closely the biological functions of these elements and especially the role of arsenic and nickel in this organ.

The most detailed information has been obtained on the selenium-containing proteins after labeling of rats in vivo with ^{75}Se, as here, by means of gel electrophoresis in conjunction with the autoradiographic measurement of the ^{75}Se-labeled proteins, high resolution protein separation could be combined with the very low detection limits of the radiotracer technique (Fig. 3). About 24 selenium-containing proteins with molecular masses in the range between 10 and 80 kDa (1 kDa = 1000 amu) could be distinguished in this way in the subcellular fractions. Several selenoenzymes with redox-functions have so far been identified and it is most likely that the selenoproteins play an important specific role in the antioxidative protection of the respiratory system.

The investigations carried out so far have indicated that numerous metal- and metalloid-containing proteins are present in the lung and may be involved in the protection against oxidative stress. More information will be obtained in studies on animal and human tissues and cell cultures which are at present in progress.

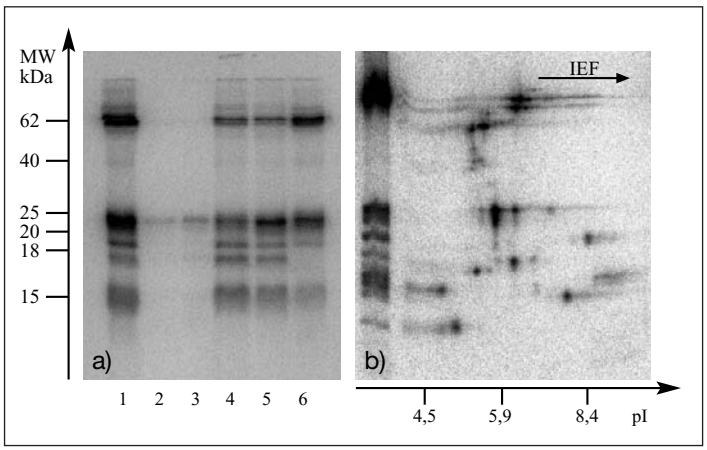

Fig. 3: Autoradiogram of the ^{75}Se-labeled proteins in the homogenate (1) and nuclear (2, 3), mitochondrial (4), microsomal (5) and cytosolic (6) fractions of the rat lung after Laemmli-SDS-PAGE (a) and in the homogenate of the rat lung after IEF/SDS-PAGE (b)

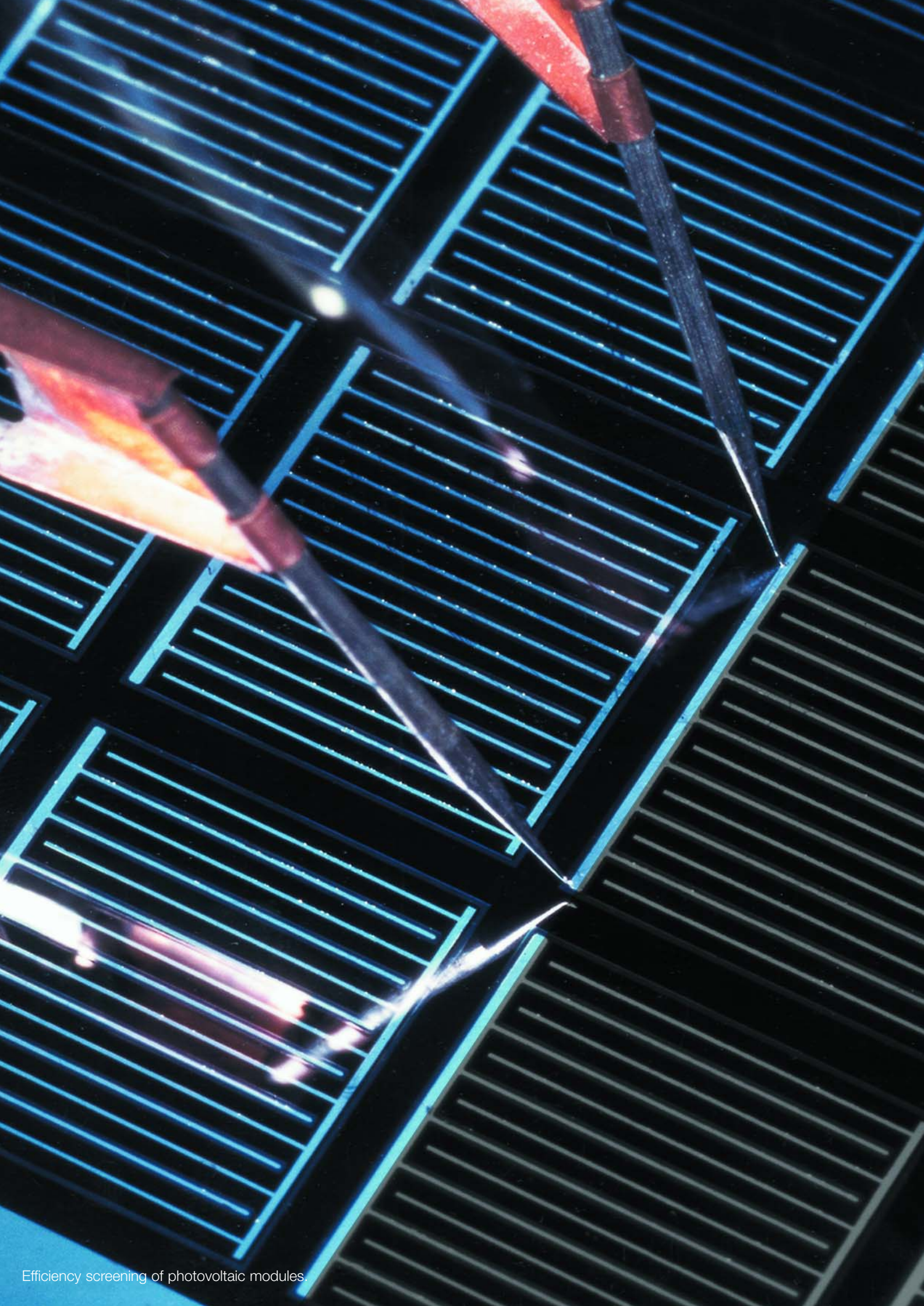

Efficiency screening of photovoltaic modules.

Scientific highlights
Solar Energy Research 2003

Interface properties of a-Si:H/c-Si hetero-structures

K. Brendel, K. Kliefoth, L. Korte, A. Laades, D. Schaffarzik, A. Schoepke, R. Stangl, M. Schmidt
■ HMI, SE1

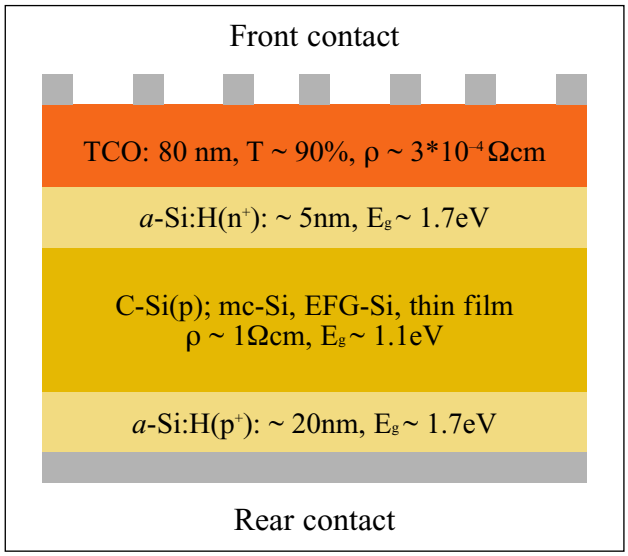

Fig. 1: Schema of a TCO/a-Si:H/c-Si hetero solar cell

The broad application of photovoltaic power systems requires a cost reduction. One way to reach this goal is the reduction of the thicknes of the silicon absorber as an expensive part of such systems i.e. the application of thin low cost silicon wafers or silicon films on glass. Both need an adjusted technology for realising solar cells. The main requirement is to keep a temperature below 550°C during the hole manufacturing process. Simultaneously the loss mechanisms like recombination of the photocarriers should be reduced in such cells for getting high efficiencies.

Silicon based heterojunction solar cells such as Transparent Conductive Oxide / amorphous – Silicon:H / crystalline Silicon are one example for such an high efficient solar cell structure which can be prepared by a complete low temperature process.

The efficiencies are dominated by the band offset for minority carrier injection from the c-Si(p) base, ΔEC, the interface state density distribution at the a-Si:H/c-Si interface, $D_{it}(E)$, and the band bending in the c-Si absorber, $q\varphi_S$, at the active hetero-transition, a-Si:H/c-Si.

The determination of these quantities is essential for developing a physically based technology. The optimum in the a-Si:H layer thickness amounts to about 5 nm. This minimises the absorption losses in the a-Si:H layer and it is possible to reach an optimum in band bending of the c-Si absorber. This very low film thickness corresponds to the emission depth of photoelectrons with kinetic energies below 10 eV. This allows to determine the work function, the position of the Fermi energy E_F and the distribution of occupied gap states $N(E)_{oc}$ of the a-Si:H layer by photoemission spectroscopy excited with energies between 4 eV and 7,5 eV. The precondition for determining $N(E)_{oc}$ is a nearly constant photoexcitation cross section and a constant density of states in the conduction band. Both are more or less fulfilled in a-Si:H.

The $N(E)_{oc}$ distributions are independent on the a-Si:H layer thickness. Only in the case of the 2.8 nm thick layer we found a deviation up to 0.4 eV above the a-Si:H valence band edge as indicated by the dotted line $E_{Va\text{-}Si}$ in Fig. 3. This hints to a contribution of photoelectrons originating from the occupied valence band states of the underlying c-Si wafer which vanishes above the valence band edge of the c-Si,

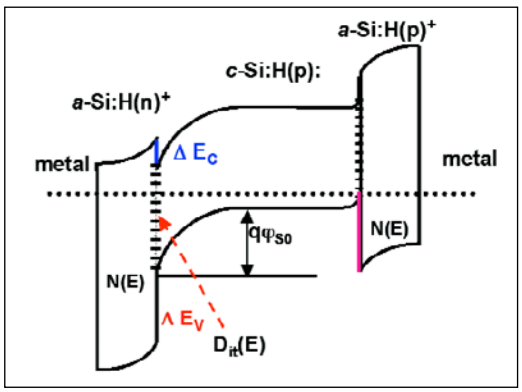

Fig. 2: Band schema of a TCO/a-Si:H/c-Si hetero solar cell. Interface state density $D_{it}(E)$, gap state density $N(E)$, conduction band offset ΔE_C, valence band offset ΔE_V and band bending $q\varphi_{SO}$ are indicated.

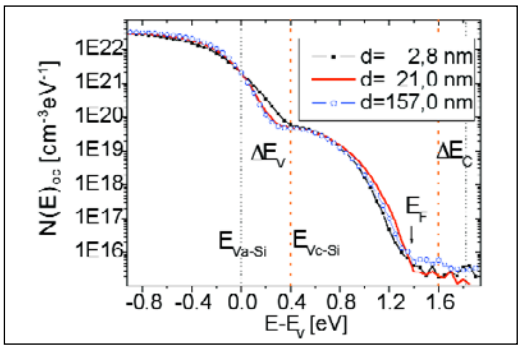

Fig. 3: $N_{OC}(E)$ of slightly n-doped a-Si:H of different film thickness prepared by PECVD on c-Si(p), ((111), 75Ωcm). The data result from constant final state yield measurements, the choosen final state energy amounts to 200 meV. Excitation energy range $h\nu = 4..7$ eV. The arrow indicates the Fermi level position $(E_F - E_{Va\text{-}Si}) = 1.33$ eV and the dotted lines indicate the position of the band edges of c-Si and a-Si:H, respectively.

marked by the dotted line $E_{Vc\text{-}Si}$ in Fig. 3. The analysis gives an valence band offset ΔE_V of 400 meV. Furthermore, the exponentially distributed valence band tail states and the deep dangling bond states at about 700 meV are clearly seen in Fig. 3.

The missing quantities like the c-Si band bending and the a-Si:H/c-Si interface state density can be determined by applying the surface photovoltage, SPV, method. In order to determine the band bending, $q\varphi_{SO}$, or the interface state density, D_{it}, we use an artificial MIS structure, where the metal electrode consists of a TCO layer and the insulator constitutes of a mica foil. Excess charge carriers were generated in the c-Si by a light pulse of $\lambda = 910$ nm wavelength and 10–160 ns pulse length. This leads to a flattening of the band bending i.e. a change of the surface space charge. This change of the surface charge can be read out by a capacitively coupled high speed oscilloscope. The obtained quantity represents the photovoltage ,U_{ph}, modified by the Dember-voltage which results from the mobility difference of electrons and holes.

Applying an additional external voltage U_{field} we are able to change the band bending by a field effect like in a MIS transistor. Thus, we can measure the c-Si band bending via the dependence of the photovoltage on the applied external voltage, $U_{ph} = f(U_{field})$. The charge components of such an MIS structure are divided into the charge located in the interface states, in the space charge of c-Si and in the charge on the metal electrode. All in all we have charge neutrality, this is true also for different applied external voltages. With this method, the thin a-Si:H layer has to be treated like an insulator without change of the trapped charge during the whole measurement. This is only fulfilled at deep temperatures because the charge transfer processes between c-Si and a-Si:H are assisted by phonons which can be frozen and hence the a-Si:H(i) layer can be treated like an insulator.

The $D_{it}(E)$ spectra in Fig. 4 indicate an excellent passivation of the c-Si surface, better or comparable to the passivation by thermally grown SiO_2 or Si_3N_4.

Further progress for SPV investigation by wavelength and intensity dependent measurements is in preparation.

Using the analytical methods for optimisation of the preparation steps, we are able to prepare hetero structure solar cells on flat p-type c-Si wafers with 17% efficiency and with about 14% on EFG silicon material.

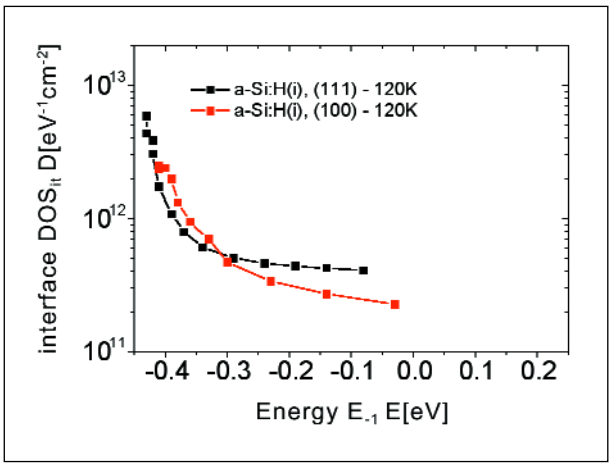

Fig. 4: $D_{it}(E)$ of the a-Si.H(i)/c-Si interface for [100] and [111] oriented Si surfaces. The a-Si:H layer thickness amounts to 20 nm.

M. Schmidt, A. Schöpke, O. Milch, Th. Lussky, W. Fuhs,
Mat. Res. Soc. Symp. Proc. Vol. 762 (2003) A19.11.1

The nature of dangling bond recombination in silicon

C. Böhme and K. Lips
■ HMI, SE1

For thin-film silicon and silicon interfaces, unpaired silicon valence electrons, so called dangling bonds (db), are known to influence recombination rates significantly. In spite of this insight, the microscopic mechanisms associated with db recombination have remained unknown in the past.

Traditional ways to investigate recombination at db centers microscopically such as the continuous wave electrically or optically detected magnetic resonance (EDMR or ODMR) can not provide quantitative information such as recombination probabilities or capture cross sections nor can they distinguish qualitatively different electronic mechanisms which occur at the same defects. Other, non-magnetic resonance based defect spectroscopy methods such as capacitance voltage or deep level transient spectroscopy lack the microscopic sensitivity to distinguishable defects.

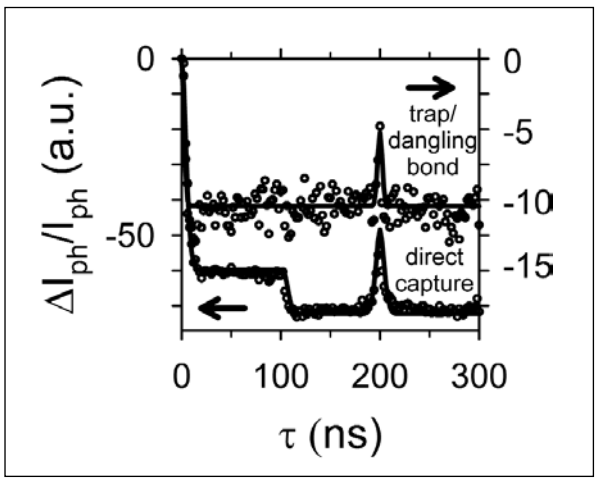

Fig. 1: PEDMR signal at db states of μc-Si:H at $T = 10$ K in case of direct capture and distant-pair-tunneling. The solid lines are theoretical predictions.

Because of this, coherent spin resonance based methods have been developed and improved at the Hahn-Meitner Institute Berlin in recent years [1, 2]. These methods, the pulsed (p) EDMR and pODMR have now been applied to different silicon thin-film materials and silicon related interfaces that are relevant for new solar cell concepts. The studies are to elaborate the qualitative nature of recombination mechanisms at db states and to clarify which of these mechanisms dominate net recombination rates. As an example, the results for hydrogenated microcrystalline silicon (μc-Si:H) are shown here. In the past, much speculation existed whether charge carriers in this material recombine at dangling bonds from trap states in band tails by distant-pair tunneling or whether they are directly captured from delocalized states. Due to the different nature of these mechanisms with regard to the coupling between defect and charge carrier or the influence of disorder, different pEDMR signatures can be expected for the two channels.

Figure 1 illustrates the photocurrent response of μc-Si:H during such a short coherent electron-spin resonant (ESR) excitation of db states. The measurement was carried out as a "recombination echo" experiment where a 180° phase change of the microwave is introduced at $\tau_{180} = 100$ ns. Since the measurement is carried out at different times after the spin ensemble starts to relax back towards its steady state, the different recombination mechanisms can be identified due to their different recombination dynamics. The measurements show that two clearly distinguishable processes are present: Firstly, a strong step-like transient with a clear echo signature at $2\tau_{180.} = 200$ ns. One can describe this observation with the predictions for recombination out of strongly coupled pair states [2] as expected for a direct capture process. Opposite to this observation, a second signature with reduced intensity is also found. This second signal does not exhibit the step-like dephasing at τ_{180} and the echo is much more narrow. This observation is indicative of recombination of weakly coupled charge carrier pairs with highly disordered local fields as it is known to exist for distant-pair tunneling. A detailed review of the nature of the different recombination channels at db centers of μc-Si:H is outlined in Ref. [3].

Beside db centers in μc-Si:H, pEDMR and pODMR have been applied to db located at the crystalline silicon / silicon dioxide interfaces (so called P_b centers) as well as to the investigation of db and band tail recombination in amorphous silicon. Even though these different materials vary greatly with regard to their morphological and defect structures, conductivity mechanisms, band gap etc., the underlying mechanisms for charge carrier recombination appear to be of similar qualitative nature. The dominant recombination process at db centers in μc-Si:H and at the crystalline silicon interface appears to be a direct capture process of electrons from the conduction band via charged excited intermediate states, so called db^{-*} (Pb^{-*} in the case of the interface): When electrons undergo transitions from a delocalized or weakly localized conduction band or band tail state, they localize first in these charged excited intermediate pair states, before they undergo an energy transition into the charged ground state. Thus, recombination at the silicon db seems to be less influenced by the respective microscopic environment of a given db and instead is determined by its own nature (size, wave function) which is known to be quite similar in different systems containing silicon db states.

[1] C. Boehme, K. Lips:
Phys. Rev. Lett., **91** (24), 246603 (2003)
[2] C. Boehme, K. Lips:
Phys. Rev. B, **68** (24), 245105 (2003)
[3] C. Boehme, K. Lips:
phys. stat. sol. (c) **1** (5), 1255-1274 (2004)

Hydrogen in ZnO

N. H. Nickel, K. Brendel
■ HMI, SE1

In the past ZnO has been attracted a great deal of interest because of its optical and electrical properties for applications such as UV light emitting diodes and lasers. However, a major drawback of ZnO is the fact that it almost always shows *n*-type conductivity. Traditionally, the *n*-type conductivity has been attributed to the presence of native defects [1]. Recently, based on first-principles calculations a new source responsible for the observed *n*-type conductivity has been suggested namely, hydrogen atoms that act as shallow donors [2]. This behavior of hydrogen is unexpected since in most semiconductors it acts as a compensating center counteracting the existing conductivity. Most recently, the theoretical prediction has been confirmed experimentally by electron paramagnetic resonance, electron nuclear double resonance, and Hall effect measurements. These measurements revealed the presence of two donors in undoped single crystal ZnO one of which was identified as a hydrogen shallow donor that occurs in a concentration of about $6 \times 10^{16} cm^{-3}$ [3].

The presence of hydrogen in *as-grown* state-of-the-art single crystal ZnO gives rise to an unexpected variety of six H-related local vibrational modes in the wave number range between 2800 cm^{-1} and 3150 cm^{-1}. The vibrational modes are assigned to antisymmetric and symmetric stretching modes of CH_X complexes with $X = 1, 2, 3$. Hence, the vibrational modes located at 2854, 2890, 2918, 2948, and 2988 cm^{-1} would be due to the stretching modes of C-H, symmetric stretching modes of $C\text{-}H_3$, symmetric stretching modes of $C\text{-}H_2$, antisymmetric stretching modes of $C\text{-}H_3$, and antisymmetric stretching modes of $C\text{-}H_2$, respectively. This assignement is supported by the observation that a significant concentration of hydrocarbons is detectable in effusion experiments.

It is not unusual that local vibrational modes in solids occur at frequencies several percent lower than in a free molecule. Thus, the local vibrational mode at 3096 cm^{-1} is tentatively assigned to N-H complexes, which is corroborated by effusion data [4]. After dehydrogenation of the ZnO crystals the local vibrational modes disappeared. This clearly demonstrates that the local vibrational modes between 2800 cm^{-1} to 3150 cm^{-1} are due to hydrogen related stretching vibrations.

From H effusion data the H density-of-states distribution (DOS) can be derived using the relation $N_H \approx \partial C_H / \partial \mu_H$, where C_H is the H concentration and μ_H is the hydrogen chemical potential [5, 6]. In Fig. 2 the H DOS for sputtered (a) and single crystal ZnO is plotted (b). The lowest H DOS is obtained for single crystal ZnO. Deconvolution shows that the spectrum is composed of six peaks with the most prominent feature at 0.86 eV. An increase of the H concentration results in a broadening of the H DOS. Interestingly, with increasing H up to 75 % of the H atoms are accommodated with binding energies larger than 1.0 eV.

The results clearly show that the presence of H in ZnO causes the formation of a variety of complexes in addition to acting as a shallow donor. Using Raman spectroscopy $C\text{-}H_X$ and N-H complexes were detected. In addition, the H density-of-states distribution reveals a number of peaks that are not yet assigned to specific centers. However, the pronounced increase of N_H for binding energies larger than 1.0 eV with increasing H content suggests the formation of larger H clusters.

[1] D. C. Look, J. W. Hemsky, and J. R. Sizelove, Phys. Rev. Lett. **82**, 2552 (1999).
[2] C. G. Van de Walle, Phys. Rev. Lett. **85**, 1012 (2000).
[3] D. M. Hofmann, et al., Phys. Rev. Lett. **88**, 045504 (2002).
[4] N. H. Nickel and K. Fleischer, Phys. Rev. Lett. **90**, 197402 (2003).
[5] W. B. Jackson et al., J. Non-Cryst. Sol. **227-230**,143 (1998).
[6] N. H. Nickel and K. Brendel, Phys. Rev. B **68**, 193303 (2003).

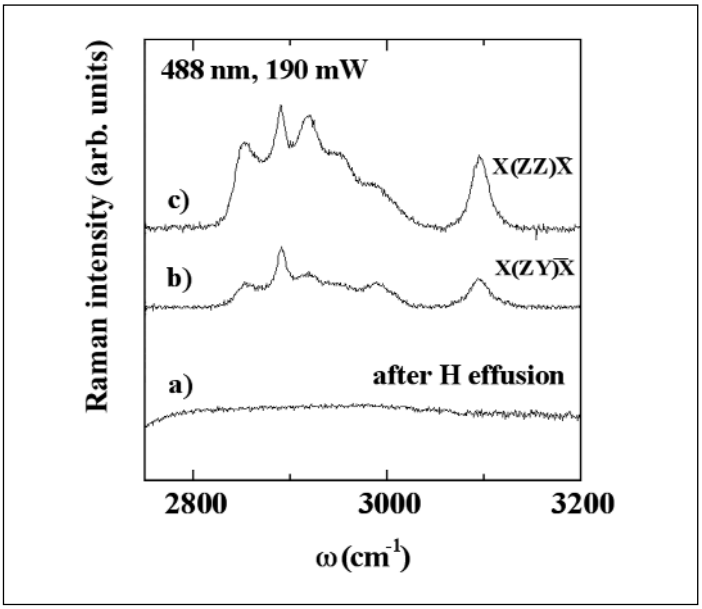

Fig. 1: Raman backscattering spectra of local vibrational modes in single crystal ZnO. Spectrum a) was measured after dehydrogenation of the sample. The spectra labeled b) and c) represent polarized Raman measurements on as-grown single crystal ZnO.

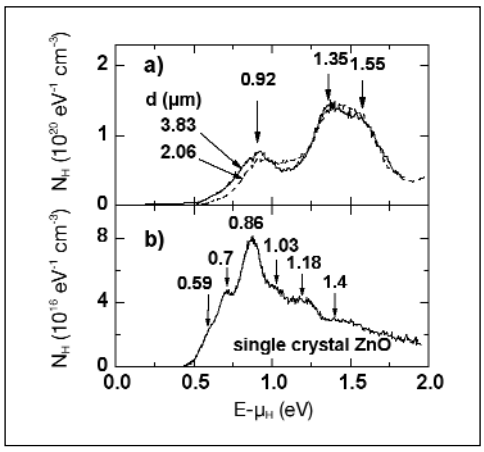

Fig. 2: H DOS in sputtered ZnO:Al (a) films and single crystal ZnO (b). The numbers along the spectra indicate the peak energies.

Electronic functionalisation of Si surfaces by thin organic layers

J. Rappich
■ HMI, SE1

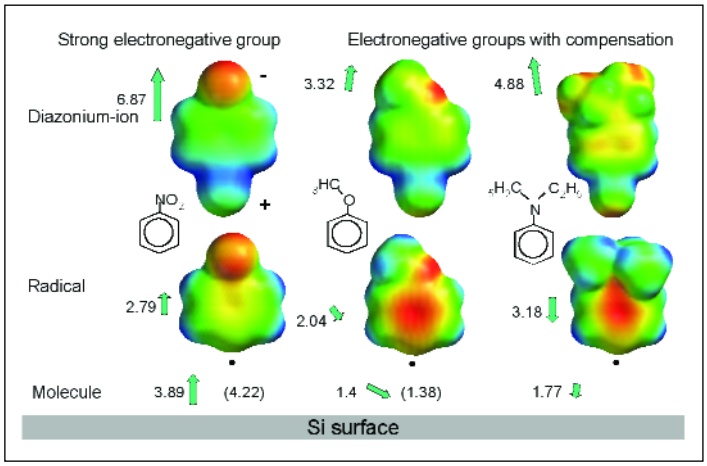

Fig. 1: Changes of the dipole strength and orientation of some organic molecules in different states (ion, radical and molecule) as calculated by DFT method (dipole strength in units of Debye, values in parenthesis are taken from literature; orientation is denoted by the arrow).

Organic materials (thin layers and polymers) become more and more important as reflected by recently developed thin film transistors, light emitting diodes (LED), and thin film solar cells, which are based on a mixture of organic polymers with C60. The great amount of possible combinations of organic groups makes them also of interest to build up especially designed buffer-layers on Si (or even on other semiconductors) to serve the following purposes:

1. Passivation of the interface to reduce recombination losses during current flow.
2. Change in band bending by surface dipoles, which induce a fixed electrical charge formed by electron donator or acceptor groups, i.e. $-CH_3$ or $-NO_2$.
3. Change in work function (i.e. band offset) of hetero structures on Si as a result of the surface dipole.
4. Formation of hydrophilic or hydrophobic surface condition for a better sticking of a deposited layer.

In order to form such organic layers on silicon we used electrochemical grafting of organic molecules on hydrogenated Si surfaces in aqueous electrolytes. The organic molecules consist of an aryl compound with a diazonium group ($^{+}{}_{2}$N-aryl-G) where G is a variable electron donor or acceptor group, which defines the orientation and strength of the dipole moment (Fig. 1).

The deposition process is performed at room temperature by applying a cathodic current to the Si electrode (electron injection into the electrolyte). Cathodic polarisation prevents the Si surface against oxidation.

In-situ photoluminescence and photovoltage, ex-situ Kelvin probe (CPD), and TEM measurements have been used to characterise changes in surface recombination velocity, band bending, work function, and interface structure. The in-situ measured change in photovoltage after and before grafting of organic molecules on the hydrogenated Si surface (ΔU_{PV}), which is identical to the change in band bending, and the ex-situ obtained work function (CPD values) are plotted in Fig. 2 against the effective dipole moment of the organic molecule perpendicular to the Si(111) surface.

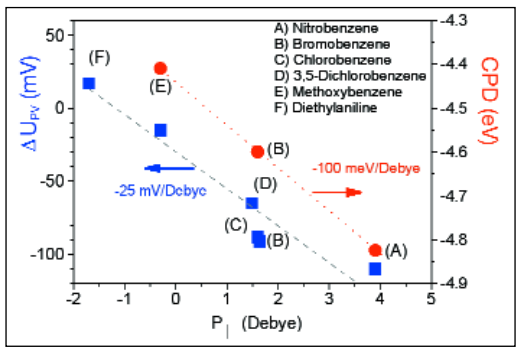

Fig. 2: Changes in band bending (ΔU_{PV}) and work function (CPD) as a function of effective dipole perpendicular to the Si(111) surface, (A to F) with the strongest and weakest electron acceptor group.

The grafting of thin layer of a diazonium compound (e.g. diethylaniline and nitrobenzene) on atomically flat p-Si(111):H surfaces induces a change of the band bending of about +20 and –110 meV, respectively. The in-situ measured band bending changes by about –25 mV/Debye. This change is lower than that measured ex-situ by SPV, indicating the screening of the effective dipole of the organic molecule by the surrounded water dipoles. In addition, the work function shifts also with the dipole moment by about –100 meV/Debye. The amount of nonradiative surface defects (N_s) increases only slightly by a factor of about 3 with respect to the perfect hydrogenated Si surface ($N_s < 10^{11} cm^{-2}$).

The electrochemical deposition of organic layers on flat n-Si(111) surface leads to the formation of a well ordered interface as observed by high resolution transmission electron microscopy images (HRTEM), see Fig. 3. Therefore, the changes in band bending is highest on flat surfaces and is less pronounced when a rough Si surface (the dipoles are no longer regularly ordered at the surface) or even a thin oxide covered Si surface is used for the deposition process [1–4].

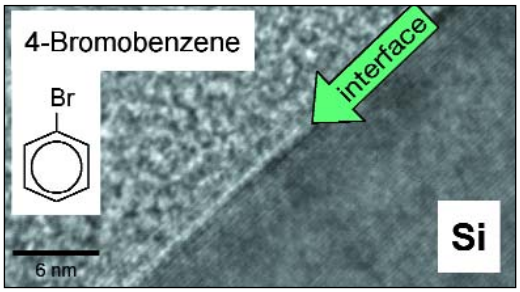

Fig. 3: HRTEM of an organic layer on n-Si(111), the arrow denotes the interface position.

Fig. 4 compares the N_{1s} NEXAFS spectra [5] obtained at flat n-Si(111) surfaces after electrochemical deposition of 4-nitrobenzene for 10 and 100 s. The broad NEXAFS spectrum after 10 s of deposition time is dominated by the σ* resonance of nitrogen at about 405 eV. Besides the broad spectrum of the σ* resonance, two narrow peaks of the π* resonance appear around 393 and 397 eV after 100 s of deposition time. The stronger resonance at 397 eV can be seen as a shoulder also after the deposition time of 10 s.

The broad peak of the σ* resonance can be assigned to nitrogen bounded to carbon and/ or oxygen. The appearance of the π* resonance is equivalent to the formation of *N=N* bonds which can arise during electrochemical polymerization of nitrobenzene.

These results show that thin organic layers can be electrochemically deposited onto Si surfaces. These organic layers are able to passivate the interface and to influence the band bending and work function of Si which is induced by charge transfer via the formed Si-C bond. The change in work function was about 100 meV per Debye. Too long electrodeposition should be avoided due to polymerization of the diazonium compound.

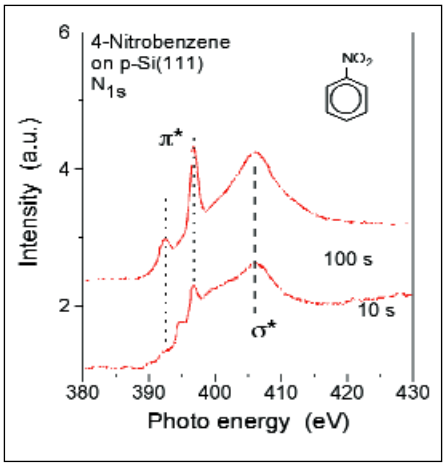

Fig. 4: N_{1s} NEXAFS spectra obtained at flat n-Si(111) surfaces after electrochemical deposition of 4-nitrobenzene for 10 and 100 s.

The next step will be the formation of electrical contacts upon these layers and to investigate these contacts in more details, even in use as hetero structure solar cells.

[1] P. Hartig, J. Rappich, and Th. Dittrich, *Engineering of Si surfaces by electrochemical grafting of p-nitrobenzene molecules*, Appl. Phys. Lett., **80**(1), 67–69 (2002)

[2] P. Hartig, Th. Dittrich, and J. Rappich, *Surface dipole formation and nonradiative recombination at p-Si(111) surfaces during electrochemical deposition of organic layers*, J. Electroanal. Chem., **524–525**, 120–126 (2002)

[3] P. Hartig, Th. Dittrich, J. Rappich, Patentanmeldung 101 30 801.9; *Verfahren zur Funktionalisierung und Passivierung der Oberfläche von Silizium-Wafern durch elektrochemische Abscheidung dünner organischer Schichten*,

[4] P. Hartig, J. Rappich, M. Portwich, R. Volkmer-Engert, Patentanmeldung 103 34 096.3; *Verfahren zum Herstellen einer Anordnung mit mehreren Schichten auf Basis eines Halbleitersubstrates und Mehrschichtanordnung*

[5] D.R. Batchelor, P.R. Bressler, P. Hartig, J. Rappich, Th. Dittrich, *NEXAFS and photoemission investigation of electrochemically deposited organic layers on p-Si(111)*; Bessy Annual Report 2001.

Do we really need another photoluminescence study on $CuInSe_2$?

S. Siebentritt, N. Rega, J. Albert, A. Zajogin
■ HMI, SE2

They have been performed since the seventies! Yes, we do. Here is the problem: good solar cells with efficiencies up to 19.2 % can be made from $Cu(In,Ga)Se_2$ with a low content in Ga, i.e. with low band gaps. To prepare thin film tandem solar cells we need $CuGaSe_2$ solar cells with an efficiency of at least 15 %. Nobody in the world makes $CuGaSe_2$ solar cells with an efficiency of even 10 %. The question is, is there a fundamental difference between the absorber materials $CuInSe_2$ and $CuGaSe_2$? Our approach is to investigate the defect spectra of these materials by photoluminescence (PL). Our previous study on $CuGaSe_2$ has already shown that the doping defects are represented by two acceptors and a shallow donor, that their relative concentrations depend on the composition. And that due to the high degree of compensation in Cu-poor material the observed emissions at lower energies are not due to new defects but due to potential fluctuations.

Can't we just compare this result to the literature data for $CuInSe_2$ and find out, if there are differences in the defect spectra? No, we can't. First of all, literature data is contradicting, no consensus has been found yet on the defects in CIS. Then, the defect spectrum is dependent on the composition. If this information is not given it is difficult to compare the spectra. And finally, to exclude differences due to different preparation methods, only spectra from $CuInSe_2$ and $CuGaSe_2$ prepared by the same method can be directly compared. There are very few studies that take all this into account. They do not agree with each other, nor with our results on $CuGaSe_2$ (although their measurement results can be explained within the frame of our model). Generally they find one acceptor less in $CuGaSe_2$ than in $CuInSe_2$.

In addition, the few studies on the luminescence of $Cu(In,Ga)Se_2$ with varying Ga content have not obtained any information on defects, they just observe that the spectra shift with the band gap.

This is where our PL investigations come in. We have $CuInSe_2$, $Cu(In,Ga)Se_2$ and $CuGaSe_2$ prepared by the same MOVPE process. We have epitaxial films without the influence of grain boundaries. We have already a detailed study on the PL of $CuGaSe_2$.

Therefore a composition, temperature and intensity dependent study of the PL of $CuInSe_2$ was performed. The figure compares the PL spectra of $CuGaSe_2$ and $CuInSe_2$ obtained for different [Cu]/[In] or [Cu]/[Ga] ratios. The shape of the spectra and their composition dependence look very similar. A detailed temperature and intensity dependent study of the $CuInSe_2$ shows that the defect spectrum of $CuInSe_2$, as of $CuGaSe_2$ consists of two acceptors and a shallow donor. They are somewhat shallower than those in $CuGaSe_2$: at 40 and 60 meV from the valence band edge and about 10 meV from the conduction band edge.

The next step is to investigate the PL spectra of $Cu(In,Ga)Se_2$ for varying Ga content. Since for Ga ratios around 80 % the $Cu(In,Ga)Se_2$ luminescence overlaps with the luminescence from the GaAs substrate, the PL measurements are supplemented by spatially resolved cathodoluminescence spectra. We find for the first time excitonic luminescence for $Cu(In,Ga)Se_2$ with a Ga ratio below 30 % or above 70 %. The defect related luminescence broadens considerably for a Ga ratio between 30 and 70 % due to disorder effects between Ga and In sites. Defect energies are extracted from temperature dependent measurements, they are compatible with a linear variation between the defect energies in $CuInSe_2$ and $CuGaSe_2$.

Therefore it is concluded that no fundamental difference concerning the defect spectra exists within the $Cu(In,Ga)Se_2$ system. Thus it is not due to the defect spectrum that solar cells made of $CuGaSe_2$ absorbers show lower efficiencies and the chance for their improvement exists.

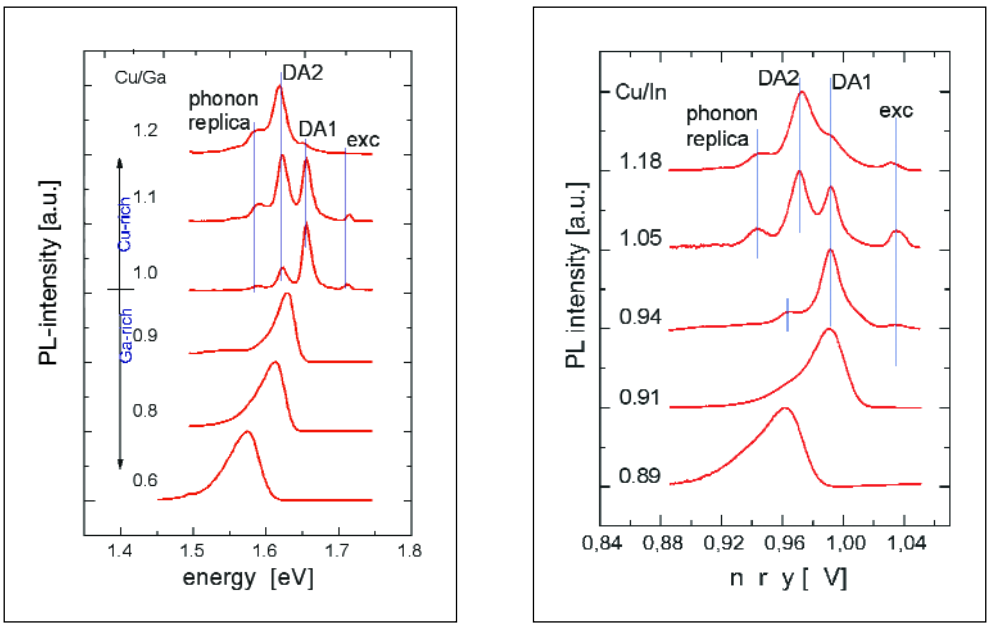

Fig. 1: PL spectra of $CuGaSe_2$ (left) and $CuInSe_2$ (right) as a function of the [Cu]/[III] ratio

A novel approach to chalcopyrite-based heterojunctions

R. Klenk, Th. Glatzel, A. Grimm, H. Steigert, I. Lauermann
■ HMI, SE2

A typical chalcopyrite-based solar module consists of five thin films deposited sequentially onto a glass substrate: a metallic back contact (molybdenum), absorber (chalcopyrite), buffer layer (CdS), window layer 1 (ZnO) and window layer 2 (ZnO:Al). Depending on the manufacturing technology additional films are added, acting as diffusion blockers or sodium source. Optimisation of production cost and yield demands a reduction in the number of processes.

Elimination of the buffer layer appears particularly attractive because its preparation requires the handling of cadmium-containing raw materials and waste. Furthermore, this film is the only one to be deposited by wet chemistry which prevents completely dry in-line manufacturing of the module.

Previous models ascribed the importance of the CdS buffer layer to the matching of lattice constants and to the prevention of sputter damage during window layer deposition. However, numerical calculations show that a very high density of defects at the heterointerface can be tolerated if certain conditions are met [1]. They include the alignment of the conduction band and the net electrical charge within the defect distribution (Fig. 1). If the buffer layer is omitted, the window layer 1 defines the pn-junction (hetero interface) and has to be modified to meet the cited requirements. Literature data [2] and theoretical considerations indicated a promising approach in which ZnO is replaced by (Zn,Mg)O. Accordingly, the goal has been to reach high efficiency with a modified solar cell where the buffer layer was omitted and the ZnO replaced by (Zn,Mg)O.

Results of structural and optical characterisation show that single phase (Zn,Mg)O films with Mg/Zn ratios of 0.15 and 0.3 can been prepared by sputtering from a single mixed target allowing straightforward integration into existing production lines. The solar cell efficiency without buffer layer increased from 6 % (ZnO) to values around 10 % for $Zn_{0.85}Mg_{0.15}O$ and reached 12.5 % after optimisation with $Zn_{0.7}Mg_{0.3}O$, the latter value being comparable to the efficiency of reference cells with buffer layer. Current transport analysis indicates that recombination at the heterointerface does indeed not contribute significantly to the diode current in optimised cells with or without buffer layer.

Formation of the direct chalcopyrite/window interface has been investigated by synchrotron-excited photo electron spectroscopy. Oxidation of the chalcopyrite surface is detected during the initial stage of window layer growth (Fig. 2). Contrary to our initial assumption that the more stable MgO releases less oxygen, thereby preserving the crucial positive interface charge, no significant differences between ZnO and (Zn,Mg)O could be found so far with respect to chalcopyrite oxidation.

Reproducibility of cell results was good as long as a certain type of absorber from the Shell-Solar pilot production had been used ($Cu(In,Ga)(Se,S)_2$, CIGSSe). The properties of the chalcopyrite absorber surface are more critical in the novel structure. Hence, future work shall focus on making the structure applicable to a wider range of absorbers, in particular wide-gap chalcopyrites. Understanding the interface formation and relating it to the electronic models is considered essential for achieving this goal.

[1] R. Klenk, Thin Solid Films **387**, 135–140 (2001).
[2] T.Minemoto, T.Negami, S.Nishiwaki, H.Takakura, Y.Hamakawa, Thin Solid Films **372**, 173–176 (2000).

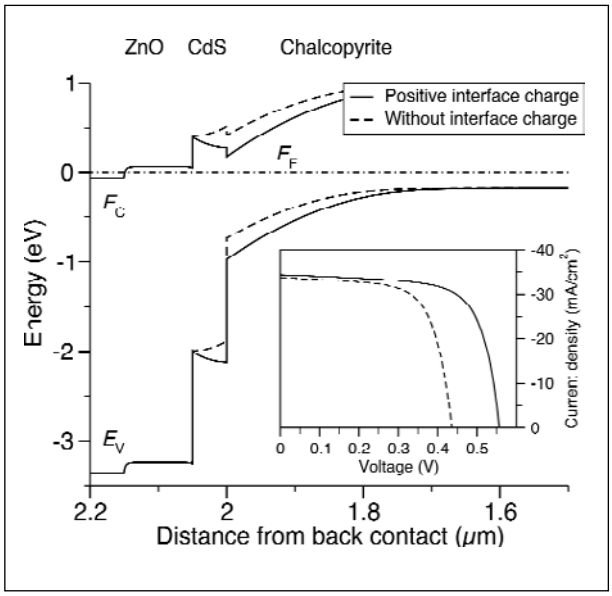

Fig. 1: Calculated band diagrams of chalcopyrite-based heterojunctions with positive and without any interface charge. The inset shows the corresponding jV characteristics. Note the loss in device performance in the absence of positive interface charge.

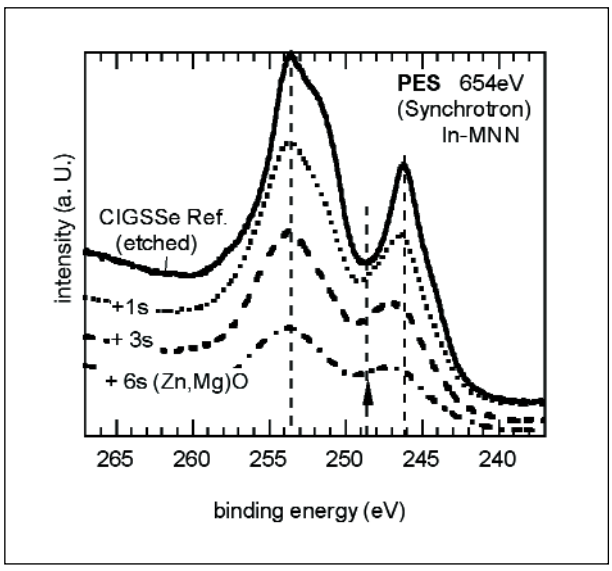

Fig. 2: Photoelectron spectra in the range of the In-MNN Auger electron. Compared to the spectrum of the clean chalcopyrite (CIGSSe), the local minimum shifts to higher energy and the shape of the main peak changes with deposition of (Zn,Mg)O, indicating oxidation of the Indium.

Novel approaches to the “lift-off” technology

S. Doka[1], D. Fuertes Marrón[1], K. Höhn[1], S. Lindner[1], A. Meeder[1], T. Münchenberg[1], M. Rusu[1], S. Wiesner[1], R. Würz[1], Th. Schedel-Niedrig[1], M. Ch. Lux-Steiner[1], K. Lips[2], W. Fritsch[3], H. Bluhm[4], M. Hävecker[4], A. Knop-Gericke[4], R. Schlögl[4]

■ 1 HMI, SE2 ■ 2 HMI, SE1 ■ 3 HMI, SF5 ■ 4 Fritz-Haber-Institut der MPG, Berlin

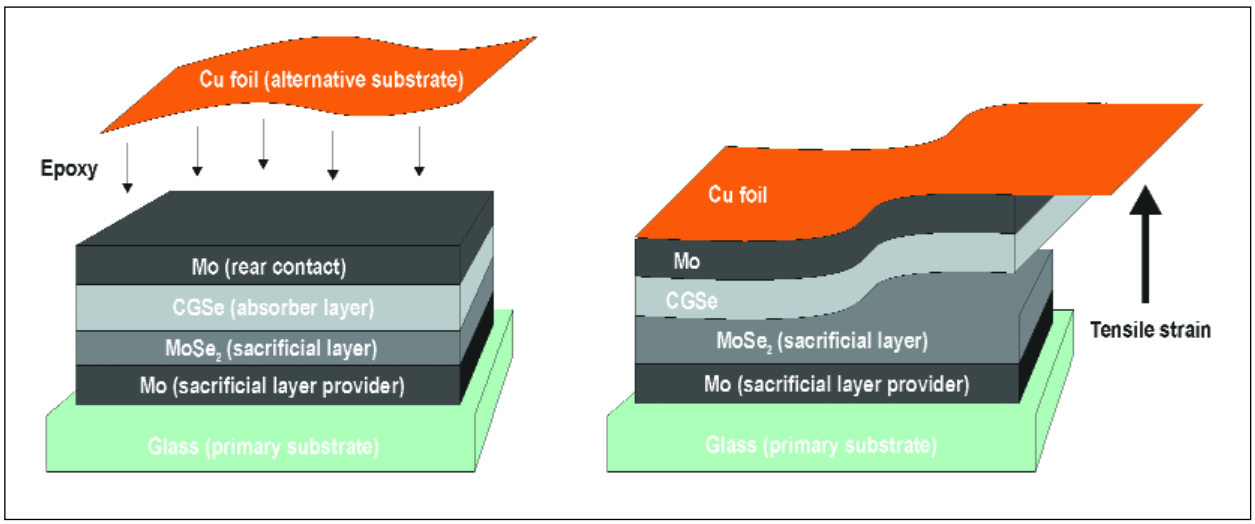

Fig. 1: Schematic view of the mechanical lift-off process proposed to transfer the thin-film $CuGaSe_2$ active layer to metallic foils.

The “lift-off” technique

The simultaneous formation of the layered chalcogenide $MoSe_2$ film between the Mo-rear contact and the absorber film during the CVD-growth of $CuGaSe_2$ thin films suggested a new approach to the lift-off process [1], which can be readily applied to these samples directly after the deposition process (Fig.1). Furthermore, no additional step is required in order to provide the sacrificial layer, as long as the $MoSe_2$ layer playing that role develops itself during the process. Indeed, the characteristic morphology, as revealed by TEM and XRD analysis [2], of the layers forming the $MoSe_2$ is nearly ideal for easily lifting the absorber layer off mechanically from its original Mo-coated glass substrate. The cleanness (i.e. absence of substrate remnants on the absorber rear surface) was checked out by means of surface-sensitive techniques KPFM and XPS/UPS. First test devices on alternative substrates have been prepared (Fig. 2).

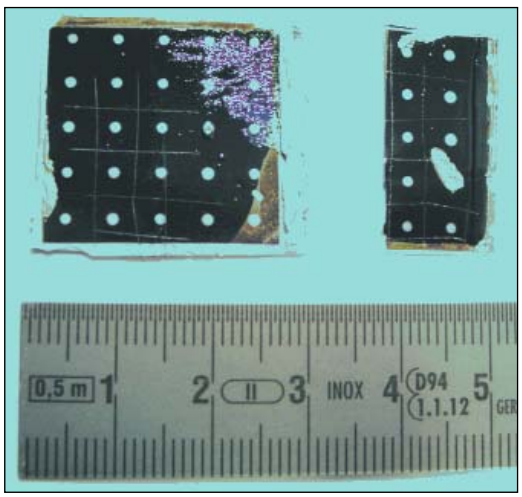

Fig. 2: $CuGaSe_2$-based solar cells transferred onto flexible metal foils by means of a new lift-off process.

"Lifted-off" thin films for EPR-investigations: An oxidation study of $CuGaSe_2$

The special bent structure of the interfacial $MoSe_2$ layer [3] permits a lifting-off of $CuGaSe_2$ thin films from the substrate simply by using adhesive tape (TESA©). X-ray fluorescence spectroscopy (XRF) doesn't reveal remnants of Mo on the backside of the lifted-off $CuGaSe_2$ film and also no traces of Ga or Cu on the substrate side are observed. Since the adhesive tape is Electron paramagnetic resonance (EPR) silent, EPR measurements on $CuGaSe_2$ thin films are therefore possible without any disturbing background signals from the substrate. The signal-to-noise ratio is enhanced by means of rolling up the film on the adhesive tape and placing it in quartz tube.

EPR measurements of $CuGaSe_2$ oxidized in air showed a broad Cu^{2+} signal (Fig. 3) [4]. It could be reduced to EPR silent Cu^{+} by annealing in He atmosphere. Chemical etching with KCN removed this signal. In order to get insight into the chemical bonding state of the Cu^{2+} and the reaction pathway to non paramagnetic Cu^{+} we performed core-level photoemission (XPS) on thin oxidized films. The formation of predominantly Ga_2O_3 and some amount of SeO_2 has been found at the surface-/near surface region after short term oxidation time for less than 4 month. Only after a long term oxidation process also $Cu^{2+}(OH)^{-}_2$ was found (Fig. 4). This $Cu^{2+}(OH)^{-}_2$ phase was reduced to $Cu^{+}_2O^{2-}$ by vacuum annealing. Etching of the films in KCN removes the oxide phase. We therefore conclude that the EPR Cu^{2+} signal originates from a $Cu^{2+}(OH)^{-}_2$ phase at the surface-/near surface region of the film.

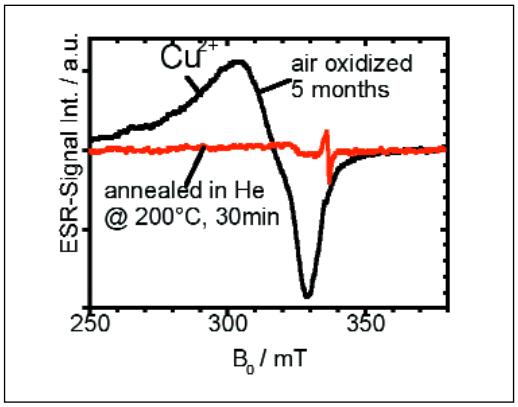

Fig. 3: EPR spectra of a $CuGaSe_2$ thin film

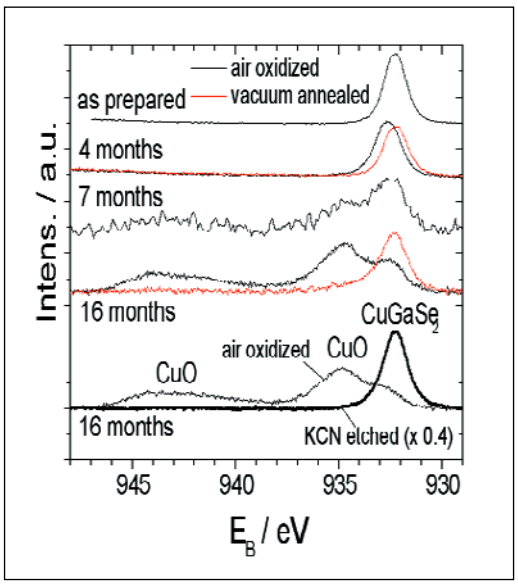

Fig. 4: Cu2p-photoemission spectra of oxidized thin films

[1] D. Fuertes Marrón, A. Meeder, Th. Schedel-Niedrig, R. Würz, M. Ch. Lux-Steiner, *Deutsches Patent für das Hahn-Meitner-Institut Berlin GmbH*, Deutsches Patent Nr. 102 47 735.B3, AT: 09.10.02, Patenterteilung: 15.04.04

[2] D. Fuertes Marrón, A. Meeder, U. Bloeck, P. Schubert-Bischoff, N. Pfänder, R. Würz, S.M. Babu,Th. Schedel-Niedrig, M. Ch. Lux-Steiner Thin Solid Films **431–432**, 237–241 (2003).

[3] R. Würz, D. Fuertes Marrón, A. Meeder, A. Rumberg, S.M. Babu, Th. Schedel-Niedrig, P. Schubert-Bischoff, U. Bloeck, M. Ch. Lux-Steiner Thin Solid Films **431–432**, 398–402 (2003).

[4] R. Würz, K. Lips, et al., Phys. Rev. B (submitted)

Understanding of the ILGAR-WEL/CIGSSe interface

Ch.-H. Fischer[1], M. Bär[1], H.-J. Muffler[1], N. Allsop[1], C. Chapus[1], M.C. Lux-Steiner[1], S. Sadewasser[1], T. Glatzel[1], C. Kelch[1], M. Kirsch[1], L. Weinhardt[2], C. Heske[2], E. Umbach[2], F. Karg[3], T. P. Niesen[3]
■ 1 HMI, SE2 ■ 2 Universität Würzburg, Experiment. Physik 2 ■ 3 Shell Solar GmbH, München

The main goal of the project is the further progress in chemical low-cost deposition methods for semiconductor thin layers, mainly the ILGAR process (Ion Layer Gas Reaction, patents by HMI). The Window Extension Layer Concept (WEL) allows the combination of buffer and intrinsic part of the window in one ILGAR-ZnO layer, i.e. one sputter step can be omitted.

Cells with ILGAR-ZnO WELs yield efficiencies (14.6 %) comparable to those with CBD-CdS (14.8 %) only on CIGSSe absorbers treated with Cd^{2+}/NH_3. To improve the WEL cell performance and to make the device completely Cd-free, the interface modifications induced by the treatment have to be understood. Our earlier studies showing the purification effects of such a treatment, have been continued. In the X-ray emission spectrum of treated absorbers about a monolayer CdS could be identified by careful correction for the excess of CIGSSe (Fig. 1, spectra d and e). SEM plan views show no great difference between the bare and treated absorber surfaces (Fig. 2a, b). But on a bare surface the ILGAR-ZnO crystals are loosely arranged on the absorber facets, whereas the treated absorber surface acts as a seed layer and lets ZnO grow as a compact film consisting of very small crystallites and a few isolated larger particles (Fig. 2c, d). HRTEM images of cross-sections of both ZnO/CIGSSe samples confirm this difference in the nm-size regime (not shown here).

Kelvin probe force microscopy revealed a reduced local work function for the treated CIGSSe either due to a shift of the Fermi level towards the conduction band or due to a reduction in electron affinity. A distinction was possible by the combination of UV-photoelectron- (UPS) and inverse photoelectron spectroscopy (IPES) probing occupied and unoccupied states, respectively. The results for CIGSSe after various treatments led to the scheme of band positions in Fig. 3.

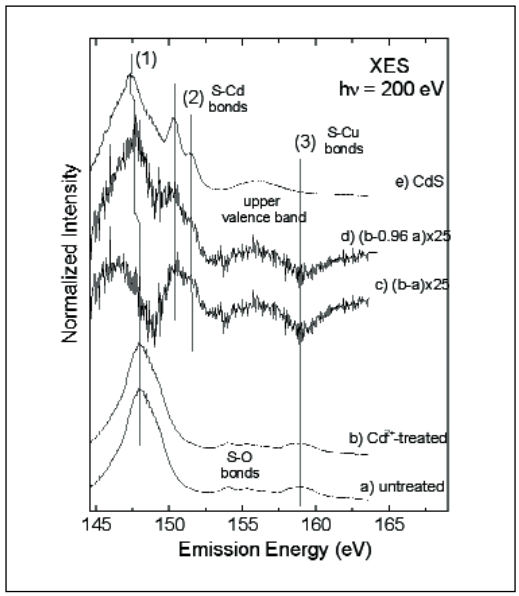

Fig. 1: S $L_{2,3}$ XES spectra of untreated and Cd^+ treated CIGSSe absorbers, difference spectra and CdS spectrum for comparison.

Only a few features can be stressed here:
- Fermi level shift towards conduction band by 0.4 eV after Cd^{2+}/ NH_3 treatment.
- Band gap energy of untreated absorber 0.5 eV higher than for Cd^{2+}/ NH_3 treated and sputtered one due to surface contaminations.
- Valence band maximum similar before and after Cd^{2+}/ NH_3 treatment (1.00/1.10).
- Absorber surfaces are *n*-type (band bending! stronger for the Cd^{2+}/ NH_3 than for the NH_3 treated one). Possible explanations: Cd^{2+} on Cu^{+} vacancies or a CdS cover layer.
- Effect on band alignment of complete ILGAR-ZnO-WEL device: Change from spike to cliff at absorber/WEL interface due to Cd^{2+}/ NH_3 treatment, therefore less recombination.

These effects on electronic properties, chemical composition, morphology and their influence on the growth of the ZnO-WEL explain the tremendous efficiency increase in the final solar cell by approx. one third when treated absorbers are used. Based on this knowledge a replacement of the Cd^{2+} in the treatment seems feasible.

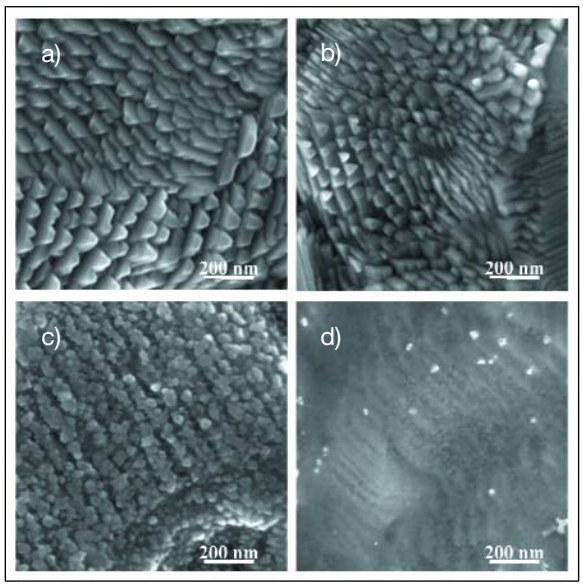

Fig. 2: SEM plan view of bare a) and Cd^{2+}/ NH_3 treated b) absorber as well as of ILGAR-ZnO on top of untreated c) and Cd^{2+}/ NH_3 treated d) CIGSSe.

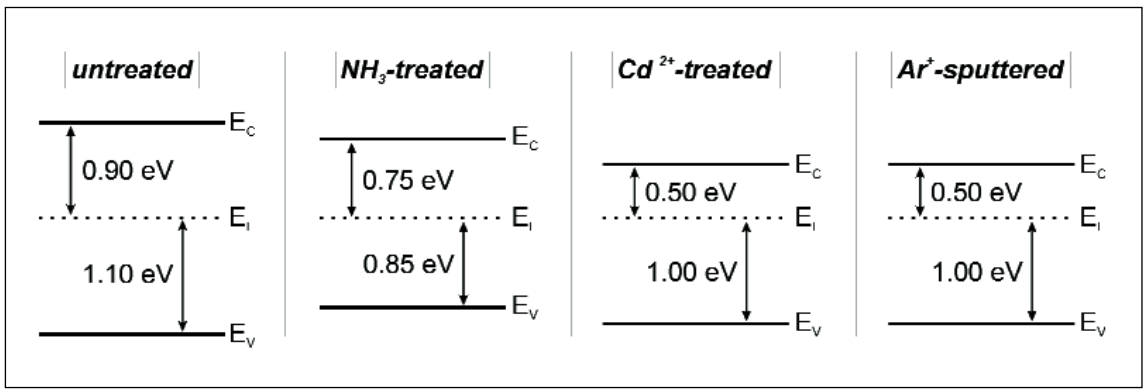

Fig. 3: Schematic band edge positions of an untreated, NH_3 and Cd^{2+}/ NH_3 treated as well as sputtered CIGSSe surface (from left to right).

Over 11 % efficient ZnS/CIGSSe thin film solar cells without undoped ZnO

A. Ennaoui, S. Sartale, B. Sankapal, T. Kropp, M. Lux Steiner
■ HMI, SE2

Goal: The objective of this research is to identify, explore, evaluate, and develop a non-vacuum process capable of making a breakthrough in the production of low cost thin-film chalcopyrite solar cells. This includes robust processing compatible with Cd-free $Cu(In,Ga)SSe_2$ (CIGSSe) thin film solar cells. To date chalcopyrite thin film emerging technology is based on CdS as a buffer layer. Elimination of CdS layer has the potential benefits of improved carrier collection in the shorter wavelength portion of the spectrum as well as reduced manufacturing waste. The present focus is on a new chemical method, of producing thick films consisting of ZnS-clusters. We adopted a coordination chemistry method to grow ZnS from colloids. The process labelled ZnS-Colloid Based Materials (ZnS-CBMs) is more efficient and cost-effective. Furthermore in contrast to standard chemical bath deposited ZnS (CBD-ZnS) presented in our previous reports [1]; there is no need to complex the Zn-cation with N_2H_2, which is highly toxic. The structure of ZnS layers is found to be of sphalerite (tetrahedrally coordinated cubic ZnS) along (111) directions.

Device performance: A series of CIGSSe devices was fabricated where the CdS layer was replaced by the new chemically deposited ZnS-CBMs. Solar cells in this study were fabricated with production scale absorbers made at Shell Solar Munich. Highly doped sputtered Ga:ZnO was directly sputtered onto CIGSSe/ZnS surface without need of undoped ZnO. Fig. 1 shows SEM (cross section) of the ZnO/ZnS/CIGSSe device structure. The conformal coverage of the absorber is obvious and the thickness of ZnS-CBMs was estimated to be around 30 nm. Fig. 2 shows the output characteristic of the solar cell. The best solar cell with ZnS-CBMs is compared in efficiency to the CdS reference device (table 1). The outcome of main interest in this work is that there is no need to have undoped ZnO and devices show low performance and greater crossover between light and dark JV curves in their as-deposited state than for devices after heating and soaking. The highest performance is obtained after annealing in Argon atmosphere at 200°C and light soaking at 25°C for 40 min.

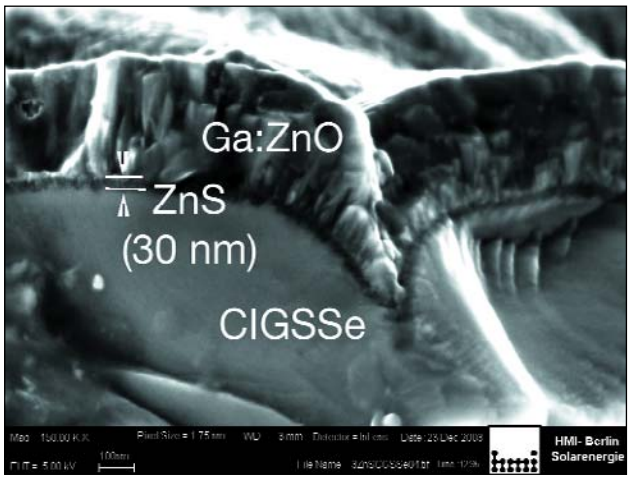

Fig. 1: Scanning Electron Micrographs (Cross section) of the Ga:ZnO/ZnS/CIGSSe structure

With the new ZnS-CBMs the light soaking effect is rather strong. The reason for this strong effect after annealing and light soaking requires further investigation. Ongoing work will investigate this issue.

Conclusion: A new strategy has been used to develop a robust process for Cd-free CIGSSe solar cells. We adopted a coordination chemistry method to grow ZnS colloids instead of using a standard CBD with highly toxic complexing agents. Obviously ZnS-CBMs process has competitive performance compared to cells made with a CdS layer and the undoped ZnO layers in CIGSSe devices is not essential. Device efficiency over 11 % was found by eliminating CdS and undoped ZnO.

[1] Ennaoui, A.; Eisele, W.; Lux-Steiner, M.; Niesen, T.P.; Karg, F., *Highly efficient Cu(Ga,In)(S,Se)$_2$ thin film solar cells with Zinc-compound buffer layers*, Thin Solid Films **431–432**, 335–339 (2003).

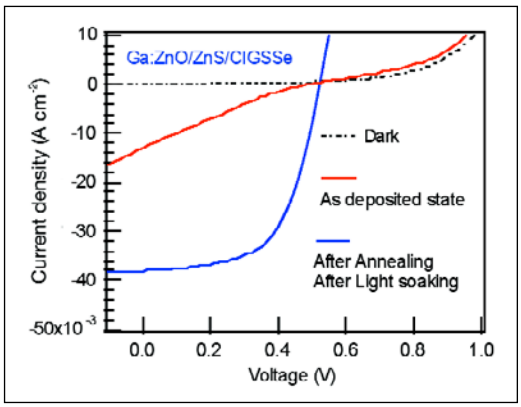

Fig. 2: J-V characteristics of the ZnS/CIGSSe thin film-based solar cell without the undoped ZnO.

Barrier	V_{oc} [mV]	J_{sc} [mA/cm^2]	FF	η [%]
Cds ref.	530	33.1	62.7	11.0
ZnS no-ALS	490	12.9	22	1.41
ZnS ALS	522.45	38	58.7	11.69

Table 1: PV parameters of CIGSSe solar cells. With CdS (ref.), before annealing and light soaking (no-ALS), after annealing and light soaking (ALS)

Coherent manipulation of well-defined electron spins in solid state

C. Meyer[1], W. Harneit[1], B. Naydenov[1], K. Lips[2], A. Weidinger[1]
■ 1 HMI, SE2 ■ 2 HMI, SE1

The size of electronic devices decreases steadily. Current research aims at devices built upon small structures or even single molecules making use of quantum mechanical properties, e.g. spins. In our group we want to make use of the spin dynamics of the endohedral fullerenes $N@C_{60}$ and $P@C_{60}$ in molecular spin electronic devices such as a quantum computer. Because the C_{60} fullerene shields the endohedral nitrogen or phosphorus atom from the environment, these molecules have exceptional spin properties, e.g. long electron spin relaxation times [1].

The cross-section of a fullerene with a group V endohedral atom is shown schematically in Fig. 1. The atom resides at the centre without any bonding to the fullerene molecule. The valence electrons of the half-filled p-shell couple to a spin $S = 3/2$. Using a solid-state ensemble of these molecules, the net-magnetisation can be measured and manipulated with pulsed electron spin resonance (ESR).

In a transient nutation experiment, the spins are rotated by a well defined angle depending on the pulse length t_p of the first pulse shown in Fig. 2. The detection is done in the x,y-plane, thus, a second pulse is needed for the readout. If the spin states "up" and "down" are taken as logic "true" and "false" (or 1 and 0), a $180°$ pulse changes the information from 1 to 0 and vice versa, thus performing a NOT operation.

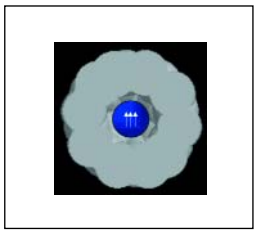

Fig. 1: Schematic cross-section of a fullerene. The Van der Waals radii are shown for the carbon atoms. The three valence electrons of the encapsulated nitrogen or phosphorous couple to a total spin $S = 3/2$.

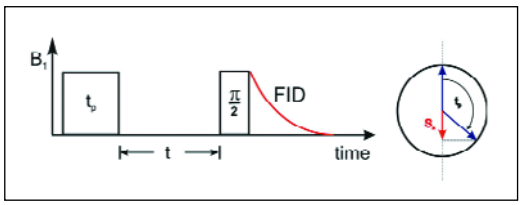

Fig. 2: ESR pulse sequence of a transient nutation experiment. The microwave field B_1 is applied perpendicular to the external field B_0. The spins are rotated by a certain angle depending on the pulse length t_p of the nutation pulse. The S_z component of the spins is rotated into the measurement plane by a $\pi/2$-pulse.

For strong fields B_1, the spins of the endohedral fullerenes behave like an $S = 1/2$ system. In Fig. 3 we show the transient nutation signal for $P@C_{60}$ (a) and $N@C_{60}$ (b) powder samples. For better illustration the data have been multiplied with an exponential function so that decay due to spin-spin relaxation is not visible. The experiment has been carried out at room temperature and is a good illustration for the exceptionally long spin lifetimes. Up to 50 (30) coherent oscillations can be measured for $N@C_{60}$ ($P@C_{60}$).

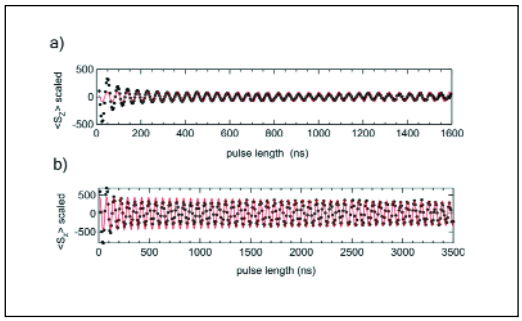

Fig. 3: Data (black) and fit (red) of the transient nutation experiment with a) $P@C_{60}$ and b) $N@C_{60}$.

For $P@C_{60}$ it is possible to excite the (1/2,–1/2) transition and the (±3/2,±1/2) transitions separately at low temperatures. If the B_1 field is sufficiently small (much smaller than the zero-field-splitting $D \sim 6$ G), the transitions will rotate with different frequencies, due to the different transition elements in the S_+ operator for a 3/2-spin.

As can be seen from equation (1) the expected

$$S_+ = \begin{pmatrix} 0 & \sqrt{3} & 0 & 0 \\ 0 & 0 & 2 & 0 \\ 0 & 0 & 0 & \sqrt{3} \\ 0 & 0 & 0 & 0 \end{pmatrix}$$

ratio of the nutation frequency of the (1/2,–1/2) transition and the (±3/2,±1/2) transitions is $2/\sqrt{3}$.

The nutation experiment at $T = 10$ K shown in fig. 4 clearly reveals this ratio. We thus could demonstrate that we have full control over the $S = 3/2$ spin system.

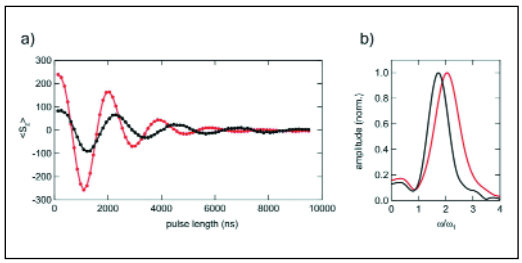

Fig. 4: a) Transient nutation of a $P@C_{60}$ powder sample at $T = 10$ K. The read line shows the the (1/2,–1/2) transition while the black line shows the (3/2,1/2) transition. b) The Fourier transform of the transient nutation signal clearly reveals the different frequencies.

[1] T. Almeida Murphy, T. Pawlik, A. Weidinger, M. Höhne, R. Alcala, J.-M. Spaeth, Phys. Rev. Lett. **77**, 1075 (1996).

$CuAlO_2$ prepared from $LiAlO_2$ by ion exchange reaction

L. Dloczik[1], Th. Dittrich[1], T. Guminskaya[1], N. Grigorieva[1], M. Ch. Lux-Steiner[1], Y. Tomm[2] in cooperation with I. Urban[3]
■ 1 HMI, SE2 ■ 2 HMI, SE5 ■ 3 BAM

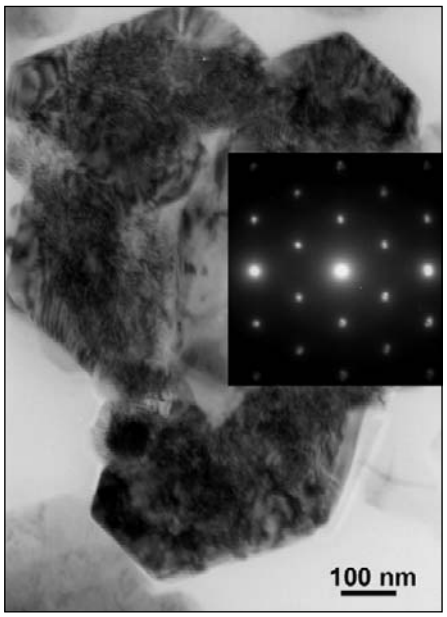

Fig. 1: Micrograph crystallites and electron diffraction pattern of $CuAlO_2$ obtained from $LiAlO_2$.

The delafossite phase of $CuAlO_2$ is a promising inorganic transparent hole conductor with a band gap of about 3.5 eV. However, there are only few and high temperature technologies available to prepare $CuAlO_2$. We showed that $LiAlO_2$ can be used as a precursor to produce $CuAlO_2$ by an ion exchange reaction at moderate temperatures [1].

The mobile Li-ions in the α-$LiAlO_2$ phase are exchanged by copper ions. This is possible because both phases have the same rhombohedral lattice structure (R3m) of layered M-O-Al-O (M corresponds to Li or Cu) and because Al-O bonds are very stable.

For the preparation, a powder of α-$LiAlO_2$ and the double molar amount of CuCl was placed into a glassy carbon boat and heated for several hours in a sealed quartz tube under high vacuum at temperatures around 400 – 500°C. The by-product LiCl and remaining CuCl were washed out and the reaction product was analyzed by electron microscopy, x-ray diffraction, reflectance spectroscopy and photovoltage spectroscopy.

Figure 1 shows small crystallites of $CuAlO_2$ which are formed after ion exchange at 475°C. A photovoltage spectrum of a layer consisting of small $CuAlO_2$ crystallites is presented in Figure 2. The photovoltage response was characteristic for *p*-type semiconductors. The band gap is 3.54 eV and the energy of the exponential states is 50 meV at room temperature. This and the absence of deep states in the forbidden gap demonstrate the high quality of the prepared $CuAlO_2$.

The obtained $CuAlO_2$ crystallites are very stable in air and vacuum. They have been covered by different absorber layers. It has been shown that hole injection takes place from dye molecules into $CuAlO_2$ under illumination. An important challenge is now to find methods for further technological processing of the $CuAlO_2$ crystallites for various applications.

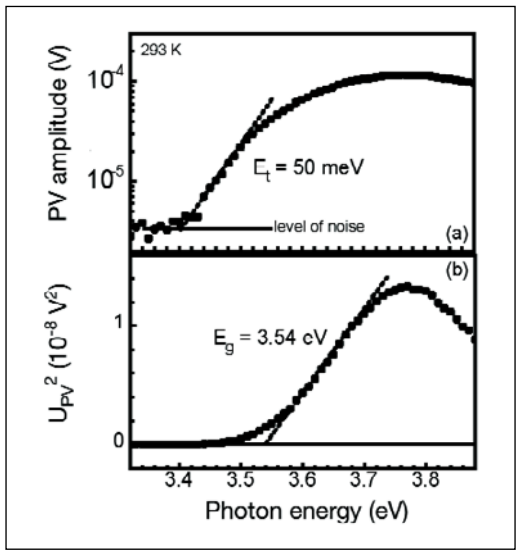

Fig. 2: Photovoltage spectra of a layer of small $CuAlO_2$ crystallites.

[1] L. Dloczik, Y. Tomm, Th. Dittrich, M. Ch. Lux-Steiner, *Verfahren zur Herstellung von $CuAlO_2$ unterhalb von 500°C durch Kristallstrukturkonforme Austauschreaktion*, Patent, pending

Vertical nanowire field effect transistor in flexible template

J. Chen[1], R. Könenkamp[1], S. Klaumünzer[2]
■ 1 HMI, SE2 ■ 2 HMI, SF4

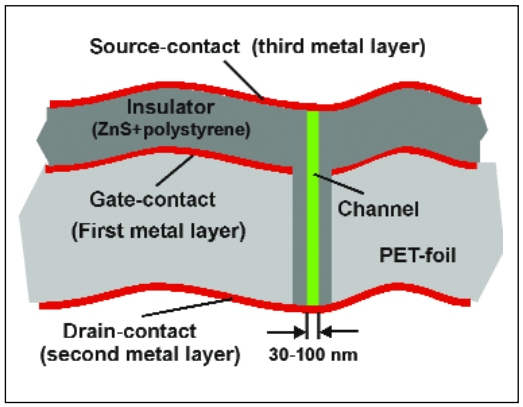

Fig. 1: Structure of a vertical nano-wire transistor

The fabrication of nanowire transistors has spurred considerable activity in material science, nanotechnology and in logic architectures. One approach to attain these goals is based on the use of hybrid structures combining the flexibility of organic materials as substrates with the device functions of inorganic semiconductors. To take full advantage of the small dimensions of nanowire devices, a vertical orientation is, however, more desirable, since in the vertical geometry packing densities up to 10^{10} cm^{-2} appear feasible. A stacking of vertical transistor layer may even lead to higher densities. Eventually reconfigurable architectures will allow a large degree of randomness in densely packed structures, thereby opening the possibility that these device structures may also be used in logic applications.

A vertical device structure with a packing density of ~10^{7} cm^{-2} recently has been realized by us [1], but the fabrication scheme and the observed large gate leakage current, limited the usefulness of this first experimental approach. However we have succeeded in fabrication of improved version of vertical nanowire transistors in flexible template. The device structure is illustrated in Fig. 1. The new device is also more robust and exhibits a strongly reduced gate leakage current. Similar to our earlier design the fabrication involves a sequential deposition of metal, insulator and semiconductor layers on a nano-structured polymeric template, consisting of a flexible self-supporting PET foil. The channels were produced by etching tracks of swift heavy ions from ISL. The first metal layer works as the gate contact. When the channel-diameter is small enough, the potential induced by the gate contact reaches radially through the whole channel and a large conductance variation between source and drain contacts can be achieved (cf. Fig. 2). Switching and amplification become possible.

The transistors are operated in the hole depletion mode with a reduced transconductance at negative gate voltages. At present the conductance variation is ~50 % for gate voltages between ± 2 V. The leakage current density is typically less than 1 % of the source-drain current. Applications of this type of transistor in flexible optical displays appear feasible. Replacement of the source, drain and gate contacts by horizontal nanowires may eventually open the way to the addressing of single transistors in a three terminal mode. As the fabrication process allows a stacking of the foil arrays at high packing density is achievable. With these prospects we understand our results as a proof-of-concept that will initiate further research on materials, techniques and device structures for this type of hybrid device.

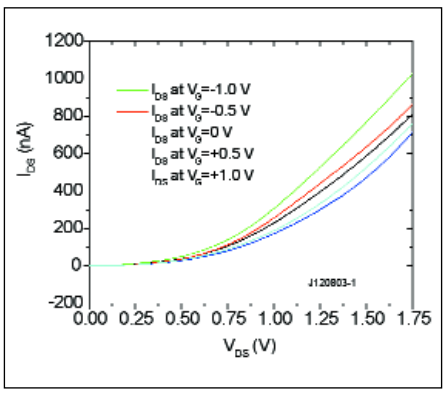

Fig. 2: Source-drain current vs. source-drain voltage of an array of about 1500 vertical field-effect-transistors. Parameter is the gate voltage VG.

[1] J. Chen, R. Könenkamp, Applied Physics Letters, **82**, 4782 (2003).
* J. Chen, R. Könenkamp, *Vertical nano-wire field effect transistor in polymer foils*, European patent Nr.: 10142913, US: 5981970, JP: 11-329334, JP: 61-4017

Synchrotron-based characterization of industrially relevant chalcopyrite solar device structures

Ch.-H. Fischer[1], M. Bär[1], A. Grimm[1], H. Jungblut[1], I. Kötschau[1], I. Lauermann[1], H.-J. Lewerenz[1], K. Rahne[1], J. Reichardt[1], K. Skorupska[1], S. Sokoll[1], M.C. Lux-Steiner[1], L. Weinhardt[2], O. Fuchs[2], C. Heske[2], C. Jung[3], W. Gudat[3], T. P. Niesen[4], S. Visbeck[4], F. Karg[4]

■ 1 HMI, SE2 ■ 2 Exp. Physik II, Universität Würzburg ■ 3 BESSY GmbH, Berlin ■ 4 Shell Solar GmbH, München

The aim of the CISSY project is the investigation of buried interfaces and surfaces in chalcopyrite thin film solar devices by means of synchrotron-based spectroscopy. In the following example the use of x-ray emission spectroscopy (XES) for the identification of secondary phases on a $CuInS_2$-absorber is shown.

In the HMI baseline process for the preparation of $CuInS_2$-absorbers an excess of copper precursor compared to the stoichiometric composition is necessary to obtain the required crystal quality and electronic properties. However, this results in the formation of a secondary, electrically conducting Cu_xS (mainly CuS) surface phase which has to be removed in order to produce efficient solar cells. This removal is usually achieved by selective etching in a KCN solution. As the use of KCN is undesirable in an industrial process, alternative ways of removing Cu_xS are sought. One method, developed by Lewerenz et al. [1], is an electrochemical (EC) etch, which removes most of the Cu_xS. However, solar cells built with the initially developed method had efficiencies below 3 %. Since, in photoelectron spectroscopy, chemical shifts of the copper peaks between $CuInS_2$ and Cu_xS are small, it was at first unclear, whether any residual Cu_xS (possibly Cu_2S), remained on the surface. EC etching of CuS is known to initially form Cu_2S [1]. The surface sensitivity of x-ray diffraction in this case is too low to resolve the matter.

Therefore, XES was utilised to examine the $CuInS_2$-absorber surfaces after different EC etches. XES is based on the excitation of core level electrons with soft X-ray radiation and subsequent fluorescence caused by the relaxation of valence electrons into the core holes. The chemical environment of the emitting atoms is thus reflected in specific spectral features due to the varying contributions of neighbouring atoms to hybridized valence states. Thus, different compounds containing the same element will have specific XES spectra.

Spectra were recorded in the CISSY end station with the XES-300 X-ray spectrometer (Scienta Gammadata) at the U41-PGM beam line at the BESSY synchrotron. S-$L_{2,3}$ spectra from EC etched samples are shown in Fig. 1, together with spectra from the as-grown sample, a KCN-etched absorber, and a Cu_2S reference. Comparison of spectrum (D) of an EC etched surface to that of the KCN-etched reference (C) reveals small differences in the upper valence band area above 153 eV. Analysis suggests that Cu_2S (shown in (E)) is present on the surface. Based on these results, the etching procedure was modified, leading to a surface that gives rise to spectrum (B), which is almost identical with the reference spectrum (A). This is verified by computing the difference spectrum (G). Furthermore, solar cells fabricated with the new procedure reach an efficiency of 8 %. This example shows the value of XES to give chemical information which is complementary to results from other spectroscopic techniques and to assist in the development of state-of-the-art thin film solar cells.

[1] M. Aggour, U. Störkel, C. Murrell, S.A. Campbell, H. Jungblut, P. Hoffmann, R. Mikalo, D. Schmeisser, H.J. Lewerenz, Thin Solid Films **403–404**, 57 (2002).

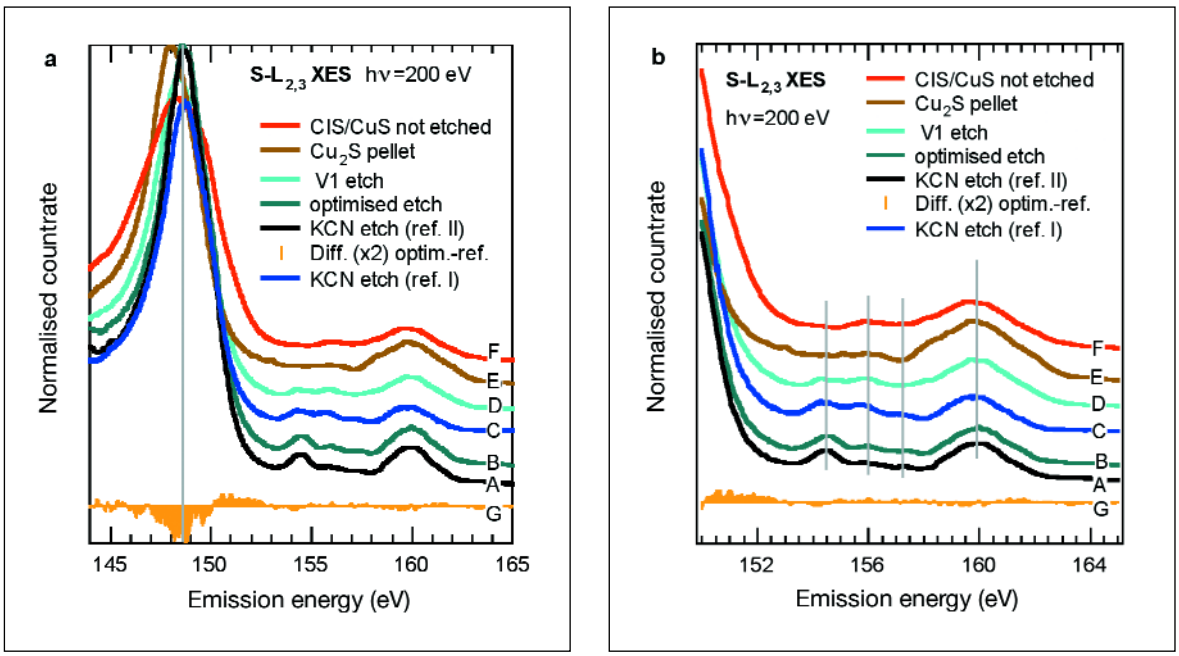

Fig. 1: a) $S\text{-}L_{2,3}$ X-ray emission spectra of a $CuInS_2$ (CIS) sample etched with KCN (A, C), an as-deposited CIS sample (F), a Cu_2S reference (E), an electrochemically etched CIS sample (old procedure, (D)), and a sample etched according to a new procedure (B). G is the difference between spectrum B (optimised procedure) and spectrum A (reference KCN-etched sample). Spectra (B) and (A) were recorded with a different detector than (C) to (F).
b) Enlarged detail of spectra showing the transitions from the upper valence band into S 2p holes. Vertical lines designate spectral features related to S-In bonds (154-158 eV) and S-Cu bonds (160 eV).

Solar cell cross section studied by Kelvin Probe Force Microscopy in ultrahigh vacuum

Th. Glatzel, H. Steigert, N. Barreau, P. Carl, S. Sadewasser, M.Ch. Lux-Steiner, D. Fuertes-Marrón, Th. Schedel-Niedrig
■ HMI, SE2

Kelvin probe force microscopy (KPFM) in ultrahigh vacuum allows to simultaneously obtain structural as well as electronic information (work function Φ) of a sample's surface with an extremely high lateral (~ 20 nm) and energy resolution (~ 5 meV).

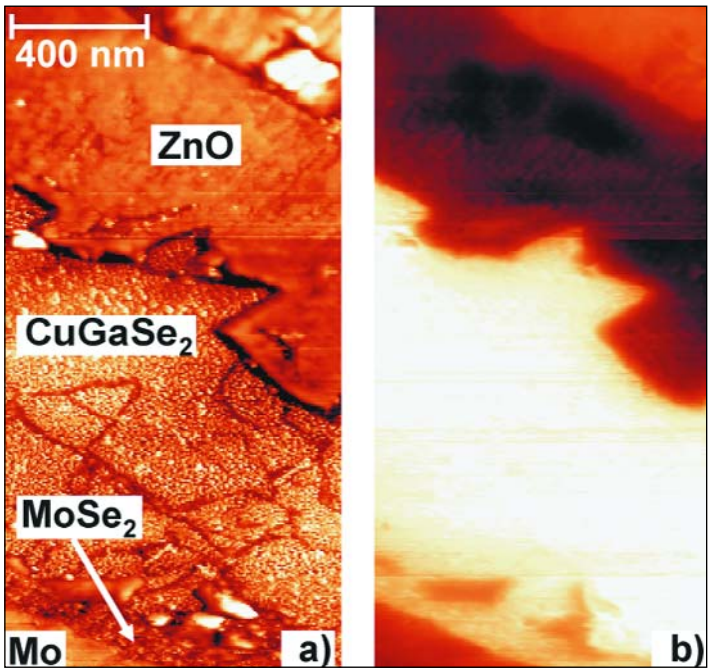

Fig. 1: Image of a $CuGaSe_2$ solar cell cross section (1000×2000 nm^2) after 60 min Ar-ion sputtering (500 eV): **a)** topography (color scale = 65 nm) and **b)** work function ($\Phi = 3.92 - 4.86$ eV).

An important issue for improving the performance of solar cells is an appropriate electronic band alignment at the various interfaces of the different layers that compose a $CuGaSe_2$ heterostructure. Typical chalcopyrite thin film solar cells consist of a Mo back contact on soda lime glass, the p-type absorber layer, a thin buffer layer and a n-type window layer. We present UHV-KPFM measurements on a cross section through a complete solar cell structure [1]. With this method we recorded absolute work function values of the different material surfaces forming the device. Detailed information was obtained especially on the interfaces after the optimization of the sample cleaning process in UHV. The cross section of the chalcopyrite solar cell was prepared by gluing two devices face-to-face and polishing with aluminum paste (grain size ~ 20 nm).

Due to polishing and cleaning in air, we expect the surface to be covered with adsorbates, inducing surface defects. This results in a reduced contrast in contrast potential (CP) of only 100 meV between the different layers. Therefore, the sample was subsequently cleaned by several soft sputtering processes using Ar-ions (500 eV) under 45° incident angle in UHV.

The topography (a) and the work function (b) of the sample after 60 min sputtering are shown in Figure 1. Due to the different sputtering rates of the materials a topographical contrast between the layers is observed. From the bottom of the images the Mo back contact, the chalcopyrite absorber ($CuGaSe_2$), and the ZnO window layer on the top can be seen. The work function image shows a clearer contrast of up to 570 meV between the different layers under dark conditions, and up to 700 meV under illumination. Between the absorber and the Mo back contact an additional layer of about 100 nm thickness with a distinct work function is observed. We attribute the additional contrast between Mo and absorber layer to an $MoSe_2$ intermediate layer. This is in agreement with recent high resolution transmission electron microscopy and scanning energy dispersive X-ray detection measurements which show the formation of an interfacial $MoSe_2$ layer with a thickness of 150 nm. The Mo/$MoSe_2$ interface is an intimate contact formed during the deposition process. For the $MoSe_2$/absorber interface we observe some voids in the interface, related to a non-homogeneous nucleation process of the crystallite seeds during the absorber deposition.

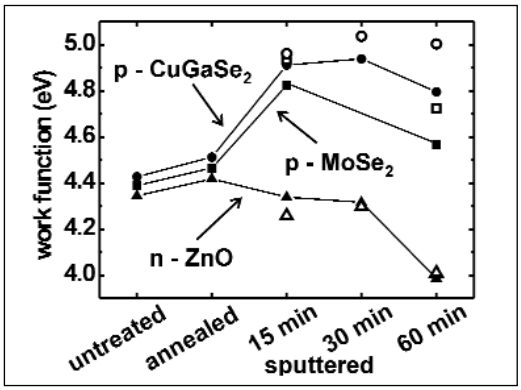

Fig. 2: Work function of the different materials in a CGSe solar cell after different surface treatments. The open symbols represent the values under super band gap illumination (~ 60 mW, λ = 442 nm).

An overview of the work function values of the different materials in dependence on the cleaning step is presented in Figure 2. The open symbols function of the absorber and the $MoSe_2$ layer changes under illumination to higher values; the illumination reduces the band bending at the *p*-type semiconductor surface. Upon further increase of the illumination intensity we observed no significant change in the work function, we assume that we achieved nearly flat band conditions at the surfaces. Under these conditions and after 15 min Ar-sputtering, the work function of $CuGaSe_2$ is 4.96 eV. For the highly *n*-doped ZnO we determine a work function of 4.26 eV. In Figure 2 it can also be seen, that up to a sputtering time of 30 min only the *p*-type semiconductors change the work function significantly. Due to the high carrier concentration of ZnO ($n \approx 10^{21}$ cm^{-3}) the effect of adsorbates on the position of the Fermi energy at the surface should be minimal. For longer sputtering times a significant reduction of the work function of all layers was measured. We attribute this to a change in the surface stoichiometry, caused by preferential sputtering of some elements. In Figure 1 the formation of clusters on the absorber surface can be seen. We relate these to metallic Ga which reduces the work function of the $CuGaSe_2$ surface. Despite this, the absorber layer reaches a nearly constant value under illumination for sputtering times up to 60 min.

[1] Th. Glatzel, D. Fuertes-Marrón, Th. Schedel-Niedrig, S. Sadewasser, M. Ch. Lux-Steiner, Appl. Phys. Lett. **81**, 2017–2019 (2002).

Chalcopyrite solar cells on flexible substrates

A. Neisser, Ch. Kaufmann, R. Klenk, R. Scheer
■ HMI, SE3

It is one of the inherent advantages of a thin film technology, that – in principle – it can be deposited on any kind of foreign substrate. So far, however, thin film solar cells are usually deposited on glass substrates. In a joint project of SE3 and SE2 the glass substrate is to be replaced by a 25 µm thick titanium foil. The resulting solar cells will then be light weight, flexible and almost unbreakable! Furthermore, with >1000 Watts/kilogram, the high specific power of such solar cells opens up completely new areas of applications for thin film photovoltaic devices, for example in solar arrays for satellites in space or airborne vehicles. An additional advantage of chalcopyrite solar cells with respect to space applications is their excellent hardness to a radiative environment (protons and electrons). A prerequisite for these applications is a high solar-to-electric conversion efficiency of >15 % at AM1.0.

The layer structure of a $Cu(In,Ga)Se_2$ solar cell on titanium foil is shown in Figure 1. The crucial $Cu(In,Ga)Se_2$ layer is prepared by physical vapor deposition using a sequential, three-stage co-evaporation process. On a laboratory scale (device area = 0.5 cm^2) the project team has reached an efficiency of 16.7 % on glass substrates. For this process, an *in situ* process control (using laser light scattering) has been developed and patented. This laser system has demonstrated high potential.

In a next step the preparation process had to be transfered from a glass substrate to a thin film metallic foil suitable for space applications. Special attention had to be paid to the increased surface roughness of a metallic foil compared to a glass substrate. It was found that substrate irregularities introduced local defects in the device structure, which primarily limited the performance of the final device. By introducing an additional substrate conditioning step this limitation, however, could be overcome (see Figure 2).

To date conversion efficiencies of reference cells on titanium are comparable to efficiencies on glass (see Table 1). The targeted efficiency of 15 % for a space dedicated device has already been realized on a small area of 0.5 cm^2. Efficiencies of more than 12 % have been reached on larger areas of up to 16 cm^2 (Table 1), which represents a world record efficiency for a flexible thin film solar cell with an area larger than 1 cm^2.

Cells have also been tested under reverse voltage bias. Such stress tests are essential with respect to module integration where partial shading of individual cells can impose high current loads on these cells. Samples have been test under reverse bias of up to –3.0 V for 30 min. The maximum current had been limited to –1.0 A, which corresponds to more than twice the short circuit current of these cells. It could be found that all samples show a reverse breakthrough which is fully reversible. Right after the reverse bias test the open circuit voltage is lower by only about 40 mV. The cell fully recovers under illumination at open circuit conditions. The initial efficiency is reached again after around 1 hour. That means that flexible CIGSe cells can be integrated in a solar cell module without any need for additional bypass diodes commonly used in existing technolgies.

Current activities focus on 1) investigating the feasibility of the unique process control for in-line deposition processes, 2) identifying physical and technological reasons for the gap in device performance between small area and large area single cells and 3) increasing the area of the single cell device from 16 cm^2 to 32 cm^2. Furthermore, the group will be involved in a test program (in cooperation with Dutch-Space and ESA) dedicated to investigate the potential of its thin film solar cells for future space application.

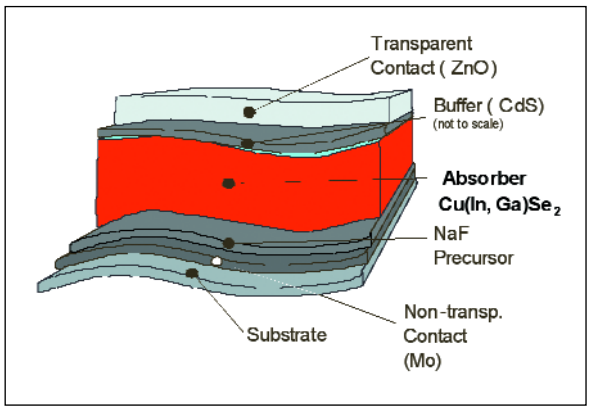

Fig. 1: Layer sequence of flexible solar cell.

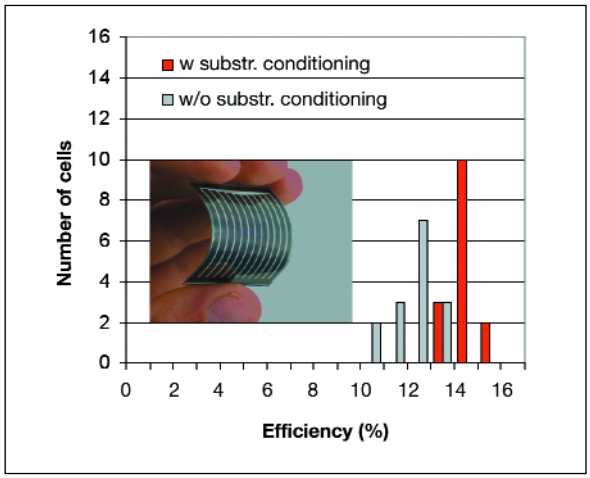

Fig. 2: Distribution of efficiencies of small area devices on a 40 × 40mm² substrate. Inset: Flexible solar cell based on $Cu(In,Ga)Se_2$ (area 16 cm²).

	area (cm^2)	V_{oc} (mV)	ff (%)	j_{sc} (mA/cm^2)	η (%)
glass	0.5	661	75	33.8	16.7
Ti	0.5	636	76	33.6	16.2
Ti	16	624	71	27.5	12.2

Table 1: Record efficiency of flexible solar cells on Ti-foil (reference on glass included for comparison).

About the mechanism of $CuInS_2$ film formation

Ch. Pietzker, R. Scheer
■ HMI, SE3

The formation of $CuInS_2$ absorber layers for solar cells by use of a sequential process is within the centre of research of the technology department. The growth initiates from metallic Cu,In layers and intermetallic compounds such as $CuIn_2$, $Cu_{11}In_9$, and $Cu_{16}In_9$. Addition of sulphur and heating of the substrate leads to the transformation into the chalcopyrite structure. In the case of $CuInS_2$ absorber layers, Cu-rich precursor layers are used resulting in a Cu-S phase as a byproduct.

The temperature profile for the sulphurisation normally includes a ramp-up phase, a holding phase, and a cool-down phase. Typical substrate temperatures in the holding phase are 500°C. The question of the investigation in the following presented is: What is the dominant kinetic limitation for the sulphurisation process? In order to answer this question, *in situ* XRD experiments during the sulphurisation have been performed. The precursor layers have been pre-annealed and transformed into the intermetallic phase $Cu_{16}In_9$. Therefore, for the present experiments the sulphurisation starts from the phase $Cu_{16}In_9$. No further intermetallic phase transformations occur during the temperature cycle. The inset in Fig. 1 shows a sketch of the layer structure at an intermediate state. Part of the $Cu_{16}In_9$ layer has been consumed and has been converted into $CuInS_2$. It is known that the growth front of $CuInS_2$ is at the front surface of the $CuInS_2$ layer. This implies that Cu and In atoms have to pass the preliminary $CuInS_2$ layer by diffusion. At the surface they react with sulphur.

A standard method for the investigation of diffusion processes is isothermal annealing and quantification of educts and products. Fig. 1 (top) shows a temperature profile for an annealing experiment at 375°C. Initially, the substrate temperature is fastly ramped to the annealing temperature. At this temperature, the annealing phase is followed. After the end of the annealing phase, the substrate temperature is ramped to the top value (600°C). Fig. 1 (bottom) shows the $Cu_{16}In_9$ XRD peak intensity as a function of time for different annealing experiments. $Cu_{16}In_9$ is the educt of the reaction. It should be emphasised that this intensity is complementary to intensity of the product $CuInS_2$. We see in the figure that $Cu_{16}In_9$ is consumed in the ramp period of the experiment at 375°C but not in the isothermal holding period. The same is valid for the XRD intensities of isothermal experiments at other temperatures. There, the isothermal period lengths have been altered. Obviously, the consumption of $Cu_{16}In_9$ and the growth of $CuInS_2$ mostly takes place in the ramp-up periods and only to a minor extend in the holding period. In other words, growth of $CuInS_2$ mainly follows a temperature law and not a time law.

In a different experiment series, this result has been confirmed: Using an identical top temperature, different ramp rates have been applied and the consumption of $Cu_{16}In_9$ as well as the formation of $CuInS_2$ have been investigated. It was found that growth of $CuInS_2$ is always finished at the end of the ramp-up period. We interprete this effect as a stress-induced growth mechanism: Due to the difference in the expansion coefficients of $Cu_{16}In_9$ ($\alpha = 3.3 \times 10^{-5}\ K^{-1}$) and $CuInS_2$ ($\alpha = 0.9 \times 10^{-5}\ K^{-1}$), a tensile stress is induced within the $CuInS_2$ layer. This stress may be released by the formation of microcracks or grain boundaries. It is assumed that the diffusion of Cu and In atoms takes place along the cracks or is promoted by stress within the $CuInS_2$ top layer. Similar growth mechanisms had been reported for the oxidation of metal layers [1].

We compared the growth of Cu-rich $CuInS_2$ layers with Cu-poor layers of $CuInS_2$ as well as with $CuInSe_2$ layers. In neither of the latter cases a similar growth mechanism has been found. The result of this study is particularly important for the $CuInS_2$ solar cell process. It allowed to omit the holding period in a sulphurisation experiment. Thereby, the process time can be reduced in favour of a higher throughput in production.

[1] H.E. Evans, Int. Mat. Rev. **40** (1), 1-40 (1995).

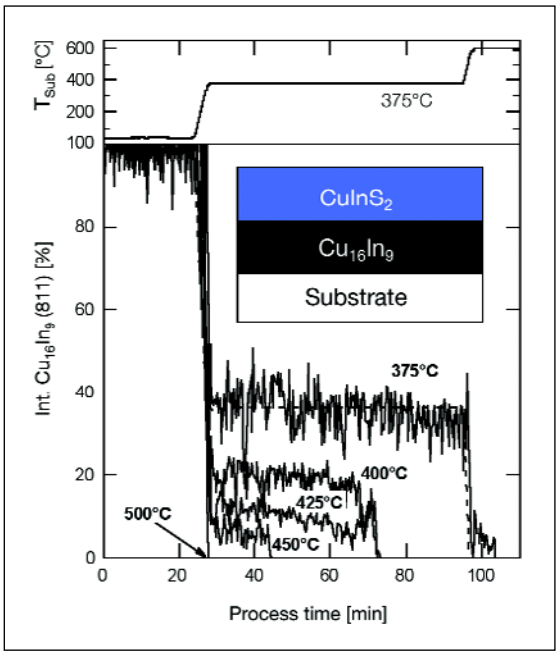

Fig. 1: (bottom) XRD intensities of the phase $Cu_{16}In_9$ as a function of process time for different temperature profiles for sulphurisation. (top) Exemplarily, the temperature profile for an experiment at 375°C is given. It includes fast ramp periods at 25 min and 95 min process time and a holding period of 60 min at 375°C. Similar are the experiments at 400°C, 425°C, 450°C, and 500°C, however, with shorter holding periods. The inset shows the layer sequence of an intermediate stage of the sulphurisation.

Local diode parameters determined by infrared thermography

I. Gavilanes-Pérez, R. Scheer
■ HMI, SE3

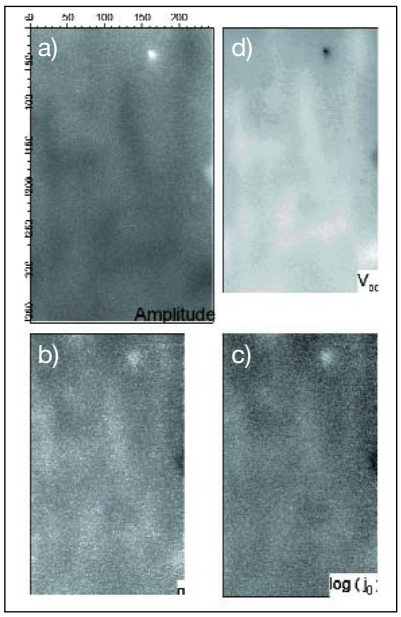

Fig. 1: a) Image of the IR amplitude at 0.74 V forward bias. Brightness proportional to current density. b) Calculated images of the spatial diode quality factor n, c) saturation current density $\log(j_0)$, and d) open circuit voltage V_{oc} of a standard $Mo/CuInS_2/CdS/ZnO$ solar cell. The sampled area is 2.5×4 mm^2. The scale gives the pixel number.

Solar cells and modules are large area devices for which the coherent action of every cell segment is of paramount importance. A defected module area of micrometer size can deteriorate the performance of up 100 cm^2 cell area. Defects can be a result of inhomogenous cell processing or of inherent variations of the diode parameters. Up to now, little is known about the spatial homogeneity of chalcopyrite thin film solar devices. A quantity of particular relevance is the open circuit voltage V_{oc} and its lateral homogeneity. Recent PL mappings of device-grade $Cu(In,Ga)Se_2$ devices revealed a variation of the quasi-Fermi level splitting of 10 meV measured at 70 K [1]. It is clear that this quantity can be translated into a variation of the open circuit voltage ΔV_{oc}. Furthermore, this variation should be larger at room temperature.

By use of lock-in thermography we calculated ΔV_{oc} for the first time from the spatial dark current density of chalcopyrite cells. Solar cells of the area 0.5 cm^2 were set in front of a IR camera. This camera allows to sample the emitted heat of the cell with 10×10 µm^2 spatial resolution. A forward bias voltage was applied to the cell. Due to the high conductivity of the front and back contact, it can be assumed that the voltage is homogeneously imposed on all cell areas. According to the local current-voltage characteristic of each cell element, the current density at each element may vary. An element with a shunt or a weak diode, for instance, will carry a higher current density. Thus it will dissipate more energy which is detected by the IR camera. Fig. 1 gives an example of an amplitude image recorded at a bias of 0.74 V. The x and y axes denote the pixel numbers. At the pixel number (165,30) a shunt is revealed by higher brightness of the image.

Images of the emitted heat are recorded for different voltages. They form a matrix of values for the dissipated power as a function of voltage for each cell element. From this a matrix of current density as a function of the voltage can be calculated. As a result, the diode characteristic for each cell element is achieved. This diode characteristic can be evaluated in terms of the diode quality factor, n, and the saturation current density, $\log(j_0)$. Finally, n and j_0 can be plotted as a gray scale image.

Fig. 1 exemplarily shows maps of n and j_0 for a $CuInS_2$ solar cell. Higher values of n and j_0 are represented by increased brightness. A cloudy variation of both parameters can be discerned. As is theoretically expected, areas of higher n values correspond to areas of higher $\log(j_0)$ values. If the n factor values from the thermography experiment are mathematically averaged over the sampled area, a value of $n = 1.6$ with a FWHM of 0.4 is achieved. The peak value is identical to the n-factor resulting from the electrical jV measurement.

The diode quality factor and the saturation current density are two quantities which determine the open circuit voltage of a device. Assuming homogenous light current generation, the V_{oc} can be easily calculated and plotted as an image. This is done in Fig. 1. A cloudy structure complementary to the amplitude image but congruent to the $\log(j_0)$ image is obtained. Only the shunt at (165,30) has a contrast differing from the $\log(j_0)$. The variation of the open circuit voltage ΔV_{oc} over the cell area is about 50 mV. A similar ΔV_{oc} value we found for a $Cu(In,Ga)Se_2$ device. Thus the thermography data are in agreement with PL measurement.

[1] K. Bothe, G. H. Bauer, and T. Unold, Thin Solid Films **403–404**, 453–456 (2002).

Experimental proof for MOCVD-specific surface reconstruction of InP(100)

T. Letzig, H.-J. Schimper, T. Hannappel, F. Willig
■ HMI, SE4

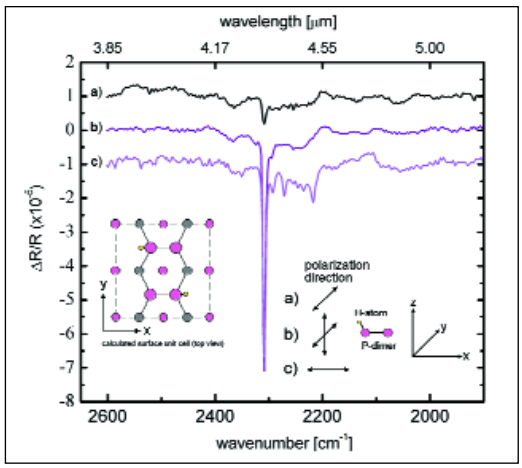

Fig. 1: Three IR difference spectra of P-H stretching vibrations at different polarizations of the incident light. For clarity, there is an arbitrary shift in vertical direction.

Metalorganic vapor deposition (MOCVD) is the method of choice for industrial growth of III-V semiconductor layers, i.e. for binary materials like GaAs and InP, and also for ternary and quaternary variants. The MOCVD growth technique is based on thermal decomposition of metalorganic precursor molecules such that a highly pure and ordered phase of the III-V solid is left behind on a suitable substrate. The method requires a proper preparation procedure and must be carried out in a suitable MOCVD reactor. For specific industrial purposes and in particular for basic science the growth of such materials is carried out without precursor molecules, just making use of the III-V chemical elements (MBE). A recent theoretical hypothesis has postulated that hydrogen will be incorporated into a specific P-rich ordered surface reconstruction of InP(100) if the material is grown via MOCVD [1]. A completely different ordered surface should be formed as the P-rich reconstruction when the material is grown via MBE. The theoretically postulated surface unit cell of the P-rich reconstruction prepared via MOCVD is characterized by a phosphorous dimer whose dangling bonds are stabilized via formation of one P-H bond (compare inset on the left hand side of Fig. 1).

We found direct experimental proof for the postulated surface reconstruction in the form of INFRARED spectra measured in ultra-high-vacuum at the MOCVD grown surface (Fig. 1). The specific IR peak showed the polarization dependence expected to arise for the theoretically proposed surface unit cell with the P-H bond. The result was achieved making use of a unique sample transfer system mounted at the exit of our MOCVD reactor. The latter provides sample transfer into UHV without suffering any surface contamination or further reconstruction. Each spectrum shown in Fig. 1 represents a difference spectrum based on a measurement carried out prior to and another after removal of all the P-H bonds from the as-grown surface. The latter state was achieved via a sufficiently thorough exposure to deuterium gas. Correspondingly, the P-H vibrations at the as grown surface appeared in the difference spectrum as a strong negative peak in Fig. 1 with wavenumber at 2308 cm^{-1} (= 4.33 μm). Polarization of the impinging light beam in y-direction did not excite this particular vibration (spectrum a). This was expected from the theoretical model (inset at the left) since the dipole moment of the P-H vibration should not show a component in this direction (compare also the inset at the lower right hand side of Fig. 1). In contrast, there was a strong peak (spectrum b) and c)) when the impinging light was polarized parallel to the x-z plane where the dipole moment of the P-H vibration has been predicted in the theoretical model. Our complete FTIR data give the first direct experimental proof for the MOCVD-specific P-rich surface reconstruction of InP(100) [2]. The latter is strikingly different from the surface reconstruction of the P-rich surface prepared via MBE. Making use of our patented MOCVD-UHV sample transfer the MOCVD prepared surface was investigated in the absence of any post-transfer preparation step.

[1] P.H. Hahn, W.G. Schmidt, Surf. Rev. Lett., **10**, 163 (2003)
[2] T. Letzig, H.-J. Schimper, T. Hannappel, F. Willig, submitted to Phys. Rev. B

Energy distribution of hot electrons in a semiconductor exposed to sunlight

M. Neges, K. Schwarzburg, F. Willig
■ HMI, SE4

Theoretical scenarios for various types of solar cells with potential solar conversion efficiencies higher than can be reached with a conventional one-band gap solar cell (so-called 3rd generation photovoltaic devices) go back more than 20 years. A specific postulate has addressed the collection of hot charge carriers at a suitable electrical contact material [1]. The corresponding theoretical postulated scenario involved a thermal distribution of hot charge carriers prepared via absorption of sunlight by the semiconductor. The distribution was characterized by a temperature parameter of several thousand degrees. The above postulate has remained a topic in the photovoltaic literature until today [2]. Surprisingly, the postulate has never been checked experimentally or via a realistic model calculation. Recently, we have addressed this question both experimentally and by a model calculation.

Experimental fingerprints of the hot electron dynamics were measured at He temperatures in InP as characteristic dips in the excitation spectrum of the photocurrent collected at a transparent hetero-contact (InP/SnO_2) (Fig. 1). Such dips are known to arise from the enhanced recombination probability when hot electrons reach exactly the bottom of the conduction band via a series of emission processes for LO-phonons (cascade). Electrons with negligible kinetic energy show the highest probability for capture by recombination centers.

The corresponding dips in the photocurrent excitation spectrum were reproduced in a Monte Carlo simulation of hot electron dynamics that incorporated all the relevant scattering processes for hot electrons and their respective temperature dependence (Inset Fig. 1). The Boltzman transport equation (BTE) was solved by means of Monte Carlo techniques for electrons that were optically generated in the conduction band. The energy range of < 0.4 eV above the lower conduction band edge was addressed in the simulations allowing for a parabolic approximation of the conduction band dispersion. Scattering with LO-phonons, acoustic phonons, impurities, and holes was considered. Conduction band to acceptor recombination was used as the dominant recombination path. The charge separating hetero-interface was mimicked as an infinite sink. The simulation was based on the above experimental data and extrapolated to room temperature.

The energy distribution of hot electrons impinging on the contact is shown in Fig. 2 for p-doped InP for both medium and small dopant concentrations. Clearly, the spikes in the calculated distributions for the energy of the hot electrons that reach the contact are highly non-thermal (thermal distributions are indicated for comparison). This is in stark contrast to the assumptions in the earlier theoretical scenario of Ross and Nozik. Implications of these results for solar cells based on the collection of hot carriers at the contact will be investigated further based on the above realistic hot electron dynamics.

[1] R. T. Ross and A. J. Nozik, J. Appl. Phys. **53**, 3813 (1982).
[2] P. Würfel and T. Trupke, Physik Journal **2**, (12), 45 (2003).

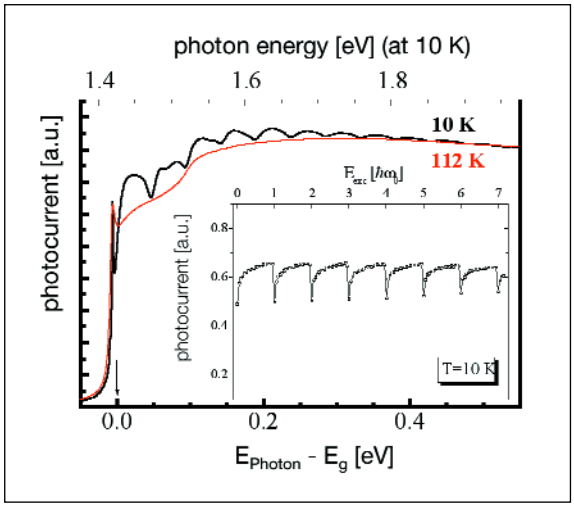

Fig. 1: Photocurrent excitation spectra at 10 K and 112 K. Hot electrons provide the excess photocurrent at low temperatures. Inset: Monte-Carlo-simulation of the photocurrent.

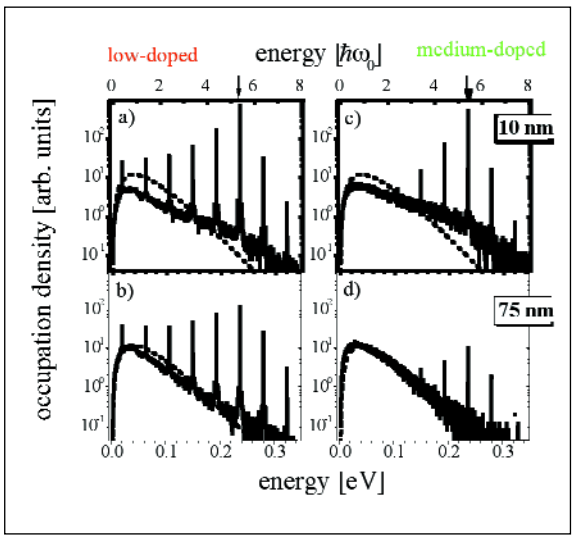

Fig. 2: Energy distribution for hot electrons that reached the contact from a starting distance of 10 and 75 nm, respectively. Note the logarithmic scale of the ordinate. The electrons were generated at room temperature with 234 meV kinetic energy above E_{CB}.

Solar cells with small band gaps built from III-V materials

H.-J. Schimper, U. Seidel, T. Hannappel, K. Schwarzburg, F. Willig
■ HMI, SE4

Hitherto the highest solar conversion efficiencies have been achieved with multi-junction cells of III-V materials, where the smallest band gap, however, is realized with a different type of material. The record example of a triple-junction cell with 36.9 percent conversion efficiency is the combination InGaP/GaAs/Ge [1]. Band gaps greater than 1.35 eV can be realized with III-V materials whose lattice constants are close to that of GaAs. Smaller band gaps, however, require III-V materials with lattice constants similar to that of InP. In principle a small band gap cell, e.g. 1 eV, can be realized also with the lattice constant of GaAs, requiring the quaternary material GaInAsN. Unfortunately, corresponding efforts have not yet resulted in an N-containing III-V material that would show a satisfactory minority carrier diffusion length.

In contrast, the present project aims at preparing a triple-junction solar cell where also the small band gaps are realized with III-V materials based on the lattice constant of InP and do not require Nitrogen to be incorporated. With the band gap combination of 0.75 eV (InGaAs), 1.15 eV (InGaAsP) and 1.7 eV (InAlAsSb) the optimum efficiency for a triple-cell can be realized.

The triple-junction cell is prepared in consecutive steps, first suitable mono-junction cells are being grown, next a double-junction cell is developed, etc. The mono-junction cell InGaAs with band gap 0.74 eV was prepared and showed a solar conversion efficiency of 8.5 percent. The mono-junction cell InGaAsP with band gap 1.2 eV showed an efficiency of

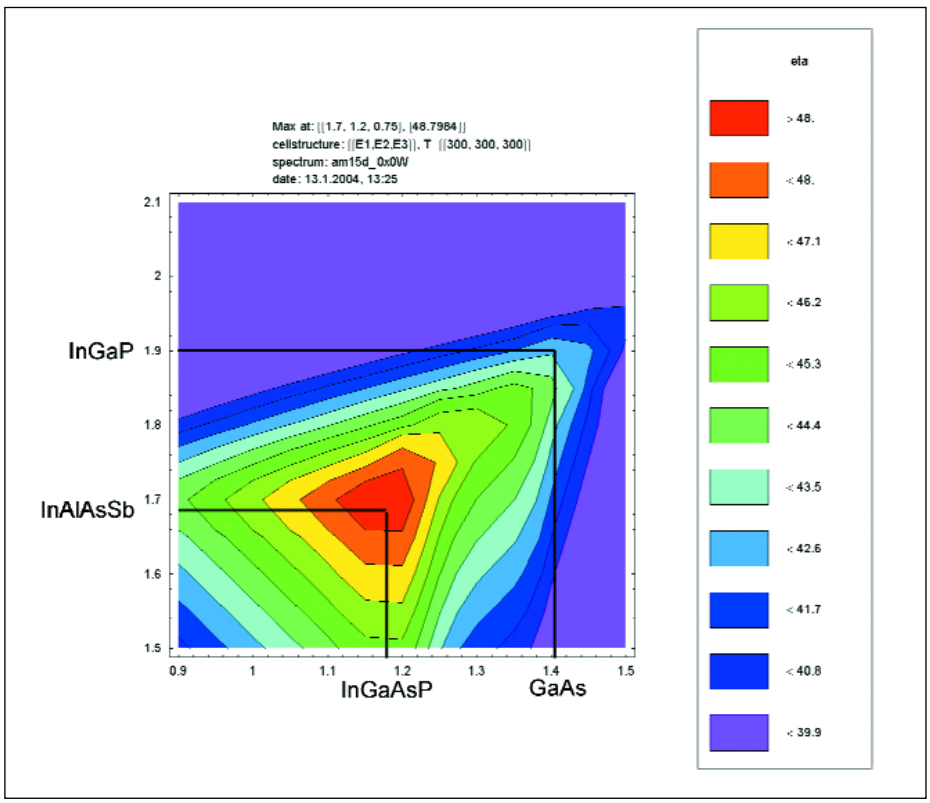

Fig. 1: Efficiencies for Triple-junction-cells with two variable bangaps for the top cells. The band gap for the bottom-cell is fixed at 0.75 eV (InGaAs or Ge)

11.3 percent. Both the cells were measured without anti-reflective (AR) coating. GaAsSb was grown with band gap 0.72 eV as alternative to InGaAs. For improving the conversion efficiency several specific preparation steps have to be implemented, one of them is photolithography. The latter facilitates mesa-etching and a lift-off technique for the preparation of the electrical contacts. This technique yields a well-defined active cell area and a well-characterized area for the electrical contacts. The former is better defined compared to contact formation via evaporation of the metal through a shadow-mask. The grid of the electrical contact can be prepared with a smaller distance between neighboring metallic strips resulting in a reduced series resistance. Compared to the same InGaAs mono-junction cell where the electrical contacts were formed via shadow-mask metal-evaporation photolithography has increased the conversion efficiency from 6.5 to 8.6 percent.

A single-layer anti-reflection coating (AR) has improved the external quantum efficiency of an InGaAs solar cell from 65 percent to 85 percent, with a corresponding increase in the conversion efficiency from 6.5 percent to 8.5 percent. The AR coating was not yet effective over the whole active spectral range and thus has to be improved further. Photolithographic preparation of the electrical contacts (compare above) is expected to raise the conversion efficiency of this cell further.

[1] King RR et. al. *Lattice-matched and metamorphic GaInP/GaInAs/Ge concentrator solar cells.* Proceedings of the World Conference on Photovoltaic Energy Conversion (WCPEC-3), Osaka, May 2003

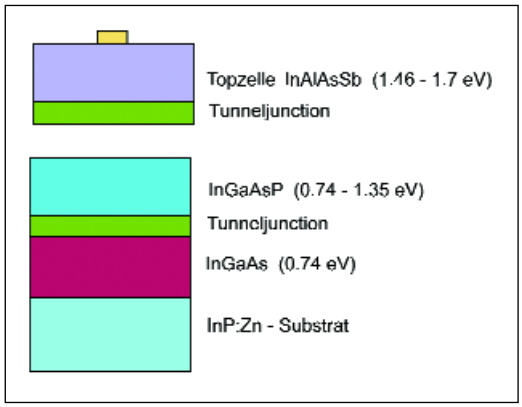

Fig. 2: Triple-junction cell on an InP substrate

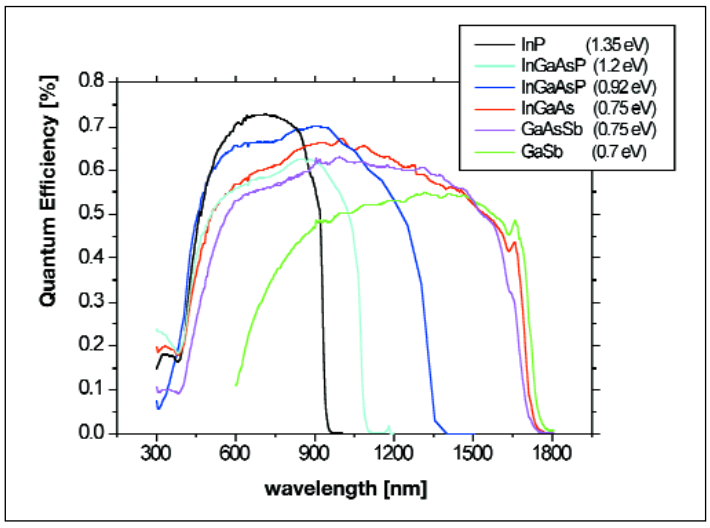

Fig. 3: External Quantum Efficiencies of single-junction-cells on InP

Chemical Surface Modification of Molybdenum-, Tungsten-Dichalcogenides for Optimal Photoeffects

A. Barkschat, H. Tributsch
■ HMI, SE5

Well-grown molybdenum- and tungsten-dichalchogenide crystals (MoX_2 with $X = S, Se, Te$) in contact with aqueous electrolytes (wet solar cells) have yielded solar energy conversion efficiencies exceeding 15 %). Efforts, however, to produce solar cells in the form of thin layers or sintered powders failed because the photoeffects deteriorated due to the participation of unfavorable crystal surfaces perpendicular to the Van der Waals interface of the two-dimensional materials (for a review see [1]). These surfaces exhibit reactive chemical bonds, which serve as recombination centers and orbitals for undesired interfacial chemistry. In order to take advantage of the abundant and environmentally friendly compounds MoS_2 and WS_2 for thin layer and composite solar cells, research towards neutralization of these recombination centers became necessary.

A useful tool for this study of photo-induced interfacial processes became imaging techniques for photocurrents (Fig. 1) [2].

They clearly show that even crystals grown of these compounds exhibit a variety of surface sites with different energy conversion properties.This is shown in Fig. 1 by applying different potentials to the photo-absorber in contact with a liquid iodide-triiodide electrolyte. While at short circuit conditions (Fig. 1, left) high photocurrents flow, they systematically decrease towards the open circuit potential (Fig. 1, right). It is recognized that different areas of the crystal behave differently and thus show different power output characteristics and different fill factors.

Studies were initiated to identify compounds which selectively interact with dangling transition metal bonds perpendicular to the layer structure. One of the best compounds investigated up to now, which positively influences such an interface is the detergent TWEEN 80. After the surface is treated with a 4 % aqueous solution of this compound for three hours, the photocurrent output is clearly improved. This is seen in Fig. 1b, which shows that this most significant effect is an improvement of the power output characteristic for different areas. This can be seen in the increased photocurrent density near the open circuit voltage (Fig. 1a and 1b, right sides).

One complication in the interpretation derives from the observation that the effects are very anisotropic. This indicates that there is a large variety of different surface conditions for which the effect of the detergent may have somewhat different results. Photoelectrochemical and also microwave-photoelectrochemical measurements are on the way to get more detailed information. It is expected that systematic research on the interaction of selected chemicals with layered-type semiconductor particles will lead to the development of nano- and polycrystalline solar cells made of these materials.

[1] A. Aruchamy (Ed.), *Photoelectrochemistry and Photovoltaics of Layered Semiconductors*, Kluwer Academic Publishers, Dordrecht (1992).
[2] A. Barkschat, PhD-Thesis, Freie Universität Berlin (2003).

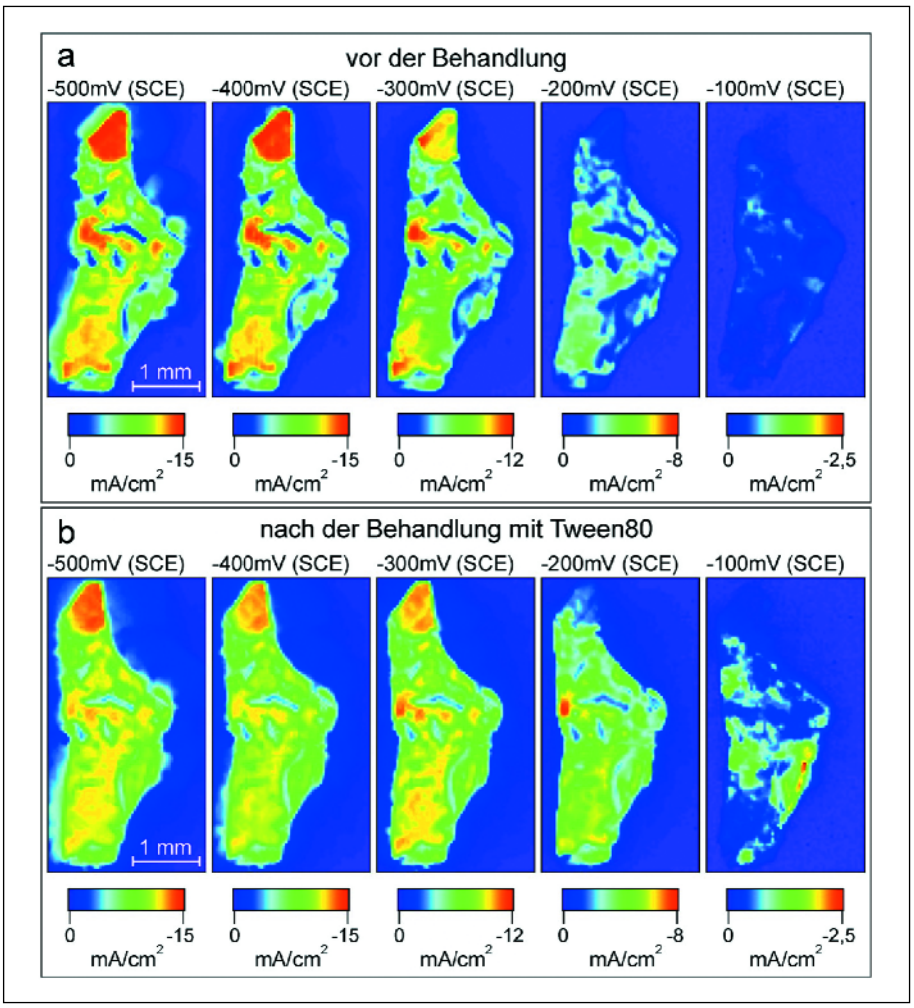

Fig. 1: shows photocurrent images of a p-WSe_2 crystal, in contact with a redox electrolyte measured at different electrode potentials, from short circuit (**left**) towards open circuit conditions (**right**). The original light to photocurrent conversion conditions (**a**) are clearly improved upon surface treatment with Tween 80 (**b**), especially towards open circuit conditions (**right**). [2]

Noble metal free catalysts for the electro-reduction of oxygen

S. Fiechter, P. Bogdanoff, G. Schmithals, I. Herrmann, I. Dorbandt, H. Tributsch
■ HMI, SE5

Introduction.
In processes converting chemical into electrical energy under clean environmental conditions, the development of the polymer electrolyte membrane fuel cell (PEM-FC) system plays a central role. However, to introduce PEM-FCs as a mass product, the nowadays used platinum-based catalysts have to be replaced by abundant transition metals.

Preparation and characterisation of catalysts.
Recently, it has been demonstrated that iron-cobalt catalysts, prepared by pyrolysis using a mixture of metal porphyrins (e.g. CoTMPP) and oxalates (e.g. FeC_2O_4) or employing carbon particles (BP) impregnated with porphyrins in an inert gas, led to electrocatalysts reducing oxygen with an efficiency comparable to platinum [1–3]. In some cases, catalytic activity is further enhanced by the addition of sulphur to the precursor. The novel catalyst exhibits a highly porous carbon structure [1–2]. Although neutron activation analysis showed Fe- and Co-concentration of less than 2wt %, no metal particles of nanometer size could be detected neither by scanning nor by transmission electron microscopy nor by x-ray diffractometry. Therefore, it was assumed that the catalytic centres must consist of metal clusters or atoms integrated into the surfaces of the in-situ formed carbon support by pyridinic-type nitrogen [4].

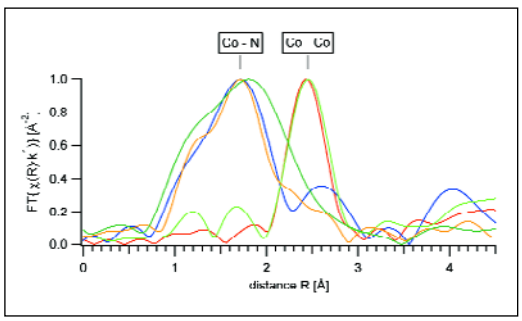

Fig. 1: Magnitude of the Fourier-transformed EXAFS functions (normalized without phase correction).

EXAFS measurements. Extended X-ray Absorption Fine Structure (EXAFS), measured at the k-edges of cobalt and iron in carbon-supported catalysts of ≤ 2wt % metal content revealed that two metal centres are present consisting of single iron or cobalt atoms, integrated in a carbon matrix via nitrogen bridges. Since the metal-nitrogen distance is identical with that found in crystalline porphyrins it is supposed that also the symmetry of the nitrogen coordinated metal atom remains unchanged.

Figure 1 shows the magnitude of Fourier-transformed EXAFS functions for the following samples: metallic cobalt (red curve), cobalt tetramethoxyphenyl-porphyrin CoTMPP (blue), heat treated CoTMPP without acid treatment (light green) and two catalysts (CoTMPP/ iron oxalate) with (orange) and without sulphur after acid treatment (dark green). The peak at 2.43 Å corresponds to the Co-Co distance of metallic cobalt (red). Pure CoTMPP exhibits a peak at 1.7 Å (blue). This value is corroborated with the Co-N distance in the chelate structure. Since the curves are not phase corrected the atomic distances found are smaller than those known from x-ray single crystal structure analysis. The curve of the heat treated CoTMPP (light green) exhibits dominant Co-Co distances while the Co-N peak is significantly reduced. It can be concluded that most of the chelate-cores are destroyed during pyrolysis and that elementary cobalt is formed. To efficiently remove the catalytic noneffective metallic particles from the heat treated samples it has been demonstrated that the addition of iron oxalate and sulphur leads to a foamed catalyst structure [2–3] where the metallic components easily could be removed by acid treatment. The sulphur-free curve (orange) closely resembles the pure porphyrine curve at the Co-N peak position but does not exhibit the typical features of the next ligands: porphyrine decomposes but a fraction of the $Co\text{-}N_4$ cores remains unchanged embedded in the carbon matrix. The course of the EXAFS curves originating from samples prepared by adding sulphur and those measured at the iron edge show similar features (dark green).

Electrochemical and surface characterisation. Electrochemical activity of the catalysts were determined in a $0.5\ \mathrm{M}\ H_2SO_4$ electrolyte using rotating ring disc electrodes under oxygen purging [2]. These electrochemical experiments were carried out in a three-electrode-system employing a saturated mercury sulfate electrode. Figure 2 shows kinetic currents of differently prepared catalysts related to the electrode surface versus voltage, calculated from Koutecky-Levich equation (Tafel-plots). Best results were obtained using a $CoTMPP/FeC_2O_4/S$ precursor. However, the high current densities of carbon-supported Pt catalyst ($20wt\,\%\ Pt$ on carbon) used as reference has not yet been achieved. It was found that high catalytic activity of the new catalysts is correlated with the surface area, determined by sorption measurements (BET) [2], that amounted up to $800\ m^2/g$ for best materials.

In contrast to conventional carbon supported electrocatalysts, where catalytic particles of nm size are deposited onto the surface of onion-shaped carbon particles of several $10\ nm$ diameter, the new catalyst type can be described consisting of in-situ formed graphite-like mesoscopic particles featuring a sponge-like matrix with cavities in the $10\ nm$ range.

Studying the reduction current density at $0.7\ V$ as a function of the electrical capacities of different electrodes, whose electrochemical active surface areas were varied, an exponent of 2.3 could be evaluated in a double logarithmic scale. Such a behaviour has not yet been observed on noble metal carbon supported catalysts. It points to the fact, that the efficiency of our catalysts is defined by the geometry of the carbon support (fractal structure) and the concentration and distribution of the catalytic centres integrated in the carbon matrix.

[1] Hilgendorff, M.; Dorbandt,I.; Schulenburg, H.; Bron, M.; Fiechter, S.; Bogdanoff, P.; Tributsch, H.: *Platinfreies Chelat-Katalysatormaterial für die selektive Sauerstoffreduktion und Verfahren zu seiner Herstellung*. DE 101 32 490 A 1, Offenlegungstag 30.01.2003.

[2] Bogdanoff; P. ;Herrmann, I.; Hilgendorff, H.; Dorbandt, I.; Fiechter, S.; Tributsch, H.: Journal of New Materials for Electrochemical Systems, 2004 in press.

[3] Bogdanoff, P.; Hilgendorff, M.; Schulenburg, H., Fieber-Erdmann, M.; Dorbandt, I.; Tributsch H.; Fiechter, S.: World Renewable Energy Congress VII, Cologne, Proceedings, Schriften des Forschungszentrum Jülich, Vol. 26 (2003) 129-132 (D.Stolten and B. Edmonts (Eds.)).

[4] Schulenburg, H.: *Ruthenium- und eisenbasierte Katalysatoren für die elektrochemische Sauerstoffreduktion in Polymerelektrolytmembran-Brennstoffzellen*; PhD-Thesis, Freie Universität Berlin, 2002.

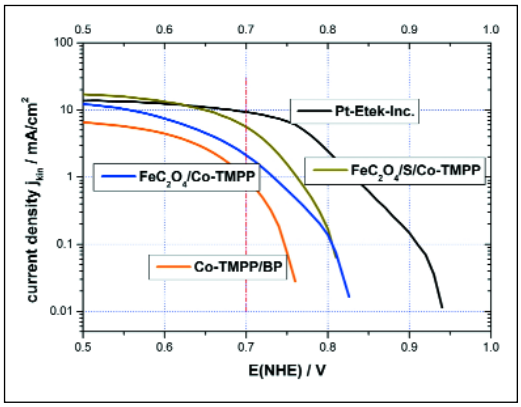

Fig. 2: Tafel-plots of differentially prepared iron-cobalt-catalysts.

Characterization and improvement of semiconductors and semiconductor junctions for solar energy conversion.

M. Kunst
■ HMI, SE5

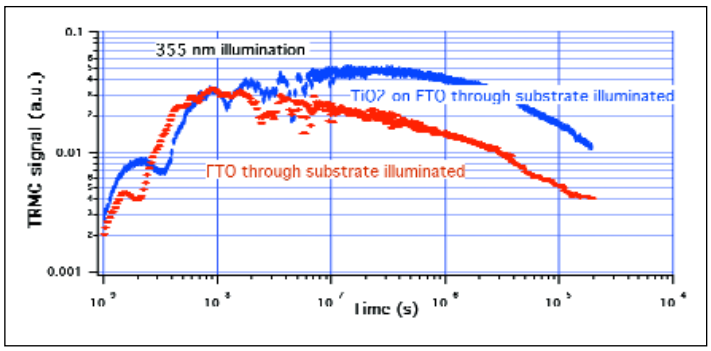

Fig. 1: TRMC signals induced by 355 nm light pulses (10 ns FWHM) in a FTO film on a glass substrate (red signal) and in TiO_2/FTO/glass sample (blue signal).

Contactless and non invasive measurements of the transient photoconductance in the microwave frequency range (TRMC measurements) as developed in the HMI offer a versatile tool for the characterization of semiconductors and semiconductor junctions.

It was shown that the *p* a-Si:H/n c-Si heterojunction can be optimized by in-situ TRMC measurements: an unambiguous relation between the surface recombination velocity monitored (in-situ) during deposition of the interface and the efficiency of a solar cell based on the same interface was observed. Further, encouraging results were obtained in the characterization of TiO_2 powders for photocatalysis: relations between TRMC data and the efficiency of for a standard photocatalytic reaction were observed.

Here some exemplary TRMC results on transparent conductive oxides will be discussed in more detail.

Transparent conductive oxide (TCO)

In several newly developed solar cells, as for example the injection solar cell, an optically transparent contact is required. Based on the experiences with thin film solar cells conductive oxides as highly doped ZnO and SnO are used. In the injection solar cell colloidal TiO_2 is deposited on F doped SnO (FTO) or In doped SnO (ITO) covered substrates. The theoretical description of the functioning of this solar cell considers the FTO (ITO) film as a metal serving as an ideal sink for electrons at the photo-active side of the device. This neglects the properties of these materials as (degenerate) semiconductors. TRMC measurements show that this is not warranted:

-Illumination of FTO films by 355 nm (super bandgap light) yields an appreciable photoconductance monitored by TRMC measurements (the red curve in Fig. 1) in spite of the low sensitivity of the TRMC technique for highly conductive samples. This signal is proportional to the excitation density. These observations point to the semiconductor character of the FTO-films.

Also TRMC measurements of colloidal TiO_2 films on FTO covered glass substrates are shown in Fig. 1. The sample is illuminated through the glass substrate, whereas the detecting microwaves are incident on the other (TiO_2) side. The initial signal is for both samples identical and consequently due to excess charge carriers (probably electrons) generated and mobile within the FTO film. However, in the TiO_2/FTO/glass sample a slowly (compared to the optical generation of excess charge carriers finished in about 10 ns) rising additional component is observed from 10 ns–100 ns. The most plausible explanation of this slowly rising signal is injection of electrons generated in TiO_2 (where they do not contribute to the TRMC signal due to the low mobility) into the FTO part of the sample. In this case the risetime is intimately related to the diffusion time of electrons generated in TiO_2 to the TiO_2/FTO interface.

Consequently in the theoretical description of the injection solar cell the semiconductor character of the FTO-coated substrate must be taken into account and band bending at the TiO_2/FTO interface must be considered.

On the Problem of (Photo)-Degradation of Solid-State Nano-Composite Solar Cells

H. Tributsch
HMI, SE5

In recent years, nano-structured solid-state solar cells have attracted significant attention. As dye sensitization solar cells they were expected to overcome problems such as electrolyte degradation, confinement deficiencies, corrosion and photochemical deterioration encountered with cells including liquid electrolytes. In the case of organic composite solar cells, the significant progress seen for polymeric diodes should be transferred to solar cell technology. While many research groups have been competing for increasing solar cell efficiencies (4 % for solid-state dye solar cells [1], 3–4 % for organic solar cells [2], problems of long-term photostability have attracted very little attention. Research performed at the Hahn-Meitner Institute using photocurrent imaging techniques and selective illumination strategies showed that there is a problem and that it is quite dramatic. While state of the art organic solar cells, which are not protected against access of oxygen and humidity, are degrading within a few hours [3], solid-state dye solar cells degrade within a few days (100 hrs) to a fraction of their performance (20 %). While in the case of organic cells the inherent instability of the polymer (PPV) and of the fullerene are responsible, in the case of solid-state dye solar cells (TiO_2/dye/CuI) accumulation of electron capturing iodine and the break-up of the apparently essential hydrogen thiocyanate electron bridge were found to be responsible [4]. This experience suggests that competition for higher efficiencies of solid-state nano-composite solar cells only may not be economical for research in the long-term. It is necessary to include phenomena, which are limiting cell stability. This will allow selection of useful components for cell development in an early stage of research. Research performed at the Hahn-Meitner Institute has shown that studies on photodegradation are especially useful in pinpointing specific mechanisms, which are essential for a long-term function of the cell. Typically those reaction steps start failing or degrading, which are critically involved in energy conversion. In this way mechanistic pathways can be identified, which also determine efficiency. The ultimate research aim should be to understand the mechanisms and to design nano-composite solar cells made-up of inherently stable components. The nano-materials involved have especially to satisfy the condition that quantum processes do not chemically modify or disrupt their interfaces, which mediate the reaction of photogenerated electrons of holes.

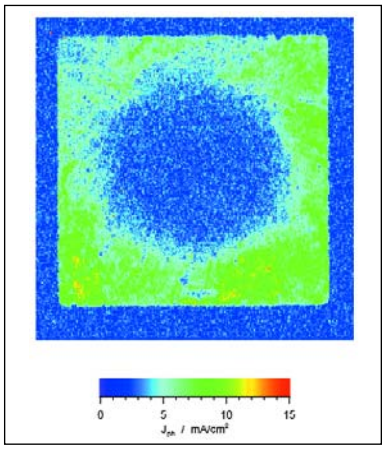

Fig. 1: A TiO_2/Ru-dye/CuI solid-state solar cell, which at the beginning showed photocurrent densities in the red/yellow range, deteriorated to the above performance (1/3 of initial) within 75 hrs under simulated solar light illumination. While the round illumination spot is clearly visible, also the surrounding area has deteriorated. This indicates that migrating photogenerated carriers are also involved.

[1] K. Tennakone, J. Bandara, K.P.M. Bandaranayake, G.R. A. Kumara, A. Konno, Jpn. J. Appl. Phys. **60**, 3558 (1986).
[2] C.J. Brabec, N.S. Sariciftci, in Conjugated Polymers, Eds. G. Hadziannou, P. Van Hutten, Wiley-VCh, Weiningen (1999).
[3] T. Jeranko, H. Tributsch, N.S. Sariciftci, J.C. Hummelen, Sol. Energ. Mat. Sol. Cells, in press (2004).
[4] P.M. Sirimanne, H.Tributsch, Sol. State Chem., in press (2004).

Successful Electrochemical Removal of Cu-S phases from $CuInS_2$ (CIS) Films

H. J. Lewerenz, B. Berenguier, M. Aggour, T. Wilhelm, H. Jungblut, M. Kanis
■ HMI, SE5

The application of the ternary chalcopyrite $CuInS_2$ on a large scale depends crucially on the omission of toxic steps and phases. One such step is the selective etching of Cu-S phases which are formed during CIS layer preparation. This is currently done with toxic KCN solutions. Previous experiments have shown that treatments of CIS in acidic vanadium(II/III) electrolytes yielded photoelectrochemical solar cells (PECS) of moderate efficiencies (1.3 %). The application of specific potential ramps as shown in Fig. 1 leads to a distinctly improved cell performance. At the start, the potential is increased from open circuit potential (–0.2 V) to 0.45 V, where the potential is kept constant for 50 s (potentials are given vs. saturated calomel electrode, SCE). The current maximum indicates a dissolution reaction, the subsequent current drop a passivating behaviour. The potential is then reduced to –0.2 V and kept for another 50 s. With each repetition of this potential scan, the dissolution current peaks at the onset of the anodic potential plateaus become smaller. Concurrently, an increase of the cathodic photocurrents at the cathodic potential plateaus is observed. The procedure is continued until the dissolution peaks are no longer discernible and the photocurrents do not change any more (treatment A). The resulting films exhibit an efficiency of 2.8 % in PECS and 4 % in solid state solar cells (cf. Fig. 5, blue curve).

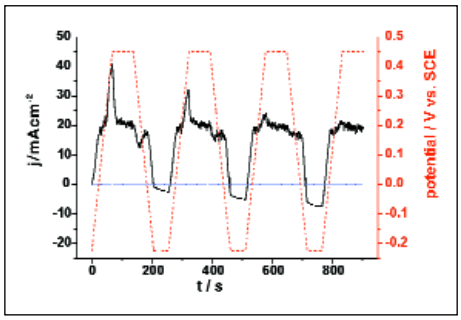

Fig. 1: Plots of current density (solid black line) and applied potential (dotted red line) vs. time during electrochemical etching in V^{2+}/V^{3+} electrolyte (treatment A). At the end of each increasing potential ramp a current maximum caused by Cu_xS-dissolution is visible, which decreases with number of repetitions.

The investigation of correspondingly treated samples by X-ray emission spectroscopy (XES) indicates that Cu-S phases still remain which are identified as Cu_2S. From the standard Gibbs energies of formation for different Cu_xS species, the dissolution potential for Cu_2S can be expected to be more anodic than that for CuS [1]. A cyclic voltammogram of an as-grown CIS sample (see Fig. 2) clearly shows peaks attributable to different corrosion reactions. The dissolution of CIS itself starts at 0.6 – 0.8 V.

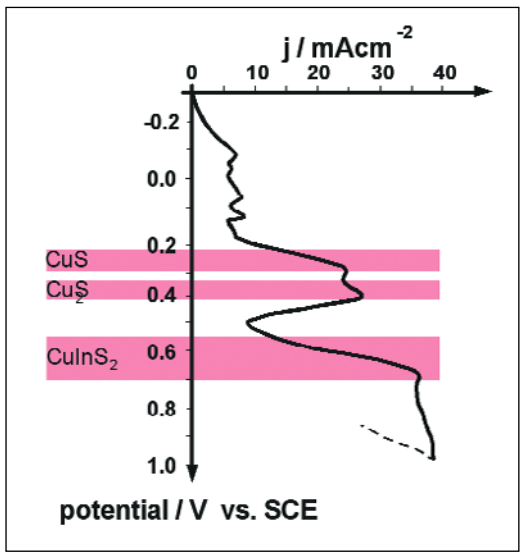

Fig. 2: First sweep of a cyclic voltammogram of a CIS film in V^{2+}/V^{3+} electrolyte; estimated dissolution potential ranges for different species are marked red.

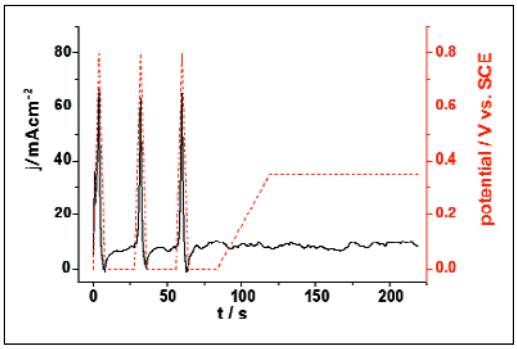

Fig. 3: Plots of current density (solid black line) and applied potential (dotted red line) vs. time during electrochemical etching in V^{2+}/V^{3+} electrolyte (treatment B). The dissolution potential sweeps were carried out with a scan speed of 50 mVs^{-1}, the last sweep was done using 10 mVs^{-1}.

Since the dissolution kinetics of Cu_2S are unknown, a short increase of the dissolution potential to 0.8 V is applied to dissolve the remaining Cu_2S and some CIS. These considerations lead to the electrochemical procedure shown in Fig. 3.

The potential is scanned between 0 V and 0.8 V and back to 0 V with a high scan rate (50 mVs^{-1}) to avoid undesired damage of the CIS substrate. Subsequently it is kept at 0 V for 50 s. This permits the removal of reaction products (and detached insoluble fragments) from the surface. The procedure is repeated for a few times (treatment B, see Fig. 3). This treatment leads, however, still to reduced solar conversion efficiencies of 1.1 % (PECS) and 3 % (solid state solar cells).

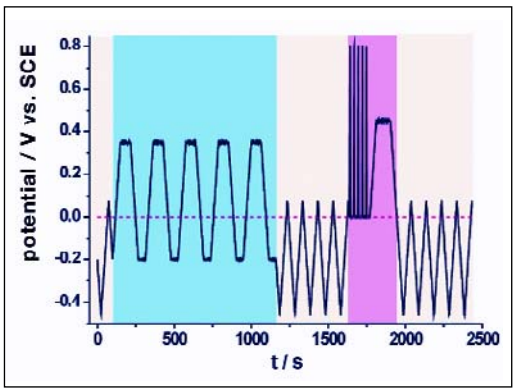

Fig. 4: Complete electrochemical potential vs. time characteristic consisting of treatment A (marked blue) and the more aggressive treatment B (marked pink). PECS evaluation steps are marked yellow.

The combination of both methods (treatment A and treatment B) leads finally to CIS layers with qualities comparable to those of KCN-etched specimen [2, 3]. Fig. 4 shows the complete potential program consisting of the modification procedures and inserted PECS testing steps which admit the in-situ control of the CIS film quality during the treatment.

Fig. 5 shows the j-V characteristic of a solid state solar cell made from a CIS sample after the combined electrochemical etching procedure (red curve). The respective characteristics are: $\eta = 8$ %, $ff = 52$ %, $V_{oc} = 0.69$ V and $j_{sc} = 10.5$ $mAcm^{-2}$. For a KCN etched reference sample $\eta = 11.2$ %, $ff = 69.4$ %, $V_{oc} = 0.72$ V, $j_{sc} = 11$ $mAcm^{-2}$ are obtained.

The results show that a directed electrochemical removal of deleterious Cu-S phases from CIS layers is possible without the use of cyanide solutions. Further improvements, particularly with respect to a simplification of the procedure are currently under investigation.

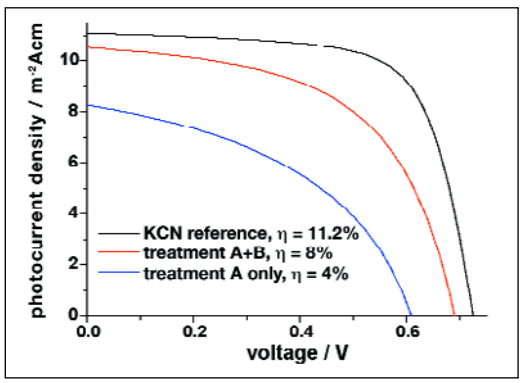

Fig. 5: Solid state solar cell characterstics of CIS layers after treatment A (blue), after combined treatment A and B (red) and after KCN-etch as reference (black). The measurements were made using an AM 1.5 sun simulator.

[1] D. Cahen, Y. Mirovsky, J. Phys. Chem. **89**, 2818 (1985).
[2] B. Berenguier, H.J. Lewerenz, patent applied for (AZ:103 44 315.0)
[3] B. Berenguier, H. J. Lewerenz, J. Electrochem. Soc. Lett., submitted.

Organisational Chart

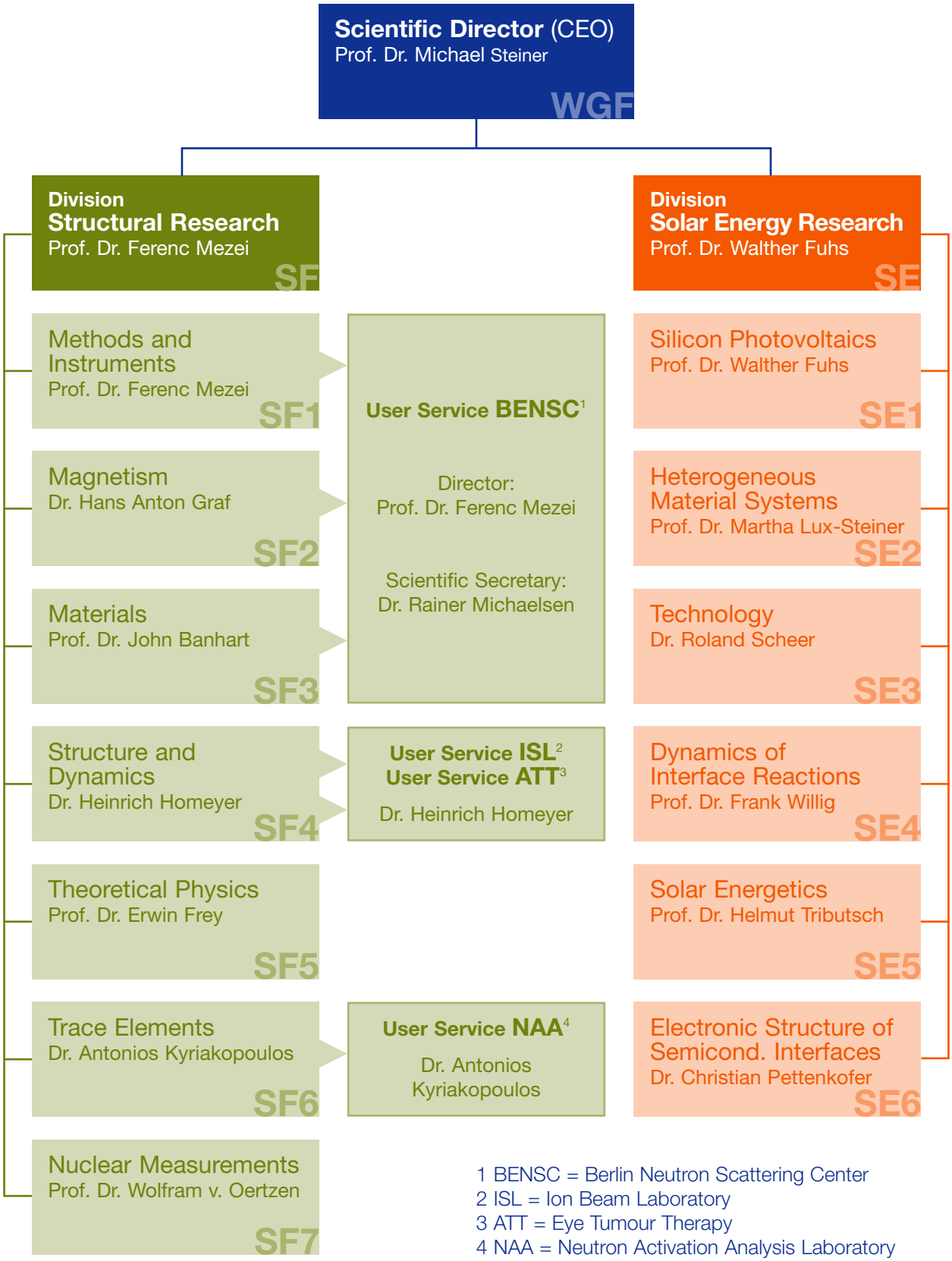

1 BENSC = Berlin Neutron Scattering Center
2 ISL = Ion Beam Laboratory
3 ATT = Eye Tumour Therapy
4 NAA = Neutron Activation Analysis Laboratory

Imprint

1. Edition
June 2004

Annual Report 2003
Selected Results

HMI-B 597
Hahn-Meitner-Institut Berlin GmbH
Glienicker Str. 100
D-14109 Berlin (Wannsee)

Coordinators
Paul Piwnicki
Phone: ++49-30-8062-3252
Fax: ++49-30-8062-2824
E-Mail: piwnicki@hmi.de

Thomas Riedle
Phone: ++49-30-8062-2634
Fax: ++49-30-8062-3199
E-mail: riedle@hmi.de

Book Design
focus werbeagentur, Potsdam
www.focuspotsdam.de

Printing
Brandenburgische Universitätsdruckerei
und Verlagsgesellschaft Potsdam mbH